UNIVERSITAT DE BARCELONA

Study of the extreme gamma-ray emission from Supernova Remnants and the Crab Pulsar

Daniel Galindo Fernández

UNIVERSITAT DE
BARCELONA

STUDY OF THE EXTREME GAMMA-RAY EMISSION FROM SUPERNOVA REMNANTS AND THE CRAB PULSAR

Daniel Galindo Fernández

Departament de Física Quàntica i Astrofísica
Facultat de Física
Universitat de Barcelona

Juny 2018

UNIVERSITAT DE BARCELONA
DEPARTAMENT DE FÍSICA QUÀNTICA I ASTROFÍSICA
Programa de Doctorat en Física
Línia de Recerca en Astronomia i Astrofísica

Study of the extreme gamma-ray emission from Supernova Remnants and the Crab Pulsar

Memòria presentada per
Daniel Galindo Fernández
per optar al grau de
Doctor en Física per la Universitat de Barcelona

Directors de la tesi:
Prof. Josep Maria Paredes Poy
Dra Roberta Zanin
Tutor de la tesi:
Dr Alberto Manrique Oliva

Barcelona, Junio 2018

Dedicado a mis padres, a Luna y especialmente a mi hija Vega.

“*Let me tell you something you already know. The world ain't all sunshine and rainbows. It's a very mean and nasty place, and I don't care how tough you are, it will beat you to your knees and keep you there permanently if you let it. You, me, or nobody is gonna hit as hard as life. But it ain't about how hard you hit. It's about how hard you can get hit and keep moving forward; how much you can take and keep moving forward. That's how winning is done! Now, if you know what you're worth, then go out and get what you're worth. But you gotta be willing to take the hits, and not pointing fingers saying you ain't where you wanna be because of him, or her, or anybody. Cowards do that and that ain't you. You're better than that!*”

– Rocky Balboa

“*Nunca dejes que nadie te diga que no puedes hacer algo. Si tienes un sueño, tienes que perseguirlo. Las personas que no son capaces de hacer algo por ellos mismos, te dirán que tú tampoco puedes hacerlo. ¿Quieres algo? Ve a por ello.*”

– Will Smith, “*En busca de la felicidad*”.

Agradecimientos

Los que me conocen saben que soy hombre de pocas palabras, por lo que esto va a ser escueto.

Quiero agradecer sobre todo a mis padres el apoyo y confianza que siempre me han brindado, para ellos no hay nada que yo no pueda hacer y eso me hace superarme cada día. Gracias por despertar en mí la curiosidad por descubrir qué sorpresas alberga el universo. A ti Papá, por esos maravillosos ratos observando el cielo nocturno cuando íbamos de camping y por enseñarme todo lo que sabías de él. A ti Mamá, por esas tardes en las que jugábamos a recitar los planetas: Mercurio, Venus, la Tierra, Marte, Júpiter, Saturno, Urano, Neptuno y "Plutón"; esto es gracias a ti.

A ti princesa, porque ¿quíen podía imaginarse que la mujer de mi vida se llamaría Luna? Sin tu apoyo y tus ánimos, en definitiva, sin ti a mi lado, no hubiese podido conseguirlo. Gracias por ser tan paciente conmigo y saber aguantarme. Te amo.

A mi preciosa hija Vega, ver cómo me sonríes me hace el hombre más feliz del mundo y me recuerda lo importante que es disfrutar la vida. Aunque aún no eres consciente de ello, sin ti esto hubiese sido mucho más difícil. Espero haber estado a tu altura.

Me gustaría agradecer también a todas las personas que me han ayudado a llegar hasta aquí.

Principalmente a mis directores, Josep Maria Paredes y Roberta Zanin por el tiempo y esfuerzo que me habéis dedicado. A Josep Maria, por darme la oportunidad de entrar en el grupo y por la amabilidad que siempre me has prestado desde que abro la puerta de tu despacho hasta que la cierro. A Roberta, por tu carácter y por acogerme cuando llegué queriendo saber de púlsares.

A Marc Ribó, por tener siempre un momento para resolverme dudas, ya desde la época del máster, a pesar de estar muy atareado. Gracias también por los consejos sobre docencia que me han hecho mejorar en cada clase que he impartido.

A Emma de Oña, por tantos *Skypes*, mails y charlas que me has dedicado, y por tener siempre una solución y explicación para cada problema científico. Pero no solo eso, gracias sobretodo por tu humor, tus comentarios sarcásticos y tu cercanía.

A toda la gente del departamento, desde JR, que con su carácter y positividad te saca de cualquier apuro burocrático haciéndolo parecer fácil, hasta mi compañero de despacho, Dani del Ser, el cual ha tenido que aguantar mis bufidos y cabreos estos años, pasando por todos los profesores y compañeros con los que he conversado y me han ayudado.

A la gente del IFAE, que desde el primer congreso de MAGIC juntos, me trataron como a uno más del grupo, y en especial a Leyre, quien apareció de repente para quedarse para siempre. Gracias por mejorar y amenizar todos los congresos que hemos compartido, por ser la mejor compañera de "shift" que he tenido y por tenderme siempre una mano cuando la necesitaba.

Y finalmente y con especial cariño, a Lidia Crespo y José Ignacio Latorre, por darme ese empujón inicial, ojalá más profesores supiesen transmitir ese interés en lo que explican.

Resumen

El descubrimiento de los rayos cósmicos a principios del siglo veinte por Victor Hess fue la primera pieza de un rompecabezas que actualmente conocemos como astronomía de rayos gamma. A pesar de que han transcurrido más de 100 años, algunas piezas importantes del puzzle están por desvelarse y otras, son aún inciertas. ¿Dónde se originan los rayos cósmicos? ¿Cómo son acelerados? ¿Cómo son emitidos los rayos gamma? Aunque aún estamos lejos de una comprensión total, el campo de la astronomía de rayos gamma ha experimentado un progreso extraordinario durante los últimos quince años. El éxito rotundo cosechado por el satélite *Fermi*, explorando el rango de altas energías, así como el éxito de los "Imaging Atmospheric Cherenkov Telescopes", a muy altas energías, han engrosado las estadísticas de fuentes que emiten rayos gamma hasta varios miles. Entre esta impresionante cantidad de fuentes, una gran variedad de clases de objetos astronómicos diferentes, tanto galácticos como extragalácticos, han sido identificados.

En nuestra Galaxia, los remanentes de supernova y los púlsares, son las dos poblaciones de objetos más numerosas que emiten radiación no-térmica. A pesar de ser objetos muy diferentes, ambos comparten un origen común: la muerte de una estrella masiva (con masa superior a 8 masas solares). Al final de la vida de ésta, una gran explosión expulsa las capas externas de la estrella por medio de una onda de choque, que se propaga a través del medio interestelar que rodeaba la estrella, comprimiendo y calentando el material barrido a su paso. A esto se le llama remanente de supernova y puede albergar en su centro el remanente de la estrella inicial en forma de estrella de neutrones. Estas estrellas de neutrones emiten radiación electromagnética periódica, inducida por su intenso campo magnético y su rotación. Si esta emisión pulsada es detectada por el observador, se les denomina púlsares.

REMANENTES DE SUPERNOVA

Está comprobado que los remanentes de supernova son capaces de acelerar partículas cargadas en su frente de choque, por medio de aceleración difusiva, hasta energías muy altas, para posteriormente inyectarlas al medio interestelar. De hecho, son comúnmente considerados como los causantes de la producción de la mayor parte de los rayos cósmicos galácticos hasta energías de 10^{15} eV (1 PeV). No obstante, todavía falta evidencia observacional de que los remanentes de supernova puedan acelerar de manera eficiente susodichas partículas hasta tales energías. Por eso, la presente tesis tiene como objetivo el estudio de la fuente Cassiopeia A (CasA), uno de los llamados "remanentes de supernova históricos" y el principal candidato de su clase a revelarse como PeVatrón, acelerador de rayos cósmicos hasta energías de 1 PeV.

Las observaciones de CasA presentadas en este trabajo, se han llevado acabo tanto con el "Large Area Telescope" (LAT) a bordo del satélite *Fermi*, como con los telescopios terrestres MAGIC y constan de mas de ocho años de datos, desde Agosto de 2008 hasta Diciembre de 2016 en el caso de *Fermi*, y de 158 horas de observación acumuladas entre Diciembre de 2014 y Octubre de 2016 con MAGIC. Tal cantidad de datos, nos

ha permitido estudiar en detalle el comportamiento espectral de la fuente a energías por encima de los 60 MeV, energía mínima alcanzable con LAT. Por primera vez, se ha detectado un corte en el espectro de rayos gamma en torno a 3 TeV, lo cual implica que la emisión observada es producida por el decaimiento de piones neutros, originados en colisiones protón-protón por una población de protones acelerados que presenta un corte exponencial en su espectro en torno a una energía de 10 TeV. Esta energía maxima a la que son acelerados estos rayos cósmicos (protones) en CasA, se queda por tanto muy corta a la hora de justificar los rayos cósmicos Galácticos de 1 PeV. Considerando que CasA era el candidato a PeVatrón por excelencia, los resultados obtenidos en esta tesis cuestionan la existencia de remanentes de supernova que se comporten como PeVatrones, y por tanto, la teoría de que éstos son la fuente principal de rayos cósmicos galácticos hasta la *rodilla*.

El estudio de las interacciones entre los remanentes de supenova y su entorno, como podrían ser las nubes moleculares, en las cuales se forman las estrellas, y por ende, ocurren las explosiones de supernova, también es de gran importancia. Se sabe que los rayos cósmicos que escapan del confinamiento del frente de choque, pueden colisionar con protones pertenecientes a la nube molecular y emitir rayos gamma mediante decaimiento de piones neutros. Esto permite que los rayos cósmicos más energéticos, que son los primeros que escapan del remanente, puedan ser observados en su posterior interacción con las nubes moleculares, pudiendo así comprobar si en algún momento el remanente ha sido capaz de acelerar protones hasta energías de en torno al PeV. En esta tesis, hemos observado con los telescopios MAGIC y *Fermi*-LAT, la región celeste en torno al remanente de supernova detectado en radio, SNR G24.7+0.6, en busca de su contrapartida a muy altas energías. SNR G24.7+0.6 está evolucionando en un medio denso y podría estar interaccionando con su entorno rico en CO, lo cual lo convierte en un buen objetivo para el estudio de esta interacción, así como de la energía máxima a la que los protones han sido acelerados. Las observaciones realizadas, han dado como resultado el descubrimiento de dos nuevas fuentes a muy altas energías. La primera, MAGIC J1835–069, relacionada con SNR G24.7+0.6, ha sido detectada hasta energías de 5 TeV con un espectro de energías que conecta bien con el obtenido por *Fermi*-LAT. Además, su posición y extensión coincide parcialmente con el de la fuente en radio, lo que es interpretado como protones que escapan del remanente de supernova y que interaccionan con una nube molecular cercana. El hecho de que la emisión gamma detectada únicamente alcanze unos pocos TeV, implicaría que los rayos cósmicos que están siendo acelerados en el remanente no superarían las pocas decenas de TeV. La segunda fuente detectada, MAGIC J1837–073, está muy probablemente asociada con un cúmulo estelar, tal y como sugiere su localización en una zona plagada de fuentes y con alto contenido molecular. La energía total en protones que emite, puede ser explicada asumiendo una inyección casi continua de rayos cósmicos durante la totalidad de la vida estimada del cúmulo estelar.

EL PÚLSAR DEL CANGREJO

La segunda parte de la tesis está enfocada al estudio y entendimiento de los púlsares. Pese al gran número de púlsares de rayos gamma observados, el comportamiento de éstos está aún por entenderse. Dónde se aceleran las partículas, qué mecanismos están en juego en la emisión de la radiación que observamos, qué energía máxima puede alcanzar esta radiación o porqué únicamente dos púlsares han sido detectados por encima de 100 GeV son solo algunas de las preguntas que aún buscan respuesta. Para tratar de dar respuesta a estas preguntas, en esta tesis nos hemos centrado en el que sin duda es el púlsar más estudiado a lo largo de todo el espectro electromagnético, el púlsar del Cangrejo. Debido a que es relativamente joven y que es el púlsar más potente de nuestra galaxia, es el objetivo perfecto para testear cualquier modelo teórico acerca de la emisión pulsada e investigar la radiación gamma que emite.

El estudio del púlsar del Cangrejo llevado a cabo, consta de más de 300 horas de observación acumuladas con los telescopios MAGIC durante un periódo de 7 años, lo que lo convierte en el análisis más extenso realizado hasta la fecha en MAGIC. El objetivo principal de este análisis, es inspeccionar el rango más alto de su espectro de energías para discernir si realmente presenta un corte en torno a algunos cientos de GeV como preveen ciertos modelos. Los resultados que hemos obtenido muestran que realmente la emisión pulsada se extiende hasta al menos 1.5 TeV, refutando cualquiera de los modelos postulados hasta el momento. Además, la curva de luz que caracteriza la emisión proveniente del púlsar por encima de 400 GeV, presenta dos picos sincronizados en fase con los picos hallados a energías más bajas. El análisis conjunto con los datos registrados por *Fermi*-LAT, nos ha permitido obtener una visión global del espectro y descubrir, que realmente el espectro de energías de ambos picos está definido por una ley de potencias de índice $\sim$3 que se extiende desde 10 GeV hasta 600 GeV y 1.5 TeV para los picos P1 y P2 respectivamente. Esta emisión pulsada, extremadamente energética, descubierta con MAGIC, únicamente puede ser producida por electrones acelerados hasta factores de Lorentz muy altos en regiones cercanas al cilindro de luz, ya sea en su interior o en su exterior, y que posteriormente colisionan y transfieren su energía a fotones térmicos. Actualmente, nuevos modelos están siendo propuestos para tratar de dar una interpretación teórica a los resultados obtenidos, no obstante, ninguno de ellos es todavía capaz de explicar satisfactoriamente a su vez el espectro y la curva de luz halladas en este trabajo.

Abstract

The discovery of Cosmic Rays in the early twentieth century by Victor Hess set the first piece of a puzzle known as gamma-ray astronomy. Despite more than 100 years have gone by, many important pieces of information are still missing or at least uncertain: Where do Cosmic Rays originate? How are they accelerated? How do they emit gamma rays?

Although we are still far from complete knowledge, the field of gamma-ray astronomy has experienced an extraordinary progress over the last fifteen years. The success of the *Fermi* satellite in the exploration of the high energy band along with the success of Imaging Atmospheric Cherenkov Telescopes in the very high energy band have grown the number of detected gamma-ray emitting sources to several thousands. Among this wealth of sources a wide variety of different galactic and extragalactic astrophysical objects have been identified.

In our Galaxy, supernova remnants and pulsars are the two most numerous populations of non-thermal objects. On one hand, supernova remnants are believed to originate the bulk of the Galactic Cosmic Rays. But, can they really efficiently accelerate particles to such energies? Full coverage of the gamma-ray energy range with X-ray satellites, *Fermi*-LAT and Imaging Atmospheric Cherenkov Telescopes, provides a unique perspective for the study of Cosmic Ray acceleration within supernova remnants. On the other hand, even though the large number of gamma-ray pulsars detected, only and exclusively two have been detected above hundred GeV. Why? Which is the mechanism at work that produces such emission? Where is this radiation being produced? Pulsars offer perfect test-benches to expand our understanding of the physics of matter in extreme conditions.

This thesis will try to unravel some of the open questions about these two very different astrophysical objects, supernova remnants and pulsars, originated in the same phenomenon.

The first part of this thesis is dedicated to introduce gamma-ray astronomy. Cosmic ray particles and gamma ray production and absorption mechanism are presented in Chapter 1. The imaging technique and analysis chain used in this work to study these energetic particles with the MAGIC telescopes are discussed in Chapter 2. Finally, the *Fermi*-LAT observation technique and data analysis procedure used for this thesis are presented in Chapter 3.

The second part is devoted to supernova remnants. After a short overview of the current knowledge of these objects (Chapter 4), two specific sources observed with *Fermi*-LAT and MAGIC telescopes, are discussed. Chapter 5 presents the observations and results obtained from Cas A, one of the historical supernova remnants and the prime candidate of its class to be a PeVatron accelerator. Chapter 6 focuses on the search of the very high energy counterpart of SNR G24.7+0.6, that is evolving in a dense medium and might be interacting with the CO-rich surrounding.

The last part of this thesis is committed to the study of pulsars. A brief review of the status of rotation powered pulsars is presented (Chapter 7) to introduce the reader onto the most studied pulsar, the Crab Pulsar. MAGIC observations of the Crab Pulsar that resulted in the largest dataset ever analyzed within the MAGIC Collaboration and led to striking results are discussed in Chapter 8 together with those obtained with *Fermi*-LAT.

Contents

Part I

ASTROPHYSICAL INTRODUCTION AND OBSERVATION METHODOLOGY

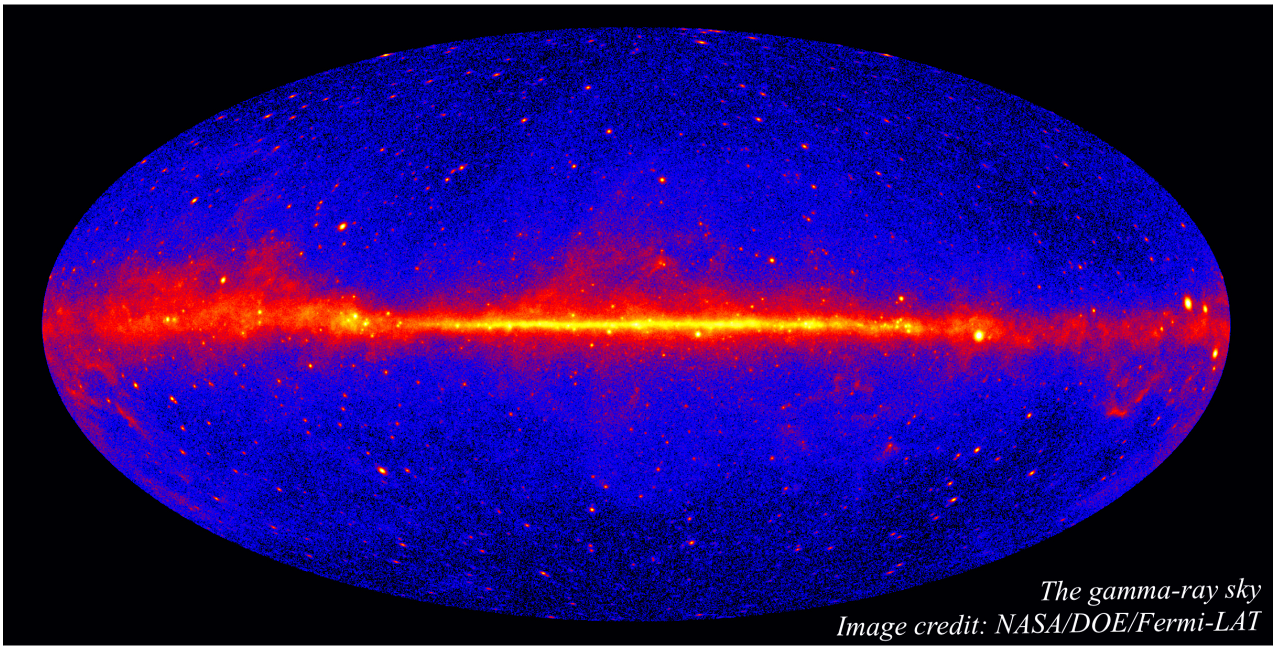

Chapter 1

High energy γ-ray astronomy

1.1 Introduction

γ-ray astronomy is the field of study that covers the observation of photons with energies above few hundreds of keV. Although theoretically there is no upper energy limit to γ-rays, only energies up to about hundreds of TeV can be observed by the current generation of detectors. Such energies cannot be attained in thermal processes as no place in the universe is hot enough to produce radiation above few MeVs. Therefore, the underlying γ-ray emission processes at work are of non-thermal nature. This non-thermal radiation is associated to the presence of accelerated charged particles, known as Cosmic Rays (CRs), that in their interaction with radiation and electromagnetic fields in the environment of different astrophysical sources produce the high energetic γ-ray emission observed.

In this chapter we cover the basics of cosmic radiation and provide a brief overview of the different processes they go through to produce the γ-ray emission we detect on Earth. Some of the potential sources originating this Very High Energy (VHE) emission are also briefly recapitulated in the last section.

1.2 Cosmic Rays

Victor Franz Hess discovered in 1912 what we nowadays call CRs. These energetic particles of extraterrestrial origin are accelerated in different astrophysical sources and propagate through the Universe. It was found that the CRs are composed of charged particles, mainly protons and Helium nuclei, as well as electrons, positrons, neutrons and other heavier elements, to a lesser proportion.

Detection of CRs, however, it is not straight forward since they are deflected and isotropized by the magnetic fields present in the Universe. Thus, γ-rays and neutrinos resulting from the interaction of CRs with matter and electromagnetic fields must be used as possible tracers to the place of their creation. CRs are currently studied following three different approaches that allow us to either detect them or their by-products:

- *Balloon experiments* dedicated to the study of the element composition of CRs within the range from $\sim 10^{11}$ to 10^{15} eV.
- *Space-based telescopes* aimed at the detection of γ-rays in the MeV-GeV energy range (e.g. *AGILE* (Tavani et al., 2009) or *Fermi* (Atwood et al., 2009)).

- *Ground-based detectors* addressed to study energies of γ-rays above the GeV range up to even more than $\sim 10^{18}$ eV.
    - *Imaging Atmospheric Cherenkov Telescopes* such as Major Atmospheric Gamma-ray Imaging Cherenkov (MAGIC) telescopes (Ferenc et al., 2005), High Energy Stereoscopic System (HESS) (Hofmann et al., 2003) or Very Energetic Radiation Imaging Telescope Array System (VERITAS) (Holder et al., 2006).
    - *Water Cherenkov Arrays* such as Pierre Auger observatory (Abraham et al., 2004) or High-Altitude Water Cherenkov (HAWC) observatory (Weisgarber, 2013).

However, in spite of the continuous improvement of the observations techniques, there are still a great variety of CRs features we cannot explain, such as what their origin is or the maximum energy they can reach.

1.2.1 The Energy Spectrum

Figure 1.1 shows the CR spectrum as measured by various experiments along the years. The flux level over the entire energy range, spanning ~12 energetic decades from 10^8 to more than 10^{20} eV, changes by more than 30 orders of magnitude. Such a spectrum is clearly of non-thermal origin as it cannot be accounted for by thermal bremsstrahlung or black-body radiation.

Approximately, the flux spectrum follows a power-law distribution given by

$$N\left(E\right)dE \propto E^{-\Gamma}dE, \tag{1.1}$$

with spectral index $\Gamma = 3$, as represented by the green dashed line in Figure 1.1. However, a close inspection highlights that between 100 GeV and 5 PeV the CR spectrum is better described by a harder spectral index of $\Gamma \sim 2.7$. Beyond the first inflection point at 5 PeV, commonly know as the *knee*, the spectrum steepens to $\Gamma \sim 3.2$ until 3 EeV where it hardens again at the second inflection point, the so-called *ankle*.

The different spectral slopes are thought to be related with a different origin of CRs. It is believed that particles below the knee are of galactic origin while those above the ankle are likely extragalactic, since particles with those energies cannot be confined within the Galaxy. At ultra-high-energies (beyond 10^{19} eV), the spectrum turns off due to the onset of inelastic interactions between CRs and photons of the Cosmic Microwave Background (CMB) radiation, as first discussed by Greisen (1966) and Zatsepin and Kuz'min (1966). At the lowest part of the spectrum, below 1 GeV, the flux also presents a cut-off due to solar modulation whereby interstellar CRs diffuse in towards the Earth through the solar wind.

1.2.2 The acceleration of cosmic rays

The formation of a power-law spectrum extending up to energies of 10^{20} eV is an important feature that any plausible acceleration process must account for. The general consensus is that CRs are accelerated via Diffusive Shock Acceleration (DSA) mechanisms, proposed by Fermi (Fermi, 1949).

The *first-order Fermi acceleration* involves a strong shock wave propagating through the Interstellar medium (ISM) with velocity V. In the case of an adiabatic shock

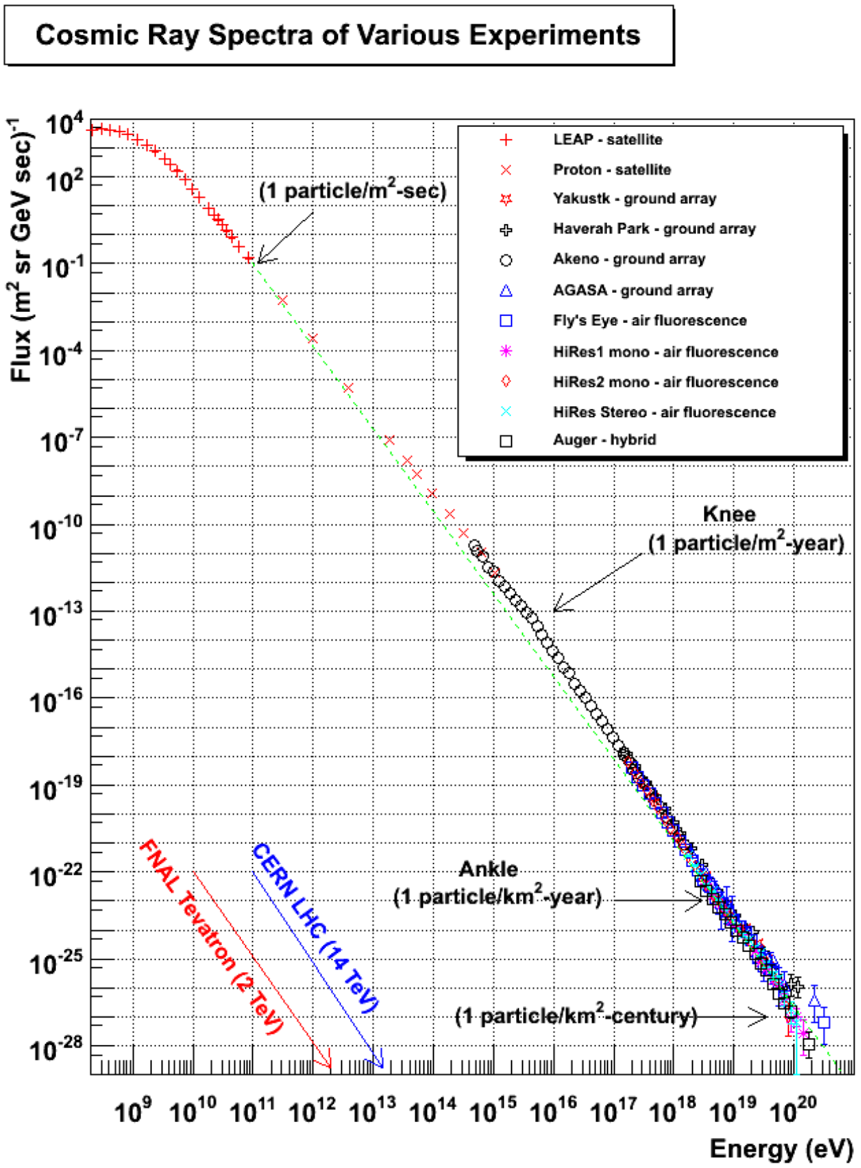

FIGURE 1.1: CR spectrum measured by different experiments. Credit: Hanlon (2012).

propagating into an ideal plasma, the gas downstream of the shock moves with a velocity of $\frac{3V}{4}$ (Longair, 2011). Particles in the upstream region crossing the shock into the downstream region receive an increase of energy of $\langle\frac{\Delta E}{E}\rangle = \frac{2V}{3c}$ (as shown in *left* of Figure 1.2) and are scattered by the irregularities of the magnetic field so that their velocity distribution becomes isotropic in the downstream frame of reference. Now, in the frame of the shocked gas, i.e. downstream region, the material upstream of the shock travels downwards with a velocity $\frac{3V}{4}$, hence, particles downstream can cross the shock again boosting their energy another $\langle\frac{\Delta E}{E}\rangle = \frac{2V}{3c}$ (*right* of Figure 1.2). This process repeats until the diffusion length of particles is larger than the size of the shock, moment at which particles are swept away from it. After k crossings, there will be $N = N_0 P^k$ particles in the shock with energies $E = E_0\beta^k$, where β and P are the average energy of the particles and the probability they remain in the shock after a

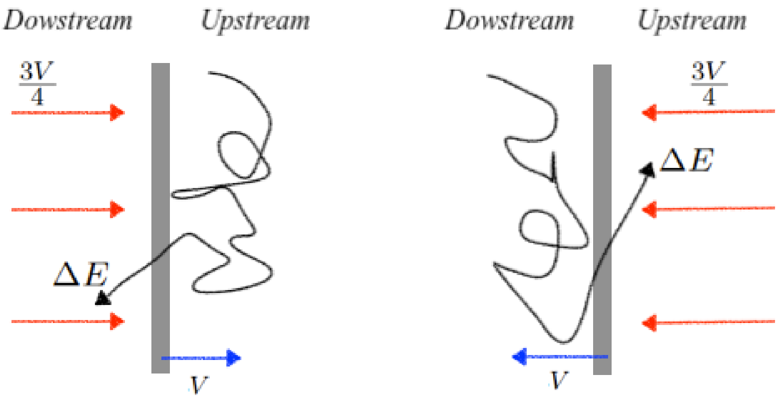

FIGURE 1.2: Sketch of the first-order Fermi acceleration mechanism. Particles upstream cross the shock into the downstream region gaining an energy of ΔE. In the same way, particles downstream can cross the shock into the upstream region gaining another ΔE. *Left*: Rest frame of the upstream region, the gas in downstream region move with velocity $\frac{3V}{4}$. *Right*: Rest frame of the downstream region, gas in upstream region move with velocity $\frac{3V}{4}$.

crossing, respectively. Combining both equations,

$$\frac{\ln(N/N_0)}{\ln(E/E_0)} = \frac{\ln P}{\ln \beta} \implies \frac{N}{N_0} = (E/E_0)^{\ln P/\ln \beta}. \tag{1.2}$$

Assuming this process repeats as not all the particles would have been able to escape the acceleration region,

$$\frac{dN(E)}{dE} \propto E^{-1+\frac{\ln P}{\ln \beta}} \tag{1.3}$$

that leads naturally to a resulting power-law energy spectrum of accelerated particles as required by the CR spectrum.

The *second-order Fermi acceleration* occurs when charged particles are scattered by moving magnetic mirrors associated with Galactic magnetic field irregularities, Figure 1.3. The energy gain per scattering event is proportional to the square of the velocity of the moving magnetic mirror and independent on the particle energy, $\langle \frac{\Delta E}{E} \rangle \propto \frac{v_{mirror}^2}{c^2}$. Assuming the particle remain within the acceleration region for some time, the particle spectrum obtained from the diffusion-loss equation follows a power-law distribution. This mechanism, however, is very inefficient as it result in a very slow gain of energy by the particles for typical velocities of the mirrors in the Galaxy.

Based on both mechanisms treated here, the maximum energy CRs can achieve is determined by (Hillas, 1984):

$$E_{max} = ZeUBR_{obj} \tag{1.4}$$

where U is the speed of the shock, Ze the charge of the particle and B and R are the magnetic field and size of the source. Therefore, potential sources of CR particle acceleration must be able to reach such energies. Some of these potential sources will be reviewed in section 1.4.

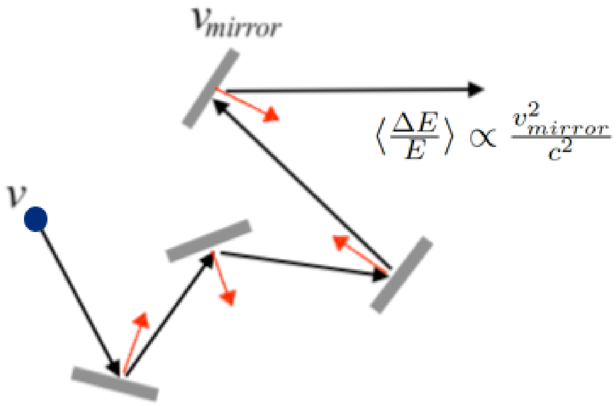

FIGURE 1.3: Sketch of the second-order Fermi acceleration mechanism. Particles with velocity v scatter against a magnetic mirror moving with velocity v_{mirror} and gain energy in each shock.

1.3 γ-ray production and absorption mechanisms

γ-rays are the most energetic photons found in nature extending from 511 keV (annihilation radiation) up to hundreds of TeVs. They are produced in interactions of charged High Energy (HE) CRs with their surrounding environment but they can also be absorbed the same way. Some of the processes relevant for γ-ray production and absorption are briefly summarized in the following. More detailed and extended treatments can be found in Longair (2011) and Aharonian (2004) and references therein.

1.3.1 Synchrotron radiation

Sychrotron radiation occurs when charged particles are under the influence of a magnetic field (see Figure 1.4).

$$q + B \rightarrow q + B + \gamma \tag{1.5}$$

HE electrons move with velocity v in a spiral path around magnetic field lines with constant pitch angle (α), as they accelerate towards the center of the orbit they emit radiation beamed in the direction of motion. The total energy loss rate by synchrotron radiation in the relativistic regime is

$$-\frac{dE}{dt} = 2\sigma_T c U_{mag} \gamma^2 sin^2\alpha \tag{1.6}$$

where σ_T is the Thomson cross-section, c the speed of light, U_{mag} the energy density of the magnetic field, γ the Lorentz factor of the electron and α the pitch angle.

The radiation spectrum resulting from a power-law distribution of electrons, $N_e(E) \propto E^{-\Gamma}$, is characterized by another power-law distribution of $N_\gamma(\epsilon) \propto \epsilon^{-\left(\frac{\Gamma+1}{2}\right)}$. The characteristic energy of photons emitted by synchrotron radiation is given by

$$E_\gamma = \frac{3}{2}\gamma^3 \hbar \frac{c}{r_g} \tag{1.7}$$

where $r_g = \gamma m_e c v sin\alpha / eB$ is the radius of the helical path.

Synchrotron emission is negligible at VHE since electrons need to be very energetics, however, synchrotron photons can have an important role as target for Inverse Compton (IC) scattering.

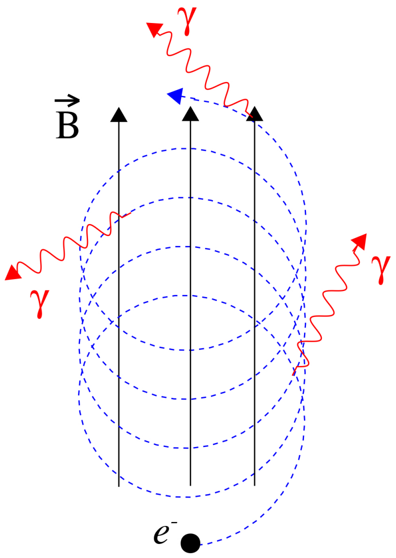

Figure 1.4: Synchrotron radiation mechanism.

1.3.2 Curvature radiation

Curvature radiation is similar to synchrotron radiation, only this time the radiation is produced by the charged particle following the curvature of the magnetic field lines (see Figure 1.5). When both processes contribute to the γ-ray emission it is called synchro-curvature radiation.

Curvature γ-rays are proportional to the curvature radius of the magnetic field r_C and the Lorentz factor of the electron γ,

$$E_\gamma = \frac{3}{2} \hbar c \frac{\gamma^3}{r_C}. \tag{1.8}$$

For a population of electrons following a power-law energy spectrum $N_e\left(E\right) \propto E^{-\Gamma}$, the resulting γ-ray spectrum will be characterized by $N_\gamma\left(\epsilon\right) \propto \epsilon^{-\left(\frac{\Gamma+1}{3}\right)}$.

This mechanism is usually at work in regions of extreme magnetic fields ($B \sim 10^{11} - 10^{13}\,\mathrm{G}$), such as pulsars, where charged particles emit synchrotron radiation very efficiently. Consequently, they quickly transit to the ground Landau level and start sliding along the magnetic field lines emitting curvature radiation with energies up to few GeVs.

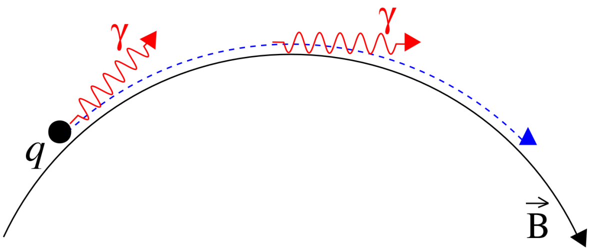

FIGURE 1.5: Curvature radiation mechanism.

1.3.3 Bremsstrahlung

Bremsstrahlung (Figure 1.6) is the radiation emitted by a charged particle accelerated in the electric field of another particle.

$$q + Z \rightarrow q + Z + \gamma \tag{1.9}$$

The energy loss rate of ultra-relativistic electrons by bremsstrahlung is given by:

$$-\frac{dE}{dt} = 4nZ^2r_e^2\alpha c\overline{g}E \tag{1.10}$$

where n is the density of atoms in the target, Z the atomic number of the target, r_e the classical radius of the electron, α the fine structure constant, c the speed of light and $\overline{g}$ the frequency averaged Gaunt factor (Heitler, 1954).

Its density dependence makes bremsstrahlung the dominant energy loss process for high relativistic electrons in dense regions. Moreover, a power-law distribution of electrons, $N_e\left(E\right) \propto E^{-\Gamma}$ results in a γ-ray spectrum of the same power-law form, $N_\gamma\left(\epsilon\right) \propto \epsilon^{-\Gamma}$.

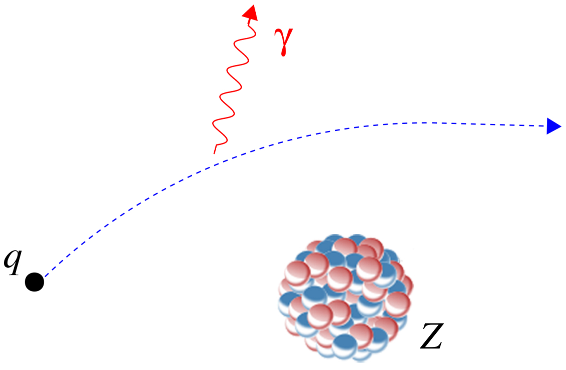

FIGURE 1.6: Bremsstrahlung radiation mechanism.

1.3.4 Inverse Compton Scattering

In IC scattering (see Figure 1.7), ultra-relativistic electrons scatter ambient photons to high energies. Unlike in Compton scattering, electrons transfer most of its energy to the target photon.

$$e^{-} + \gamma_{low} \rightarrow e^{-} + \gamma_{high} \tag{1.11}$$

This process can occur in two different regimes depending on the photon energy in the rest frame of the electron:

Thompson regime: the photon energy in the electron's frame is much less than $m_e c^2$ and the probability of scattering is given by the Thompson cross section, that is independent of the energy, $\sigma_T = \frac{8\pi}{3} r_e^2$. The maximum energy the photon can reach after the scattering is $E_{max} \sim 4\gamma^2 E_\gamma$, where γ is the Lorentz factor of the electron and E_γ the inicial energy of the photon in the laboratory frame.

Klein-Nishina regime: the photon energy is much higher than $m_e c^2$, and the electron transfer all its energy to the photon in one interaction. The cross section can be approximated as $\sigma_{K-N} = \pi r_e^2 \frac{1}{x}(\ln 2x + \frac{1}{2})$. Here r_e is the classical electron radius and x is the ratio $\frac{m_e c^2}{\hbar\omega}$.

The energy losses in both regimes have different dependency on the electron energy, while in the Thompson regime the loss rate is proportional to the square of the electron energy, in the Klein-Nishina regime it is almost energy independent. Therefore, for a power-law distribution of electrons, $N_e(E) \propto E^{-\Gamma}$, the resulting γ-ray spectrum for the Thompson regime has a power-law form of $N_\gamma(\epsilon) \propto \epsilon^{-\frac{(\Gamma+1)}{2}}$ while for the Klein-Nishina regime the γ-ray spectrum follows $N_\gamma(\epsilon) \propto \epsilon^{-(\Gamma+1)}$.

IC is one of the most important γ-ray production processes. Although the efficiency of the production depends on the density of the photon field, CMB photons provide a persistent and unavoidable source of targets for this process.

A special case of IC scattering is produced when electrons emit low energy synchrotron photons that are up-scattered by the same electron population to γ-ray energies. This process known as Synchrotron-Self-Compton (SSC) radiation is of special importance in regions with high magnetic fields such as pulsars.

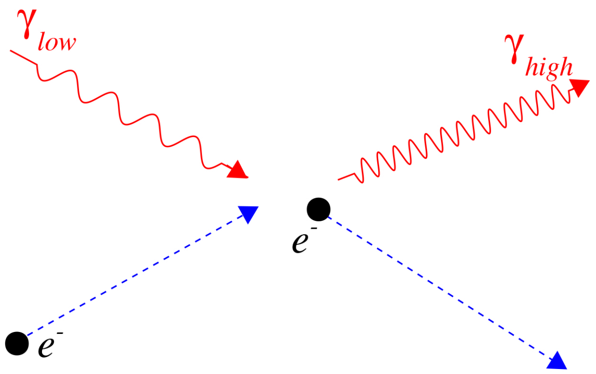

FIGURE 1.7: IC radiation mechanism.

1.3.5 Pion decay

The interaction of primary particles with target nucleus present in the acceleration region or with the ISM result on emission of neutral pions (π^0) and charged pions

($\pi^{\pm}$) with equal probability. Neutral pions have short lifetimes ($\sim 10^{-16}\,\mathrm{s}$) before decaying into two γ-rays while charged pions have longer lifetimes ($\sim 10^{-8}\,\mathrm{s}$) and decay generally into muons (Figure 1.8).

$$\pi^0 \rightarrow 2\gamma \tag{1.12}$$

$$\pi^+ \rightarrow \mu^+ + \nu_\mu \tag{1.13}$$

$$\mu^+ \rightarrow e^+ + \nu_e + \overline{\nu}_\mu \tag{1.14}$$

$$\pi^- \rightarrow \mu^- + \overline{\nu}_\mu \tag{1.15}$$

$$\mu^- \rightarrow e^- + \overline{\nu}_e + \nu_\mu \tag{1.16}$$

If the energy spectrum of pions follows a power-law of $N_\pi(E) \propto E^{-\Gamma}$, then the resulting γ-ray spectrum has the same index, $N_\gamma(\epsilon) \propto \epsilon^{-\Gamma}$.

The identification of pion decay γ-rays is difficult due to the contribution of the leptonic processes already mentioned, however, it can become very significant in dense mediums.

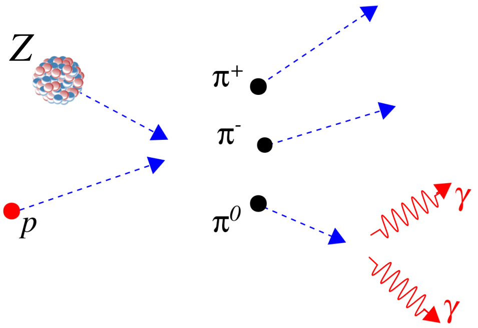

FIGURE 1.8: Pion decay radiation mechanism.

1.3.6 $e^- - e^+$ annihilation

Annihilation occurs when a charged particle collides with its antiparticle, producing two photons carrying away the energy and momentum of the system (Figure 1.9).

$$e^- + e^+ \rightarrow \gamma + \gamma \tag{1.17}$$

For $e^- - e^+$ annihilation occurring at their rest frame, γ-rays are produced with energies $E_\gamma = m_e c^2 = 511\,\mathrm{keV}$. This is the minimum energy a γ-ray can obtain in the process.

1.3.7 Pair production

Two pair production:
The interaction of a HE photon with a low-energy photon above a certain threshold,

$$E_1 E_2 > \left(m_e c^2\right)^2 \frac{1 - cos\theta}{2} \tag{1.18}$$

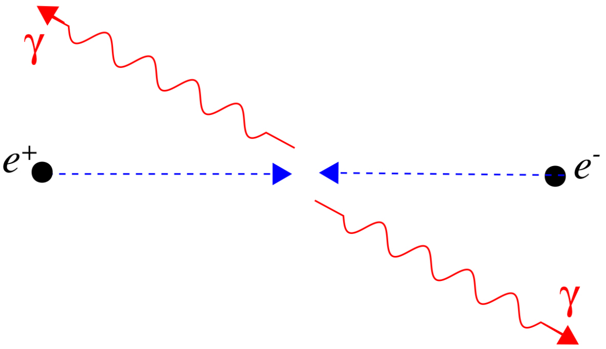

FIGURE 1.9: $e^- - e^+$ annihilation mechanism.

would result in the production of a pair $e^- - e^+$ (Figure 1.10).

$$\gamma_{high} + \gamma_{low} \rightarrow e^- + e^+ \tag{1.19}$$

The maximal efficiency of this process results from integrating the cross section over all the collision angles and it is reached for photon energies satisfying $\frac{E_1 E_2}{(m_e c^2)^2} \approx 3.7$. Therefore, for a VHE γ-ray the reaction would be maximized with Ultra-Violet (UV) to Infrared (IR) photons.

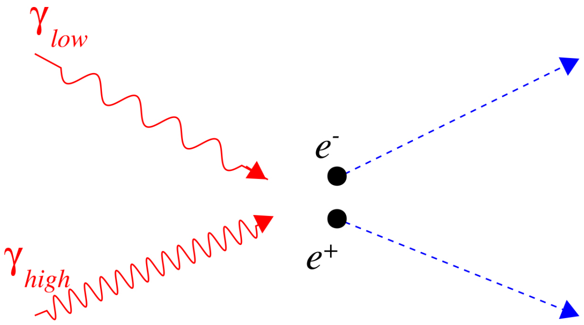

FIGURE 1.10: Pair creation mechanism.

Magnetic pair production:
$e^- - e^+$ pairs can also be created when photons interact with magnetic fields (Figure 1.11).

$$\gamma + B \rightarrow e^- + e^+ \tag{1.20}$$

The mean free path of photons moving with an angle θ_B with respect of a magnetic field is characterized by (Ruderman and Sutherland, 1975)

$$\lambda_B = 6\frac{m_e c^2}{eBsin\theta_B} e^{\left(\frac{8}{3}\frac{B_{cr}}{B\sin\theta_B}\frac{m_e c^2}{\epsilon}\right)} \tag{1.21}$$

where ϵ is the energy photon and $B_{cr} = m_e^2 c^3/e\hbar \approx 4.4 \cdot 10^{13}$ G is the critical magnetic field relevant to quantum effects.

This process is very relevant in presence of high magnetic fields, such as in pulsars (see Chapter 8) where magnetic pair production limits the detection of VHE γ-rays.

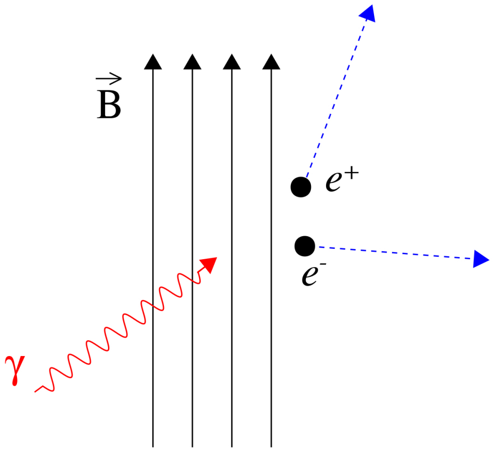

FIGURE 1.11: Magnetic creation mechanism.

1.4 VHE γ-ray sources

A great variety of astrophysical sources can be responsible for the acceleration of CRs and the subsequent production of the γ-rays observed. In the following a very brief description of these sources is given. For Supernova Remnants (SNRs) and pulsars, that are the main subjects of this work, a more extended recapitulation can be found in Chapters 4 and 7, respectively.

- *Galactic sources*

Supernova Remnants are the lefts-over of the Supernova (SN) explosions of a star. The remnant expanding into the ISM shocks and sweeps up material along the way. Particles in the shock are accelerated to VHEsies and are suspected to be the main source of CRs below the knee. Of the more than 270 SNRs listed in Green's catalog, more than 100 have been confirmed by *Fermi* to emit at HEs (Acero et al., 2016b).

Pulsars are rapidly rotating and highly magnetized Neutron Stars (NSs) born in core-collapsed SN explosions. These small-sized stars (10 km diameter) are very dense objects emitting extremely periodic radiation. Currently, more than 200 pulsars have been detected at HEs (Abdo et al., 2013) but only two pulsars have been observed to emit at TeV energies, the Crab Pulsar (Ansoldi et al. (2016), details in Chapter 8) and Vela pulsar (Djannati-Atai et al., 2017).

Pulsar Wind Nebulae (PWNe) are created in SN explosions. The magnetized wind released by the central NS is confined by ambient material forming a shock wave beyond which a magnetic bubble of relativistic particles builds up, the Pulsar Wind Nebula (PWN). Relativistic particles in the PWN produce synchrotron radiation and upscatter ambient photons (from the star, ISM or CMB) producing IC emission at HE energies (Gaensler and

Slane, 2006). PWNe are amongst the most common class of VHE emitters (37 sources so far) and the most dominant class of Galactic TeV sources with 19 PWNe firmly identified and another 10 strong candidates (Abdalla et al., 2017).

γ-ray binaries are systems formed by a compact object (usually a NS or a black hole) and a massive O-B type star. If the compact star is a pulsar, wind-wind interaction occurs forming a shock wave where particles are accelerated. Those accelerated particles scatter stellar photons via IC producing VHE radiation. So far, only 6 γ-ray binaries have been identified.

- *Extragalactic sources*

  Active Galactic Nuclei (AGN) are galaxies hosting a super massive black hole in its center. The black hole is surrounded by a disc of material, where two jets develop perpendicularly carrying out the angular momentum of the material accreted. In the jets, particles accelerate producing electromagnetic radiation across the whole electromagnetic spectrum. AGN are classified based on their observational properties that depend on the viewing angle, the accretion rate and the mass of the central black hole (refer to Urry and Padovani (1995) for a full AGN classification). They are believed to be one of the most powerful non-thermal sources of the Universe and therefore they are the most copious emitters at HE-VHE with more than 1800 detections.

  Gamma-Ray Bursts (GRBs) are the most violent astrophysical events known to date, releasing energies of $> 10^{51}$ erg in a short flash that last from seconds to few minutes. GRBs are believed to be originated in the merging of two NSs (Abbott et al., 2017). More than 1400 GRBs have been identified at high energies by the *Fermi* Gamma-ray Burst Monitor since its launch (Narayana Bhat et al., 2016), however, they are still undetected at VHEs.

  Starburst galaxies are galaxies with a high star formation rate compared to the usual star forming regions in most galaxies. The high birth rate leads to high rate of SNs explosions that accelerate particles through DSA mechanisms and radiate γ-rays at the highest energies. To date, NGC 253 is the only γ-ray starburst galaxy detected (Acero et al., 2009).

Chapter 2

Ground-Based γ-ray observations: IACTs and MAGIC telescopes

2.1 Introduction

γ-ray astrophysics is based on the study of the most energetic photons found in nature, however, their observation is problematic since the atmosphere is opaque to radiation more energetic than UV photons. Satellites are thus the best instruments to observe γ-rays from keVs to GeVs (see chapter 3). Nonetheless, given the very low flux of γ-rays at energies above a hundred of GeVs and the small collection area of satellites, space-based observations are extremely inefficient.

Despite the atmosphere rapidly dissipates incoming energetic particles (50% absorption at 20km height above 1 MeV), indirect ground detection is still possible. Incident particles initiate atmospheric showers that result in secondary products that ground-based telescopes can efficiently detect. These cascades provide invaluable information on the primary particles hitting the atmosphere and allow us to trace CRs back to their initial properties.

The first part of this chapter is dedicated to the physical description of the showers produced in the atmosphere and the imaging technique used to observe them. The second part is addressed to the description of the hardware and software of the MAGIC telescopes used in the major part of this thesis.

2.2 Extensive Air Showers

Extensive Air Showers (EASs) are cascades of particles initiated either by very HE CRss or by γ-rays interacting with the molecules of the Earth's atmosphere. Depending of the nature of the primary particle entering the atmosphere, the EASs produced are classified as Electromagnetic (EM) or hadronic and present different properties.

2.2.1 Electromagnetic Showers

When a γ-ray enters the upper part of the Earth's atmosphere, it interacts with the Coulomb field of the atmospheric molecules generating an electron-positron pair which in turn lose their energy through bremsstrahlung. This cycle of pair production - bremsstrahlung produces an electromagnetic cascade composed of only photons,

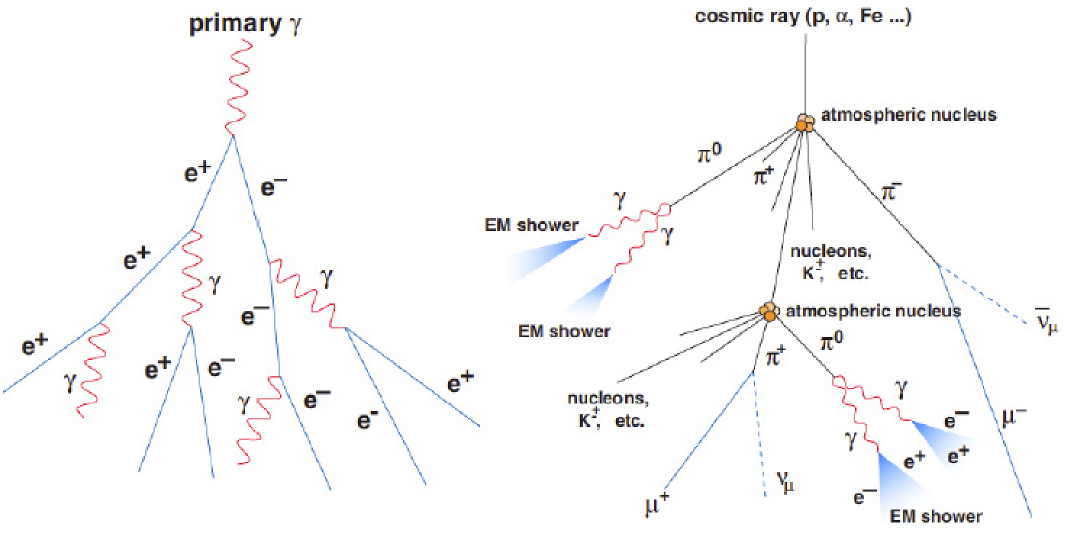

FIGURE 2.1: Diagram of an EM (*left*) and Hadronic (*right*) induced showers. From Wagner (2006).

electrons and positrons (*left* panel of Figure 2.1). The cascade terminates when the energy of the resulting particles is that of the *critical energy* E_c[1], i.e. when energy lost by ionization processes dominates over bremsstrahlung. Below this energy, the electron flux attenuates rapidly by ionization and the shower dies out.

2.2.2 Hadronic Showers

Hadronic showers are the predominant type of EASs produced in the atmosphere. Incoming hadrons interact with atmospheric nuclei producing mainly pions (∼89%) of all charges, kaons (∼9%) and other light nucleus. These secondary particles contribute in a different way to the development of the shower. Hadrons and charged pions continue to interact producing subsequent generations of particles until the energy per nucleon reach the minimum energy needed for pion production, 1 GeV. Next, charged pions decay into muons and these muons into electrons, positrons and neutrinos (see section 1.3.5) that initiate an EM shower. On the other hand, neutral pions decay directly into two γ-rays that also trigger an EM shower (*right* panel of Figure 2.1).

The variety of particles and the interaction time involved in hadronic showers produce an asymmetric and longer development compared to electromagnetic showers. Besides, the larger transverse momentum of the secondary particles in hadronic collisions also confers a wider lateral spread compared to the electromagnetic scenario (see Figure 2.2).

2.3 Atmospheric Cherenkov Radiation

Particles produced on induced EASs might be of relativistic nature and travel through the atmosphere at velocities greater than the speed of light in air. Those relativistic charged particles produce the so-called Cherenkov radiation (Čerenkov, 1937).

---

[1] ∼80 MeV and ∼86 MeV for photons and electrons, respectively.

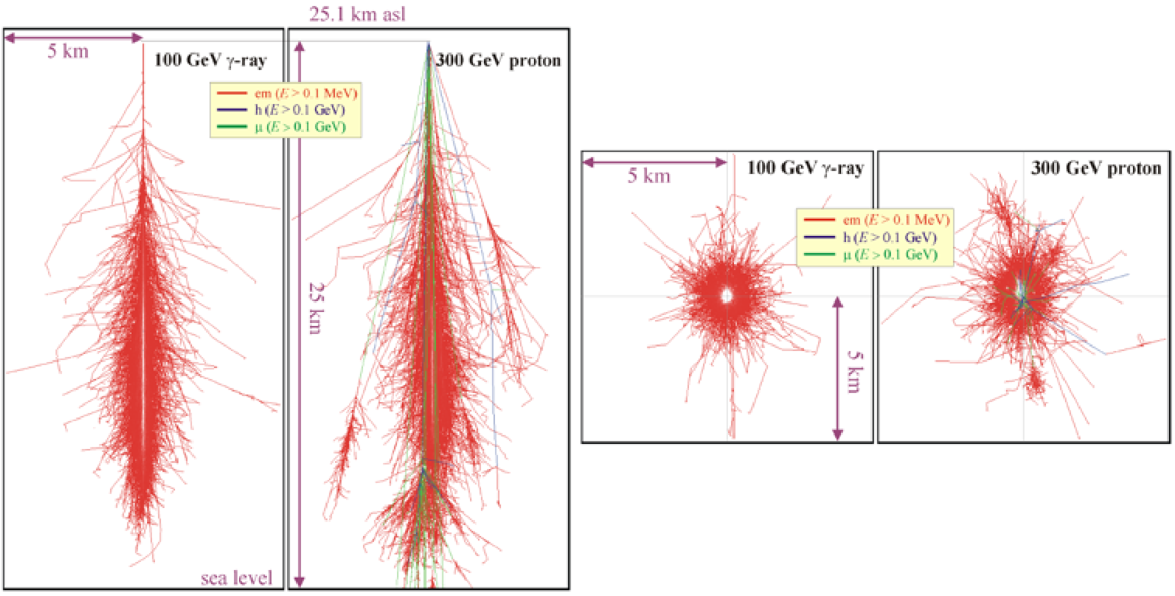

FIGURE 2.2: Monte Carlo simulation showing the longitudinal (*left*) and lateral (*right*) development of EM and Hadronic showers induced by primary particles with energies of 100 and 300 GeV, respectively. From Hrupec (2008).

2.3.1 Cherenkov Radiation

Charged particles moving in a dielectric medium polarize the surrounding molecules that in turn depolarize shortly after. The shift in the distribution of charges causes them to emit dipole radiation. If the velocity of the particle is lower than the speed of light in such medium the radiation emitted is incoherent. However, for the case of velocities larger than the speed of light, the radiation adds up coherently on a cone along its trajectory, the Cherenkov cone (see Figure 2.3):

$$\cos(\theta_C) = \frac{c}{vn(\lambda)} \tag{2.1}$$

where $n(\lambda)$ is the refraction index of the medium.

The number of photons produced by an ultra-relativistic particle per unit length and unit of wavelength in air is given by (Beringer et al., 2012):

$$\frac{d^2N}{dxd\lambda} = \frac{2\pi\alpha}{\lambda^2}\left(1 - \frac{c^2}{v^2n^2(\lambda)}\right) \approx 370\sin^2\theta_C(\lambda)\left[eV^{-1}cm^{-1}\right] \tag{2.2}$$

being $\alpha \approx \frac{1}{137}$ the fine structure constant.

2.3.2 Cherenkov radiation produced in the atmosphere

The Cherenkov radiation produced by an air shower is composed of the emission from many particles at different heights in the atmosphere. A single particle traveling across the atmosphere emits at an angle of θ_C with respect to its trajectory, however, θ_C depends on the refractive index n that changes depending on the altitude (Aharonian

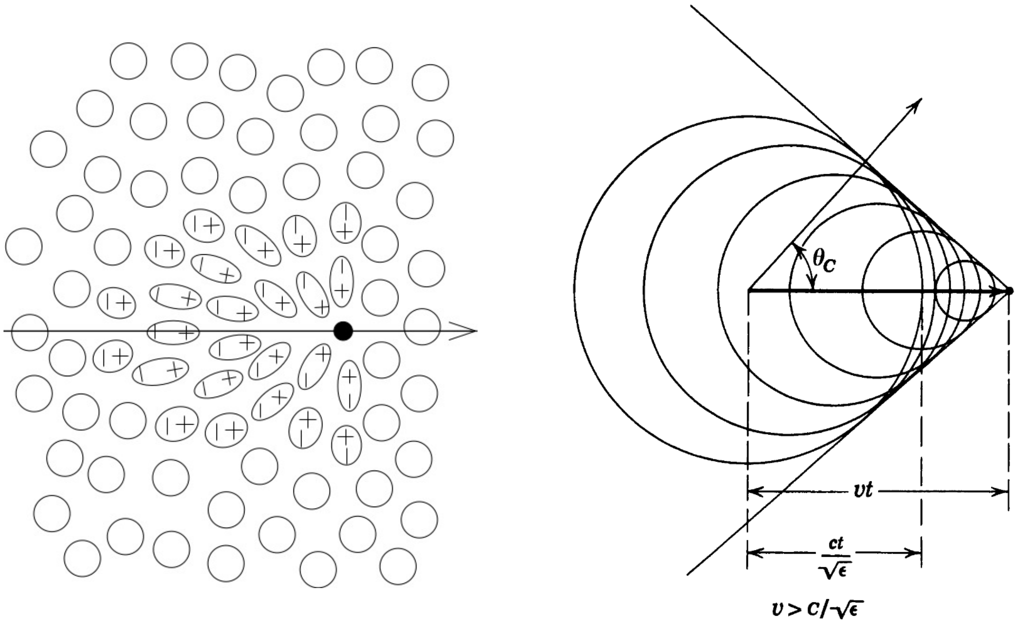

Figure 2.3: Cherenkov Radiation. *Left:* Molecules polarized by a moving charge. *Right:* Representation of the Cherenkov angle θ.

et al., 2008) as:

$$n = \rho_0 \times e^{(-\frac{z}{h_0})} + 1 \tag{2.3}$$

with $\rho_0 = 2.9 \times 10^{-4}$ and $h_0 = 7250$m. The resulting emission produced by an individual particle at ground level is then a *donut* ring shape (see Figure 2.4). Consequently, the superposition of the individual rings formed by all the particles in the air shower generate a circular light pool on the ground (see Figure 2.5, *left*). The lateral photon distribution of the pool is almost flat within a radius of $\sim$ 120m centered at the core of the shower, followed by the *hump* where the photon density starts to decrease (see Figure 2.5, *right*). The *hump* is a geometrical feature consequence of an increase in

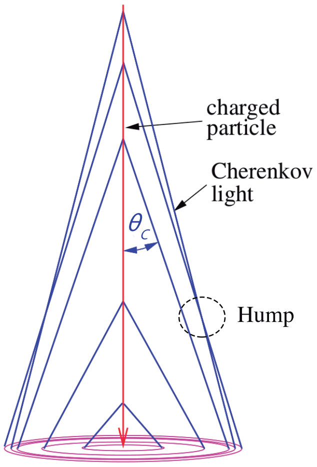

Figure 2.4: Cherenkov emission produced by a particle at different heights. The total emission produced by a single particle produce a donut on the ground.

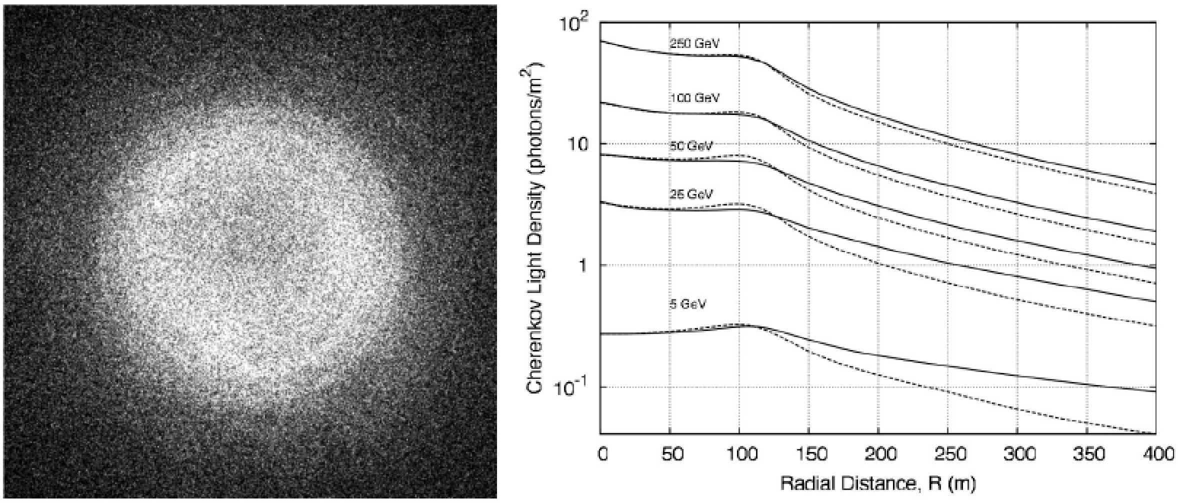

FIGURE 2.5: *Left:* Cherenkov light pool produced by all the particles of an air shower induced by a 300 GeV γ-ray particle. *Right:* Density profile of the light pool for different energies of the primary γ-ray. Full lines represent vertically incident particles while dashed lines show particles with high incident zenith angles.

the angle θ_C along the trajectory of the particle, that causes that photons emitted at different heights fall at the same position on the ground as can be appreciated in Figure 2.4. The Cherenkov photon density inside the pool varies depending on the primary particle origination the shower (see Figure 2.6). For EMs showers the number of Cherenkov photons produced is proportional to the energy of the γ inducing the shower. However, hadronic showers deviate from this linear relation and produce widespread distributions with low densities for low energetic incident hadrons.

Moreover, Equation 2.2 indicates that the Cherenkov light intensity increases rapidly

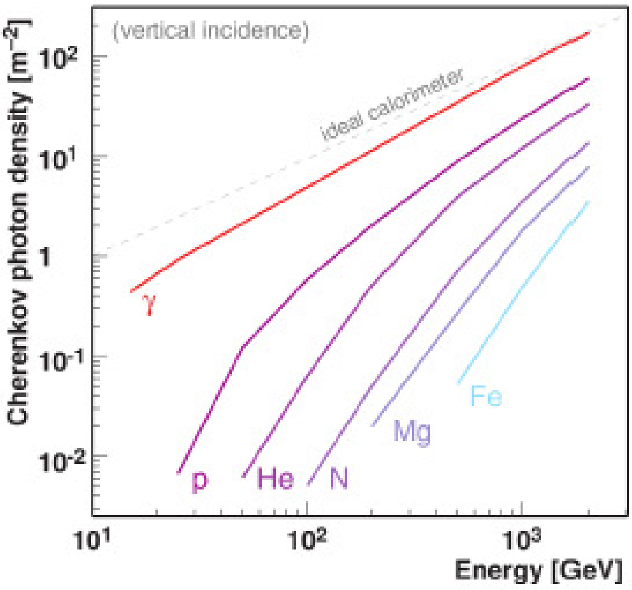

FIGURE 2.6: Cherenkov photon densities inside the light pool for different primary particles as a function of the primary energy. From Wagner (2006).

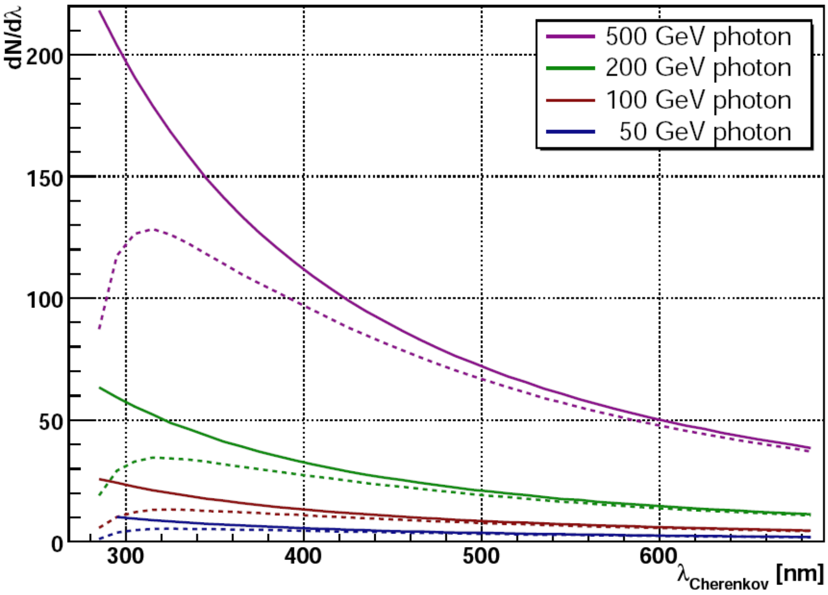

FIGURE 2.7: Cherenkov radiation from a γ-ray induced shower. Full lines show the unabsorbed spectrum, while dashed lines represent the spectrum measured at the MAGIC site after atmospheric absorption is produced. From Wagner (2006).

towards smaller wavelengths causing that most of the photons are emitted in the UV band. However, due to attenuation processes in the atmosphere, the actual Cherenkov light observed peaks at the UV-blue wavelengths (330 nm), independently of the incident particle's energy as shown in Figure 2.7. The spectral extinction of the radiation occurs as a result of the scattering of the Cherenkov light by air molecules (*Rayleigh scattering* behaving proportional to λ^{-4}) and aerosols (*Mie scattering* proportional to $\lambda^{1-1.5}$) along with strong absorption in the UV and IR regime by the presence of ozone and water vapor, respectively.

EASs develop rapidly and last for about 100μs reaching their shower maximum (i.e. height at which the number of particles in the cascade is maximum) at a height of 10 km above sea level for primary γ-rays of ten to hundred GeVs. The typical duration of the Cherenkov light emitted by a γ-ray induced air showers is of 3 ns while for hadronic induced showers it last approximately 10 ns.

2.4 Imaging technique and IACT design

When Imaging Atmospheric Cherenkov Telescopes (IACTs) are positioned inside the Cherenkov light pool produced by an EAS, part of this light is reflected by the mirrors and registered by the cameras. Since Cherenkov radiation is emitted at an angle θ_C that is dependent on the refraction index n, from equation (2.3) it is clear that photons emitted at higher altitudes have smaller θ_C values and are projected closer to the center of the camera. The recorded image has therefore an elliptical shape since it represents the shower development, with the major axis of the ellipse related to the shower axis. A schematic representation of the EAS as seen in the focal plane of the camera is shown in Figure 2.8. Additionally, the number of photons recorded along the longitudinal extension of the shower is connected to the amount of shower particles

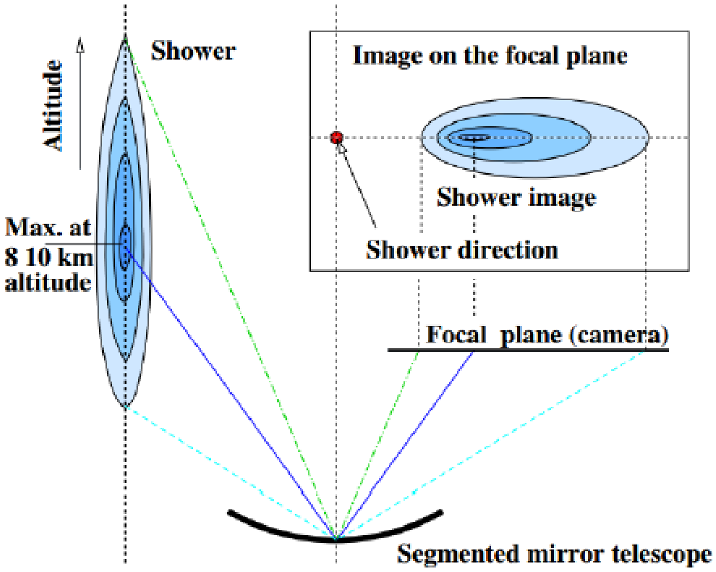

FIGURE 2.8: Illustration of the imaging atmospheric Cherenkov technique: reflection of the Cherenkov light emitted by an EAS into the camera. Taken form Völk and Bernlöhr (2009).

produced. On the other hand, the lateral width of the registered image is related to the transversal development of the cascade.

Instrument aiming to detect the Cherenkov radiation has to fulfill then two important requirements, a large collection area to detect the scarce number of photons arriving at ground level (of the order of 10 for a shower initiated by a γ-ray of 1 TeV, see Figure 2.6) and a fast electronic system to catch the short-lasting Cherenkov light. Nonetheless, IACTs have to face another impediment to detect γ-ray initiated showers; the background contribution. Hadrons are the main background contributors. On one side, due to the random magnetic deflections they suffer in the Universe they reach the atmosphere isotropically and cannot be associated to any specific source. On the other side, they are much more abundant than γ-rays with an hadron-to-γ ratio of 1000 at 1 TeV and are capable of triggering the detectors. Hadronic showers, however, owing to their different development in the atmosphere, they produce different projected shapes on the camera (see Figure 2.9), feature that can be used as a discrimination tool. A less important background component are muonic showers since they can be easily discriminated due to their ring-like shape in the camera. Furthermore, there are also irreducible sources of isotropic background, like cosmic leptons producing identical electromagnetic showers to those produced by γ-rays, or diffuse γ-rays coming from the galactic plane.

Detection and characterization of EM showers is not an easy task, that is why modern instruments build preferably stereoscopic or multiple systems (e.g., MAGIC or HESS, respectively) in order to image the EM shower from different angles for improved reconstruction of the direction of the primary γ-ray and to apply coincidence requirements to reject single-telescope triggers for a better background suppression.

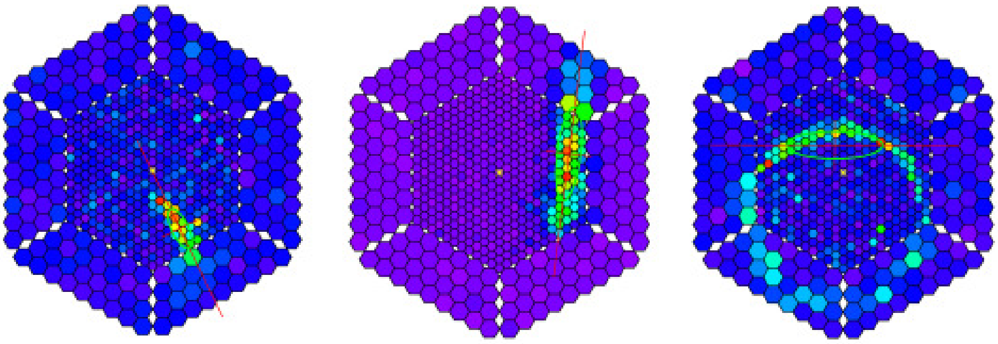

FIGURE 2.9: Registered air showers produced by different types of particles with the MAGIC's old camera. *Left:* Shower image originated by a primary γ-ray. The shower axis points to the source located at the center of the camera. *Middle:* Hadronic induced shower with random direction. *Right:* Ring-like shower image produced by a muon.

2.5 MAGIC telecopes

MAGIC is an stereoscopic system of two 17 meter diameter IACTs located at the Observatorio del Roque de Los Muchachos on the Canary Island of La Palma at an altitude of 2235 m above sea level. MAGIC has undergone many upgrades since its construction ended in 2003. Until 2009, MAGIC-I (M1) was a stand-alone IACT with integral flux sensitivity of 1.6% of the Crab Nebula flux in 50 hours of observation (Aliu et al., 2009). In 2009, MAGIC-II (M2) became operational lowering the energy threshold of the system to 50 GeV at low zenith angles and boosting the sensitivity to 0.76% of the Crab Nebula flux in 50 hours for energies greater than 290 GeV (Aleksić et al., 2012b). Currently, after the major upgrade the telescopes underwent in 2011-2012 (Aleksić et al., 2016a), the system has reached an integral sensitivity of $(0.66 \pm 0.03)\%$ of the Crab Nebula flux in 50 hours above 220 GeV (Aleksić et al., 2016b).

In the following, a brief description of the MAGIC subsystems will be given together with a description of the MAGIC analysis chain used for this thesis. For further information the reader is referred to Aleksić et al. (2016a,b).

2.5.1 MAGIC Subsystems

Structure and Drive System:
The telescopes are mounted on alt-azimuthal frames driven by two motors per telescope on a 20m circular railway (see Figure 2.10). The structure of the MAGIC telescopes is light-weight (~5.5 tons), allowing fast reaction to transient events such as γ-ray bursts, and stiff (made of carbon fiber-epoxy), avoiding deformations of the structure. For any orientation of the telescopes, the deformation is lower than 3.5 mm (Bretz et al., 2009). The camera is located at the focal distance of ~17m and held by a tubular arch.

Reflector:
Each of the telescopes has a 17m diameter parabolic reflector, which allows to preserve the temporal structure of the light flashes reflected on the focal plane. Reflectors are tessellated in 247 individually movable mirror panels of 0.5 m^2 in

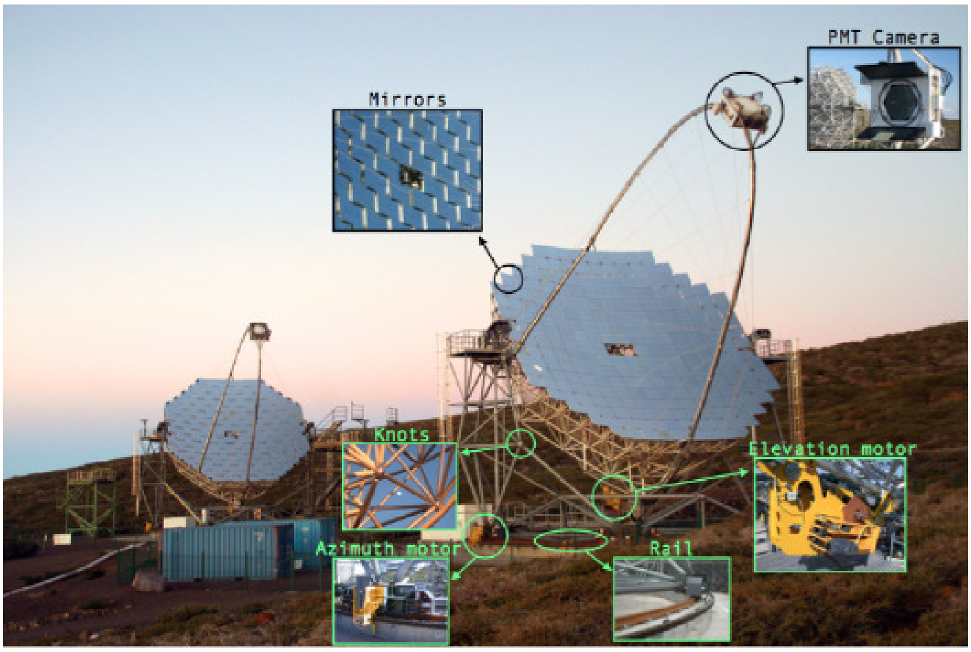

FIGURE 2.10: Insight of different sub-systems of the MAGIC telescopes.

M1 and 143 mirror panels of 1 m^2 in M2, for a total reflection area of ~236m^2. Any bending of the structure due to the heavy weight of the camera (~0.8 tons) can be corrected by an active optic that re-orients the mirrors, the so-called Active Mirror Control (AMC).

Camera:
Both cameras present a circular shape of ~1.2 m diameter and a Field of View (FoV) of 3.5°. The camera is composed of 1039 Photo Multiplier Tube (PMT), each of them with 0.1° FoV (see Figure 2.11). The PMTs typically reach a maximum quantum efficiency of ~32% in the UV band and provide a response of the order of ~1 ns. PMTs are connected to High Voltage (HV) regulators that can reduce the camera gain in order to avoid damaging the photomultipliers.

Calibration System:
The calibration system permits on one hand to maintain a uniform gain across the camera and on the other hand to monitor the behavior of the electronic chain. The MAGIC calibration system provides fast light pulses at different wavelengths and different intensities in order to calibrate the dynamic range of the camera photo-sensors and their readout.

Readout and Data Acquisition (DAQ) system:
The electric pulses at the base of the PMTs are converted into optical pulses and the signal is transmitted to the Counting House. In the Counting House, the optical signals are split into two branches and reconverted into electronic signals in the receiver boards. One of the branches goes to the trigger system, whereas the other goes to the DAQ. The DAQ in turn digitalizes the electronic signals and records them into raw data files.

Trigger:
The trigger discriminates Cherenkov showers from the Night Sky Background

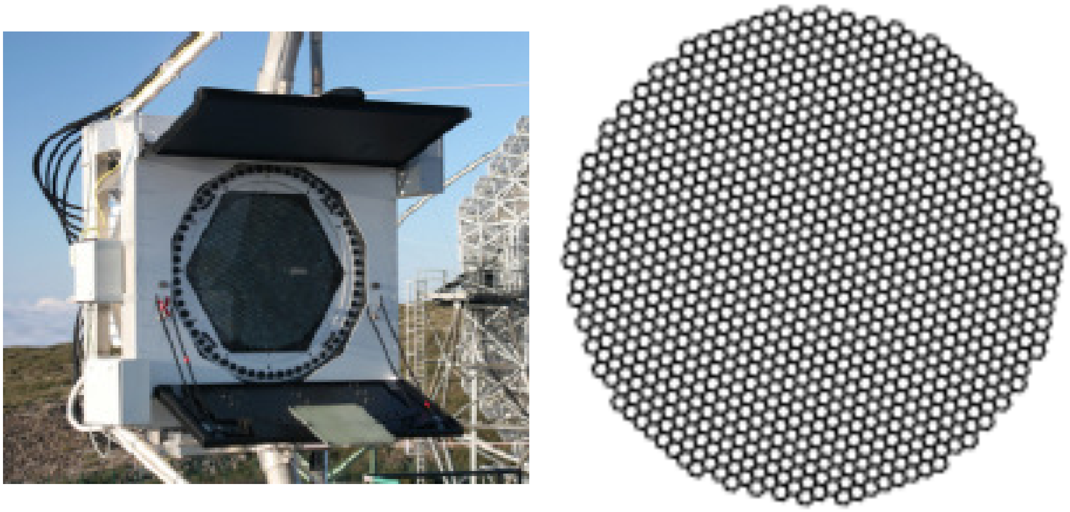

FIGURE 2.11: *Left:* Front-side of the upgraded M2 camera. *Right:* Pixel layout of the upgraded M2 camera.

(NSB) light by keeping only fast pulses ($<$5ns) which are detected simultaneously in a compact region of the cameras.

Other subsystems:
GRB alert system monitors any alert from a possible GRB event in the sky.
Weather systems control the weather conditions to evaluate if observations can be performed and provide information of the atmosphere used afterwards for data correction.

2.5.2 MAGIC data taking

2.5.2.1 Brightness Conditions

Nowadays, MAGIC telescopes can be operated to observe under dark conditions, i.e. nights with no moon in the sky, and moon conditions, i.e. nights with the moon in the sky. On average every year about 1500 hours of dark time observation are scheduled, of which $\sim$40% is lost mainly due to bad weather conditions and technical problems. Operating the telescopes during moonlight and twilight time increases the number of hours of observation by about 40% ($\sim$600 hours per year). However, data taken during moon time have some drawbacks, such as an increase of the energy threshold of the analysis or higher systematics on the flux normalisation. For some specific analyses, a higher energy threshold might not be important and therefore moon time data are as useful and usable as dark time data (see Chapter 5).

Moonlight conditions are evaluated taking the NSB light on a dark night (NSB_{Dark}) as a reference. Depending on brightness of the sky the HV settings of the PMTs have to be changed accordingly. For NSB levels up to $12 \times \mathrm{NSB}_{\mathrm{Dark}}$ standard HV settings ($\sim 1.25\,\mathrm{kV}$) can be used, however, higher NSB levels (up to $20 \times \mathrm{NSB}_{\mathrm{Dark}}$) require reducing the gain of the PMTs by a factor of ~ 1.7 (reduced HV settings). Observations can be extended to even higher NSB levels using the UV-filters recently installed, however UV-filters have not been used in this thesis. The performances of MAGIC telescopes under dark and moonlight conditions are examined in Aleksić et al. (2016b) and Ahnen et al. (2017), respectively.

2.5.2.2 Pointing modes

MAGIC can observe a source in two different modes, *On/Off* tracking mode or false-source tracking mode, also known as Wobble mode (Fomin et al., 1994).

- ***On/Off* mode:** The source position is always located at the center of the camera. Additional observations of an Off region (i.e. region with no VHE γ-ray sources in it) is therefore needed to properly estimate the background contribution. Off observations have to be taken under the same conditions (zenith angle, NSBs, weather conditions, etc). The drawbacks of this observation mode are that *On/Off* observations need higher observation time as half of it must be devoted to an off region aside of the high risk of not matching the exact same observation conditions.
- **Wobble mode:** The telescope tracks alternatively four opposite directions in the sky located at an offset of 0.4° from the source position (see *left* panel of Figure 2.12). Each of these positions are observed for about 20 minutes. This mode profits from the fact that the background is estimated from the same data sample as the signal and thus guarantees similar conditions and same exposure. Wobble mode also has a drawback regarding the γ-ray detection efficiency, which is estimated to be reduced by 20% due to the smaller trigger area around the source position (see Figure 2.12 *right* panel).

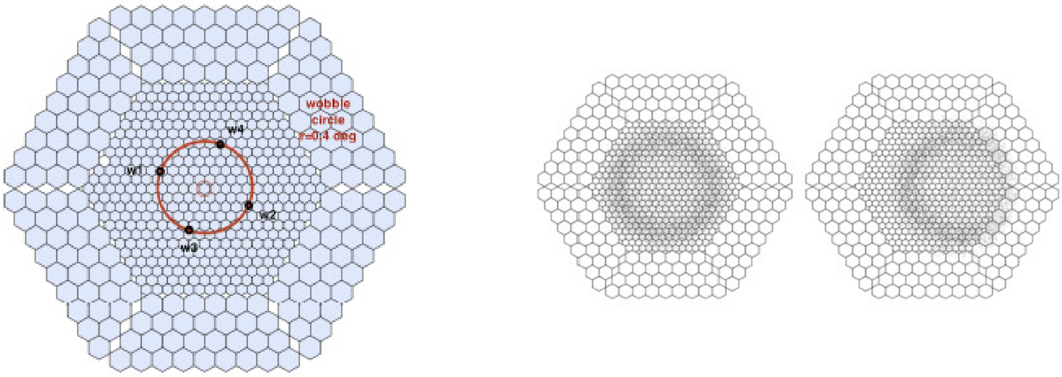

FIGURE 2.12: Representation of the Wobble observation mode. *Left:* Display of the camera with the four wobble positions located at 0.4° from the camera center. The source is positioned and observed at each wobble position, the other three simultaneous positions can be used to estimate the Off events of the observation. *Right:* Monte Carlo simulated γ-ray events for an observation with the source at the camera center (left) and offset 0.4° from the camera center (right). It is important to remark that these figures represent the old design of the camera as opposed to Figure 2.11 (see section 2.5.1). From Bretz et al. (2005).

2.5.3 MAGIC data analysis

Within the MAGIC Collaboration, the Magic Analysis Reconstruction Software (MARS) software (Moralejo et al., 2009, 2010; Zanin et al., 2013) is used to perform the data analysis. MARS is a collection of classes and executables written in

C++ language within the ROOT[2] software framework. The standard analysis chain of MAGIC stereo data is composed of the following steps:

- Signal extraction and calibration to determine its intensity (in Photoelectron (phe)) and arrival time, performed with `sorcerer`.
- Image cleaning and parametrization of the shower image with `star`.
- Stereoscopic image reconstruction of the data from both telescopes through `superstar`.
- γ/hadron separation and reconstruction of the energy and direction of the shower by means of a Random Forest (RF) method and energy Lookup Tables (LUTs) with `coach` and `melibea`, respectively.
- Sky map computation (`caspar`) and determination of the significance (`odie`), spectrum and light curve (`flute`) of the source.

2.5.3.1 Calibration

Calibration consists of extracting from the raw data recorded by the DAQ the arrival time and intensity of the signal, and converting it into the number of phe by means of the so-called *F-Factor* method described in Mirzoyan (1997).

2.5.3.2 Image cleaning

At this step, calibrated events consist of a signal per pixel. However, only some pixels of the camera are illuminated by the Cherenkov light of an EAS and contain information of the shower whereas the others are just noise from the NSB and the electronics. In order to discard pixels containing just noise to obtain the image of the EAS we perform an image cleaning. The image cleaning is based on the definition of *core* and *boundary* pixels, which hold the information of the shower, following a combination of signal intensity and timing information, and the rejection of the rest of the pixels. Within this thesis, two different image cleaning algorithms have been used: the absolute image cleaning (Aliu et al., 2009) and the sum image cleaning (Aleksić et al., 2011; Lombardi, 2011).

- *Absolute image cleaning:*
  This algorithm discriminates pixels by their photoelectric charge, classifying them into *core* and *boundary* pixels. A pixel is classified as *core* if its charge is above a certain signal threshold Q_{core} and its arrival time is within a time window, $\Delta t_{core} = 4.5\,\mathrm{ns}$, from the mean arrival time of its neighboring pixels. The arrival time requirement is founded on the fact that Cherenkov light emitted by a γ-ray induced air shower is much shorter than the signal produced by the NSB. Additionally, *core* pixels must have at least another contiguous *core* pixel in order to avoid misclassification of spurious pixels unrelated to the shower. On the other hand, *boundary* pixels are pixels with at least one adjacent *core* pixel, a charge above a certain threshold Q_{bound} and an arrival time within a time window, $\Delta t_{bound} = 1.5\,\mathrm{ns}$, from the mean arrival time of the *core* pixels. Charge thresholds for *core* and *boundary* pixels, Q_{core} and Q_{bound}, change according to

---

[2] see https://root.cern.ch/ for more detail

the observational conditions (e.g. moon-light intensity, weather) and are listed in Table 2.1.

- *Sum image cleaning:*
  Unlike for the absolute image cleaning, the sum cleaning is not based on individual pixels but in groups of 2 to 4 pixels whose summed charge is above a given signal threshold, Q_{sum}. Pixels passing this condition and whose arrival time is within a certain time window, Δt_{core}, are designated as *core* pixels. Note that the summed charge thresholds vary depending on the number of pixels and the noise of the observation as $4 \times Q_{core}$, $3 \times 1.3 \times Q_{core}$ and $2 \times 1.8 \times Q_{core}$, for groups of 4, 3 and 2 pixels respectively. The values of Q_{core} depend on the sky brightness and are listed in Table 2.1. Time windows for the different group of pixels are independent on the sky brightness and are fixed to 1.1 ns, 0.7 ns and 0.5 ns for groups of 4, 3 and 2 pixels respectively. *Boundary* pixels are classified as such if they are contiguous to at least one *core* pixel, they have a charge signal Q_{bound} above 3.5 phe and their arrival time is within 1.5 ns with respect to the adjacent *core* pixel.

As mentioned, charge thresholds applied for image cleaning are highly dependent on the observational conditions. Stronger moonlight conditions would require then higher charge thresholds in order to avoid contamination from a much higher NSB than in dark nights. However, increasing charge thresholds implies discarding low charge events, hence increasing the energy threshold of the analysis. Current MAGIC image cleaning levels for different sky brightnesses are reported in Table 2.1.

Sky Brightness [$\times$NSB$_{\text{Dark}}$]	Hardware Settings	Charge Thresholds Q_{core} / Q_{bound} [phe]
1 (Dark)	standard HV	6.0 / 3.5
1-2	standard HV	6.0 / 3.5
2-3	standard HV	7.0 / 4.5
3-5	standard HV	8.0 / 5.0
5-8	standard HV	9.0 / 5.5
5-8	reduced HV	11.0 / 7.0
8-12	reduced HV	13.0 / 8.0
12-18	reduced HV	14.0 / 9.0

TABLE 2.1: Image cleaning levels and hardware settings used for different sky brightness observations.

2.5.3.3 Image parametrization

After the image cleaning, the image parametrization with Hillas parameters (Hillas, 1985) is performed. In this step, an ellipse is fitted to the surviving pixels of each individual image as shown in Figure 2.13. Some of the Hillas parameters used to parametrize the shower image are listed here:

Source independent parameters that are not related to the position of the source.

Size Total charge contained in the image (in phe). It is correlated to the energy of the primary γ-ray.

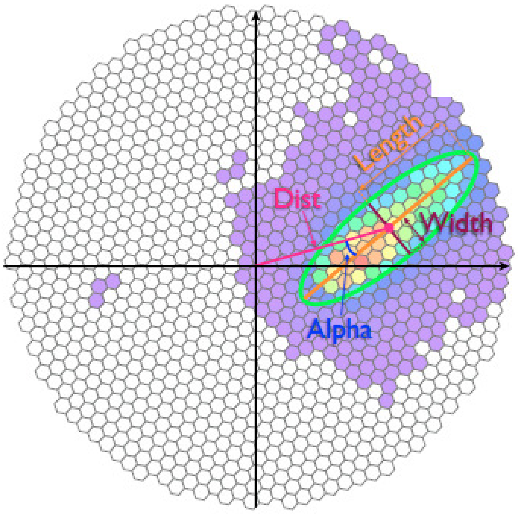

FIGURE 2.13: Hillas parametrization of a recorded shower image.

Width Longitude of the minor axis of the ellipse, related to the transversal development of the shower.

Length Longitude of the major axis of the ellipse, related to the longitudinal development of the shower.

Conc(N) Fraction of the image size contained in the N brightest pixels. This value is expected to be higher in γ-ray induced showers.

Source dependent parameters that are computed according to the position of the source in the camera plane.

Dist Angular distance between the image centroid and the position of the source in the camera.

α Angle between the direction of the major axis and the line connecting the image centroid with the position of the source in the camera. γ-ray induced showers present smaller angles than hadronic showers.

Time dependent parameters useful to discriminate between hadronic and EM showers since the latest develops faster.

Time RMS Root Mean Square (RMS) of the arrival time of the image, normally for a gamma event is narrower than for hadronic showers.

Time gradient Linear coefficient of the fitted arrival time projection along the major axis of the ellipse.

Directional parameters used to differentiate between the top and the bottom of the shower.

M3Long Third momentum of the charge distribution along the major axis.

Assym Distance between the image centroid and the pixel with largest charge.

Image quality parameters useful to discard noisy images.

LeakageN Fraction of the signal contained in the N outermost rings of the camera to the total signal.

Number of islands Number of cluster of pixels after image cleaning.

2.5.3.4 Data quality selection

Once the shower has been parametrized, data selection is needed in order to reject bad quality data and ensure a final good quality sample.

Data can be affected by different factors, the most importants being bad weather and hardware problems. The evaluation of bad weather is usually based on the sky clearness (or *cloudiness*). If observations are carried out under cloudy conditions, the rate of events registered will be lower than in optimal conditions. Therefore, by monitoring the rate of events it is possible to identify and reject bad weather data. As an important remark, rate of events are corrected by the zenith distance of the observation, since at a larger zenith angles we expect lower rates due to a larger layer of atmosphere. Usually, fluctuations of ±20% of the corrected mean rate are expected for observations with optimal weather conditions. For the results presented in this thesis, we discarded any data with *cloudiness* higher than 40% or events with rates outside the ±20% range of confidence from the corrected mean rate (Figure 2.14).

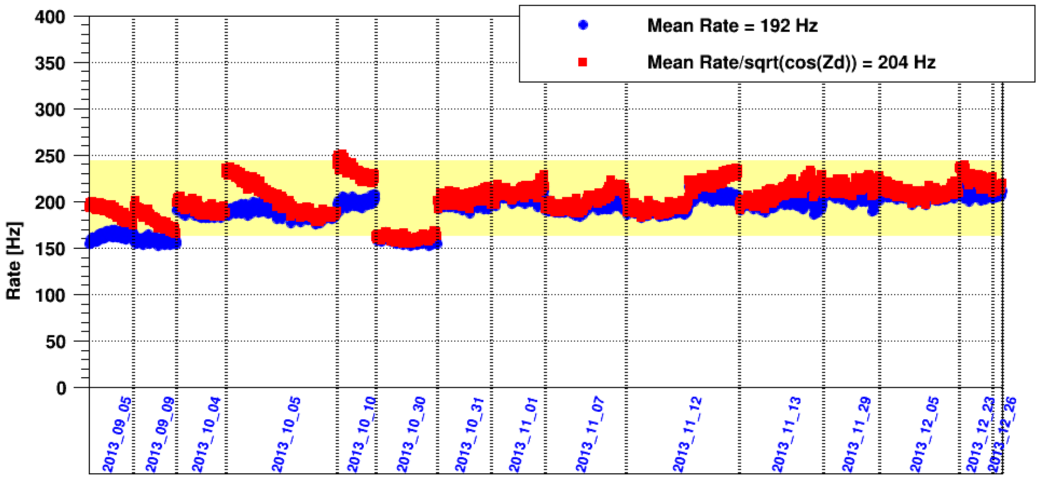

FIGURE 2.14: Data quality selection based on the corrected mean rate for an observation of the Crab. Data with rates differing more than 20% from the corrected mean rate (represented by the yellow band) were discarded.

2.5.3.5 Stereoscopic parameters

Up to this point in the analysis chain, any data treatment was applied to the data files of each telescope separately. At this step, the information of the data sets from the two telescopes is merged and new stereoscopic image parameters are created. Some of the stereoscopic parameters are:

Impact Parameter describing the perpendicular distance between the pointing direction and the shower axis (see *top* panel of Figure 2.15).

Shower Axis characterized by the impact point on the ground and the direction of the shower, defined by the intersection of the major axes of the two images (for the same event) on the ground and the camera plane, respectively (*bottom* panel of Figure 2.15).

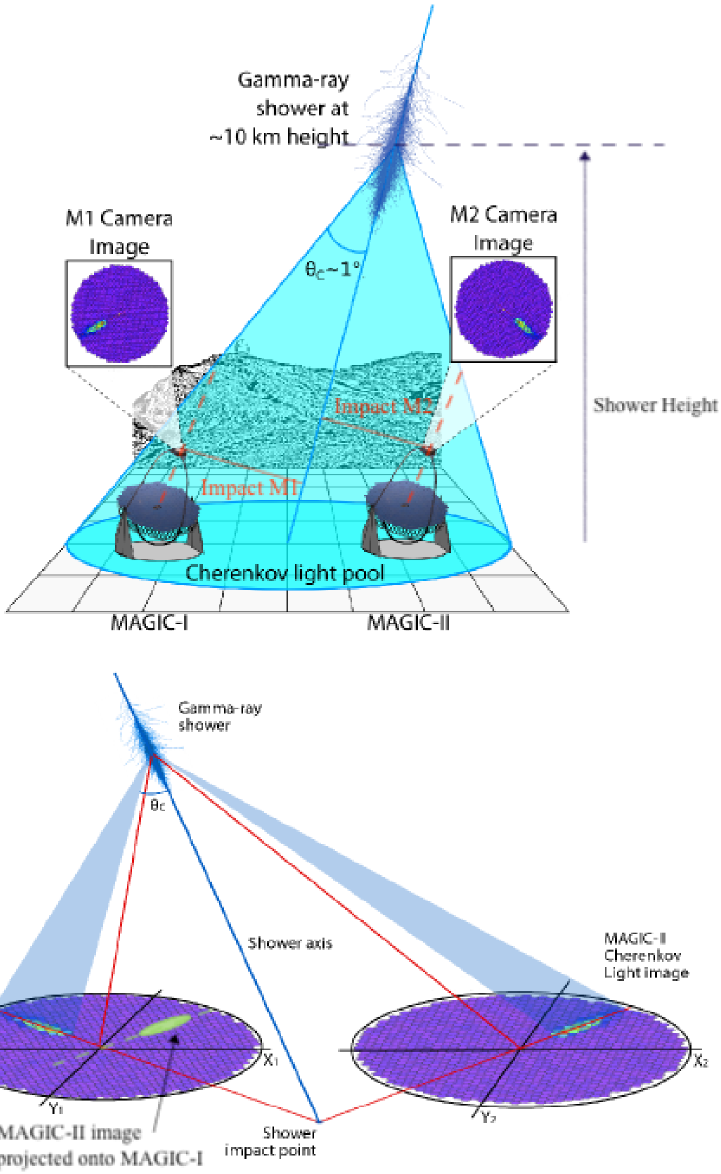

FIGURE 2.15: *Top*: Representation of an air shower observed in stereoscopic mode. The impact parameters of the telescopes are represented by red solid lines. The shower maximum height has also been illustrated. *Bottom*: Scheme of the shower axis reconstruction principle. The impact point on the ground is determined by the intersection of the prolongation of the major axis of the two images. The direction of the shower is determined by the intersection of the two images on the camera plane (M2 image, green ellipse, has been represented onto M1 for illustration purposes). Adapted from Giavitto (2013).

Shower Height that gives the height of the shower maximum. The shower height is related to the energy of the incident particles; the higher the energy of the particle the deeper it penetrates into the atmosphere and therefore the closer its maximum is to the ground.

2.5.3.6 γ/hadron separation

Most of the showers triggered by MAGIC are of hadronic origin as mentioned in section 2.4. It is therefore necessary to efficiently separate γ-ray induced showers from background events. To carry out this separation, MAGIC uses a multivariate classification method based on decisional trees, called RF (Albert et al., 2008). In order grow the trees, the RF must be 'trained' first with event samples of known nature, such as γ-ray events from Monte Carlo simulations and hadronic events obtained from off-source data. Both of them must have similar observational conditions, i.e. weather, background light and zenith conditions, than the data of the source we are analysing. The RF uses then a set of Hillas parameters to compute the decision trees (100 trees are typically used in MAGIC) and discriminate between hadron and γ-rays. Initially, a decision tree is started by applying a cut on a random parameter to divide the data sample into two sub-samples called branches. The value of the cut is chosen by minimizing the so-called *Gini*-index (Gini, 1921):

$$Q_{Gini} = 4\frac{N_\gamma}{N}\frac{N_h}{N} \tag{2.4}$$

where N is the total number of events and N_γ and N_h, the number of γ rays and hadrons, respectively. This process is repeated iteratively for each branch until a sub-sample consists of only events of one nature. Each of the ending branches are labeled as 0 or 1 depending on whether they contain γ rays or hadrons, respectively. At this point, the RF is applied to the real data. Each recorded event passes through all the decision trees computed and is assigned a value according to its ending branch in each of the trees. The mean value obtained over the number of decision trees passed is defined as the *hadronness* and ranges from 0 to 1. γ-like events peak at 0 while hadronic events peak at 1. The *hadronness* parameter provides a powerful tool to discriminate between γ rays and hadronic induced showers.

2.5.3.7 Arrival direction reconstruction

In order to reconstruct the arrival direction of the primary γ-ray, MAGIC uses the *Disp* method (Fomin et al., 1994; Lessard et al., 2001) that was initially proposed for stand alone observations. This method is based on the fact that EASs projected onto the camera have an elliptical shape with their major axis related to the shower axis, and therefore to their incoming direction, as explained in section 2.4. The source position lies then along the major axis of the ellipse at a certain angular distance from the center of gravity of the image. This distance is characterized by the *disp* parameter (Zanin et al., 2013). The *disp* is computed by means of a RF algorithm (same concept as in section 2.5.3.6) trained on a sample of Monte Carlo simulated γ-ray events for with the correct source position in known. Each image passes then the decisional trees and a value of the *disp* is assigned. However, the *disp* method returns a degenerated reconstructed source position on either side of the image centroid for each telescope, resulting in four solutions for stereoscopic observations as can be

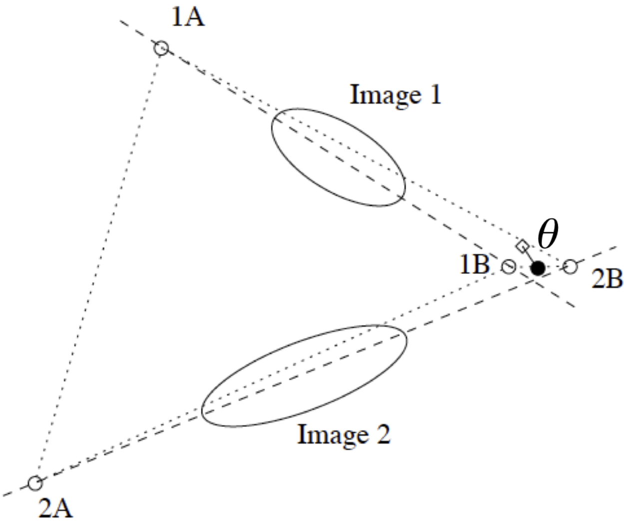

FIGURE 2.16: Sketch of the stereo *disp* RF determination. Shower axis are represented with dashed lines. Both *disp* reconstructed positions per telescope (1A, 1B, 2A, 2B) are shown with empty circles. Angular distances between different reconstructed positions are shown with dotted lines. The final reconstructed position (the filled circle) is a weighted average of the two closest '1' and '2' points. The true source position is marked with a diamond. The angular distance between the true position and the final reconstructed position is θ. Adapted from Aleksić et al. (2016b).

seen in Figure 2.16. Angular distances between the different reconstructed source positions of each telescopes are calculated (dotted lines in Figure 2.16) and the pair of positions with the smallest distance is chosen. The reconstructed source position is then determined by the average of the two estimated positions weighted with the number of pixels in each image. The angular distance between the reconstructed position of the source and its real position is characterized by the parameter θ, see Figure 2.16, an important parameter in signal identification (section 2.5.3.10).

2.5.3.8 Energy reconstruction and energy resolution

The energy estimation of a registered event is performed by means of LUTs. LUTs are created using simulated γ-rays, with known energy E_{true}, to relate the energy of an event to the impact parameter and the Cherenkov photon density for each telescope. The estimated energy E_{est} is then computed as the weighted average of the mean true energy E_{true} over both telescopes.

The energy resolution of the observations is given by the Gaussian fit to the peak of the $(E_{est} - E_{true})/E_{true}$ distribution and provides an estimation of the energy reconstruction. The distance from zero of this distribution gives the energy bias. Figure 2.17 shows the energy resolution achieved after the last MAGIC upgrade along with its energy bias for different zenith angles.

The energy threshold of an analysis, E_{thr}, is defined as the peak of the E_{true} distribution of γ-ray simulated events after using the same cuts applied to the real data events, such as zenith, *hadronness* and *theta*. The value of the energy threshold is highly

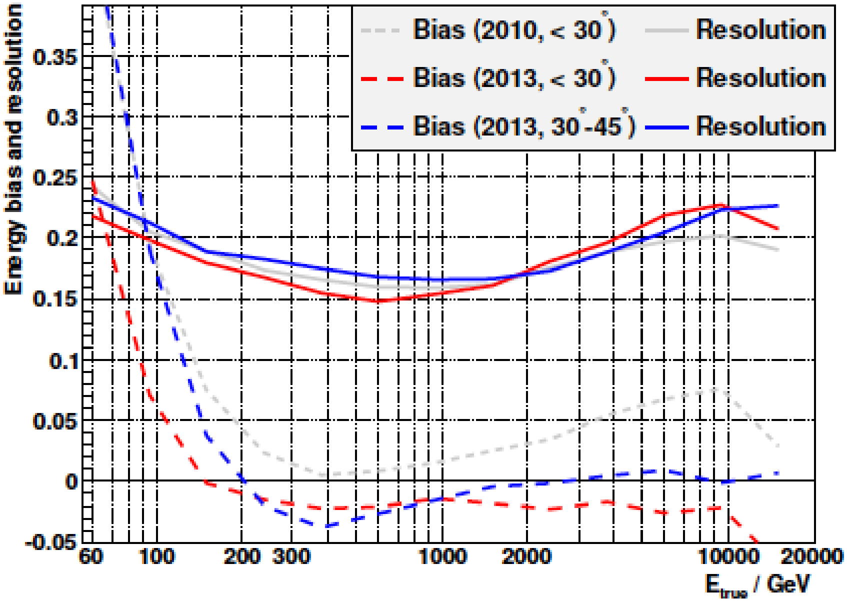

FIGURE 2.17: MAGIC energy resolution and bias for different epochs and zenith angles. From Aleksić et al. (2016b).

dependent on the *size* parameter and therefore each observation/analysis has it is own energy threshold.

2.5.3.9 Background estimation

Background estimation is extremely important as it must take into account the inhomogeneities of the camera acceptance and the different star fields. For wobble observations, the background is estimated from the same data set as follows; in the first wobble position, the source lies in one half of the camera (per definition) while it lies on the other half for the second wobble position. In consequence, the events whose arrival direction fall in the half of the camera that does not contain the source are taken for the background subtraction (Figure 2.18).

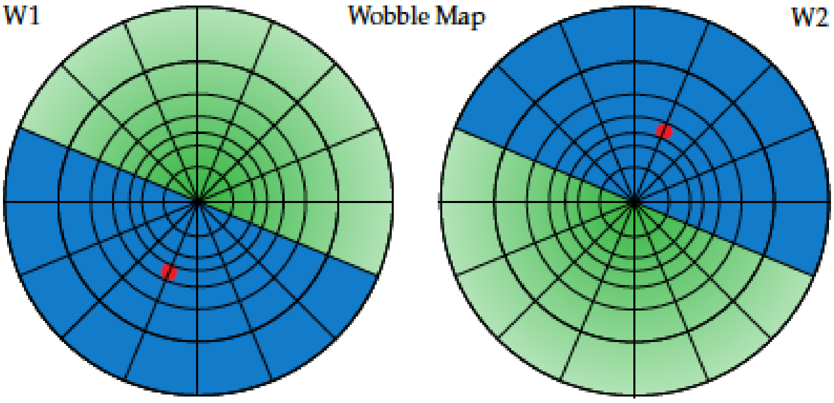

FIGURE 2.18: Illustration of the background estimation from wobble observations. The source position is represented in red. Green zones characterize the half of the camera from which the background is calculated. From Vovk et al. (2018).

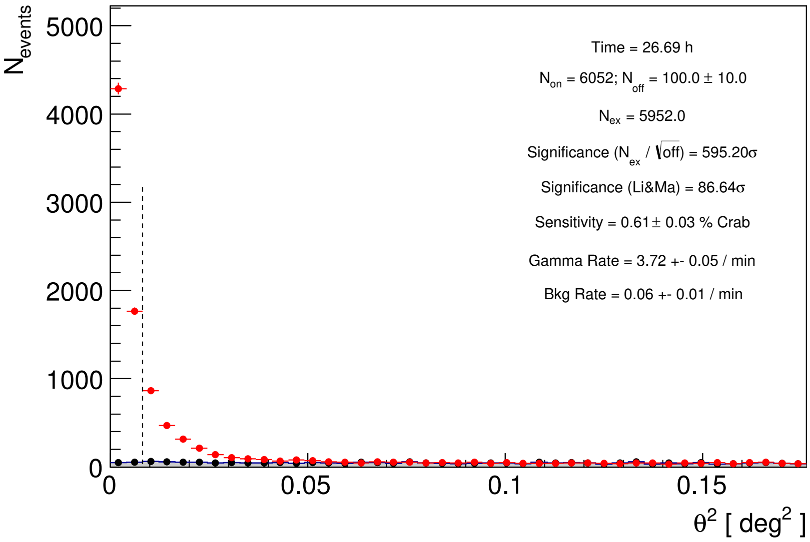

FIGURE 2.19: θ^2 distribution of an observation of the Crab taken in wobble mode. On and Off events are plotted in black and red, respectively. The vertical dashed line represents the cut performed for the signal extraction.

However, this simple approach for background estimation has drawbacks when the source of analysis is an extended object or a complex region. First, not knowing the shape of the source may result in an over-estimation of the background and thus spoiling the signal. Second, signal from overlapping sources cannot be distinguished. To overcome these issues, the *Exclusion map* technique implemented in `SkyPrism` (Vovk et al., 2018) is used in order to exclude from the background computation any region containing previously known sources.

2.5.3.10 Signal identification

The γ-ray signal identification has to be performed through parameters able to discriminate between EM and hadronic induced showers. Usually, the square of the parameter θ, i.e. the angular distance from the real source position to the reconstructed one (see section 2.5.3.7), is used since the distribution of γ-ray events peak towards small values while hadronic events produce a rather flat distribution (see Figure 2.19). The signal region is therefore determined by a cut on the θ^2 parameter. The significance of the signal from the source, σ, is calculated according to Li and Ma (1983) equation 17:

$$\sigma = \sqrt{2\left(N_{On}\ln\left[\frac{1+\alpha}{\alpha}\left(\frac{N_{On}}{N_{On}+N_{Off}}\right)\right] + N_{Off}\ln\left[\alpha\left(\frac{N_{Off}}{N_{On}+N_{Off}}\right)\right]\right)} \quad (2.5)$$

where N_{On} are the number of events passing the θ^2 cut at the source position and N_{Off} the background events. Background events are estimated from an analogous θ^2 cut at n different off positions (located at the same distance from the camera centre than the source) derived from the same dataset in case of wobble observations or from an specific off-sample in case of On/Off observations (section 2.5.2.2). The parameter α is inversely proportional to the number of Off positions selected.

Although θ^2 distributions are important for signal searches, they provide no information about the morphology of the sources. For this purpose, the so-called Skymaps are used. Skymaps are two dimensional histograms representing the reconstructed arrival direction of the γ-ray events, transformed into the sky coordinates, after background subtraction. The resulting skymap is smoothed by a Gaussian function with variance equal to the square of the angular resolution, i.e. the standard deviation of a 2-dimensional Gaussian fit to a point-like γ-ray source. This is also known as the Point Spread Function (PSF): the radius containing 68% of the γ-ray events from the point-like source.

2.5.3.11 Region modelling

Morphological analyses in MAGIC requiring a parametrization of the form, extension and position of the source/region are performed with `SkyPrism`. `SkyPrism` first computes the Instrument Response Functions (IRFs) of MAGIC, based on data and Monte Carlo simulations, and applies them to an assumed source model. This model, together with the estimated background map (see section), is fit to the recorded sky images to estimate the flux of the sources in the observed region. This is performed via a maximum likelihood fitting method like in *Fermi* (see section 3.3.5). The 2-dimensional spatial fit can also be combined with an spectral fit to obtain the spectral parameters of the sources in the model.

2.5.3.12 Differential Spectrum

The calculation of the differential γ-ray spectrum of the observed source is the last step in the analysis chain. Defined as:

$$\frac{d\Phi}{dE} = \frac{dN_\gamma}{dE dA_{eff} dt_{eff}} \tag{2.6}$$

is measured in $\left[\mathrm{photons\,TeV^{-1}\,cm^{-2}\,s^{-1}}\right]$, where N_γ is the number of γ rays detected, t_{eff} the effective time of the observation and A_{eff} the effective area. The effective collection area defines the area around the telescopes on which air showers can be observed folded with the detection efficiency. The collection area is highly dependent on the γ-ray energy and zenith angle of the observation as can be appreciated in Figure 2.20. For more information on the different parameters mentioned here and their estimation for the current MAGIC setup, please address to Aleksić et al. (2016b).

The differential spectrum obtained is binned in estimated energy which may differ from the true energy spectrum due to finite resolution of the telescopes. To correct for this bias an unfolding procedure is applied (Albert et al., 2007b). Mathematically, both energy distributions are related by:

$$Y(y) = M(x, y)S(x)dx + N(y) \tag{2.7}$$

where Y and S are the estimated and true energy distributions, respectively, M the migration matrix that represents the probability that an event with a certain true energy is measured with a certain estimated energy due to the resolution of the detector, and N the noise. Therefore, the unfolding procedure aims to determine the true energy distribution given a certain migration matrix and estimated energy distribution. As

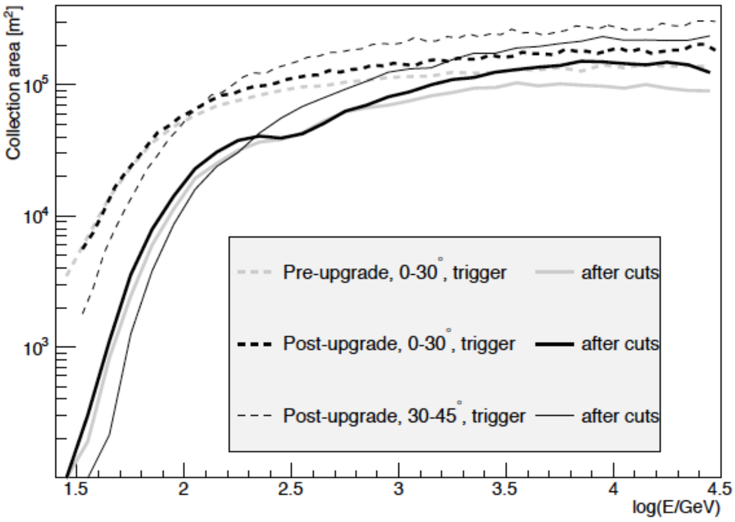

FIGURE 2.20: Effective collection area of the MAGIC telescopes before and after selection cuts, for different observation zenith angles and MAGIC periods.

the migration matrix is not often invertible, a least square minimization (ξ_0^2) with the addition of a regularization term to avoid unstable results is applied (Anykeyev et al., 1991):

$$\xi^2 = \xi_0^2 + \frac{\theta}{2} Reg \tag{2.8}$$

Within MAGIC, several unfolding methods are used, (Bertero, 1989), (Tikhonov and Arsenin, 1979) and (Schmelling, 1998). The main difference among them is how the regularization term has been implemented.

Chapter 3

Space-Based γ-ray detector: *Fermi*-LAT

3.1 Introduction

Very energetic γ-rays can be detected by ground-detectors via atmospheric Cherenkov imaging as explained in chapter 2, however, low energy γ-rays are much more efficiently absorbed in the atmosphere, by Compton scattering and photoelectric absorption, preventing the detection of HE particles. Hence, the detection of MeV-GeV photons has to be carried out outside the atmosphere by space-born detectors.

Already in the 60s, space γ-ray telescopes were observing the Universe. A huge quality jump was achieved when the Compton Gamma-Ray Observatory (CGRO) with Energetic Gamma-Ray Experiment Telescope (EGRET) onboard was launched in the 90s to explore the radiation from 0.05 MeV to ∼30 GeV. The CGRO mission ended in 2000 and ever since, no space based experiment observed the γ-ray sky above 100 MeV until *AGILE* and *Fermi* satellites were launched. *Fermi*-Large Area Telescope (LAT) with a wider FoV (2.4 to 0.5 steradians) and a much better sensitivity ($<6\times10^{-9}$ to $\sim10^{-7}\,\mathrm{cm^{-2}\,s^{-1}}$) than EGRET was a real breakthrough on the detection of GeV γ-rays opening new scientific objectives.

In the first of this chapter, a brief overview of the different systems onboard of *Fermi*-LAT will be given, to focus on the LAT data analysis chain in the second part.

3.2 The Fermi Large Area Telescope

The LAT is an imaging, wide FoV ($\sim$2.4 sr), electron-positron pair conversion telescope sensitive to gamma rays of energies from 20 MeV up to more than 500 GeV, with an on-axis effective area of $\sim$8000 cm^2 above 1GeV (Atwood et al., 2009).

Launched on 2008 June 11, LAT is the primary instrument aboard the Fermi Gamma-ray Space Telescope, which also carries the Gamma-ray Burst Monitor. *Fermi* orbits the Earth in 96 minutes at an altitude of 565 km and scans the entire sky every three hours. Designed to measure the directions, energies, and arrival times of incident γ-rays over a wide FoV, the *Fermi*-LAT is composed of 16 'converter-tracker + calorimeter' modules arranged as a 4 × 4 array that is covered by an Anticoincidence Detector (ACD) and attached to a DAQ system (Atwood et al., 2009). A brief description of these main components (see Figure 3.1) is presented in the following:

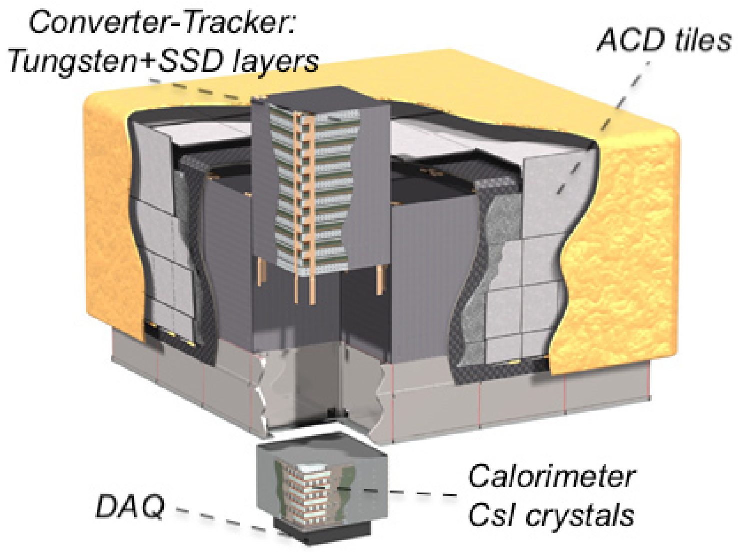

FIGURE 3.1: Scheme of the different subsystems of the *Fermi*-LAT.

Converter-tracker:
Each converter-tracker has 16 planes of tungsten interleaved with 18 layers of Silicon Strip Detectors (SSDs). Incident photons convert in the tungsten foils and the charged particles produced are tracked by the successive planes of SSDs (see Figure 3.2), allowing the reconstruction of the incident photon direction and the rejection of background, i.e. charged CRs.

The tracker is divided into two regions to compromise between achieving a good angular resolution at low energies and maximizing the effective area (important at high energies). The 'front' region, consisting of the first 12 silicon tracking planes, has thin converters to optimize the PSF[1] at low energy. The 'back' region, 4 silicon tracking planes, are about 6 times thicker in order to maximize the effective area. With this configuration the sensitivity of the LAT is balanced between the front and back tracker sections.

---

[1] The PSF is energy dependent, at low energies as 100 MeV, its PSF is $\sim 6^\circ$ and at high energies as 100 GeV is 0.03°.

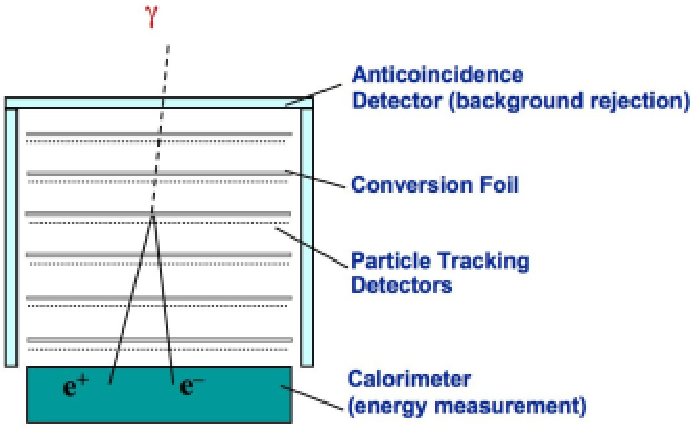

FIGURE 3.2: Sketch of an incident γ-ray converting into a pair of charged particles in the tungsten foils and tracked up to the DAQ by the SSDs planes.

Calorimeter:
Each calorimeter module has 96 CsI(Tl) crystals arranged horizontally in 8 layers of 12 crystals each, Figure 3.1. When charged particles reach the calorimeter, the CsI crystals absorb their energy and re-emit it in form of light that is in turn detected and read out by photodiodes mounted on both ends of the crystal. The difference in light levels on both photodiodes provides a determination of the longitudinal position of the energy deposition along the CsI crystal.

Anticoincidence detector:
Charged CRss can also produce particle showers inside the tracker and, since they outnumber γ rays by 3 to 5 orders of magnitudes, they introduce an important background that can spoil the signal detection. For this reason an ACD covers the other subsystems. Its purpose is to detect charged particles entering the system and reject them. The ACD has 89 plastic scintillator tiles in a 5×5 array on the top and 16 tiles on each side (see Figure 3.1). The ACD is segmented in order to minimize the so-called backsplash effect where secondary particles from electromagnetic showers, created by the incident HE photon, can Compton scatter and create false signals in the ACD from the recoil electrons.

Data acquisition system:
The DAQ collects the information from the other subsystems and makes the initial distinction between unwanted signals from CRs and real γ-ray signals. It also provides an on-board science analysis to search for transients (Atwood et al., 2009).

Data registered by LAT are transmitted to the LAT Instrument Science Operation Center, in Stanford, where are analyzed and submitted to different quality cuts. Finally, it is made available in the *Fermi* Science Support Center web-page[2].

---

[2] http://fermi.gsfc.nasa.gov/ssc/data/

3.3 *Fermi*-LAT data analysis

The *Fermi* Science Support Center provide high-level data, mainly lists of photons after selection cuts and IRFs. IRFs describe the performance of the detector as a function of incidence angle, photon energy and position within the conversion-tacker where photons are converted, among other parameters.

High-level data has to be further processed in order to extract scientific results. The analysis is usually performed using the publicly available *Fermi* Science Tools[3] currently at their v11r5p3 version. In particular, throughout this work we also used *Fermipy*[4] (Wood et al., 2017), a python software package that provides a high-level interface for analyzing the data and that automatizes the analysis with the *Fermi* Science Tools.

In the following a brief description of the analysis workflow will be given. For any deeper understanding on each of the tools within the software, the reader is referred to Wood et al. (2017) and the online documentation of the *Fermi* Science Tools[5].

3.3.1 Event-level Classification

Although automatically performed by the LAT Instrument Science Operations Center, the event-level classification is a key process for further steps in the data analysis.

First, the event reconstruction is performed by the LAT subsystems (i.e. the tracker, calorimeter and ACD). The calorimeter measures the raw energy of each event and uses it to determine their tracks in the tracker, which are then used iteratively to refine the energy measurement. This is combined then with the ACD reconstruction that facilitates the separation of the γ-rays from the background charged particles. Once the energy and track reconstruction are completed, each event is submitted to Classification Trees, in a similar procedure to the one used in MAGIC (section 2.5.3.6), that determine their best physical parameters, such as the arrival direction and the energy. The current simulation and reconstruction framework is the so-called PASS 8 which greatly improves the background rejection and the energy resolution, along with a better PSF, with respect to previous *Passes*. A detailed analysis of all the improvements that PASS 8 provides can be found in Atwood et al. (2013).

After the event reconstruction process, each event is submitted to selection cuts that determine their probability of being photons and the quality of their reconstruction. These selection cuts separate events into different event classes. In turn, event classes are further subdivided into event types that depend on where the photon pair conversion occurs and the instrument observation setup. Each class and event type is characterized by its own IRF, hence, depending on the type of analysis required or even the source of interest, some classes and types are better suited than others.

The event classes used in this thesis are SOURCE, CLEAN and ULTRACLEANVETO. Usually, for point-like and moderately extended source analysis the SOURCE event class (the standard class) is used as it provides an overall low residual background. When a precise analysis above few GeVs is required, the CLEAN class is preferred over SOURCE as the background rate is of the order of 2-4 times lower. Otherwise, for low energy analysis the ULTRACLEANVETO class provides a 2 to 4 times lower

---

[3] https://fermi.gsfc.nasa.gov/ssc/data/analysis/software/

[4] http://fermipy.readthedocs.io/en/latest/

[5] https://fermi.gsfc.nasa.gov/ssc/data/analysis/scitools/overview.html

background rate between 100 MeV and 10 GeV. At the same time, as mentioned previously, each event class is partitioned in three event types, front/back, PSF and Energy Dispersion (EDISP), with no cross-membership events between them.

> Front/Back: Standard and sole event type in previous *Passes*. Photons detected in the front part of the detector have better angular resolution than those arriving at the back section.
>
> PSF: All the events are divided into quartiles depending on their direction reconstruction quality, with PSF3 being the best one and PSF0 the worst. This event type is preferably used for analysis aiming at source localization or morphologic studies.
>
> EDISP: All the events are divided into quartiles depending on their energy reconstruction quality, with EDISP3 being the best one and EDISP0 the worst. This event type is preferably used for analysis of known sources and aiming at computing their energy spectra.

Pass 8 Release 2 Version 6 IRFs provide the current description of the instrument response for each class and event type. Some relevant (for this thesis) performances as a function of photon energy within PASS 8 are shown in Figure 3.3.

3.3.2 Data Selection

Prior to any *Fermi* analysis, a data selection must be carried out in order to keep only the events that are best suited to the particular analysis being performed, as aforementioned in section 3.3.1. Once the event class has been selected, some additional cuts are required to reject bad data or possible background sources spoiling our dataset. For all of the analysis presented within this work, only good quality events (`DATA_QUAL>0`) taken in nominal science configuration (`LAT_CONFIG=1`) have been used. An additional cut is performed to avoid possible data contamination from photons produced on the Earth's limb (lying at zenith angles $\theta_z > 113°$), that can reach energies up to few GeVs. Thus, data registered with $\theta_z > 90°$ and a rocking angle (angle between the z-axis of the spacecraft and the zenith) of $|\theta_r| < 52$ have been discarded (see Figure 3.4). Data selection cuts presented here has been performed by the *gtselect* and the *gtmktime* tools.

3.3.3 Region Model

To extract accurate information from the source of study, one must account for any possible external contribution affecting the source. On one hand, at MeV energies the sky is highly dominated by diffuse emission, thus an accurate model of this background emission is crucial. Through this work, we used the Galactic diffuse emission model and the isotropic model developed by Acero et al. (2016a)[6]. The isotropic model includes extragalactic diffuse emission and residual CR emission. On the other hand, due to the large PSF in the MeV energy range, nearby sources also contribute to the total counts of our source. For the greatest accuracy, a precise source model is essential to attenuate the influence of surrounding sources. Usually, for this purpose the latest *Fermi*-LAT source catalog is used as a starting point. In this thesis we used the LAT 2-year and LAT 4-year Point Source Catalog (2FGL and 3FGL catalog, respectively).

---

[6] https://fermi.gsfc.nasa.gov/ssc/data/access/lat/BackgroundModels.html

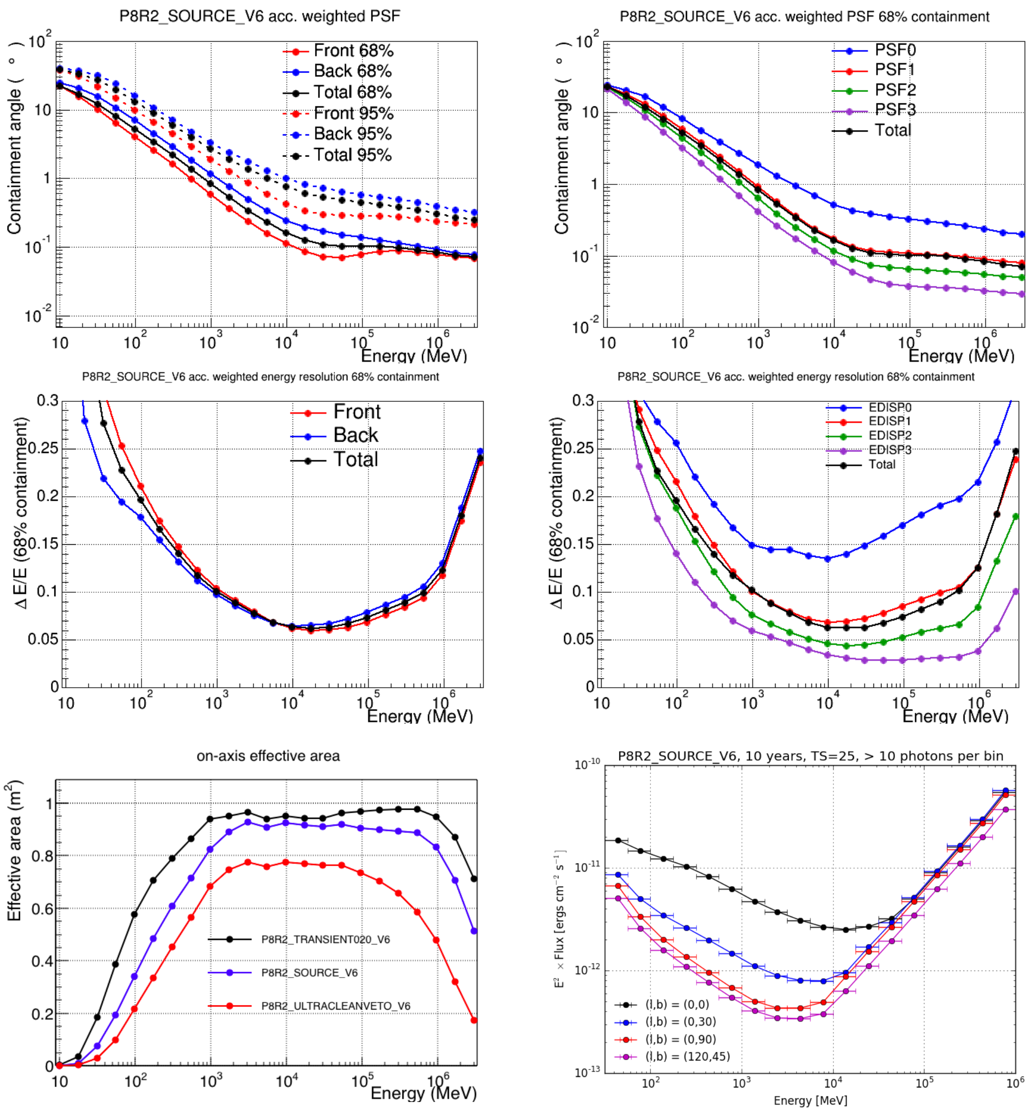

FIGURE 3.3: *Fermi*-LAT performance plots for the current PASS 8.

The position and spectral information of detected sources within and to some extent outside the Region Of Interest (ROI) are included. Models, however, can be iteratively improved by adding newly detected sources or even excess spots that can be putative sources. For specific cases where a known extended source was lying within the ROI, extended templates available in the web page[7] were also used.

3.3.4 Exposure Corrections

3.3.4.1 Livetime Cube

Fermi-LAT IRFs vary depending on the angle between the spacecraft normal and the direction to a source. Therefore, the registered counts (i.e. events associated to a source) depend on the observation time the source spent at a given angle and the effective area at that angle. In addition, as the orientation of the LAT telescope is constantly changing due to its rotation, a given source is observed at different

---

[7] https://fermi.gsfc.nasa.gov/ssc/data/access/lat/4yr_catalog/

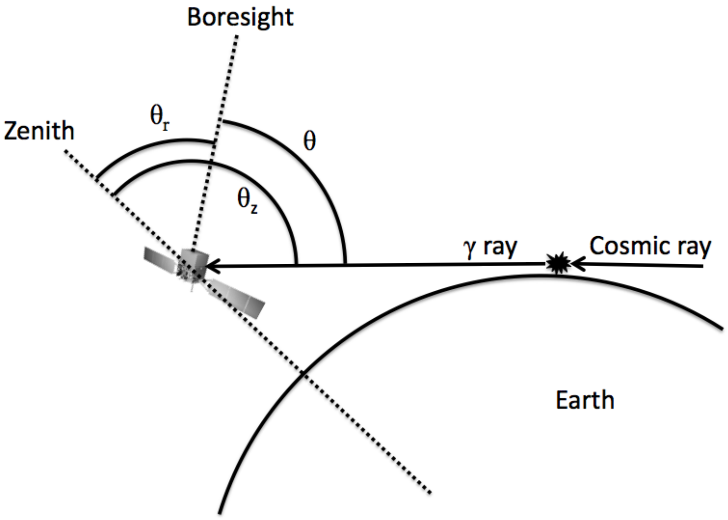

FIGURE 3.4: Representation of an observed Earth's limb γ-ray. The zenith (θ_z) and the rocking angle (θ_r) are shown. From Ackermann et al. (2013a).

inclination angles and thus with different performances. Proper handling of this inclination angle dependency is therefore crucial for the analysis. The array of the integrated observation times as a function of the angle at every point in the sky is called livetime cube and is computed by the *gtltcube*.

3.3.4.2 Exposure Map

The exposure map is defined as the total exposure for a certain position on the sky that produces counts in your analysis region. Since the PSF of the LAT at low energies is significantly large (see Figure 3.3 for reference), sources outside the ROI, i.e. acceptance cone centered at the source of interest, might contribute to the emission detected. To compensate for this, exposure maps are usually computed several degrees larger ($10-20^{\circ}$) than the analysis region. This step is done with *gtexpcube2*.

3.3.5 Likelihood Fitting

Counts detected by *Fermi*-LAT have many intrinsic variables (e.g. energy, position, etc), therefore even with a large data sample, any binning of the parameter space will result in a small number of counts per bin. Thus, the Poissonian distribution characterizes the observed counts in those bins. The probability of detecting n_i counts in the ith bin is given by $p = m_i^{n_i}\frac{e^{-m_i}}{n_i!}$ where m_i is the expected number of counts (model dependent parameter).

The likelihood is the product of the probabilities of observing the detected counts in each bin, consequently

$$\mathcal{L} = e^{-N_{exp}} \prod_i \frac{m_i^{n_i}}{n_i!}$$

defines the likelihood with N_{exp} the total number of counts predicted by the model.

If we reduce the bin size up to the point where each bin is characterized by only one count, the likelihood becomes

$$\mathcal{L} = e^{-N_{exp}} \prod_i m_i$$

This is called unbinned likelhood and it is more accurate than the binned likelihood. However, it can only be used for small data samples, otherwise it is so time consuming that becomes prohibitive.

In general terms, the likelihood describes the probability that the observed data could have been originated from a given input region model. The model, as mentioned in the previous sections, consists of many spectral parameters describing the sources within the ROI. Fitting repeatedly the model to the data while varying the spectral parameters of the sources allows us to compare the different likelihoods obtained for each set of parameters. The best model is determined by the set of spectral parameters that maximize the likelihood. The maximum likelihood fit is performed with *gtlike*. Note that the spectral parameters of the sources in the model can be frozen or freed to vary during the likelihood calculation depending on the analysis performed and the type of sources. Usually, weak and/or distant sources from the center of the ROI, that do not contribute much to the counts of the source studied, are frozen to ease the convergence of the model. Specific criteria are used for each specific analysis.

Once the maximum likelihood has been obtained, the goodness of the likelihood fit is estimated by means of a Test Statistic (TS) defined as:

$$TS = -2ln\left(\frac{\mathcal{L}_{null}}{\mathcal{L}_{test}}\right)$$

where $\mathcal{L}_{null}$ and $\mathcal{L}_{test}$ are the likelihood values for the null hypothesis and our tested model respectively. TSs are extremely important when we analyze complicated regions, as they allow us to compare two nested models (one derives from the other by adding n additional parameters) and estimate if one model is preferred over the other. It has been proven that TS behave approximately as the square of the scientific significance, $TS = \sigma^2$, (Mattox et al., 1996). $TS = 25$ is normally accepted as the detection threshold of a source.

At this step, one can check the consistency of the model by computing the so-called TS map. TS maps are significance maps resulting from moving an hypothetic source through each position of the ROI and maximizing the likelihood in each of them, taking into account our source model. Excess regions, either point-like or diffuse, that have not been accounted for in the model will appear in the map. TS maps are very useful to identify sources that might be covered by the emission of stronger sources. New sources identified in the TS map have to be introduced into the model to run the whole analysis again. This is an iterative process that must be performed until a flat TS map is obtained, implying no significant sources are being omitted in our model.

The output obtained after the maximum likelihood fit contains then the flux expectation and the spectral parameters of each source of the model for the full energy range. In order to obtain the Spectral Energy Distribution (SED), the energy range is divided in narrow bins and an independent maximum likelihood analysis is run in each of them. For these independent energy-binned likelihood fits, all the parameters in the model are fixed to the ones resulting from the analysis of the full energy range except for the normalization of our source of interest.

Part II

SNRs: CR ACCELERATORS

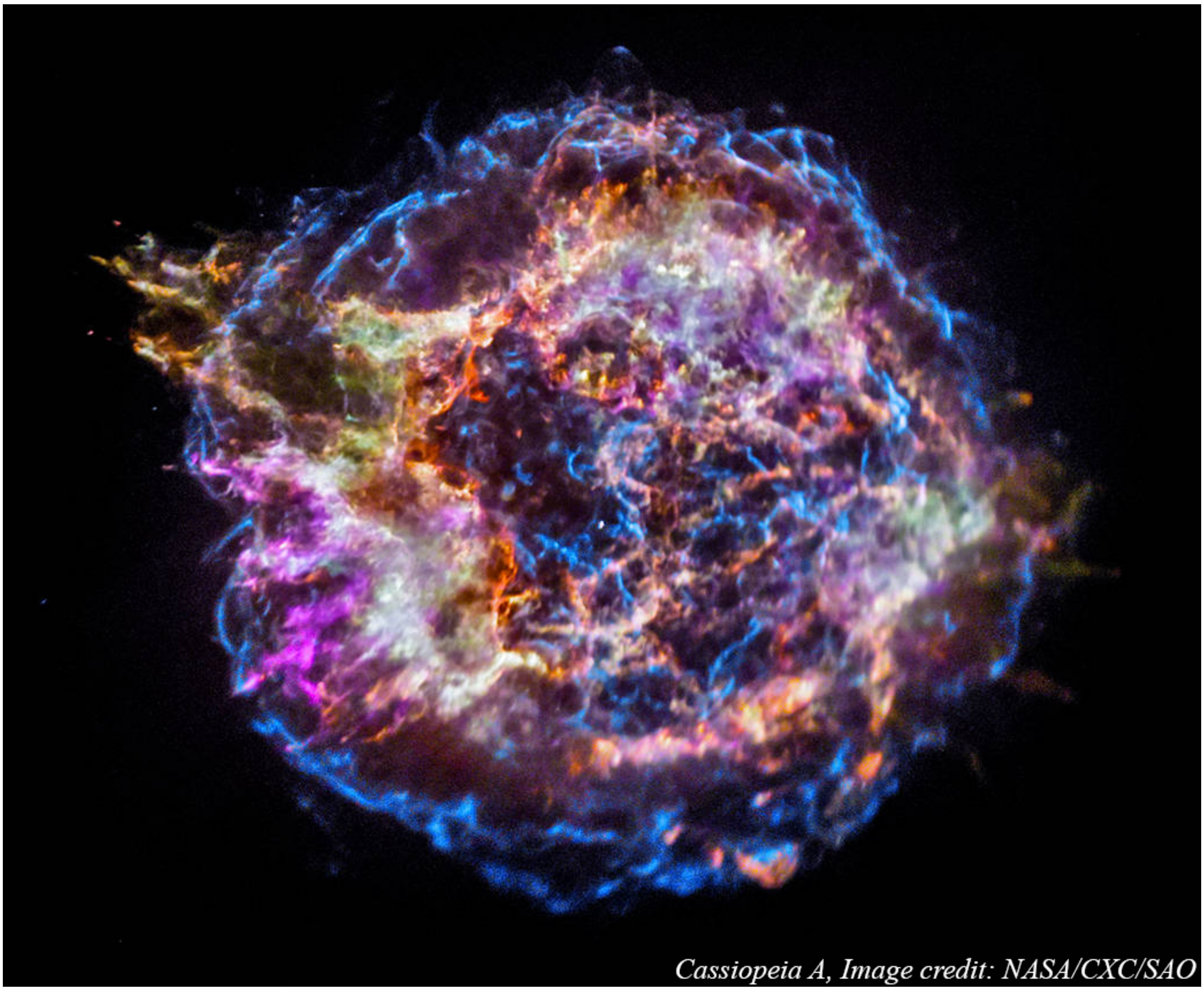

Cassiopeia A, Image credit: NASA/CXC/SAO

Chapter 4

Supernova Remnants

4.1 Introduction

SNRs have been for long time believed to be the main source of Galactic cosmic rays with energies up to $\sim 10^{15}$ eV, the so-called *knee* of the CR spectrum. This argument is based on the fact that Supernovae (SNe) release an energy of 10^{51} erg at a rate of a SN every 40 years (Tammann et al., 1994), thus, only a reasonable percentage (10%) of their energy needs to be converted into acceleration of CRs in order to account for the Galactic CR flux, $\sim 10^{40}\,\mathrm{erg\,s^{-1}}$. However, although the presence of very HE electrons in SNRs can be easily proven through non-thermal X-ray observations, acceleration of hadronic CRs up to PeV energies still lacks of any observational evidence. Consequently, SNRs have not yet been confirmed as *the* Galactic CR accelerators up to the *knee* energies.

This chapter discusses the current understanding on SNRs along with the expectations of γ-ray emission within these objects or from their interaction with surrounding Molecular Clouds (MCs).

4.2 Types and evolution

SN explosions are extremely powerful phenomena that emit more than 10^{49} erg in form of radiation. The explosion is triggered at the end of a star's lifetime by two different mechanisms depending on the nature of the progenitor.

- Type Ia or thermonuclear SNe occur when the progenitor, a white dwarf, reaches the Chandrasekhar mass limit ($\sim$1.4 $M_\odot$) by mass accretion in a binary system. At that time, the white dwarf undergoes a collapse that the electron degeneracy pressure cannot counteract and explodes disrupting the system and blowing away its companion. The resulting SNR is often a symmetrical shell with no central compact object.
- In contrast to type Ia, all other SNe take place when the progenitor is an isolated massive star with an initial mass comprised of between 8 and 40 $M_\odot$. After these stars have burned all the nuclear energy in their cores, they cannot produce any more energy to sustain the pressure exerted by the gravitational force and implode ejecting material at thousands of kilometers per second. The remnant object after the SN explosion is a NS for initial masses of 8-25 $M_\odot$ or a black hole for masses higher than 25 $M_\odot$. These are usually known as core-collapsed

SNe. Since massive stars are usually found in star forming regions, SNRs are often associated to giant MCs.

The expelled stellar ejecta carry away the kinetic energy of the SN explosion ($\sim 10^{51}$erg) into the surrounding circumstellar and interstellar material forming the SNR. The expanding ejecta create a Forward Shock (FS) that is unaltered as it sweeps up surrounding material during the first phase of the SN evolution called *free expansion* phase. A Reverse Shock (RS) starts to form at the contact discontinuity, i.e. a surface between two different materials with different density but similar pressure and velocity, that separates shocked interstellar material and stellar ejecta. When the swept up mass of ambient medium is of the order of the mass of the ejecta, the RS starts propagating inwards into the stellar ejecta. In turn, the ejecta is shocked by the RS and increases its temperature up to the point where the expansion becomes adiabatic and is driven by thermal pressure of the gas, the *Sedov* phase. The SNR keeps expanding and cooling adiabatically until it reaches a temperature of $\sim 10^6$K, at which ionized atoms capture free electrons and radiate their excitation energy. During this *radiative* phase, thermal pressure drops and the expansion slows down. Finally, when the swept up material accumulated becomes much larger than the stellar ejecta, the shell breaks and the SNR disperses into the surrounding medium.

Different types of SNRs have been observed in nature, *shell-like*, *composite* and *mixed-morphology* remnants. Shell-like remnants emit their radiation from a shell of shocked ISM (like CasA, *left* panel of Figure 4.1). Composite remnants, apart from an interacting outer shell they additionally contain a central PWN (such as SNR G24.7+0.6). Mixed-morphology remnants are radio shells containing primarily thermal X-ray central emission, probably arising from the evaporation of dense clumps of interstellar material that were not disrupted by the shock (White and Long, 1991), an example of a mixed-morphology remnant is W28 shown in the *right* panel of Figure 4.1.

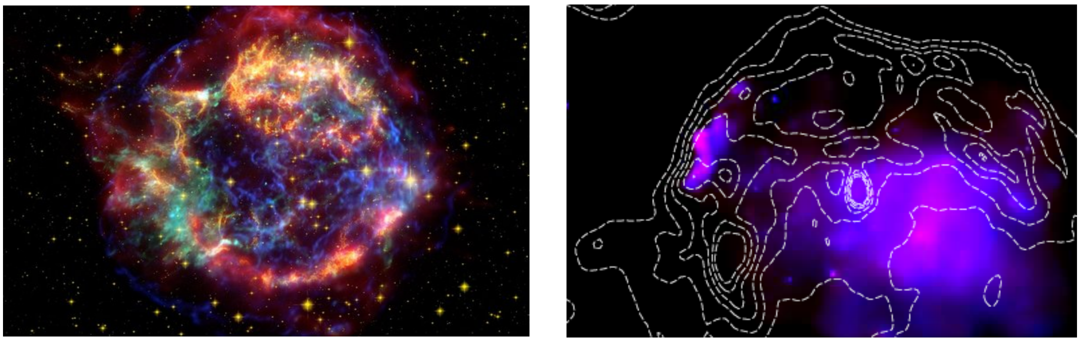

FIGURE 4.1: *Left:* Shell-type SNR: CasA. *Spitzer* IR, *Hubble* and *Chandra* X-ray data are represented in red, orange and blue, respectively. *Right:* Mixed-Morphology SNR: W28. *XMM*-Newton data in the 0.3-1.0 keV and 1.0-7.0 keV bands are represented in magenta and blue, respectively. The VLA 1.4 GHz contours of the radio shell are overlaid in white.

4.3 Cosmic ray acceleration

Relativistic particles in SNRs can be efficiently accelerated via DSA, which naturally provides a power-law spectrum with an spectral index of ~2 (Drury, 1983; Malkov and

Drury, 2001). In its initial version (Bell, 1978a,b), particles are scattered repeatedly through the shock front by magnetostatic inhomogeneities upstream of the shock and a turbulent magnetic field downstream reaching energies of $\sim 10^{14}$ eV, an order of magnitude below the knee (Lagage and Cesarsky, 1983). This energetic shortage can be solved considering strong magnetic field amplification in the upstream region, due to CR driven instabilities (Bell and Lucek, 2001), increasing the maximum energy of accelerated particles to values of 10^{15}-10^{16}eV observed at the knee.

CR acceleration in SNRs is tied to the production of γ rays resulting from the interaction between accelerated CR protons and the ambient medium, followed by the subsequent π^0 decay. However, detection of γ-rays is not necessarily a direct evidence of proton acceleration since they can also be originated through leptonic processes, mainly IC scattering of CMB photons provided that the magnetic field in the acceleration region does not exceed $\sim 10\mu$G, where synchrotron radiation dominates. The presence of accelerated electrons come naturally from the non-thermal X-ray spectra observed in several SNRs. The same multi-TeV electrons responsible of the IC γ-ray emission produce X-ray synchrotron emission at keV energies when they interact with the B-field of the SNR. The flux ratio between X-ray synchrotron and IC γ-ray emission produced by the same population of electrons (Aharonian, 2004) is:

$$\frac{f_{IC}\left(E_\gamma\right)}{f_{sy}\left(\epsilon_X\right)} \sim 0.1 \left(\frac{B}{10\mu G}\right)^{-2} \tag{4.1}$$

There are, however, some unambiguous signatures of γ-rays produced from pion decay: *i)* Low-energy cut-off in the spectrum peaking at $\sim$70 MeV (i.e. *pion bump*), threshold energy at which γ-rays are produced in the decay (Figure 4.2, *top*). *ii)* γ-rays with energies greater than 100 TeV corresponding to protons accelerated up to 1 PeV, energy range where leptonic proceses are inefficient (Figure 4.2, *bottom*). *iii)* Detection of neutrinos radiated during the decay of pions (see Section 1.3.5). And *iv)* Spatial correlation of γ-ray emission and dense mediums, e.g MCs. In this last case, CR protons are expected to produce γ rays in their interaction with the surrounding medium, however, this is not granted in leptonic scenarios.

Therefore, the observation of a $\sim$70 MeV cut-off in the spectra, so far detected in three middle-aged SNRs; W44 and IC443 (Ackermann et al., 2013b) and W51C (Jogler and Funk, 2016), as well as the detection of illuminated MCs, would provide a proof that CRs are being accelerated in SNRs. However, the detection of multi-TeV particles (inelastic interactions of CR protons with interstellar gas produce neutrinos of energy $E_\nu \sim 50\,(E_p/1\,\mathrm{PeV})$ TeV and gammas of energy $E_\gamma \sim 100\,(E_p/1\,\mathrm{PeV})$ TeV (Kelner et al., 2006)) would be irrefutable proof that SNRs can accelerate CRs up to the knee and account for the Galactic CR spectrum observed.

4.4 PeVatrons

SNRs can only accelerate protons up to a maximum energy, E_{max}, given by Gabici (2017):

$$E_{max} \sim \frac{1}{3}\left(\frac{B}{\mu\mathrm{G}}\right)\left(\frac{u_s}{1000\,\mathrm{km/s}}\right)\left(\frac{R_s}{\mathrm{pc}}\right)\mathrm{TeV} \tag{4.2}$$

being u_s the velocity of the shock and R_s the shock radius.

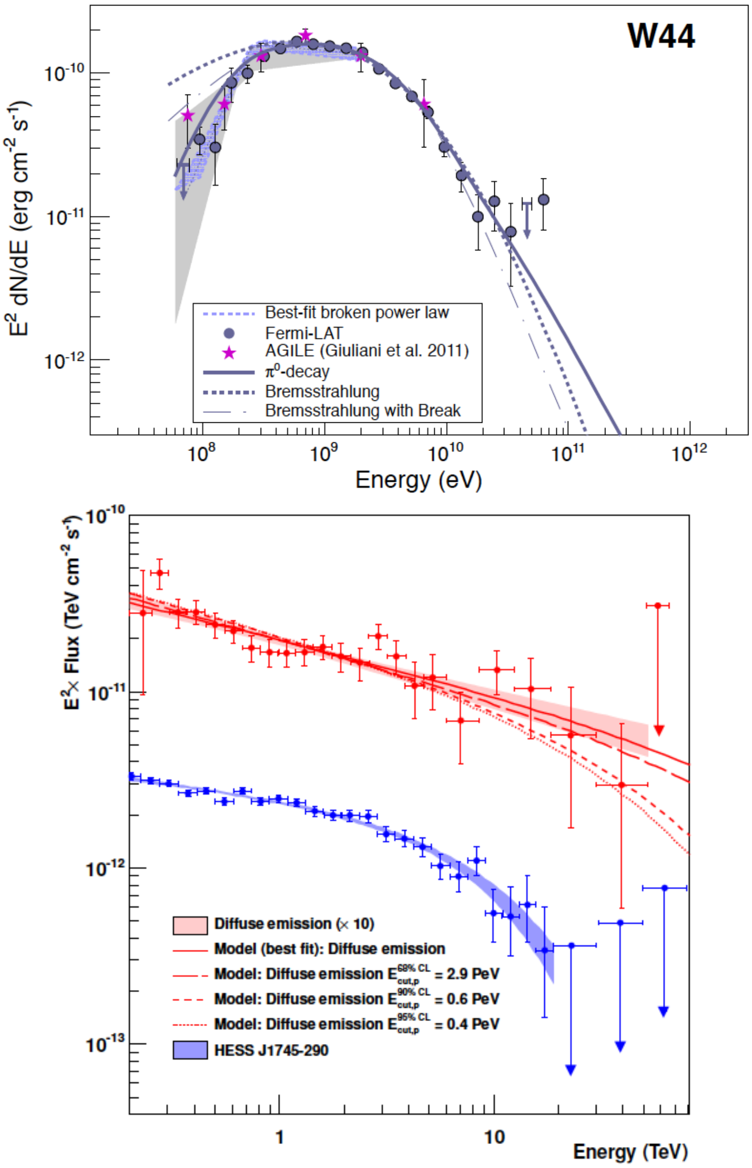

FIGURE 4.2: Hadronic-like spectral features. *Top:* γ-ray spectra of W44 from Ackermann et al. (2013b). The spectra exhibits a break at $\sim$200 MeV establishing its hadronic origin. *Bottom:* γ-ray spectra of the first PeVatron (red) detected in the Galaxy from Abramowski et al. (2016). Although the acceleration of PeV protons in SNRs has not yet been observed, this detection confirms that protons can be accelerated up to the knee within our Galaxy.

For typical values of the interstellar magnetic field ($\sim$3 μG), acceleration of PeV particles is impossible unless magnetic field amplification by plasma instabilities (Bell, 2004) is assumed. The acceleration of PeV protons needs very high shock velocities only attainable during a short period at the transition between the free expansion and Sedov phase. Top panel of Figure 4.3 shows the γ-ray spectrum produced in a SNR at different epochs after the SN explosion. Multi-TeV γ-rays could only be detected during few hundred years (curve 1) since the highest energy CRs diffuse away from the SNR, as pointed out by Ptuskin and Zirakashvili (2005). Already 2000 yr after the explosion (curve 2), PeV and even high TeV CRs have escaped the SNR producing a cut-off in the γ-ray spectrum at the high energies. Since the highest CRs continue

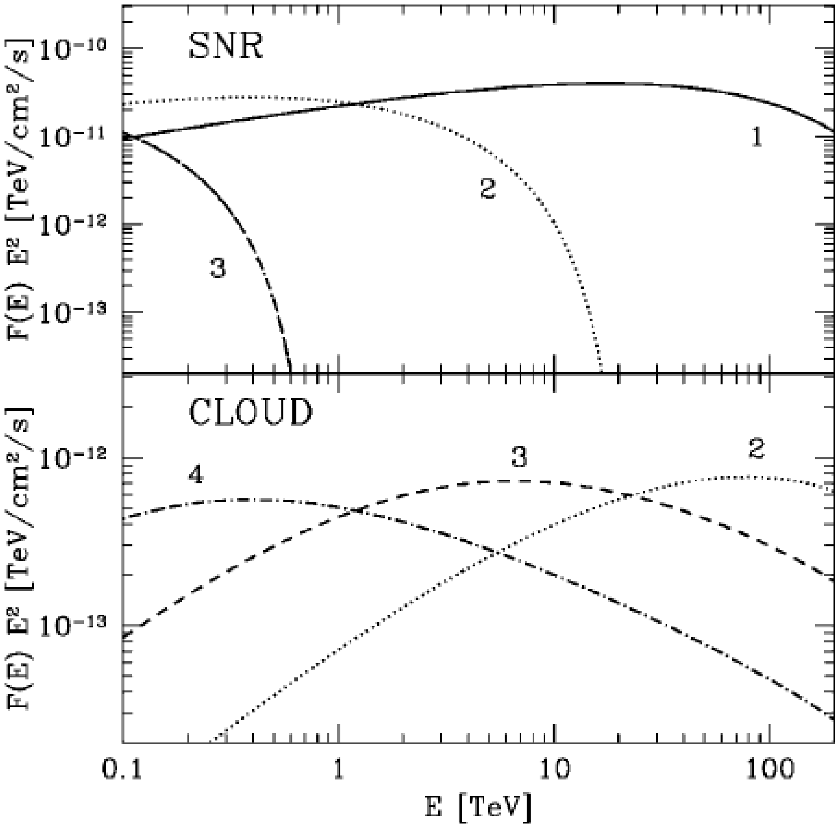

FIGURE 4.3: γ-ray spectra from the SNR (*top*) and from a MC of mass $\sim 10^4 M_\odot$ located 100 pc away from the SNR (*bottom*). Curves refer to different epochs after the SN explosion: 400 yr (*1*), 2000 yr (*2*), 8000 yr (*3*) and $\sim 10^4$ yr (*4*). The system is located at 1 kpc from the observer. From Gabici and Aharonian (2007).

escaping the SNR and the CR acceleration at the shock is less and less efficient (due to a decrease of the shock velocity as a result of the resistive force exerted by the swept up material), the cut-off in the spectrum shifts to lower energies with time. Thus, SNRs act as PeVatron accelerators only during a short time window of few hundred years. This strong restriction limits the number of potential PeVatron candidates to a small fraction.

Still, runaway PeV particles can be detected on their interaction with associated MCs, located in the vicinity of the SNR, that enhance the γ-ray emission.

4.5 SNRs interacting with MCs

Massive stars that originate SNRs are usually born in massive MCs (Chevalier, 1999), this often leads to interactions between the SNR and the cloud. About 10% of the identified SNRs are believed to be interacting with a MC (Reynoso and Mangum, 2000).

CR protons escaping from SNRs have a power-law proton distribution $\Phi_p(E) = K_p E_p^{-\Gamma}$. A time Δt after they escape, CR protons diffuse away a distance of (Aharonian and Atoyan, 1996)

$$R(E) = \sqrt{6 D_{ISM}(E)\,\Delta t} \tag{4.3}$$

where $D_{ISM}(E)$ is the diffusion coefficient of the ISM. A MC of mass M located within the diffusion radius (e.g. at distance d) can then be illuminate by CRs producing a γ-ray flux of:

$$F_{\gamma}(E) \propto \frac{\sigma_{pp}}{d^2}\frac{M}{m_H}K_p(E_{\gamma})^{-\Gamma} \tag{4.4}$$

where σ_{pp} is the cross section of proton-proton interaction and m_H the hydrogen mass.

This estimation is under the assumption that the diffusion coefficient within the MC does not differ much from the Galactic one, $D(E) = 10^{28}\left(\frac{E}{10\mathrm{GeV}}\right)^{0.5}\,\mathrm{cm}^2\,\mathrm{s}^{-1}$ (Dermer, 1986), and therefore, CRs penetrate freely into the cloud. If CR exclusion is taking place, i.e. a diffusion coefficient much smaller than the Galactic diffusion coefficient, low energy CRs cannot propagate inside the MC and a low energy cut-off appears in the CR spectrum. For a detailed analysis on how CR spectra and the resulting γ-ray emissions are affected by the suppression of the diffusion coefficient in MCs, the reader is addressed to Gabici et al. (2007).

Bottom panel of Figure 4.3 shows the γ-ray spectrum at different epochs resulting from the interaction of runaway particles with a nearby MC of mass $\sim 10^4\mathrm{M}_{\odot}$. γ-ray flux from the MC it is not detectable during the first thousand years after the SN explosion since CRs have not had time to reach the cloud. Initially, γ-ray emission is produced by the highest energy particles since they are released first from the SNR and propagate faster. As time passes, lower and lower energy particles reach the cloud an produce observable emission while the highest energy particle have already lost theirs through proton-proton interaction. This results in a shift of the maximum of the spectrum to lower energies with time. Multi-TeV γs could be observed in a time window going from less than 2000 yr to more than 10^4 yr after the SN explosion. Despite that the γ-ray flux from MCs is weaker than in SNRs, the larger detection window of the former loosens significantly the intrinsic emission time restriction imposed by SNRs. Note from equation that the flux of γ-rays from a MC depends on the mass of the latter, thus, dense MC will be easier to detected and are better observation targets.

Leptonic contribution to the MC γ-ray emission is neglected since; electrons from the SNR cannot reach sufficient energy due to synchrotron losses to escape confinement and secondary electrons produced in the cloud rapidly cool via synchrotron emission in the magnetic field of the MC.

Concluding, in the case of short lived CR accelerators, e.g. PeVatrons, the presence of a nearby MC where runaway CRs interact, might facilitate the detection of multi-TeV photons.

Chapter 5

A cut-off in the TeV γ-ray spectrum of the SNR Cassiopeia A

5.1 Introduction

Among the already known SNRs, Cassiopeia A (Cas A) appears as one of the few good candidates for the study of hadronic CR acceleration up to PeV energies. The precise knowledge of the age of this core-collapsed SNR (330 yrs), the remnant of a historical SN in AD1680, allows the determination of many otherwise free parameters when studying its morphology and spectral shape. Located at a distance of $3.4^{+0.3}_{-0.1}$ kpc and with an angular diameter of 5 $'$ (Reed et al., 1995), it is the brightest radio source outside our solar system. In fact, Cas A is bright all over the electromagnetic spectrum, offering an excellent opportunity to study particle acceleration.

Cas A has been extensively observed in radio wavelengths (Medd and Ramana, 1965; Allen and Barrett, 1967; Parker, 1968; Braude et al., 1969; Hales et al., 1995). Most of the emission comes from a bright radio ring of ∼1.7 pc radius and a faint outer plateau of ∼2.5 pc radius (Zirakashvili et al., 2014), although a distinct emission coming from several compact and bright knots has also been identified (Anderson et al., 1991). The spectral index of the radio flux can vary from ∼0.6 to ∼0.9 over the remnant. Several emission regions were also identified in the X-ray band (Gotthelf et al., 2001; Maeda et al., 2009; Grefenstette et al., 2015; Wang and Li, 2016). In the gamma-ray domain, *Fermi*-LAT detected the source at GeV energies (Abdo et al., 2010a) and later derived a spectrum that displays a low energy spectral break at 1.72 ± 1.35 GeV (Yuan et al., 2013). In the TeV energy range, Cas A was first detected by High Energy Gamma Ray Astronomy (HEGRA) (Aharonian et al., 2001) and later confirmed by MAGIC (Albert et al., 2007a). VERITAS has recently reported a spectrum extending well above 1 TeV (Kumar et al., 2015; Holder, 2017), with a spectral index larger than the Fermi-LAT index of 2.17 ± 0.09. The spectrum seems to steepen from the *Fermi*-LAT energy range to the TeV band, according to all IACT measurements. Still, the statistical and systematic errors are too large for a final conclusion.

Multi-wavelength modeling of Cas A observations has not yet resulted in a clear discrimination between hadronic and/or leptonic origin of the observed radiation in the GeV to TeV energy range (i.e. Berezhko et al. 2003; Vink and Laming 2003; Yuan et al. 2013; Saha et al. 2014; Zirakashvili et al. 2014). However the break in the *Fermi*-LAT spectrum at ∼1 GeV combined with the observations at TeV energies suggest that the observed gamma-ray flux has either a pure hadronic origin or that several emission mechanisms (proton-proton interaction, IC and/or Bremsstrahlung) are involved. Indeed, several plausible acceleration regions have been identified in Cas A. *Chandra* X-ray images (Gotthelf et al., 2001) and high-resolution Very Large Array (VLA) radio synchrotron maps (Anderson and Rudnick, 1995) show a thin outer edge to the SNR that has been interpreted to represent the FS where the blast wave encounters the circumstellar medium (DeLaney and Rudnick, 2003). The cold SNR ejecta expands supersonically outward from the explosion center producing a strong shock where its relatively high magnetic field (Cowsik and Sarkar, 1980) can be amplified and hence accelerate CRs to PeV energies (Bell, 2004, 2013). This scenario was reinforced by the observations of year-scale variability in the synchrotron X-ray filaments of Cas A (Uchiyama and Aharonian, 2008), which require a magnetic field amplification at the shock of the order of mG. High-resolution observations (Gotthelf et al., 2001; Morse et al., 2004; Patnaude and Fesen, 2007; Helder and Vink, 2008) also show a RS formed well behind the FS that decelerates the impinging ejecta. The parameters that characterize the RS can be significantly different from the ones describing the FS, enhancing different dominant radiation mechanisms on each zone. For instance, IC contribution, up-scattering the large Far Infrared (FIR) photon field of Cas A itself (with energy density of $\sim 2\,\mathrm{eV/cm^3}$ and temperature of 97 K, Mezger et al. 1986), is more significant in a region of lower magnetic field, as otherwise it would be suppressed due to fast cooling of electrons. Hard X-ray observations (Grefenstette et al., 2015; Siegert et al., 2015), if of synchrotron origin, prove the presence of relativistic electrons with Lorentz factor $\gamma_e \geq 100$, which can also produce gamma rays through relativistic bremsstrahlung.

In the following, we present an accurate spectral measurement of Cas A at multi-TeV energies obtained by MAGIC. We also derived the spectrum obtained with *Fermi*-LAT, selecting events with the best energy reconstruction, to extend the spectrum to lower energies and also have sufficient overlap at VHEs. The full spectrum obtained from ~60 MeV to ~10 TeV is investigated here to determine the underlying mechanisms powering the young remnant, constraining the maximum energy of the accelerated particles and their nature.

5.2 *Fermi*-LAT data analysis

The GeV emission of Cas A was revisited using 3.7 yr of LAT observations (Yuan et al., 2013). The derived spectrum is well-represented by a broken power-law with a significant break of 6.9σ at ~1.7 GeV. To compare with the observations performed with MAGIC telescopes, and also to update and improve the spectrum, we analysed 8.3 yr of LAT data (from August 4, 2008, MET 239557417, to December 6, 2016, MET 502702784) on a 15° × 15° region around the position of Cas A[1] (see Figure 5.1). We selected events with energy between 60 MeV and 500 GeV and applied the usual cuts and corrections recommended by the *Fermi*-LAT collaboration (removing intervals when the rocking angle of the LAT was greater than 52° or when parts of the ROI were observed at zenith angles larger than 90°, as well as enabling energy dispersion). In order to derive the energy spectrum we applied a maximum likelihood estimation analysis in 12 independent energy bins from 60 MeV to 500 GeV, modeling the Galactic and isotropic diffuse emission using the templates *gll_iem_v06.fits* and *iso_P8R2_ULTRACLEANVETO_V6_v06.txt* provided by the *Fermi* collaboration (see Chapter 3.3.1 for a description of this IRF). During the broad-band fit, all the

---

[1] The analysis on a 30° × 30° region yields compatible results.

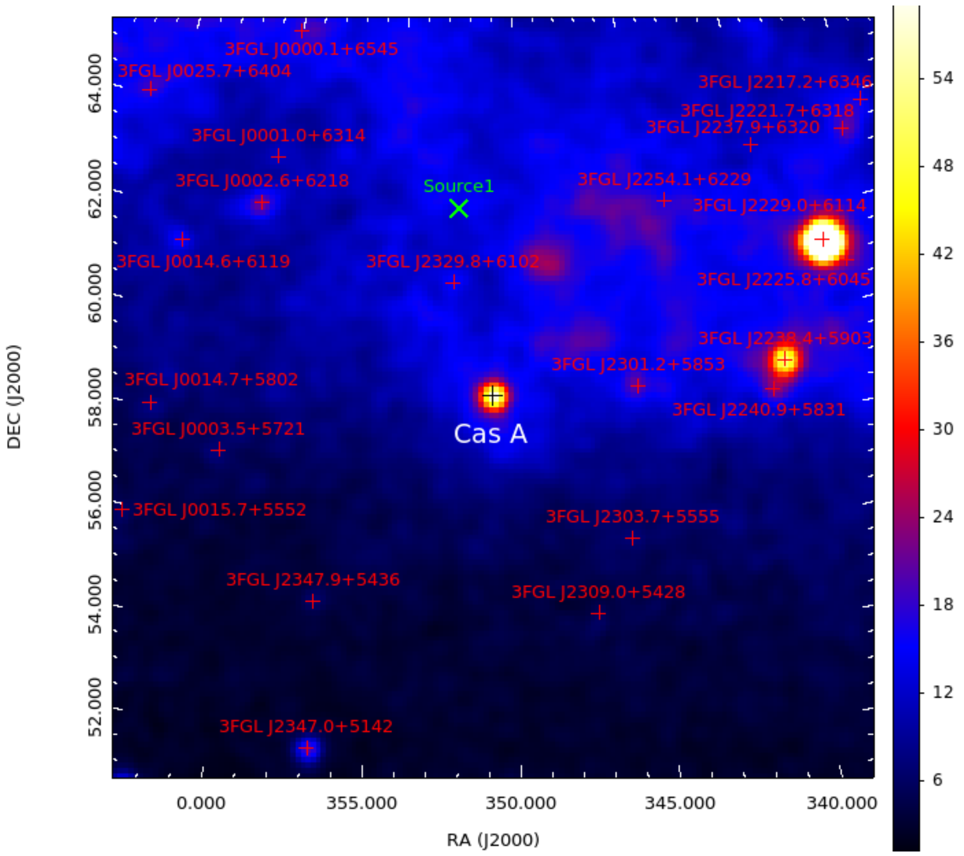

FIGURE 5.1: 15°×15° *Fermi*-LAT counts map centered at the nominal position of Cas A above 1 GeV (MET 239557417 to MET 378691203). 3FGL sources, within our ROI, used in this analysis are plotted in red. Source1, added in our model to account for a significant residual excess is represented in green.

sources in the third *Fermi*-LAT source catalog (3FGL) within the ROI were included. A source located ∼3.7° away from Cas A at (RA,DEC)=(352.3°, 62.5°) was added during the fitting process to account for a significant residual excess found in the TS map (with TS= 45.08, dubbed as Source1 in Figure 5.1). The spectral parameters of the sources in the model were fixed to those from the catalog, except for sources within 5° from the candidate location and the normalisation of the two diffuse background components. Following the results obtained by Yuan et al. (2013) we used a smooth broken power-law function to fit the broadband spectrum of Cas A

$$dN/dE = N_{\mathrm{o}} \left(\frac{E}{E_o}\right)^{-\Gamma_1} \left(1 + \left(\frac{E}{E_b}\right)^{-(\Gamma_1 - \Gamma_2)/\beta}\right)^{-\beta} \tag{5.1}$$

with the parameter β fixed to 1 and the energy break to E_{b}=1.7 GeV. $\mathrm{E_o}$ is the decorrelation energy fixed to 1 GeV. In order to ensure the highest accuracy in the energy reconstruction we used the EDISP event type. Each of the four partitions (EDISP0-3) was analyzed separately and combined later by means of a joint likelihood fit. The SED was obtained by fitting the source normalisation factor in each energy bin independently using a power-law spectrum with a fixed spectral index of 2. For each spectral point we required at least a TS of 4, otherwise Upper Limits (ULs) at the 95% Confidence Level (CL) were computed.

Observation conditions	Time [h]
Dark and Standard HV	42.2
Moon and Standard HV	77.7
Moon and Reduced HV	38.1
All configurations	158.0

TABLE 5.1: Effective observation time of the different hardware and sky brightness conditions under which Cas A samples were taken.

5.3 MAGIC data analysis

Observations were performed between December 2014 and October 2016, for a total observation time of 158 hours after data quality cuts. They were carried in wobble mode, with a standard wobble offset of 0.4° (section 2.5.2.2 for deeper information). All the data correspond to zenith angles between 28 and 50 degrees and most of them (∼73%) were taken during moonlight time (see Table 5.1), under NSB levels that could be up to 12 times brighter than during dark nights. A significant part of the data (∼24%) were obtained under reduced HV settings: the gain of the PMTs is lowered by a factor ∼1.7 to decrease the damage inflicted by background light on the photodetectors during strong moonlight time. The main effect of moonlight in the performance of the telescopes is an increase in the energy threshold (see section), which for zenith angles between 30 and 45 degrees goes from ∼100 GeV during dark conditions to ∼300 GeV in the brightest scenario considered. As achieving a low energy threshold was not critical for this project, Moon observations provided a unique way to accumulate observation time. For a detailed study of the performance of the MAGIC telescopes under moonlight the reader is referred to (Ahnen et al., 2017).

Data have been analyzed with the standard tools used for the analysis of MAGIC data, described in section 2.5.3. Data were first divided into different samples according to their background light level (see Table 2.1). Each sample was analyzed independently with its own *Off* dataset and Monte Carlo simulations. *Off* data and Monte Carlo simulations were tuned to properly reproduce the telescope response under the corresponding observation conditions. Only at the last step of the analysis the data from different samples were merged and a unified spectrum was produced. For the reconstruction of the spectrum a point-like source was assumed and typical selection cuts with 90% and 75% γ-ray efficiency for the γ-ray/hadron separation and sky signal region radius were applied, respectively (Aleksić et al., 2016b). Three *Off* regions were considered for the background estimation. Figure 5.2 shows the significance map of a small data sample of ∼15 hours taken during dark time.

5.4 Results

Figure 5.3 shows the reconstructed SED obtained with the MAGIC telescopes (black solid points). Red solid line is the curve obtained that best fits the MAGIC data assuming a power-law with an exponential cut-off (EPWL):

$$\frac{dN}{dE} = N_0 \left(\frac{E}{E_0}\right)^{-\Gamma} \exp\left(-\frac{E}{E_c}\right) \tag{5.2}$$

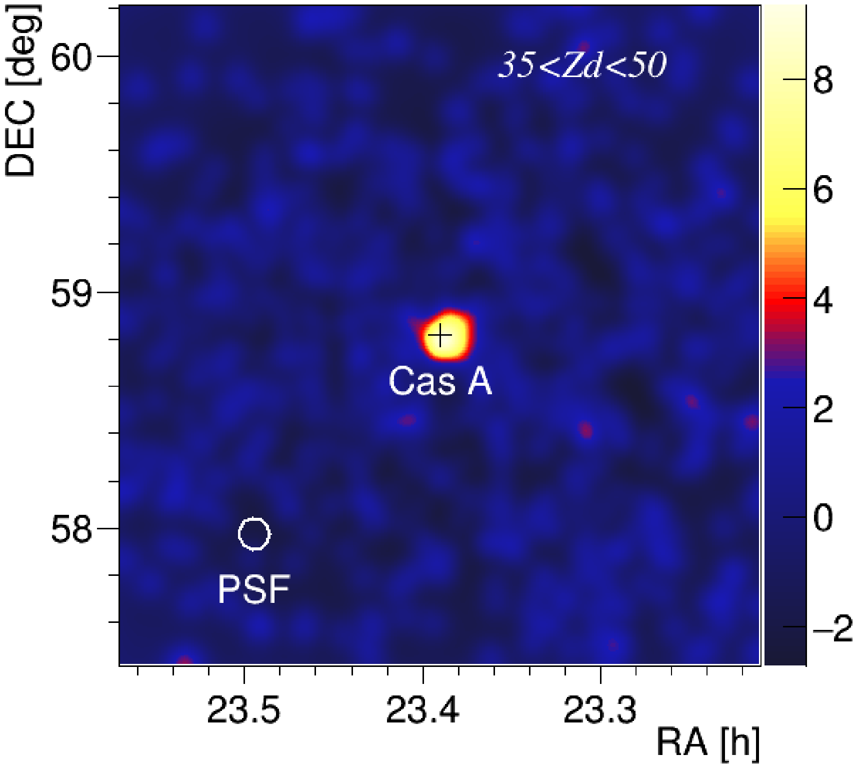

FIGURE 5.2: MAGIC significance map above 600 GeV of a region of 2.5°×2.5° centered in Cas A. This map was produced using only ∼15 hours of dark observations at zenith angles between 35 and 50°.

with a normalisation factor $N_0 = (1.1 \pm 0.1_{stat} \pm 0.2_{sys}) \times 10^{-11}$ TeV^{-1}cm^{-2}s^{-1} at a decorrelation energy $E_0 = 433$ GeV, a spectral index $\Gamma = 2.4 \pm 0.1_{stat} \pm 0.2_{sys}$ and a cut-off energy $E_c = 3.5 \left({}^{+1.6}_{-1.0}\right)_{stat} \left({}^{+0.8}_{-0.9}\right)_{sys}$ TeV. The spectral parameters of the tested models $\theta = \{N_0, \Gamma, E_c\}$ are obtained via a maximum likelihood approach. The data inputs are the numbers of recorded events (after background suppression cuts) in each bin of estimated energy $E^i_{\rm est}$, both around the source direction ($N^{\rm On}_i$) and in the three Off regions ($N^{\rm Off}_i$). An additional set of nuisance parameters μ_i for modeling the background are also optimized in the likelihood calculation. In each step of the maximization procedure the expected number of gammas in a given bin of estimated energy ($E_{\rm est}$) is calculated by folding the gamma spectrum with the MAGIC telescopes response (energy-dependent effective area and energy migration matrix). The background nuisance parameters and the statistical uncertainties in the telescopes response are treated as explained in (Rolke et al., 2005).

The probability of the EPWL fit is 0.42. We tested the model against the null hypothesis of no cut-off, which is described with a pure power-law. The probability of the power-law fit is 6×10^{-4}. A likelihood ratio test between the two models favors the one that includes a cut-off at ~ 3.5 TeV with 4.6σ significance.

Figure 5.4 compares the fit residuals for the two tested models: power-law and EPWL. The residuals are here defined as $N^{\rm obs}_{\rm On}/N^{\rm exp}_{\rm On} - 1$, where $N^{\rm obs}_{\rm On}$ is the number of observed events (including background) in the On region and $N^{\rm exp}_{\rm On}$ is the number of events predicted by the fit in the same region. All the bins in estimated energy which contain events are used in the fits, but only those with a 2σ significance gamma-ray excess are shown as SED points in the upper panel of Figure 5.3.

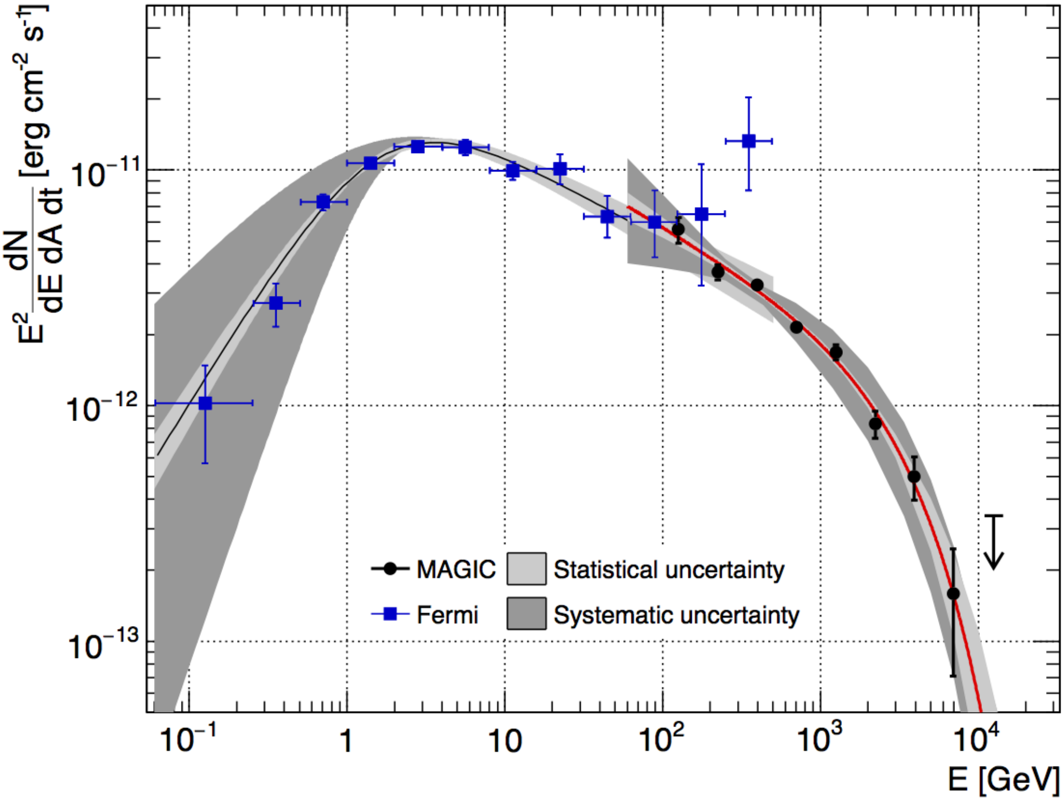

FIGURE 5.3: SED measured by the MAGIC telescopes (black dots) and *Fermi*-LAT (blue squares). The red solid line shows the result of fitting the MAGIC spectral points with equation 5.2. The black solid line is the broken power-law fit applied to the *Fermi*-LAT spectrum.

One of the biggest systematic uncertainties of the IACT technique is related to the possible variations of the atmospheric transparency, or of the light throughout the different telescope elements, resulting in a modification of the recorded Cherenkov light yield from showers. The systematic uncertainty due to an eventual mismatch on the absolute energy scale between MAGIC data and Monte Carlo simulations was constrained to be below 15% in Aleksić et al. (2016b). By conservatively modifying the absolute calibration of the telescopes by ±15%, and re-doing the whole analysis, we can evaluate the effect of this systematic uncertainty in the estimated source spectrum. This does not produce a simple shift of the spectrum along the energy axis, but changes also its hardness. Even in the unlikely scenario in which, through the 158 h of observations, the *average* Cherenkov light yield was overestimated by 15% relative to the Monte Carlo, by applying the corresponding correction the resulting spectrum is still better fit by an EPWL at the level of 3.1σ. In the also unlikely scenario in which the light yield was underestimated, the EPWL is preferred over the power-law at the 6.5σ level. The systematic uncertainties in the flux normalization and spectral index were retrieved from the publication reporting the performance of the MAGIC telescopes during moonlight (Ahnen et al., 2017). The systematic errors in the cut-off energy were estimated from the values of E_c obtained when modifying the absolute light scale by ±15 percent.

For the *Fermi*-LAT analysis, a broken power-law function with normalisation factor $\mathrm{N_o} = (8.0 \pm 0.4) \times 10^{-12}$ $\mathrm{MeV^{-1}cm^{-2}s^{-1}}$, and indexes $\Gamma_1 = 0.90 \pm 0.08$ and $\Gamma_2 = 2.37 \pm 0.04$ is obtained and showed in Figure 5.3, blue solid squares. The light

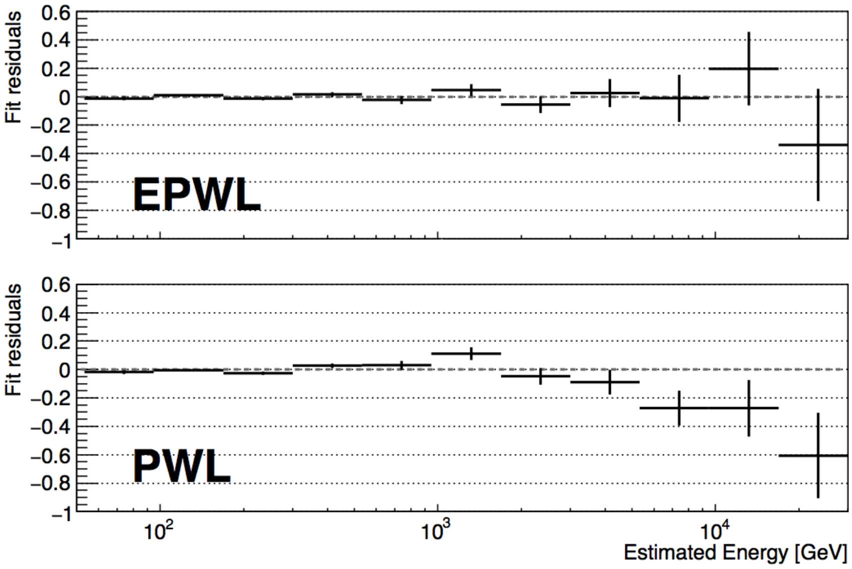

FIGURE 5.4: Relative fit residuals for the two tested models fitting the MAGIC spectral points: power-law with exponential cut-off (upper panel) and simple power-law (lower panel). The error bars are calculated so that they correspond to the total contribution of each estimated energy bin to the final likelihood of the fit.

grey shaded area shows the statistical errors of the obtained broken power-law fit whereas the dark one marks the uncertainty coming from the imperfectness in the Galactic diffuse emission modeling, dominating the Cas A flux uncertainties at low energies. The later was obtained by modifying the galactic diffuse flux by ±6 percent. Note that the systematic error due to the diffuse background is greatly reduced above 3 GeV.

5.5 Discussion

MAGIC observations of the youngest GeV- and TeV-bright known SNR have allowed us to obtain the most precise spectrum of Cas A to date, extending previous results obtained with Cherenkov instruments up to ∼10 TeV. In the MAGIC energy range, the spectrum is best-fit with a power-law with exponential cut-off function with index ∼2.4 and an energy cut-off at E_c ∼3.5 TeV. These findings provide a crucial insight into the acceleration processes in one of the most prominent non-thermal objects in our Galaxy.

We also analysed more than 8 years of LAT data and obtained a spectrum that confirms the one by Yuan et al. (2013). Below ∼1 GeV Cas A shows a hard spectrum with index ∼0.9. Above a few GeV, the spectrum measured with *Fermi*-LAT falls quickly with a photon index of ∼2.37, which is compatible within errors with the one measured using the MAGIC telescopes.

To investigate the underlying population of particles, we have used the radiative code and Markov Chain Monte Carlo fitting routines of *naima*[2] (Zabalza, 2015), that allows us to derive the present-age particle distribution. The code uses the parametrisation of neutral pion decay by Kafexhiu et al. (2014), the parametrization

---

[2] https://github.com/zblz/naima

of synchrotron radiation by Aharonian et al. (2010) and the analytical approximations to IC up-scattering of blackbody radiation and non-thermal bremsstrahlung developed by Khangulyan et al. (2014) and Baring et al. (1999), respectively.

We first considered the possibility that the gamma-ray emission was originated by an electron population, described by a power-law with exponential cut-off function, producing Bremsstrahlung and IC radiation in the gamma-ray range, and synchrotron radiation at lower energies. The photon fields that contribute to the IC component are the ubiquitous 2.7 K CMB and the large FIR field measured in Cas A, with a value of $\sim 2\,\mathrm{eV/cm^3}$ at 100 keV. Fixing the photon field to this value, we can obtain the highest possible density of electrons allowed by the VHE flux. Then we can constrain the maximum magnetic field for which the synchrotron radiation produced by the derived population does not exceed the radio and X-ray measurements[3]. The multi-wavelength SED is shown in Figure 5.5, with the radio emission displayed in purple dots (Medd and Ramana, 1965; Allen and Barrett, 1967; Parker, 1968; Braude et al., 1969; Hales et al., 1995; Ade et al., 2014), soft SUZAKU X-rays are marked in red (Maeda et al., 2009) and hard International Gamma-Ray Astrophysics Laboratory (INTEGRAL) X-rays in blue (Wang and Li, 2016). In the gamma-ray regime, the LAT points are shown in cyan and the MAGIC ones in green. The MAGIC points can be described by an electron population with amplitude at 1 TeV of $2{\cdot}10^{34}\mathrm{eV}^{-1}$, spectral index 2.4 and cut-off energy at 8 TeV up-scattering the FIR (brown dash-dot line) and the CMB photons (green dashed line). The comparison with the X-ray part of the SED constraints the magnetic field to $\mathrm{B}\lessapprox 180\ \mu\mathrm{G}$. The resulting emission from the leptonic model is shown in Figure 5.5. A relatively low magnetic field and a large photon field could be fulfilled in a RS evolving in a thin and clumpy ejecta medium which provides a moderate amplification of the magnetic field and large photon fields in the clumps which are observed as optical knots. The same population of electrons would unavoidably produce Bremsstrahlung radiation below a few GeV (see green dotted line in Figure 5.5[4]). The emission observed with *Fermi*-LAT at the lowest energies constrain the density to $\mathrm{n}\sim 1\ \mathrm{cm}^{-3}$, still compatible with the smooth ejecta density (Micelotta et al., 2016). The model is generally compatible with the X-ray points and with MAGIC spectrum above a few TeV, it is consistent with the radio measurements, but fails to reproduce the γ-ray spectrum between 1 GeV and 1 TeV, being a factor 2-3 below the measured LAT spectrum. In addition, to accommodate a magnetic field of the order of ~1 mG, as reported in Uchiyama and Aharonian (2008), the amplitude of the electron spectrum would need to be decreased at least by a factor 100, rendering a negligible IC contribution at the highest energies.

Indeed the GeV-TeV emission of Cas A is usually attributed to accelerated protons. Assuming a population of CRs characterised with a power-law function with an exponential cut-off to fit the gamma-ray data from 60 MeV to 15 TeV, and a target density of 10 cm^{-3} (Laming and Hwang, 2003). The proton spectrum is best-fit with a hard index of 2.21 and an exponential cut-off energy of 12 TeV, which implies a modest acceleration of CRs to VHE, well below the energy needed to explain the CR *knee*. The proton energy above 1 TeV is $5.1{\cdot}10^{48}$ erg, which is only ~0.2% of the estimated explosion kinetic energy of $\mathrm{E_{sn}} = 2 \cdot 10^{51}$ erg (Laming and Hwang, 2003). The total energy stored in protons above 60 MeV amounts to $9.9 \cdot 10^{49}$ erg.

---

[3] This constraint is due to the fact that, as reported in section 5.1, several emission regions, likely associated to different particle populations, were identified at those wavelengths.

[4] Note that the structure in the spectral shape around 2 MeV is due to the transition between the two asymptotic regimes described in Baring et al. (1999), used in the *naima* code.

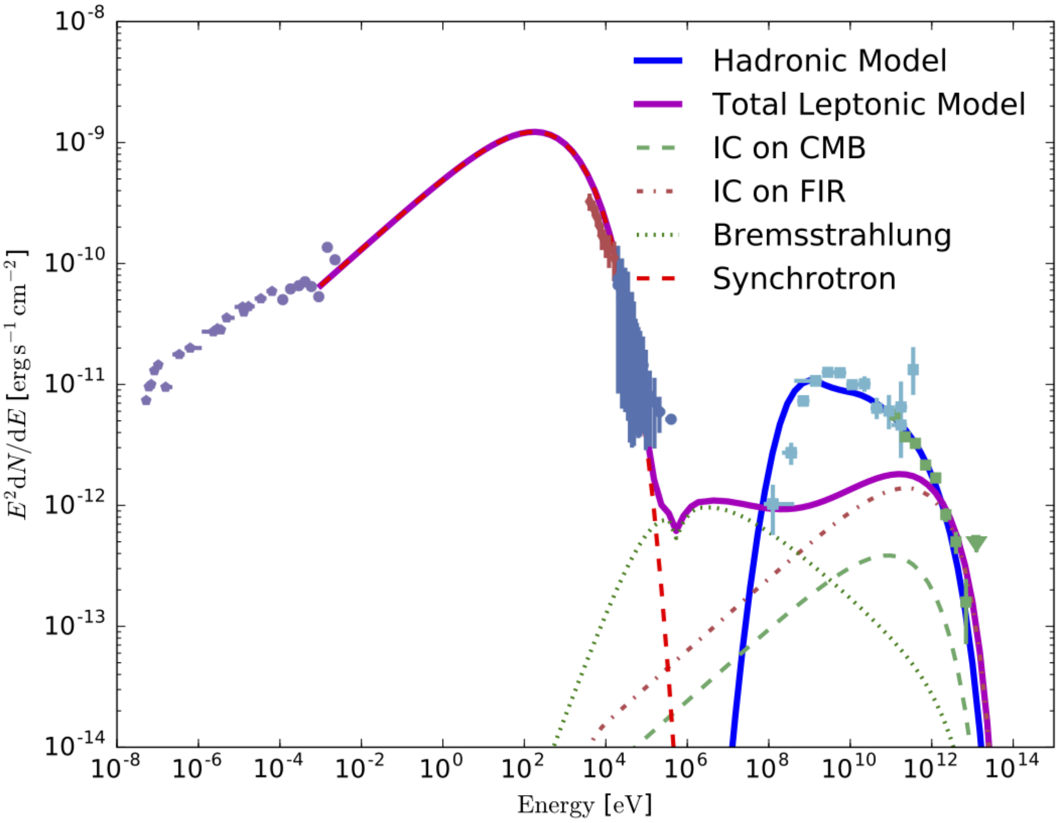

FIGURE 5.5: Multi-wavelength SED of Cas A. The different lines show the result of fitting the measured energy fluxes using *naima* and assuming a leptonic or a hadronic origin of the GeV and TeV emission.

The flat spectral index is in agreement with the standard theory of diffuse shock acceleration, but the low cut-off energy implies that Cas A is extremely inefficient in the acceleration of CRs at the present moment. The characteristic maximum energy of these accelerated protons can be expressed, for standard parallel shock acceleration efficiency (see e. g. Lagage and Cesarsky 1983), as:

$$E_c^p \simeq 450(\frac{B}{1\ \mathrm{mG}})(\frac{t_0}{100\ \mathrm{yr}})(\frac{u_s}{3000\ \mathrm{km/s}})^2\eta^{-1}\ \mathrm{TeV}, \tag{5.3}$$

where $u_s \sim 10^3$ km/s is the speed of the FS, $t_0 \sim 330$ yrs is the age of Cas A and $\eta \geq 1$ is the acceleration efficiency (the ratio of the mean free path of a particle to its gyroradius), which is ∼1 in the Bohm diffuse regime. Even assuming a magnetic field as low as a few tens of μG, a poor acceleration efficiency $\eta \gg$10 has to be invoked to accommodate the low cut-off energy found. Alternatively, Cas A may also be located in a very diffusive region of the Galaxy, resulting in a very fast escape of protons of TeV and higher energies.

5.6 Conclusion

We report for the first time in VHE, observational evidence of the presence of a cut-off in the VHE spectrum of Cas A. The spectrum measured with the MAGIC telescopes can be described with a power-law with exponential cut-off at ∼3.5 TeV, which is preferred over a power-law scenario with 4.6σ significance. This result implies that even if all the TeV emission was of hadronic origin, Cas A could not be a PeVatron at its present age.

Several emission regions must be active to explain the radio, X-ray, GeV and TeV emission of Cas A. A purely leptonic model cannot explain the GeV-TeV spectral shape derived using LAT and MAGIC data, as previously suggested based on observations at lower energies (Atoyan et al., 2000b,a; Zirakashvili et al., 2014; Saha et al., 2014). A leptonic population is undoubtedly necessary to explain the emission at radio and X-ray energies. Indeed, the bright steep-spectrum of the radio knots and the bright radio ring, demand an average magnetic field of ∼1 mG (Vink and Laming, 2003), whereas the faint plateau surrounding Cas A, seen in *Chandra* continuum images, is consistent with a lower magnetic field, which might contribute to the observed emission above 1 TeV.

However, the bulk of the HE and VHE γ-rays must be of hadronic origin. Cas A is most likely accelerating CRs, although to a rather low energy of a few TeV. Even if some leptonic contribution at VHE produced by IC cannot be excluded, this would not affect our conclusion that acceleration in Cas A falls short of the energies of the *knee* of the CR spectrum.

A detailed study of the cut-off shape is crucial to understand the reason behind this low acceleration efficiency, displaying different characteristics if due to escape of CRs, to the maximum energy of the accelerated CRs, or some other mechanism. Observations with the future Cherenkov Telescope Array (CTA, Actis et al. 2011), with a superior angular resolution and sensitivity, will allow detailed spectroscopic investigation on the cut-off regime (Romoli et al., 2017), providing new insights on the acceleration processes in Cas A.

Chapter 6

Discovery of TeV γ-ray emission from the neighborhood of the supernova remnant G24.7+0.6 by MAGIC

6.1 Introduction

SNR G24.7+0.6 is a $0.5^\circ \times 0.25^\circ$ center-filled SNRs located at a distance of ∼5 kpc (Reich et al., 1984; Leahy, 1989). It was discovered at radio frequencies as a couple of incomplete shells centered at $\mathrm{RA_{J2000}} = 278.57^\circ$ and $\mathrm{DEC_{J2000}} = -7.09^\circ$, and a linearly polarized central core with a flat radio spectrum of $\alpha = -0.17$ (Reich et al., 1984), indicating the presence of a central PWN powered by an undetected pulsar. With an estimated age of 9.5 kyrs (Leahy, 1989) it belongs to the class of middle-aged SNRs interacting with MCs as suggested by observations in the IR energy band and by the detection of ^{13}CO J=1-0 line at 110 GHz (Galactic Ring Survey, Jackson et al. 2006). Petriella et al. (2008, 2012) discovered several molecular structures, including a molecular arm extending into the center of the SNR and two clouds bordering the remnant. An observation using VLA also revealed several ultracompact H II regions within the SNR. The presence of many young stellar objects in the interaction region between the SNR and the MCs (Petriella et al., 2010) also suggests that SNR G24.7+0.6 might be triggering star formation (see Figure 6.1).

In X-rays, the SNR was observed with the Einstein Observatory. Although not included in the Einstein catalog of SNRs (Seward, 1990), Leahy (1989) derived a flux over the entire SNR region of $(3.9 \pm 0.9) \times 10^{-13}\,\mathrm{erg\,cm^{-2}\,s^{-1}}$ obtained from a very scarce statistics image. The same data yield an UL to a differential flux under the assumption of a point source ($<2'$ diameter) and extended (circle of $8'$ radius) emission of $< 1 \times 10^{-12}\,\mathrm{erg\,cm^{-2}\,s^{-1}}$ and $< 3 \times 10^{-12}\,\mathrm{erg\,cm^{-2}\,s^{-1}}$, respectively. No pulsar or PWN has been found yet, although an attempt was done with *XMM*-Newton (OBS. ID:0301880301, PI: O. Kargaltsev). Unfortunately, a strong flare affected the observation, reducing the useful exposure to only 3.5 ks and limiting the sensitivity of the observations.

At GeV energies, *Fermi*-LAT (Atwood et al., 2009) has proved to be efficient detecting SNR (Acero et al., 2015, 2016b; Ackermann et al., 2016). Above 100 MeV, two populations of SNRs seem to be emerging: a population of young, X-ray bright, SNRs (Abdo et al., 2011; Tanaka et al., 2011) and a second one including evolved

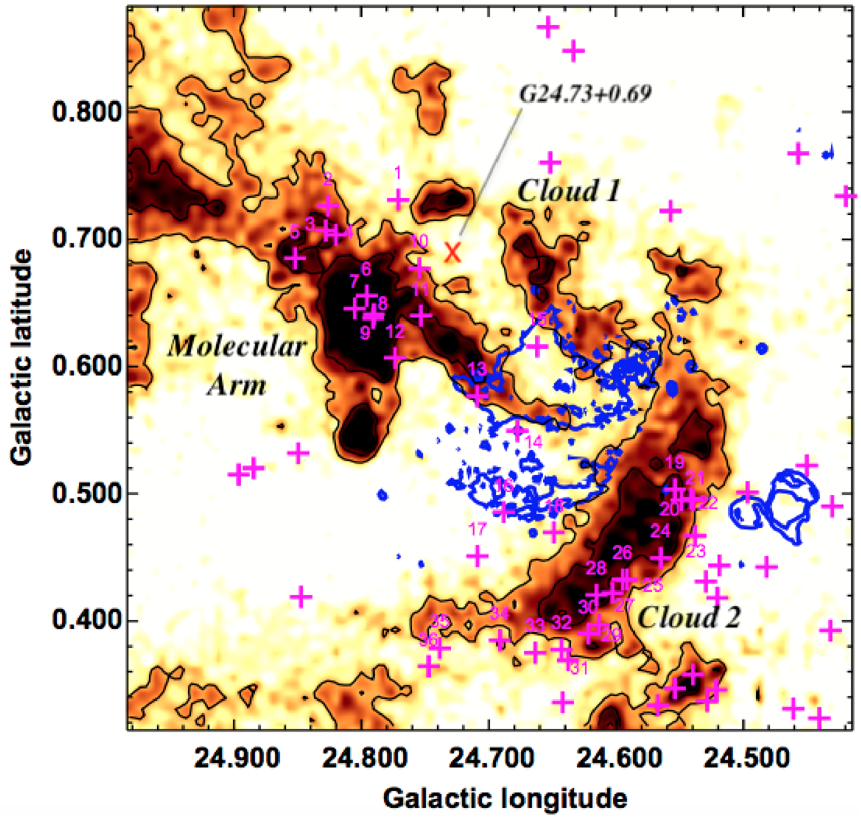

FIGURE 6.1: ^{13}CO J=1-0 emission integrated between +38 and +50 km s^{-1}. Blue contours show the radio emission at 20 cm of SNR G24.7+0.6 from the Multi Array Galactic Plane Imaging Survey. Magenta crosses indicate the position of young stellar objects detected with *Spitzer*. The red cross shows the position of the star and star forming region G24.73+0.69. Adapted from Petriella et al. (2010).

GeV-bright SNRs, interacting with MCs (Reichardt et al., 2012; Abdo et al., 2010b). SNR G24.7+0.6 belongs to the second group. Although initially associated with the pointlike source 3FGL J1833.9–0711, it appears in the first *Fermi* SNR catalog (Acero et al., 2016b) as an extended source ($TS_{\rm ext} = 24.89$) with a gaussian morphology of radius $0.25^\circ \pm 0.04^\circ_{\rm stat} \pm 0.12^\circ_{\rm sys}$ centered at $RA_{\rm J2000} = 278.60^\circ \pm 0.03^\circ_{\rm stat} \pm 0.1^\circ_{\rm sys}$ and $DEC_{\rm J2000} = -7.17^\circ \pm 0.03^\circ_{\rm stat} \pm 0.03^\circ_{\rm sys}$. The *Fermi*-LAT extension is compatible with the radio size, but offset by 0.08° towards the star-forming region G24.73+0.69. Its extension at energies larger than 10 GeV was confirmed by the presence of the SNR in both, the catalog of extended sources in the Galactic plane (FGES, Ackermann et al. (2017)) and the third catalog of hard *Fermi*-LAT sources (3FHL, Ajello et al. (2017)). SNR G24.7+0.6 has been, in fact, identified with FGES J1834.1–0706 and 3FHL J1834.1–0706e. The 3FHL tag confirms the hard spectral nature of the source, thus a potential VHE gamma-ray emitter. The spectral results of the sources identified with the SNR G24.7+0.6 are all compatible within each other showing that the energy spectrum is well-represented with a power-law function of index ~ 2.2. We take as reference from now on the spectral results in the FGES catalog (Ackermann et al., 2017): a photon index of 2.28 ± 0.14 and an integral flux from 10 GeV to 2 TeV of $(5.37 \pm 0.66) \times 10^{-10}$ erg cm^{-2} s^{-1}.

Above ~500 GeV, the region is covered by the HESS Galactic Plane Survey (HGPS, Deil et al. (2015)). The HGPS shows a large and bright source, dubbed HESS J1837–069 (Aharonian et al., 2005, 2006)), located ∼ 0.9° away (at $\mathrm{RA_{J2000}} = 279.41°$ and $\mathrm{DEC_{J2000}} = -6.95°$) from SNR G24.7+0.6. HESS J1837–069 has an elliptical extension of $0.12° \pm 0.02°$ and $0.05° \pm 0.02°$ (with an orientation angle $\omega = 149° \pm 10°$ counterclockwise with respect to the positive Galactic latitude axis) at energies above 200 GeV. The power-law spectrum of HESS J1837–069 exhibits a photon index of 2.27 ± 0.06 and an integral flux above 200 GeV of $(30.4 \pm 1.6) \times 10^{-12}\mathrm{cm^{-2}s^{-1}}$. Deeper observations of the region around HESS J1837–069 (Marandon et al., 2008) led to a more detailed morphological analysis resulting in a new position of HESS J1837–069 offset 0.05° from the initial report at $\mathrm{RA_{J2000}} = 279.37° \pm 0.008°$ and $\mathrm{DEC_{J2000}} = -6.92° \pm 0.008°$ with a size of $0.22° \pm 0.01°$. These observations also revealed a second source located to the South of HESS J1837–069, when considering the International Celestial Reference System (ICRS). No official name was attributed to this potential new source. However, no significant emission from the SNR G24.7+0.6 region was claimed. Recent results from the new HGPS (Abdalla et al., 2018) characterize the region of HESS J1837–069 as a three Gaussian morphology with a total extension of $0.36° \pm 0.03°$. This region of the sky was also covered by HAWC at energies above 1 TeV. The second HAWC catalog (Abeysekara et al., 2017) shows a 15σ-excess compatible with the position of HESS J1837–069 after ≈ 1.5 year observation time.

In this chapter, we study the whole observation dataset available of the region centered around SNR G24.7+0.6 with *Fermi*-LAT in the energy range between 60 MeV and 500 GeV. We also explore with the MAGIC telescopes the region around it to investigate the spectral behavior above 150 GeV of a possible counterpart and to constrain the emission region observed by *Fermi*-LAT around the SNR.

6.2 *Fermi*-LAT data analysis

We analyzed ∼8 years of data, spanning from 4 August 2008 (MET 239557417) to 13 June 2016 (MET 490060804), with energies between 60 MeV and 500 GeV. The CLEAN event class was chosen for this analysis since the source is expected to be extended as reported in latest results, (Acero et al., 2016b). In addition, it benefits from a lower background above 3 GeV with respect to the standard SOURCE event class. The corresponding IRF, P8R2_CLEAN_V6, was used. For this analysis we used the PSF event type partition (see Chapter 3.3.1 for more details) and applied specific zenith angle cuts, to reduce the background from the Earth limb, to each of the quartiles. Thus photons with zenith angles larger than 70, 75, 85 and 90 for PSFs ranging from PSF0 to PSF3 were excluded. Each of the quartiles was analyzed independently and combined at later stages of the analysis by means of a joint likelihood fit.

We performed a maximum likelihood analysis in a circular region of 20° radius centered on the radio source position ($\mathrm{RA_{J2000}} = 278.57°$; $\mathrm{DEC_{J2000}} = -7.09°$), this region is referred as the ROI. The emission model for our ROI includes the LAT sources listed in the 3FGL (Acero et al., 2015) within a region of 30° radius around SNR G24.7+0.6 and the diffuse gamma-ray background models; the Galactic diffuse emission modelled by *gll_iem_v06.fits* and the isotropic component by *iso_P8R2_CLEAN_V6_PSFX_v06.txt* (where X identifies the number of the PSF quartile), including the instrumental background and the extragalactic radiation. Sources lying within 4° from the source of interest were fit with all their spectral parameters left free. For sources between 4° and 7°, as well as the Galactic diffuse and

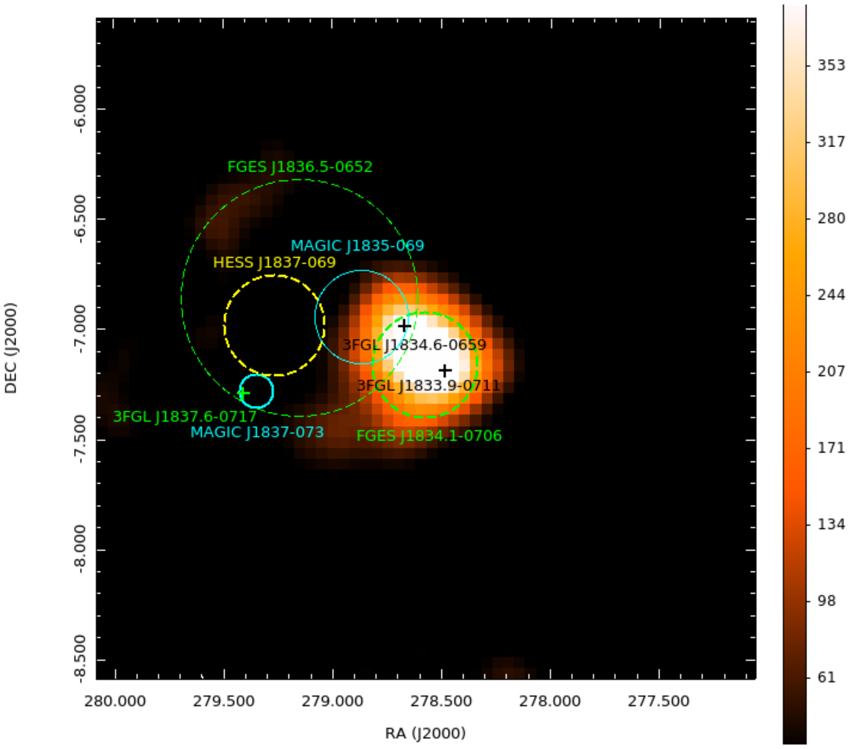

FIGURE 6.2: 3° × 3° Fermi-LAT residual map (i.e. TS map) of the region centered at SNR G24.7+0.6 after removing the sources 3FGL J1834.6–0659 and 3FGL J1833.9–0711 from the source model. A single extended source, FGES J1834.1–0706, results in a better fit value.

isotropic components, only their normalisation parameters was allowed to vary. All the spectral parameters for sources located farther than 7° from the source of study remained fixed in the maximum likelihood fit.

Due to strong contamination from diffuse emission in the Galactic plane at low energies and the large PSF, both mainly below 1 GeV, in order to study the morphology of the source we performed a specific analysis to the LAT data above 1 GeV in a 8°×8° region centered on the SNR G24.7+0.6 radio position. Given that our source of interest might be associated with two 3FGL sources (3FGL J1834.6–0659 and 3FGL J1833.9–0711), which are tagged as 'confused', meaning that they are regions with significant photon excesses (i.e. can arise from a wrongly modeled background or a confused source pile-up), we removed them from the model to study in more detail the residual map, Figure 6.2. We found that replacing these sources with a single point-like source (we called it FGES J1834.1–0706 as in Ackermann et al. 2017) located at the radio position increases the fit value (i.e. likelihood value). We performed a *localisation procedure*[1] within a region of 3°×3° to determine the correct position of FGES J1834.1–0706 and we tested for a possible extended morphology modeling our source with a Gaussian function rather than a point-like source. Assuming a power-law spectral shape with spectral index -2, we performed an iterative likelihood fit for values of the source extension[2] ranging from 0.01° to 1.01° with a step of 0.1°.

---

[1] http://fermipy.readthedocs.io/en/latest/advanced/localization.html

[2] http://fermipy.readthedocs.io/en/latest/advanced/extension.html

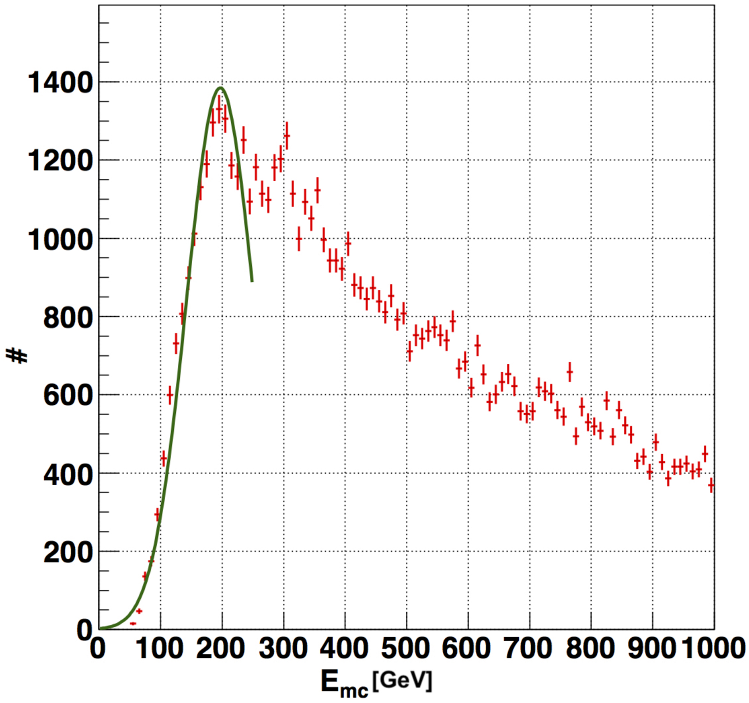

FIGURE 6.3: Energy threshold of the MAGIC observations. A gaussian function has been fit to determine the peak of the γ-ray simulated distribution (refer to section 2.5.3.8).

For the spectral analysis we split the 60 MeV–500 GeV energy range into 10 logarithmically spaced bins. We required that each spectral point has at least a TS $= 4$, otherwise 95% CL ULs were computed.

6.3 MAGIC data analysis

MAGIC telescopes observed SNR G24.7+0.6 between April 5th and August 29th, 2014, for a total of 33 hours, at zenith angles between 35° and 50°, yielding an analysis energy threshold of ~200 GeV (see Figure 6.3). The observations were performed in wobble-mode at four symmetrical positions 0.4° away from the source, so that the background can be estimated simultaneously. After quality cuts, which account for hardware problems, unusual background rates and bad atmospheric conditions, ~31 hours of dark-time high quality data were selected.

The analysis was performed using the MARS software and following the standard analysis chain explained in Chapter 2. In particular, we derived On-maps of γ-like events based on their arrival directions in sky coordinates. On-maps need a reliable background determination in order to minimize the contribution of hadronic CRs surviving data selection cuts. To reconstruct the background maps from wobble observations we use the Exclusion Map technique implemented in `SkyPrism` package (Vovk et al., 2018). The Exclusion Map technique allows us to estimate the background with no need of prior knowledge of the position of the source under evaluation while we exclude from the computation regions containing known sources. On and Background maps are used as input files for a two-dimensional maximum likelihood fit of the source model that is performed using the *Sherpa* package (Doe et al., 2007; Freeman et al., 2001). Specifically, the source model is constructed and optimized by using an iterative method in a likelihood approach. First, a single source is added to a model containing only the isotropic background. Different positions and extensions of the source are evaluated and the values maximizing the likelihood value are assigned to the source. A second source is added to the model and the same procedure is executed; positions and extensions for both sources are re-calculated. Following the approach explained in section 3.3.5, these two nested models are compared through their maximum likelihood fit value and the one that better represents the data is kept. Additional sources are iteratively introduced to the model until the maximum likelihood fit is no longer improved. For the spectral analysis of the best-fit model obtained, we performed an additional one-dimensional maximum likelihood fit using `SkyPrism`.

6.4 Results

The obtained significance skymap, represented in Figure 6.4 in the ICRS coordinate system, shows significant extended emission at energies larger than 200 GeV. The two-dimensional likelihood morphological analysis led to the detection of three distinct sources:

- The brightest source is identified with HESS J1837–069 (Aharonian et al., 2006; Marandon et al., 2008). It presents an extended morphology characterized by a single Gaussian of $0.23° \pm 0.01°$ size centered at RA_{J2000}=$279.26° \pm 0.02°$ and

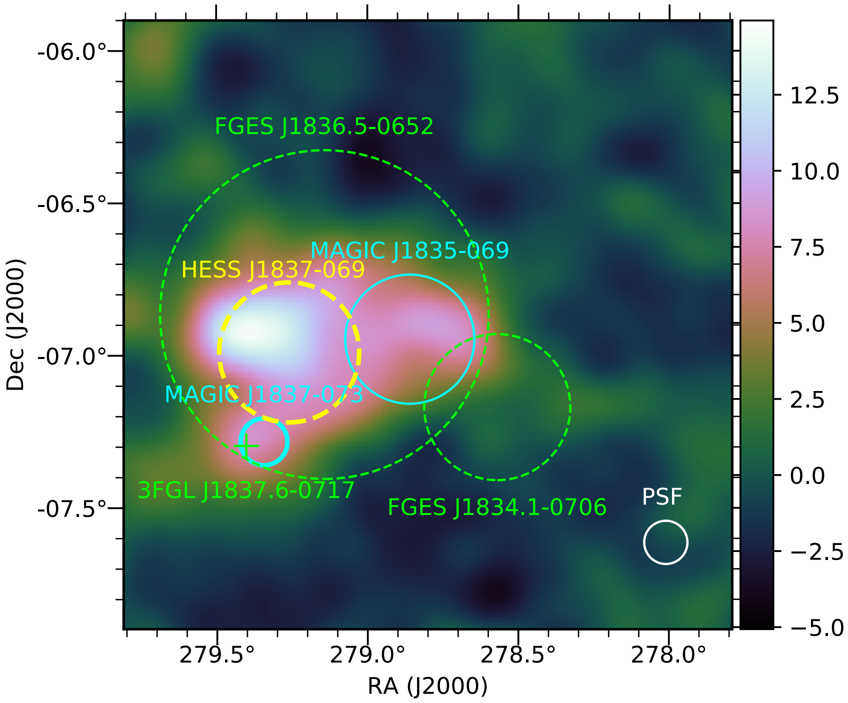

Figure 6.4: 2° × 2° significance map of the region obtained with MAGIC. The extension of MAGIC J1835–069 and MAGIC J1837–073 are represented by the thin and thick blue circles, respectively, while *Fermi*-LAT sources from FGES and 3FGL catalogs in the FoV are displayed by green dashed lines and a cross. The position and extension of HESS J1837–069 as measured in this work are displayed by a yellow dashed circle.

	F_0 [TeV^{-1} cm^{-2} s^{-1}]	Γ	E_0 [TeV]
HESS J1837–069	$(4.4 \pm 0.2) \times 10^{-12}$	2.29 ± 0.04	1.25
MAGIC J1837–073	$(1.7 \pm 0.1) \times 10^{-12}$	2.29 ± 0.09	0.95
MAGIC J1835–069	$(1.4 \pm 0.2) \times 10^{-12}$	2.74 ± 0.08	1.31

TABLE 6.1: Fitting spectral parameters of the three sources detected by MAGIC. For all of them the best fit function is a power-law with a photon index, Γ, and a normalisation factor F_0 at the decorrelation energy E_0.

DEC$_{J2000}$=$-6.99° \pm 0.01°$. This emission is also associated with the extended source FGES J1836.5–0652 in the *Fermi*-LAT catalog of extended sources in the Galactic plane.

- The excess to the South from HESS J1837–069 is significantly resolved at 7.7σ level. It has a Gaussian morphology with an extension of $0.08° \pm 0.05°$ centered at RA$_{\mathrm{J2000}} = 279.34° \pm 0.14°$ and DEC$_{\mathrm{J2000}} = -7.28° \pm 0.24°$. Spatially coincident with the hotspot reported in Marandon et al. (2008) at 11σ level, we dubbed it MAGIC J1837–073 since no name was previously attributed to it. This source is also coincident with 3FGL J1837.6–0717 reported in the Third Catalog of *Fermi*-LAT sources (Acero et al., 2015).
- The third significant source is, for the first time, detected at VHE, and it is named MAGIC J1835–069. Detected at 13.5σ (TS =181) it is significantly extended and well modelled by a Gaussian of $0.21° \pm 0.05°$ centered at RA$_{\mathrm{J2000}} = 278.86° \pm 0.23°$ and DEC$_{\mathrm{J2000}} = -6.94° \pm 0.05°$. Its center position is offset by 0.34° (1.5σ away) with respect to the center of the SNR G24.7+0.6. In particular, it lies between two extended sources detected above 10 GeV by *Fermi*-LAT, FGES J1836.5–0652 and the FGES J1834.1– 0706, being the first associated to HESS J1837–069 and the second to the SNR G24.7+0.6.

Figure 6.5 shows the SEDs obtained for the three sources using the above-described morphologies as extraction regions. The spectral fit parameters are summarized in Table 6.1. The differential energy spectrum of HESS J1837–069 is well represented by a power-law function with a photon index of 2.29 ± 0.04 and an integral flux above 200 GeV of $(7.2 \pm 0.3) \times 10^{-11}\,\mathrm{erg\,cm^{-2}\,s^{-1}}$. The spectrum obtained is compatible within statistical errors with those measured by HESS, 2.27 ± 0.06 in Aharonian et al. (2006) and 2.34 ± 0.04 in Marandon et al. (2008). For MAGIC J1837–073, the best spectral fit model is a power-law with a 2.29 ± 0.09 photon index and an integral flux above 200 GeV of $(1.5 \pm 0.1) \times 10^{-11}\,\mathrm{erg\,cm^{-2}\,s^{-1}}$. The emission fades away above 3 TeV, and the calculated 95% CL UL at 6 TeV does not constrain any potential cut-off. Finally, the energy spectrum of MAGIC J1835–069 is best fit by a power-law function with a photon index of 2.74 ± 0.08 and an integral flux above 200 GeV of $(4.4 \pm 0.6) \times 10^{-11}\,\mathrm{erg\,cm^{-2}\,s^{-1}}$.

The results obtained with our *Fermi*-LAT analysis are in good agreement with the previously published ones. Two sources are detected in the surrounding of SNR G24.7+0.6; FGES J1834.1–0706 and the counterpart of the MAGIC source MAGIC J1837–073, 3FGL J1837.6–0717. The first shows an extended Gaussian emission of $0.24° \pm 0.01°$ centered at RA$_{\mathrm{J2000}} = 278.57° \pm 0.01°$ and DEC$_{\mathrm{J2000}} = -7.19° \pm 0.02°$ (see Figure 6.2), offset by 0.1° from the radio position. The significance of the extension is of

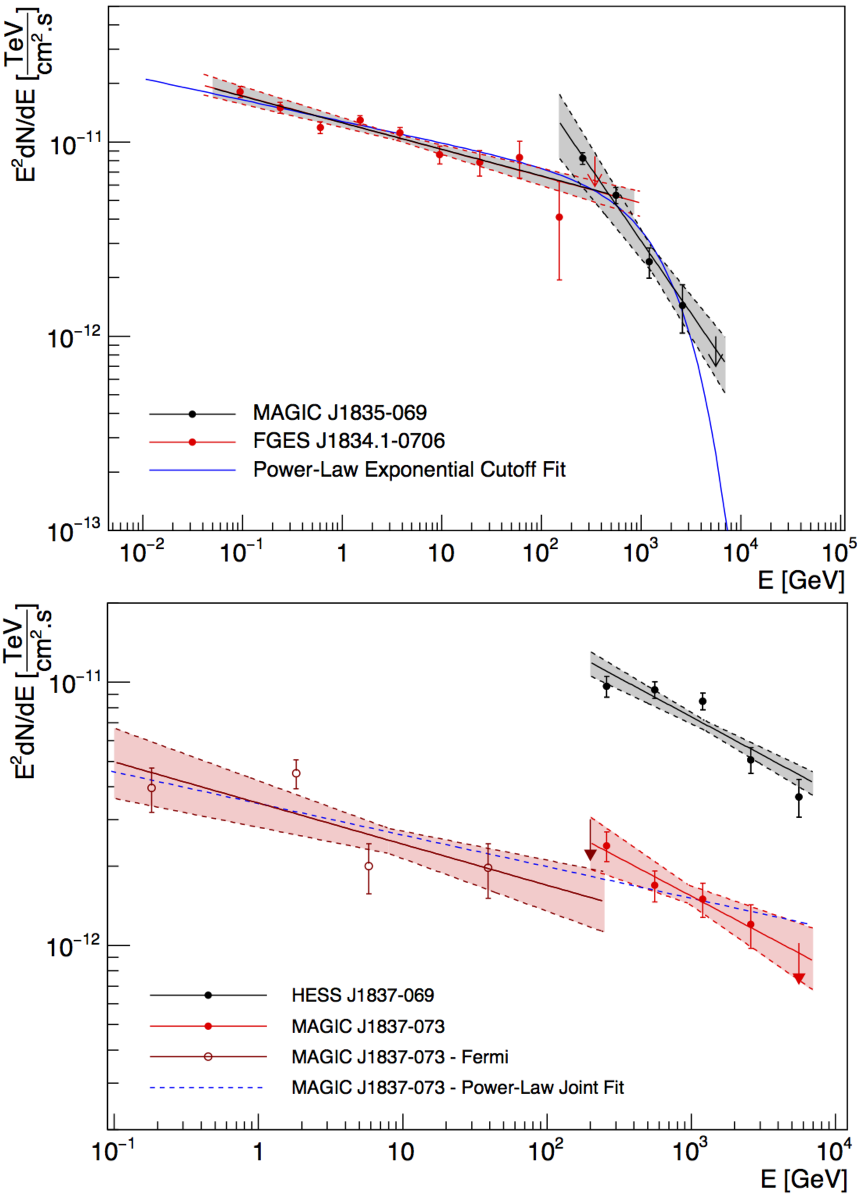

FIGURE 6.5: *Top:* SED of FGES J1834.1–0706 (red circles) and MAGIC J1835–069 (black circles) between 60 MeV and 10 TeV. In the *Fermi* energy range the spectrum follows a power-law of index 2.14 while it softens in the MAGIC range to an index of 2.74. The EPWL fit for the whole energy range is represented by a blue curve. Light gray bands are the statistical uncertainties. *Bottom:* SED of HESS J1837–069 (black) and MAGIC J1837–073 (red), measured by MAGIC between 200 GeV and 10 TeV. Solid lines represent the power-law fits applied to each spectrum. Light shaded bands are the statistical uncertainties. The spectrum measured for MAGIC J1837–073 with *Fermi*-LAT along with its power-law fit are represented in dark red. Blue dashed line represents the joint χ^2 fit of MAGIC J1837–073 between 60 MeV and 10 TeV.

11.4σ ($\mathrm{TS_{ext}} = 131$[3]). This result is in agreement with the one published in the FGES catalog. As stated in section 1, we consider as reference analysis the one of the FGES catalog, thus we refer to the source found in our analysis as FGES J1834.1– 0706.

---

[3] It was calculated from $\mathrm{TS_{ext}} = \mathrm{TS_{gauss}} - \mathrm{TS_{point}}$ as stated in Lande et al. (2012)

The energy spectra obtained with our *Fermi*-LAT analysis from 60 MeV to 500 GeV for FGES J1834.1– 0706 and MAGIC J1837–073 are represented in Figure 6.5. MAGIC J1837–073, for which we used the morphology derived in the MAGIC analysis, exhibits a power-law spectrum with a photon index of $\Gamma = (2.15 \pm 0.05)$ and a normalisation factor of $N_0 = (3.9 \pm 0.4) \times 10^{-8}\,\mathrm{TeV^{-1}\,cm^{-2}\,s^{-1}}$ at the decorrelation energy of 8 GeV. The mismatch between the flux level obtained by the two instruments is well within the systematic uncertainties, estimated to be of the order of 15% for MAGIC. A joint χ^2 fit of MAGIC J1837–073 between 60 MeV and 10 TeV results in a similar power-law of photon index $\Gamma_{\chi^2} = (2.12 \pm 0.02)$ with a factor of $N_0 = (1.52 \pm 0.1) \times 10^{-12}\,\mathrm{TeV^{-1}\,cm^{-2}\,s^{-1}}$ at 1 TeV. On the other hand, FGES J1834.1–0706 shows a power-law spectrum with a photon index of $\Gamma = (2.14 \pm 0.02)$ and a normalisation factor of $N_0 = (2.9 \pm 0.1) \times 10^{-7}\,\mathrm{TeV^{-1}\,cm^{-2}\,s^{-1}}$ at the decorrelation energy of 5.8 GeV. In this case, the energy spectrum of FGES J1834.1– 0706 connects smoothly with that of MAGIC J1835–069 even though the extraction regions are not exactly the same, thus suggesting that the two sources most likely have a common origin. Under this assumption, we performed a joint χ^2 fit between 60 MeV and 10 TeV that resulted in a power-law function with an exponential cut-off (hereafter, EPWL), $F_0 \left(\frac{E}{E_0}\right)^{-\Gamma} e^{-\frac{E}{E_C}}$, where F_0 is the prefactor; E_0 is the decorrelation energy; E_C is the cut-off energy and Γ is the photon index. The resulting fitting parameters are provided in Table 6.2.

	F_0 [$\mathrm{TeV^{-1}\,cm^{-2}\,s^{-1}}$]	Γ	E_C [TeV]	E_0 [GeV]
EPWL	$(9.1 \pm 3.0) \times 10^{-10}$	2.12 ± 0.02	1.9 ± 0.5	92

TABLE 6.2: Joint χ^2 fit spectral parameters for SNR G24.7+0.6 from 60 MeV to ∼10 TeV. Photon index, Γ, normalisation factor F_0 at the decorrelation energy E_0 and cut-off energy are presented.

6.5 Discussion

We observed the FoV of SNR G24.7+0.6 with the MAGIC telescopes, following the detection of a hard-spectrum source reported by the LAT collaboration (Ackermann et al., 2016), coincident with the position of the remnant. The analysis of 31 hours of data using the *Sherpa* package on the reconstructed skymap resulted on the detection of three different sources in the MAGIC data set. The brightest one, located at RA_{J2000}=279.26° ± 0.02° and DEC_{J2000}=−6.99° ± 0.01°, has been previously reported by the HESS collaboration and dubbed HESS J1837–069. The spectral features derived by MAGIC in this region are compatible within errors with the ones reported by HESS. To the South, MAGIC J1837–073, a separated gamma-ray excess located ∼ 0.34° away from HESS J1837–069 is detected at a level of 7.7σ. The spectrum of this source extends to low energies, suggesting an hadronic origin of the emission. The region was subject of observations with *XMM*-Newton (Katsuta et al., 2017) in a search for a Multiwavelength (MWL) counterpart of the GeV emission they detect (G25B in Figure 6.6). No PWN, SNR, or pulsar with spin-down luminosity $> 1 \times 10^{34}\,\mathrm{erg\,s^{-1}}$ was found in the region. However, the region is rich in molecular content at velocities $v = 45 - 65\,\mathrm{km\,s^{-1}}$ and the analysis of the X-ray observations reveals a large number of point sources, suggesting a stellar cluster. Assuming a distance of $d = 5\,\mathrm{kpc}$ (Katsuta et al., 2017), the total luminosity above 100 MeV of MAGIC J1837–073 amounts to

$L_\gamma = 7.7\times10^{35}\,\mathrm{erg\,s^{-1}}$, which will imply a density on CRs of $W_p \approx 2.1\times10^{50}\,\mathrm{erg}\left(\frac{\mathrm{cm}^{-3}}{n}\right)$, being n the ambient proton density. This number is comparable to the ones found in other clusters such Westerlund 2 (Yang et al., 2017) or Cygnus Cocoon (Ackermann et al., 2011). Such large luminosity could be achieved by assuming a quasi-continuous injection of CRs, powered by the kinetic energy released for instance in the winds of massive stars ($\sim 1\times10^{38}\,\mathrm{erg\,s^{-1}}$), integrating during the cluster lifetime (typically $\sim 1\times10^{4}$ yrs).

Finally, the statistical test performed allows us to resolve MAGIC J1835–069 ($\mathrm{RA_{J2000}} = 278.86° \pm 0.23°$; $\mathrm{DEC_{J2000}} = -6.94° \pm 0.05°$) from HESS J1837–069 at a 13.5σ level. Moreover, the projected distance of the new gamma-ray enhancement to the pulsar associated to HESS J1837–069 (for a distance of 6.6 kpc, from Gotthelf and Halpern (2008)), is more than ∼65 pc, which, if not impossible, makes the association between the two sources unlikely. MAGIC J1835–069, however, partially overlaps with the emission detected with LAT. Indeed, a new analysis presented by Ackermann et al. (2017) describes the complex region with three very extended sources, being the MAGIC source comprised between two sources; FGES J1836.5–0652, which includes also HESS J1837–069, and FGES J1834.1–0706 which is consistent with 3FHL J1834.1–0706e on the position of the SNR G24.7+0.6. The flux measured with MAGIC is in good agreement with the one measured by LAT, extending the spectrum from 60 MeV

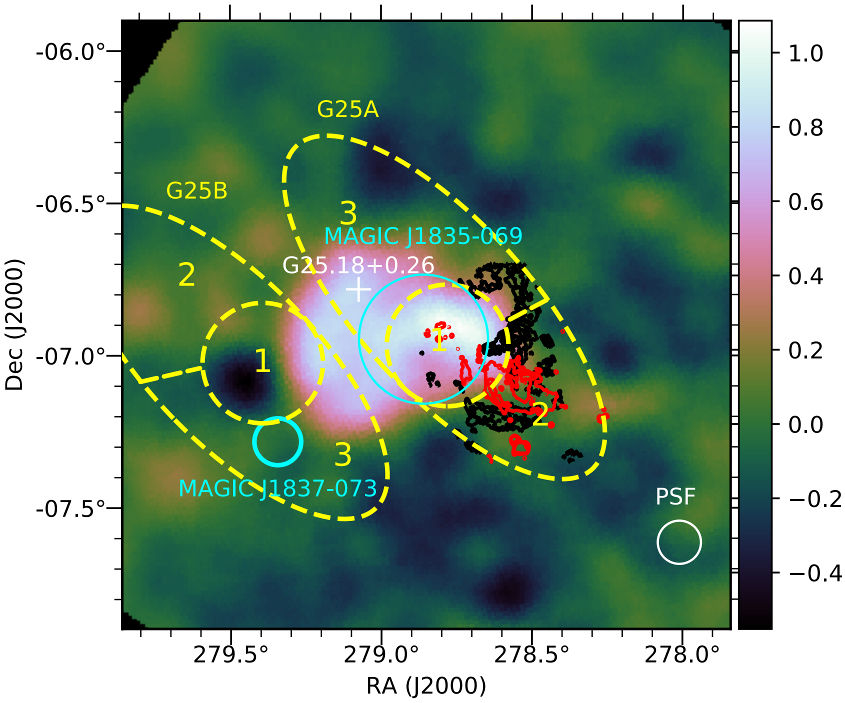

FIGURE 6.6: Residual map derived from MAGIC data after subtracting the emission from HESS J1837–069 and MAGIC J1837–073. Over the MAGIC map, the SNR G24.7+0.6 radio emission and CO contours are overlaid in red and black, respectively. CO contours are selected from 10 K to 50 K in step of size 4 to emphasize the cloud spacial distribution. The yellow dashed ellipses (G25A and G25B) along with their three components represent the *Fermi*-LAT sources found within the region by Katsuta et al. (2017). The white cross displays the position of the OB association/cluster G25.18+0.26 identified through X-ray observation by Katsuta et al. (2017).

to 10 TeV with a spectral photon index of ∼2.7. The VHE broad band spectral shape shows a clear break in the GeV-TeV regime. This change of slope can be described by a power-law with an exponential cut-off at $E_C = 1.9\,\mathrm{TeV}$. The source shows an extended morphology and it is offset 0.34° with respect to center of the remnant, in a region where the later seems to be blowing an IR shell. The measured offset translates onto a projected size of 30 pc at the distance of 5 kpc. The CO-rich surrounding of SNR G24.7+0.6 could be originating the detected GeV-TeV emission, and the offset between the emission detected by LAT and the MAGIC source could be interpreted in terms of diffusion mechanism similar to what was proposed for IC 443 (Torres et al., 2008, 2010), since the diffusion radius of runaway protons of 100 GeV could account for this distance. However the large error in the position and the complexity of the region in the GeV regime prevents further conclusions in that sense. Nevertheless, in this scenario and similarly to other evolved SNRs, the VHE LAT/MAGIC combined spectrum model can be explained as a result of proton-proton interaction between the CRs accelerated in SNR G24.7+0.6 and the ones in the surrounding gas. The total luminosity above 100 GeV amounts $L_\gamma = 7.5 \times 10^{34}\,\mathrm{erg\,s^{-1}}$, which translates to a total energetics stored in accelerated protons of $W_p = 1.3 \times 10^{50}\,\mathrm{erg}\left(\frac{\mathrm{cm}^{-3}}{n}\right)$.

A second scenario involving a yet-undiscovered PWN associated to the remnant cannot be discarded. At a distance of d∼5 kpc, the separation between MAGIC J1835–069 and the position of the remnant is within the range of offsets found in VHE PWNe (see Figure 6 from Abdalla et al. (2017)). The corresponding surface brightness, in the energy range from 1 to 10 TeV, would be $\sim 1.2 \times 10^{30}\,\mathrm{erg\,s^{-1}\,pc^{-2}}$. Applying the correlation found by Abdalla et al. (2017) (S∼ $\dot{E}^{0.81\pm0.14}$), an extremely bright $\dot{E} \sim 1.4 \times 10^{37}\mathrm{erg\,s^{-1}}$ pulsar should be powering the VHE source. Both the upper and the lower limit of the spin-down luminosity (S∼ $\dot{E}^{0.67}$ and S∼ $\dot{E}^{0.95}$, respectively) seem unrealistically large for not being detected either in gamma ray or radio. However, the strong confusion due to the several extended sources in the field limits the detection of such pulsars in the GeV regime. In addition, the extension of the PWN would exceed the SNR size, rendering this scenario unlikely if the putative PWN is connected to the SNR.

Recently, Katsuta et al. (2017) carried out a study of the γ-ray emission coming from the region around, $\mathrm{RA_{J2000}} = 279.22°$ and $\mathrm{DEC_{J2000}} = -7.05°$, with the *Fermi*-LAT telescope. They found that the emission detected is divided into two elliptical extended region, G25A and G25B, composed of 3 components each (see Figure 6.6). For G25A, all three components have the same spectral shapes while for G25B, the G25B1 component has a harder spectrum than the other two. Due to their elongated morphology and spectral similarity (similar surface brightness and hard energy spectra; $\Gamma = (2.14 \pm 0.02)$ and $\Gamma = (2.11 \pm 0.04)$, respectively), they suggested that both γ-ray emissions are produced by the same astrophysical object. In addition, through X-ray observations of the region with *XMM*-Newton they found the candidate young massive OB association/cluster, G25.18+0.26 (Figure 6.6). They proposed that both extended γ-ray emissions (G25A and G25B) are associated with an star forming region driven by G25.18+0.26. Assuming the scenario proposed by Katsuta et al. (2017) in which either the accelerated particles are interacting with regions of enhanced gas density or particles are being accelerated within these regions, current TeV telescopes like MAGIC should reveal a diffuse γ-ray emission from the whole G25A and G25B regions. However, as seen from the maps, MAGIC only detects emission from the G25A1 component that is coincident with MAGIC J1835–069. We can conclude it is unlikely that the emission detected at VHE with MAGIC comes from the OB association/cluster G25.18+0.26 detected in X-rays.

6.6 Conclusion

MAGIC observations of the FoV of the SNR G24.7+0.6 resulted in the discovery of a new TeV source in the Galactic plane, MAGIC J1835–069, detected above $\sim$150 GeV. MAGIC J1835–069 lies 1.5σ away from SNR G24.7+0.6, which is in turn associated with the *Fermi* source FGES J1834.1–0706. Based on the good agreement between the LAT and MAGIC spectral measurements, the two sources are likely to be associated. The link with the SNR is also plausible if one considers the diffusion radius of particles to explain the observed offset. The GeV-TeV emission observed by *Fermi* and MAGIC can be interpreted as CRs accelerated within the remnant interacting via proton-proton collisions with the CO in the surrounding medium.

A second statistically significant detection of a slightly extended γ-ray signal from the south of HESS J1837–069 is reported. The spectrum of the source extends to 3 TeV with no sign of an spectral break. This detection is believed to be produced by CRs interacting with a stellar cluster. If confirmed, MAGIC J1837–073 will be part of the scarce group of similar objects like Westelund 1 and 2 or the Cygnus cocoon and may contribute to a better understanding of whether these objects can account for the Galactic CR flux.

Part III

THE PARTICULAR CASE OF THE CRAB PULSAR

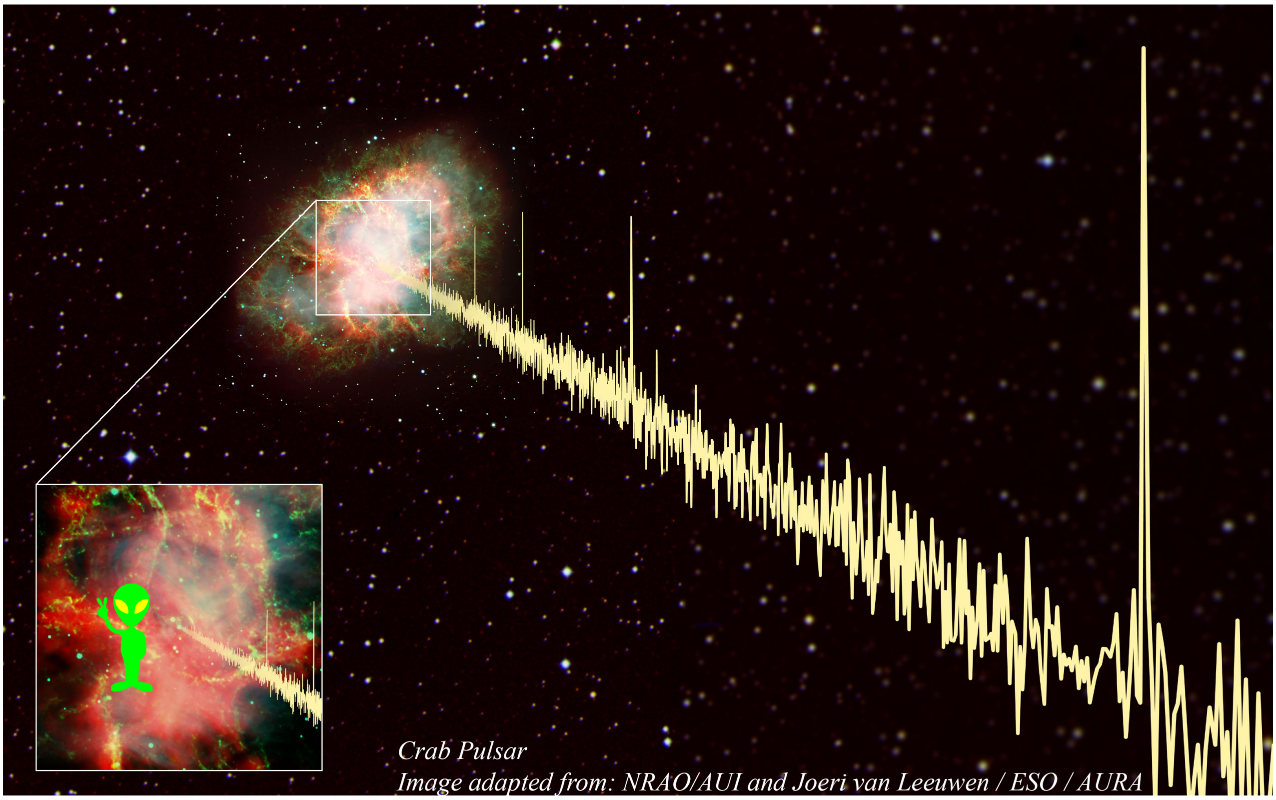

Crab Pulsar
Image adapted from: NRAO/AUI and Joeri van Leeuwen / ESO / AURA

Chapter 7

Rotation Powered Pulsars

7.1 Introduction

Pulsars (PULSating stARS) are commonly defined as rapidly-rotating highly-magnetized NSs that emit very regular pulsed emission. This emission, mainly of non-thermal origin, can be detected over the whole electromagnetic spectrum.

Little green men was the explanation given to the first pulsar observation. In 1967, the radio signal detected by Jocelyn Bell Burnell turned out to be emission from the source PSR B1919+21, the first object recognized as a pulsar (Hewish et al., 1968). Ever since, the number of detected pulsars has grown rapidly to the more than 2400 radio pulsars currently listed (Beskin et al., 2015). Nevertheless, despite the large number of pulsars observed and the huge improvement in detection techniques/instruments, our understanding of how and where particles emit the radiation being observed at Earth remains incomplete.

This chapter presents the current understanding on rotation powered pulsars (i.e. pulsars extracting their energy from the rotation) and reviews the main γ-ray emission models postulated so far.

7.2 Origin and properties

NSs are the remnants of massive stars (8-25$M_\odot$) whose core collapsed during the SN explosion, when nuclear reactions were no more capable of balancing the gravitational collapse. After nuclear burning, if the star mass is larger than the Chandrasekhar limit ($\sim$1.4$M_\odot$), but not great enough to overcome the neutron degeneracy pressure to become black holes ($\sim$3$M_\odot$), the star evolves into a NS, i.e. beta reactions take place transforming most of the electrons in neutrons (Kalogera and Baym, 1996).

NSs have a core radius of about 10 km and a typical observed mass between 1.4 and 2$M_\odot$, although theoretically they could reach a mass of 3$M_\odot$ (Kalogera and Baym, 1996; Chamel et al., 2013). Conservation of both the magnetic flux and the angular momentum gives the NS a strong magnetic field (B$\sim$ 10^{12}G) and a very rapidly rotating behavior, with periods ranging from milliseconds to seconds. The rotational energy of the pulsar is converted into electromagnetic and particle energy, slowing down its rotation. Considering the magnetic field of the NS as a dipolar B-field, the rotational

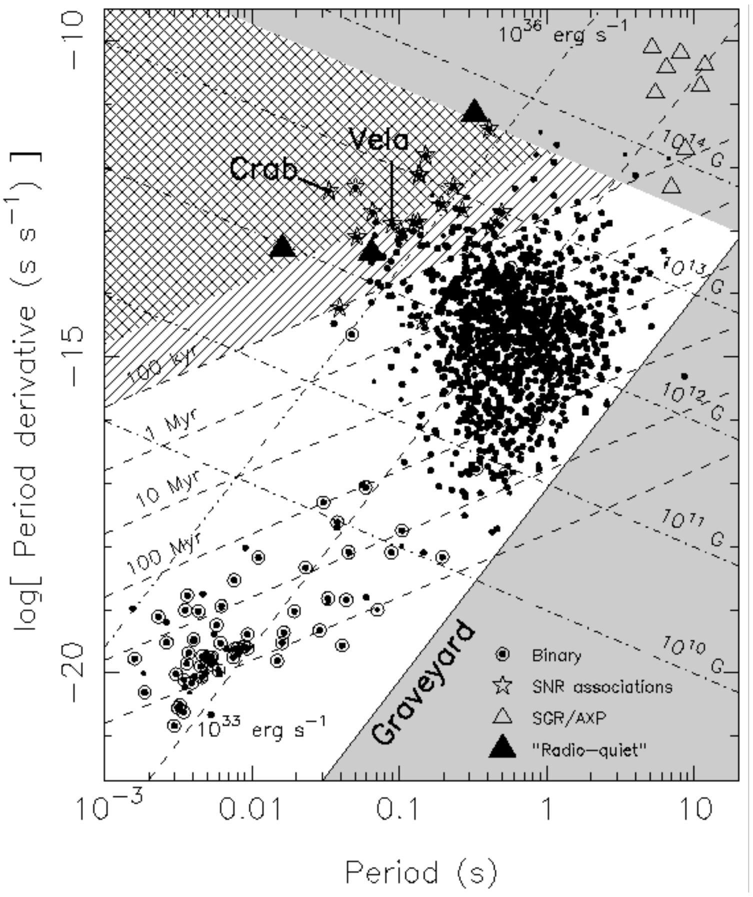

FIGURE 7.1: $P\dot{P}$-diagram of detected pulsars. Known association of pulsars are also represented. Dashed lines represent the characteristic age, spin-down luminosity and B-fields. From Lorimer and Kramer (2004).

energy loss rate can be therefore equated to the magnetic dipole radiation as follows

$$\dot{E} = I\Omega\dot{\Omega} = -4\pi^2 I\frac{\dot{P}}{P^3} \tag{7.1}$$

where $\Omega = 2\pi/P$ is the angular frequency of the NS and I the moment of inertia. This is the so-called spin-down luminosity and ranges from $\sim 10^{28}$ to $\sim 10^{38}$ erg/s.

The pulsar rotational age can be estimated assuming that the change in the pulsar angular velocity, $\dot{\Omega} = -\kappa\Omega^n$, is due to magnetic dipole radiation losses, where κ is a positive constant and n is the braking index, $n = \ddot{\Omega}\Omega/\dot{\Omega}^2$, obtained differentiating the equation for $\dot{\Omega}$. Integrating $\dot{\Omega} = -\kappa\Omega^n$, assuming n is constant throughout the lifetime of the pulsar and higher than 1, and $\Omega \ll \Omega_{t=0}$, the characteristic age is then defined by

$$\tau \approx -\frac{\Omega}{(n-1)\,\dot{\Omega}} = \frac{P}{(n-1)\,\dot{P}} \tag{7.2}$$

For the case of a magnetic dipole field, $n = 3$ (Becker and Pavlov, 2002), the age of the pulsar is given by

$$\tau \approx -\frac{\Omega}{2\dot{\Omega}} = \frac{P}{2\dot{P}} \tag{7.3}$$

The characteristic age must be taken with care as it only represents an upper limit of the true age of the pulsar. Recently, Johnston and Karastergiou (2017) showed that the braking index is in fact changing during the evolution of the pulsar. This new understanding could naturally explain for example the change in the braking index observed in PSR J1846-0258 in about 6 years (Archibald et al., 2015).

The magnetic field at the surface of the NS can also be calculated within the dipole field approximation and is given by (Manchester and Taylor, 1977)

$$B_s \approx 6.4 \times 10^{19} \sqrt{P\dot{P}} \tag{7.4}$$

The evolution and properties of pulsar populations can be summarized in a $P\dot{P}$-diagram (Figure 7.1). The age and magnetic flux lines are derived from equations 7.2 and 7.4 respectively. Two populations of pulsars can be distinguished: canonical pulsars and Millisecond Pulsarss (MSPs). Canonical pulsars are identified by the large clump in the diagram and associated with the younger pulsars. As pulsars grow old, they are spun-down by magnetic braking and their emission weakens according to equation 7.1 until they become invisible, i.e. moving downward to the right in Figure 7.1. Some 'death' pulsars in binary systems can spin up again by accretion (Alpar et al., 1982; Radhakrishnan and Srinivasan, 1982) and they enter the MSP region located at the lower left corner of the $P\dot{P}$-diagram.

7.3 Global magnetospheric description

As a first approximation, pulsars can be modeled as perfect conductors whose charge is located on the surface of the star (Deutsch, 1955). Surface charges induce a powerful electric field perpendicular to the surface and parallel to the magnetic field. This component of the electric field exceeds gravitational forces by many orders of magnitude

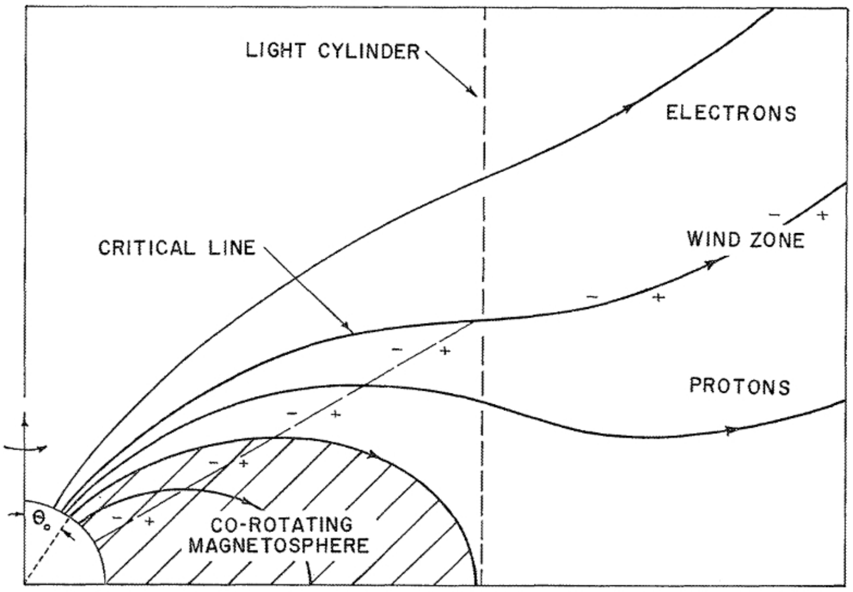

Figure 7.2: Schematic representation of the Goldreich-Julian magnetosphere model for an aligned rotator. The thin long dashed line represents the null surface ($\mathbf{\Omega} \cdot \mathbf{B} = 0$), zone where the charge density ρ_{GJ} changes sign. From Goldreich and Julian (1969).

and it is capable of ripping off charges from the star filling the space around the pulsar (i.e. the magnetosphere) with plasma. The charge density in the magnetosphere follows then the so-called Goldreich-Julian density (Goldreich and Julian, 1969):

$$\rho_{GJ} = \frac{\nabla \cdot E}{4\pi} \approx -\frac{\Omega \cdot B}{2\pi c}. \tag{7.5}$$

The Goldreich and Julian (1969) simplified description of the magnetosphere for an aligned rotator is represented in Figure 7.2.

The pulsar magnetosphere should therefore be close to a force free magnetosphere where magnetic field lines and plasma particles co-rotate with the star out to a radial distance of

$$R_{LC} = \frac{c}{\Omega} = \frac{Pc}{2\pi}. \tag{7.6}$$

This distance is known as the light cylinder and delimits the magnetosphere. Beyond the light cylinder, magnetic field lines (known as open field lines) can no longer close back to the NS surface and flow outwards in a spiral structure as shown in Figure 7.3. Charged particles sliding along open field lines leave the pulsar magnetosphere into the pulsar wind zone (see Figure 7.2).

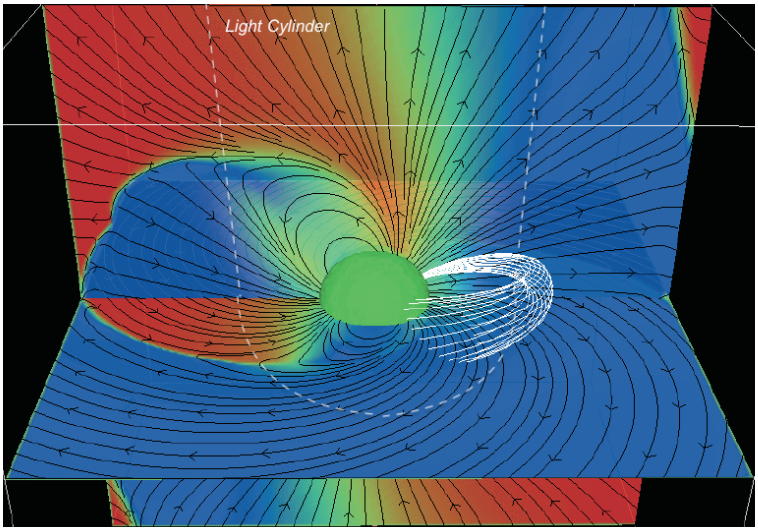

FIGURE 7.3: MagnetohydroDynamic (MHD) simulation of an oblique rotator with an angle of 60° between the magnetic and rotation axis. B-field lines are represented in an horizontal and vertical slice. White dashed lines delimitate the light cylinder. Adapted from Spitkovsky (2006).

7.4 Pulsar γ-ray emission

Given the necessity to have acceleration regions where the non-thermal emission is produced, in the standard paradigma of high-energy pulsars ad-hoc acceleration regions (i.e. gaps) were introduced. Gaps are pair starved regions, related to the open magnetic field lines, where the charge density departs from the Goldreich-Julian density, $\rho \neq \rho_{GJ}$, enabling an electric field (parallel to the magnetic field) to build up and accelerate charged particles.

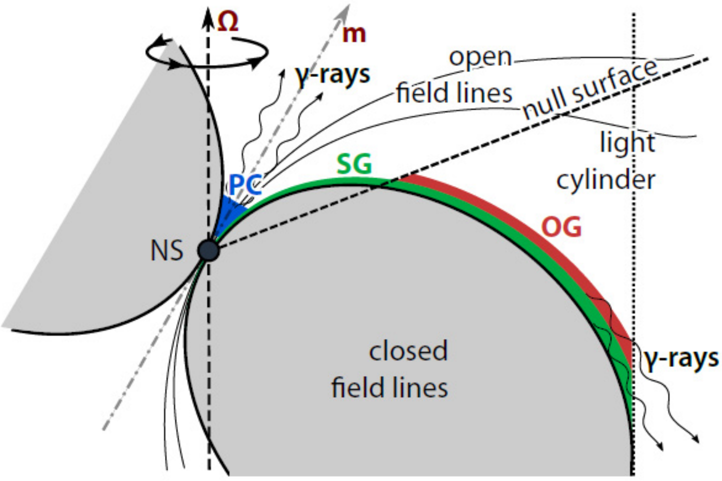

FIGURE 7.4: Location of the acceleration regions in the pulsar magnetosphere. From Giavitto (2013).

Depending on the location of the acceleration gaps, depicted in Figure 7.4, three main magnetospheric scenarios have been proposed for the production of γ-rays.

- *Polar Cap* (PC): At the PC (i.e. the region mapped out on the stellar surface by the footprints of the open magnetic field lines), due to the current outflow along open magnetic field lines, a vacuum gap (Ruderman and Sutherland, 1975) or a space-charge limited flow (Arons and Scharlemann, 1979) accelerator is formed. Gaps are self-limited by the development of pair cascades. At altitudes where particles reach high Lorentz factors and emit γ-ray photons via curvature radiation, pair cascades are activated by these energetic photons, thus feeding the region with enough charges to equalize again the Goldreich-Julian charge density and stopping the growth of the gap. This spatial upper limit of the gap is the so-called Pair Formation Front (PFF), and it is usually produced at ~ 1 stellar radius from the NS surface. In PC models, γ-rays are emitted via curvature radiation by $e^{\pm}$ moving along the curved magnetic field lines. However, since the gap is formed close to the stellar surface where the magnetic field is very strong, HE photons are absorbed via magnetic pair production constraining the maximum energy of emitted γ-rays (Baring, 2004). Therefore, the energy spectrum predicted by the PC model is characterized by a super-exponential cut-off (Daugherty and Harding, 1996). Figure 7.5 shows the pulsar phase profiles, also known as LCs, predicted by PC models. LCs present a double peaked structure with almost any peak phase separation as long as the viewing angle, i.e. inclination angle between the observer and the rotational axis of the pulsar, is small (less than 30°). For greater viewing angles, the PC cannot accommodate wide-separated double peaks, e.g. the Crab Pulsar. Note that as the emission is strongly beamed, both peaks come from only one of the poles as shown in Figure 7.5.

- *Slot Gap* (SG): The SG model was first presented as an extension of the PC model (Arons, 1983). Inside the PC, $E_{\|}$ is strong and the PFF forms close to the NS surface, whereas at the PC rim $E_{\|}$ vanishes. Near this edge, the electric field decreases and a larger distance is needed to accelerate charged particles up to Lorentz factors able to trigger pair production. The PFF grows to higher altitudes becoming asymptotic to the last closed field line near the

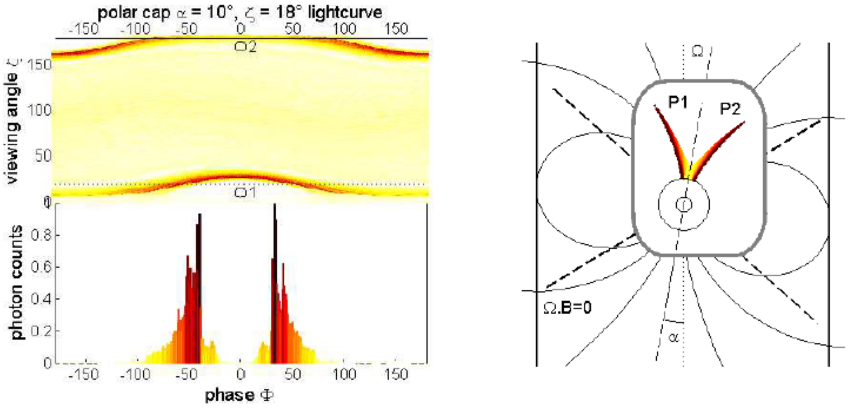

Figure 7.5: Phase plot illustrating the change in the Light Curve (LC) as seen at different observation angles (*Top-Left*). LC, and sketch of the emission in the PC model for an inclination angle of 10° (*Bottom-Left* and *Right*, respectively). Dashed lines represent the null charge surface. From Grenier and Harding (2006).

light cylinder (Muslimov and Harding, 2004; Harding, 2007). The radiation from the high altitude SG consists of two components: curvature radiation from primary electrons at the highest energies, and synchrotron from both primaries electrons and secondary particles produced by lower altitude cascades. The resulting energy spectrum is therefore characterized by a simple exponential cut-off. SG models predict double peaked LCs where each peak is produced by the accumulation of photons (i.e. caustics, see Figure 7.6) due to time-of-flight delay and aberration from the trailing side of each pole (Figure 7.7).

- *Outer Gap* (OG): The OG model (Cheng et al., 1986; Romani and Yadigaroglu, 1995; Cheng et al., 2000; Takata et al., 2006), initially proposed by Cheng et al. (1986) focuses on charge-depleted regions along open field lines crossing the null surface, where $\mathbf{\Omega} \cdot \mathbf{B} = 0$. Particles are accelerated by the strong developed $E_{\|}$-field to Lorentz factors of $\Gamma \sim 10^{7}$ and efficiently emit photons via curvature

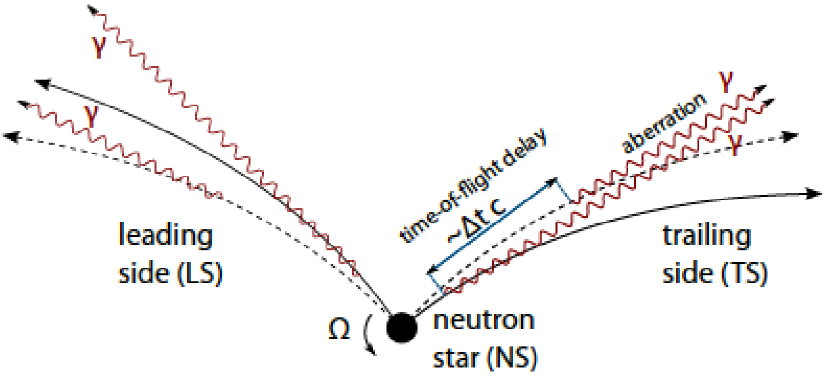

Figure 7.6: Scheme of the formation of caustics. Solid and dashed black curves represent the same magnetic field line at t and $t + \Delta t$, respectively. γ-rays emitted by the same electron moving along the magnetic field lines are displayed in red. The caustic only forms at the trailing edge due to time-of-flight delay and aberration. From Giavitto (2013).

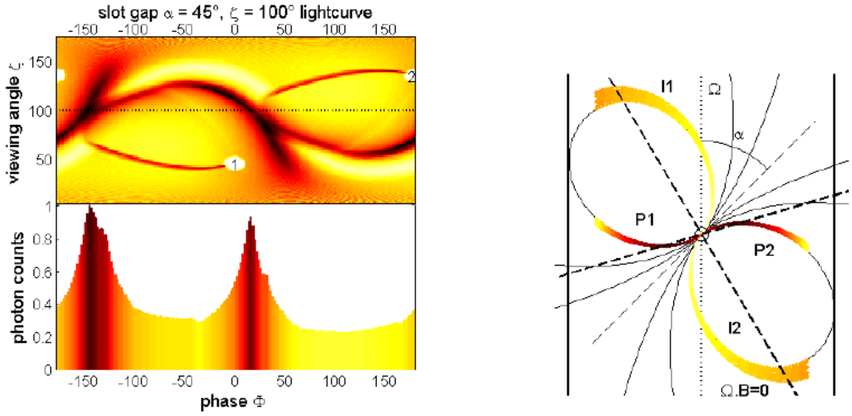

FIGURE 7.7: Same as Figure 7.5 for the SG model with an inclination angle of 45°. From Grenier and Harding (2006).

radiation. Accelerated charged particles induce particle cascades self-regulating the growth of the gap and shorting out $E_{\parallel}$. At that high altitudes, pairs are created via photon-photon process (using thermal photons from the NS surface) since the magnetic field is too low, orders of magnitude weaker than near the surface, for magnetic pair production. In this region, the maximum γ-ray energy is determined by the balance between the energy gained through acceleration and losses by curvature radiation due to the bending of the magnetic field lines (Hirotani, 2013). Consequently, the energy spectrum falls more gradually than in PC model, producing an exponential cut-off. In the OG emission model, the observer sees emission associated with only one magnetic pole, since the acceleration region develops only above the null surface. The LC predicted presents two peaks coming from the caustics produced at the trailing field lines as in the SG models, Figure 7.8.

Alternative models to the magnetospheric scenarios have also been proposed to explain the observed emission. These models locate the particle acceleration region and production of γ-rays in the so-called pulsar wind zone. The pulsar wind zone is the

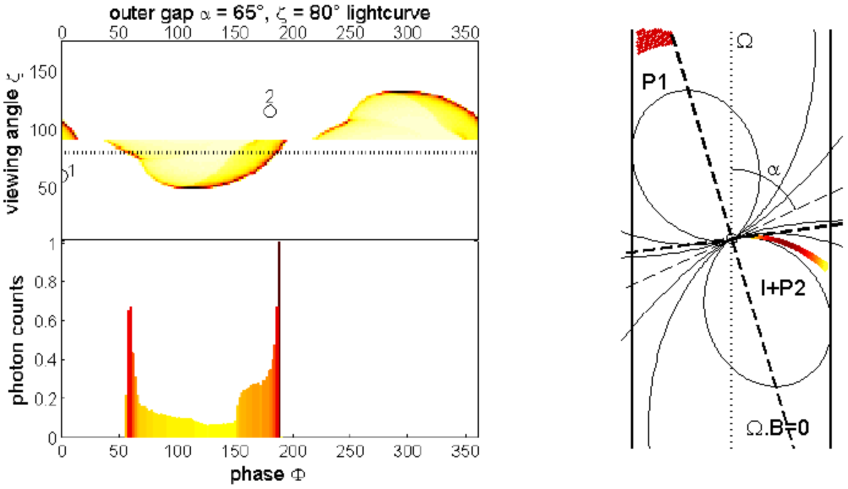

FIGURE 7.8: Same as Figure 7.5 for the OG model with an inclination angle of 65°. Note that the OG develops only above the null surface. From Grenier and Harding (2006).

region between the light cylinder and the termination shock. This region is populated by a relativistic magnetized wind ($\gamma \sim 10^6$) formed by particles that have escaped the magnetosphere (i.e. unshocked pulsar wind).

- *Striped Wind:* The striped pulsar wind model as an alternative site for the production of γ-ray emission was introduced by Kirk et al. (2002) based on Coroniti's work (Coroniti, 1990). Beyond the light cylinder, owing to a non-parallel magnetic and rotation axis, open magnetic field lines propagate outwards forming a striped morphology. A current sheet, i.e. region across which the B-field direction reverses, oscillates around the equatorial plane as the pulsar rotates, connecting the equator with field lines of opposite polarity every half period (Figure 7.9). The sheet corrugations increase their amplitude linearly with distance from the star. At high latitudes, the magnetic field does not change sign, and therefore current sheets are not present. Particles are believed to be accelerated through magnetic reconnection in current sheets, specifically at X-points where magnetic field re-arranges and a reconnection electric field is at play (Figure 7.10). Those accelerated particles are then advected by magnetic islands (i.e. plasmons) where they emit synchrotron radiation that is in turn

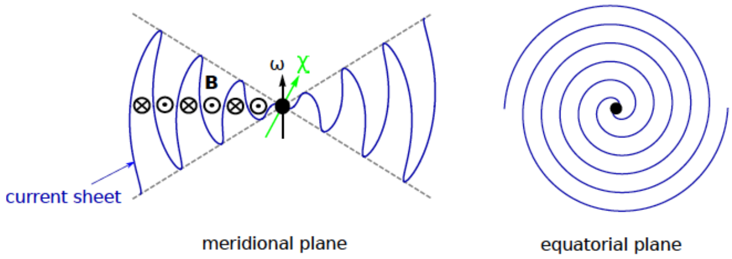

FIGURE 7.9: Striped wind for an oblique rotator. In the meridional plane the striped wind develops with a current sheet (blue curve) separating B-fields of opposite polarity. In the equatorial plane the wind forms a perfect spiral. From Mochol (2017).

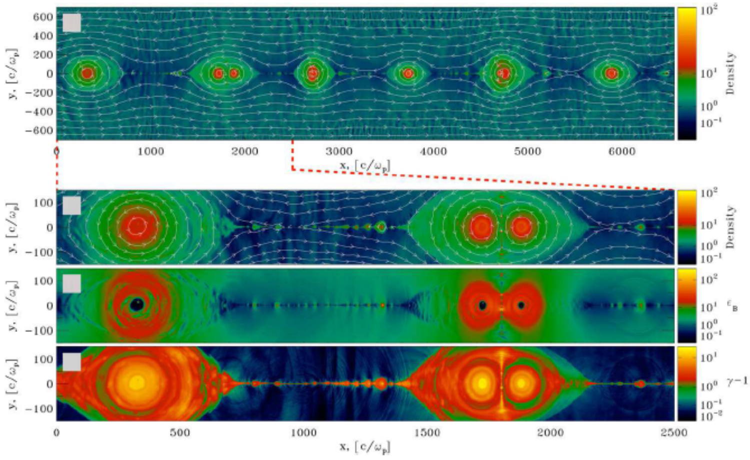

FIGURE 7.10: Structure of current sheets from particle-in-cell simulations. First two panels illustrate the particle density with magnetic field lines overlaid. Third panel shows the magnetic energy and bottom panel the kinetic energy per particle. In the second panel, X-points are identified in the region between plasmoids where magnetic field lines reconnect. From Sironi and Spitkovsky (2014).

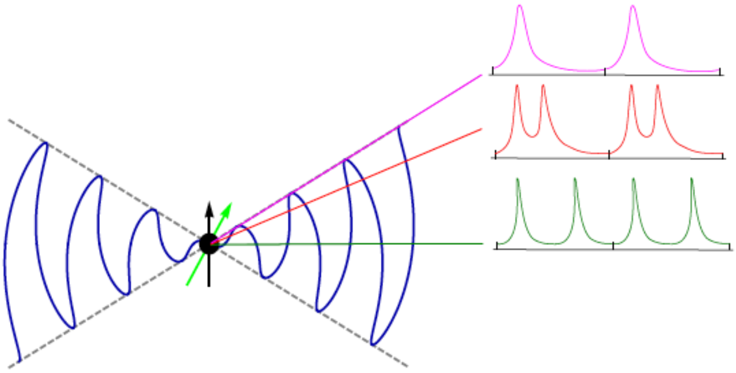

FIGURE 7.11: Representation of different pulse profiles observed from the striped wind at different viewing angles. Emission comes from the current sheet when crossing an imaginary sphere of radius r_0. From Mochol (2017).

upscattered via IC mechanism giving rise to a SSC spectral component at VHEs (Mochol and Pétri, 2015; Mochol, 2017). In the striped wind model, the emission is strongly beamed into a cone of $1/\Gamma$ in the radial direction (Γ is the Lorentz factor of the wind). Therefore, only emission in the direction of the observer will be detected. Moreover, assuming that each corrugation of the current sheet radiate when crossing an imaginary sphere of radius r_0, an observer will see up to two pulses depending on the viewing angle as illustrated in Figure 7.11. In the case of a double-peaked structure, the pulse profile may also present a 'bridge' emission whose intensity varies in function of the observation angle.

- *Unshocked Wind:* The state of the wind is characterized by the ratio of electromagnetic to kinetic energy flux of particles in it. When ejected from the light cylinder the wind is electromagnetically dominated and changes in its way to the termination shock to kinematically dominated. How this transition occurs is still a matter of debate (sigma problem). However, one possibility is to assume that there is an acceleration region present in the unshocked wind where the toroidal magnetic field (Figure 7.3) dissipates and converts energy into energy of relativistic particles. Bogovalov and Aharonian (2000) and Aharonian et al. (2012) showed that beyond a certain radius, R_W in Figure 7.12, the particle acceleration is completed and accelerated particles move tangentially to the light cylinder in straight lines. These particles in turn IC scatter magnetospheric photons moving radially outwards (Figure 7.12), producing γ-ray emission. The non-zero angle (θ) between electrons and photons will greatly boost the energy of the scattered photons. It is important to remark that only particles moving towards the observer will produce observable emission. Moreover, LCs in this emission model should mimic those of the target photon field but slightly shifted in phase due to time-of-flight delay.

Currently, the detection of TeV pulsed emission from the Crab Pulsar (Ansoldi et al., 2016) cannot be explained by any of these models in the way they were initially presented. New and revisited models accounting for this specific VHE emission will be overviewed in Chapter 8.

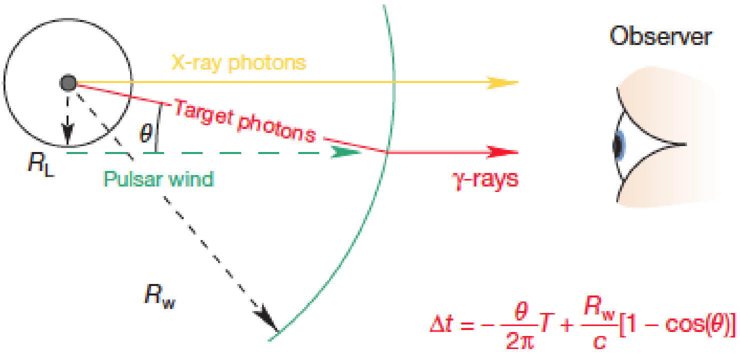

FIGURE 7.12: Geometry of the unshocked wind model. Trajectories of the different particles, with their interaction angle, θ, are illustrated. R_L represent the light cylinder radii and R_W the radii at which particles are accelerated and emit radiation. The time-of-flight delay between X-ray photons from the star surface and γ-rays produced via IC is estimated in the bottom right corner. From Aharonian et al. (2012).

Chapter 8

TeV pulsed emission from the Crab Pulsar detected by MAGIC

8.1 Introduction

The Crab Pulsar, PSR J0534+220, is a young NS with a rotational period of 33.65 ms. It was created after the SN explosion SN1054. The Crab is the most powerful pulsar in our Galaxy, with a spin-down luminosity of 4.6×10^{38} erg s^{-1}. It is one of the few pulsars detected across the electromagnetic spectrum, from radio up to gamma rays, and one of the brightest at high energies ($0.1<E<10$ GeV, Fierro et al. 1998; Kuiper et al. 2001; Abdo et al. 2010c; Aliu et al. 2008). The exceptionality of this source was underlined by the discovery of pulsed emission at energies up to 400 GeV (Aliu et al., 2011; Aleksić et al., 2012a).

The Crab Pulsar emission profile is characterized by three components: two pulses separated by ∼0.4 in phase and detected at all energies, from centimeter radio ($E{\sim}10^{-4}$ eV) to VHE gamma rays ($E>100$ GeV), and a third component, the bridge, which is defined as the pulse phase between the Main Pulse (P1) and the Second Pulse (P2). P1 is the peak with the highest intensity at radio frequencies and defines phase 0, whereas P2, which is often referred to as the interpulse, is weaker at radio frequencies. The amplitude of the three components, however, exhibits a strong energy dependence (Kuiper et al., 2001). At hard X-rays, P2 starts to dominate over P1 up to few MeVs where the trend changes and the emission from P1 is more intense than P2. In the gamma-ray regime, P2 becomes dominant once again above 25-50 GeV. In the case of the bridge, its emission is only substantial between ∼1 keV and ∼10 MeV and in the ∼50-150 GeV energy window, as reported in Aleksić et al. (2014).

The first year of *Fermi* observations of the Crab Pulsar spectrum validates the consensus view of magnetospheric scenarios reporting a spectral cut-off at ($5.8\pm0.5_{stat}$ $\pm1.2_{syst}$) GeV (Abdo et al., 2010c). However, the gamma-ray emission later discovered at VHE (Aliu et al., 2011; Aleksić et al., 2011, 2012a), is not compatible (at more than a 6σ CL) with an exponential cut-off in the spectrum and thus highly unlikely to be based on synchro-curvature magnetospheric emission. This unexpected spectral component, described by a steep power-law function (with a photon index of approximately 3.5) between 25 and 400 GeV, required an ad-hoc explanation (Aliu et al., 2011; Aleksić et al., 2011, 2012a). Some of the new postulated models proposed the same synchro-curvature mechanism responsible for the sub-TeV emission, yet under extreme conditions (Bednarek, 2012; Viganò and Torres, 2015), whereas others proposed a new mechanism to be at work: IC scattering on seed photon fields (from IR to X-rays).

In the case of IC radiation, different VHE gamma-ray production regions have been considered; from the acceleration gap in the pulsar magnetosphere (Aleksić et al., 2011; Hirotani, 2011; Lyutikov et al., 2012; Harding and Kalapotharakos, 2015) to the ultra-relativistic cold wind outside the light cylinder (Aharonian et al., 2012; Bogovalov and Aharonian, 2000; Mochol and Pétri, 2015).

In this chapter, we revisit the first 5 years of *Fermi*-LAT data of the Crab from 100 MeV to 300 GeV and we analyze more than 300 hours of excellent quality data of the Crab recorded with MAGIC telescopes from 2007 to 2014, both in stand-alone and stereoscopic mode. The main goal of this work was to shed some light on the origin of this VHE spectral component. In particular, we looked for the highest energy reached in the spectrum of the Crab Pulsar and for any potential spectral features of the peaks.

8.2 *Fermi*-LAT data analysis

The analysis was performed on 1742 days of data (∼4.8 years) taken in survey mode from the 4^{th} August 2008 (MET 239557417) to the 13^{th} May 2013 (MET 390096003). Only events with the highest quality reconstructed energies between 100 MeV and 300 GeV within a ROI of 30° radius around the source were selected. Data taken at zenith angles $>100°$ where the Earth's albedo γ-rays increase the background contamination were excluded. In addition, data periods of reported Crab glitches or flares (see Appendix A) were also excluded from the data sample to avoid timing errors during the analysis.

Due to the long period analyzed in this work and the high spin-down luminosity of the Crab Pulsar, its rotational behaviour must be known precisely for a correct calculation of the timing properties. Hence, we made use of the monthly updated ephemerides provided by the Jordrell Bank Observatory[1] (Lyne et al., 1993) to phase-fold the γ-rays detected during the observation time. The phase-folding was applied by the *TEMPO2* timing package (Hobbs et al., 2006). In order to generate highly accurate LCs, an extra energy dependent data selection taking into account the performance of the instrument at different energies was performed. Therefore, only photons of energy E_{MeV} within an angle $\theta < max\,[6.68 - 1.76log10(E_{MeV}), 1.3]^{\circ}$ around the pulsar position were kept for the LC computation (Abdo et al., 2010c).

The spectral analysis was performed in 18 independent energy bins, using a maximum likelihood method with the old PASS7 IRF (*P7SOURCE_ V6*), in a 26 °× 26° square region centered on the Crab position. Our constructed model for the ROI accounts for 73 point-like sources and 1 extended source, IC443, extracted from the second *Fermi*-LAT source catalog (2FGL), as well as the Galactic diffuse emission and the extragalactic isotropic diffuse emission modelled by *gal_ 2yearp7v6_ v0* and *iso_ p7v6source*, respectively (see Figure 8.1). Among all the spectral parameters, only those for sources within 7° from the Crab were left free. Additionally, normalization factors for sources within 14° were also allowed to vary during the maximum likelihood fitting process.

Note that depending on the pulsar component we want to study, i.e. P1, P2 or Bridge, the phase interval of the analysis has to be chosen accordingly since they are not active during the whole period of the pulsar. Moreover, the normalization factor of all the sources in the model have to be scaled down to the considered pulsar phase.

---

[1] http://www.jb.man.ac.uk/research/pulsar/crab.html

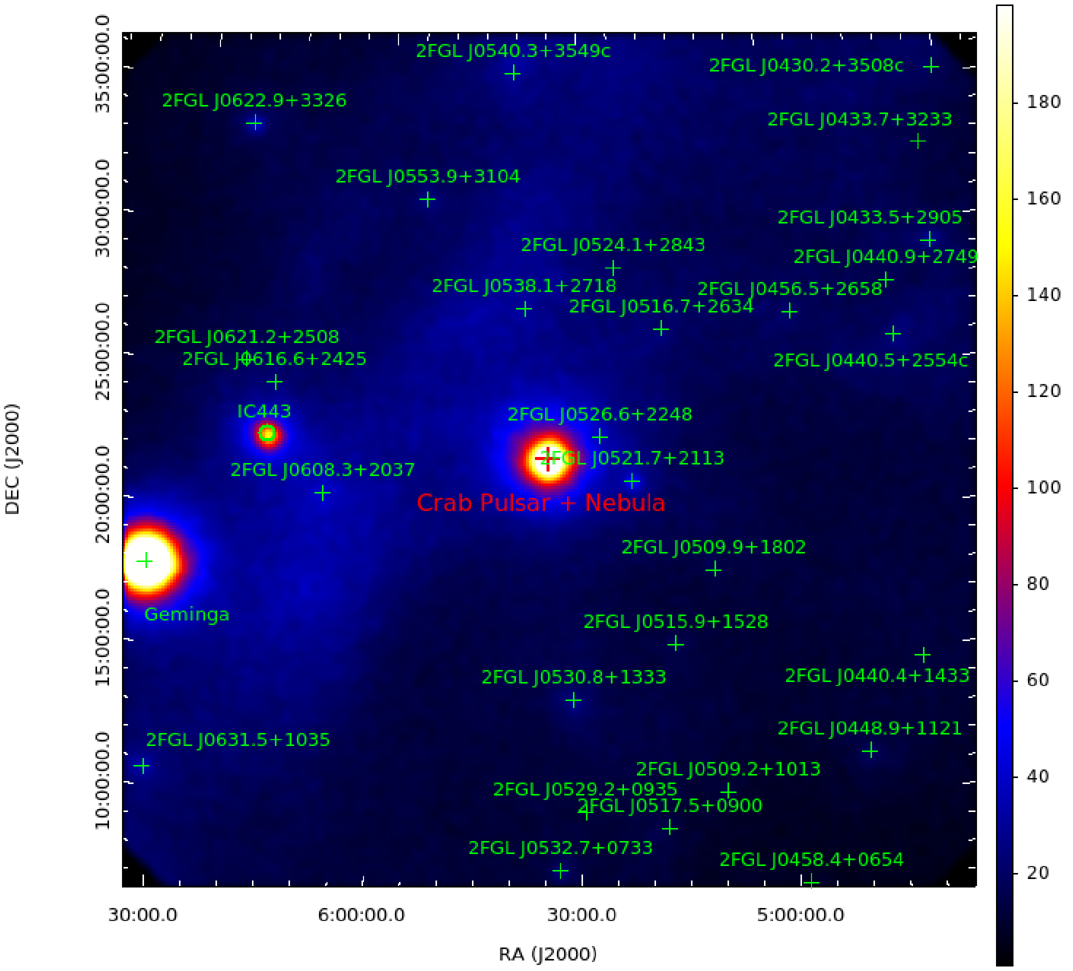

FIGURE 8.1: *Fermi* counts map, between 100 MeV to 300 GeV, centered at the nominal position of Crab (MET 239557417 to MET 342576000). 2FGL sources, used in this analysis are plotted in green. The Crab Pulsar + Nebula system has been represented by a red cross.

Based on Abdo et al. (2010c), we used the phase interval definition stated in Table 8.1 for the nebula and pulsar components. Moreover, as can be appreciated in Figure 8.1, the position of the pulsar and the nebula are coincident to within the angular resolution of LAT. Thus, owing to the spatial coincidence of both pulsed and unpulsed emission, one has to also estimate the nebula contribution to properly compute the pulsar spectrum. While the pulsar emission dominates over the nebula in the on pulse interval, i.e. P1-P2-Bridge (see Table 8.1), the nebula stands out in the off-pulse phase, i.e. from 0.52 to 0.87, where the pulsar turns out. Therefore, in the off-pulse interval the emission observed above the diffuse background is associated exclusively to the nebula.

8.2.1 Crab Nebula spectral description

Prior to the analysis of the pulsar and its spectral characterization, we run a maximum likelihood pre-analysis for the nebula for events belonging to the off-pulse. We find that the emission of the Crab Nebula is well characterized by a broken power-law

Component	Phase Interval	
	FERMI	MAGIC
P1	0.87–1.07	0.983–1.026
P2	0.27–0.47	0.377–0.422
Bridge	0.08–0.26	0.026–0.377
Nebula / off-pulse	0.52–0.87	0.52–0.87

TABLE 8.1: Definition of the Crab phase intervals.

defined as,

$$\frac{dN(E)}{dE} = N_{sync}\left(\frac{E}{\mathrm{GeV}}\right)^{-\alpha_{sync}} + N_{IC}\left(\frac{E}{\mathrm{GeV}}\right)^{-\alpha_{IC}} \tag{8.1}$$

as shown in Figure 8.2.

In fact, the emission from the nebula has two differentiated components, synchrotron and IC, described by simple power-laws; first and second members of the right part of the equation 8.1, respectively. Below ~300 MeV the synchrotron emission produced by accelerated electrons in the nebular magnetic field dominates while IC on FIR, CMB and synchrotron emitted photons is responsible for the emission above this energy. Since the flux obtained has been calculated from the off-pulse and the nebula emits over the whole period of the pulsar, the resulting flux has to be normalized to the total phase interval (factor $\frac{1}{0.35}$). The fit parameters for both components are summarized in Table 8.2. The spectral parameters presented here are compatible within errors with those presented in Abdo et al. (2010c) after renormalizing to the total phase. After characterizing the Crab Nebula spectrum, it is introduced into our constructed source model as an additional background source with its spectral parameters fixed. Once

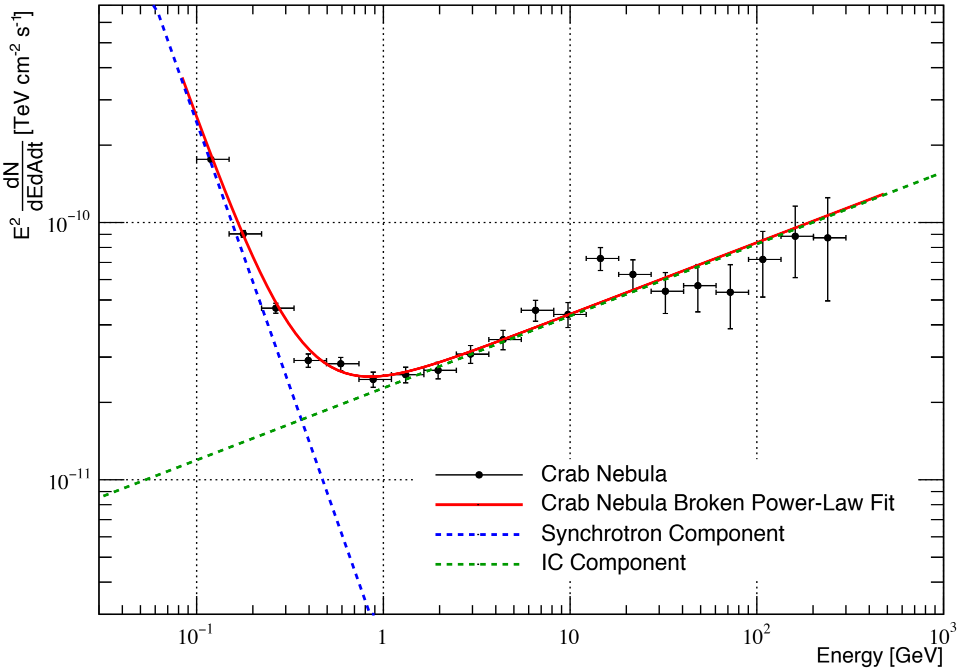

FIGURE 8.2: SED of the Crab Nebula obtained with LAT. The broken power-law fit to the spectral points is shown by the red curve. Synchrotron (blue dashed line) and IC (green dashed line) components are represented by two different power-laws.

	$N_{sync/IC}$ [MeV^{-1} cm^{-2} s^{-1}]	α
Synchrotron	$(1.41 \pm 0.7) \times 10^{-12}$	4.1 ± 0.3
IC	$(1.5 \pm 0.1) \times 10^{-11}$	1.72 ± 0.03

TABLE 8.2: *Fermi*-LAT results of the spectral fit of the Crab Nebula to a broken power-law function. Errors indicate 1σ statistical uncertainties. The normalization factors are computed at the decorrelation energy of 1 GeV.

the emission/contamination from nebula has been estimated, the spectral analysis of the different components of the Crab Pulsar can be performed by re-running the maximum likelihood fit for each specific phase interval.

8.3 MAGIC data analysis

The analysis was performed by using the MAGIC software, MARS, following the standard procedure reviewed in Chapter 2. In this work, we used all the data taken in stereoscopic mode, until April 2014, when pointing at the Crab. The selected sample includes observations performed at zenith angles up to 70°. In order to increase the statistics we also reanalyzed Crab mono data recorded between 2007 and April 2009 at zenith angles smaller than 30°. Both mono and stereo data samples were taken partially in *On* and, partially, in wobble mode, the latter pointing at two symmetric positions 0.4° away from the source. Data affected by hardware problems and bad atmospheric conditions were removed from the analyzed data sample. An additional selection based on the rate of gammas received per day was applied to ensure the highest quality data possible. Hence, days differing by more than 30% of the mean rate were discarded for the analysis (see Figure 8.3). In the case of the Crab Pulsar, the background above ∼100 GeV is not dominated by hadrons but by γ rays from the Crab nebula. Therefore, we applied background rejection cuts specifically optimized for a gamma-dominated background and specified that at least 90% of our Monte Carlo gamma rays survive those cuts. The cut optimization is based on the maximization of the modified formula (17) by Li and Ma 1983:

$$\sigma_\gamma = \sigma_{\text{Li\&Ma}}\left(N_{\text{on}}\frac{\Gamma_{\text{TP}}}{\Gamma_{\text{OP}}} + \alpha N_{\text{ex}}, N_{\text{on}}, \frac{\Gamma_{\text{TP}}}{\Gamma_{\text{OP}}}\right)$$

where:

N_{on} is the number of events in the off-peak region that survive the hadronness and θ^2 cuts.

N_{ex} is the total number of excess events from the Crab Nebula.

Γ_{TP} and Γ_{OP} are the relative widths of the peak regions (TP=P1+P2) and the off-pulsed region, respectively.

α is the ratio between the energy fluxes of the Crab Nebula and the Crab Pulsar, as found in Aleksić et al. (2012a) and Aleksić et al. (2012b), respectively.

This formulation simulates the significance observed from the pulsar considering as background the hadronic and nebula events derived from the nebula excess and the power-law spectrum for the pulsar found in Aleksić et al. 2012a. After the cuts mentioned, data resulted in 97 hours and 221 hours of effective time for the mono and the stereo samples, respectively. Given that the considered data sample spreads over seven years, with different instrument performance, we divided it into nine analysis periods, each with its corresponding Monte Carlo simulation. The whole data sample was then further subdivided into three zenith angle ranges to better account for the corresponding dependence of the image shower parameters at the cut optimization stage. This resulted in 19 data sub-samples, each period with at least some low zenith angle data used to monitor the instrument performance. RF matrices and energy LUTs were produced separately. Figure 8.4 shows the effective area for four representative datasets: mono, and stereo in the three zenith angle ranges. The differential energy spectra obtained for each independent analysis were later on combined, once weighted with the exposure, when applying the unfolding procedure to correct for the energy bias and the detector finite energy resolution (see Chapter 2). We tested five different unfolding methods described in Albert et al. (2007b) and verified their consistency within statistical errors. The ULs to the differential flux were obtained by following the Rolke et al. (2005) method under the assumption of a Gaussian background and 20% systematic uncertainty in the flux level. Hereafter, the ULs will be given at 95% CL. As for *Fermi* data, the pulsar rotational phase of each event was defined by using the TEMPO2 package (Hobbs et al., 2006) and the monthly ephemeris publicly provided by the Jodrell Bank Observatory (Lyne et al., 1993).

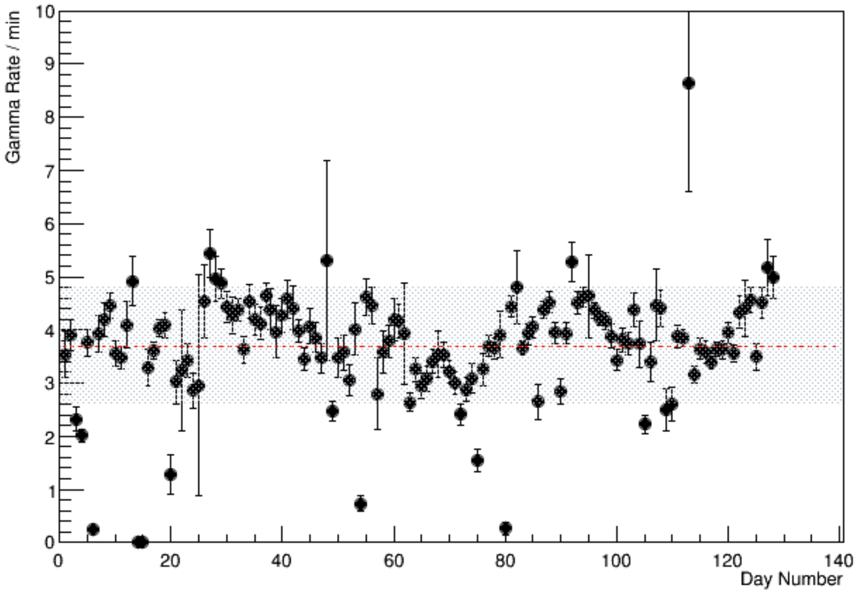

FIGURE 8.3: Distribution on a day-to-day basis of the rate of gammas registered by MAGIC for the low zenith data sample (data within 5° and 35°). Days outside the 30% of the mean rate (shaded region) were discarded. The red dashed line represent the mean rate of the data sample: 3.67 gammas per minute.

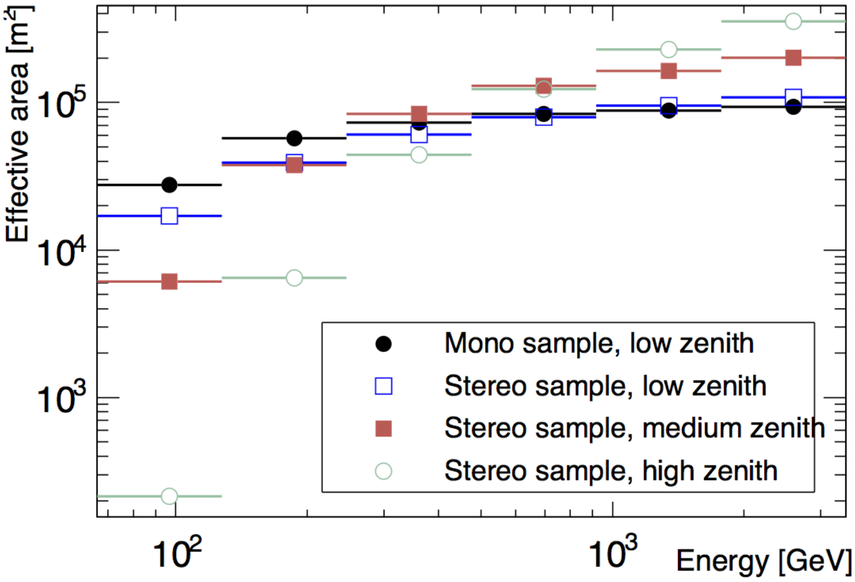

FIGURE 8.4: Effective area, after background rejection cuts, for four representative data subsamples.

8.4 Results

8.4.1 Light curve in the *Fermi* range

Using the data selection cuts described in section 8.2 for our ROI, we detected a total number of 97068 events at the Crab position. After accounting for the diffuse and nebula contributions, we estimated in 69900 the number of pulsed γ-ray events. Figure 8.5 shows the corresponding γ-ray LC in the full energy range from 100 MeV to 300 GeV. The LC shows two clear peaks, P1 and P2 with a significant bridge emission in between. The corresponding significances found for each of the components are 213σ (P1), 159σ (P2) and 50σ (Bridge).

Looking at the peak shapes shown in Figure 8.5, it can be noticed that they have different behaviors. The highest peak (P1) shows a slight asymmetry in its rise and fall, while the second peak (P2) is clearly asymmetric with steeper fall than rise. For this reason, we used asymmetric functions to fit both peaks. In particular, we used two half-Lorentzian profiles with different widths for the leading an the trailing edges, defined by:

$$L(x) = C_0 \begin{cases} \frac{1}{1+\left(\frac{x-\phi}{HWHM^L}\right)^2}, & x < \phi \\ \\ \frac{1}{1+\left(\frac{x-\phi}{HWHM^T}\right)^2}, & x > \phi \end{cases}$$

where C_0, ϕ, $HWHM^L$ and $HWHM^T$ identify the amplitude, peak position, and Half Width at Half Maximum (HWHM) for the leading and trailing edges of the peaks, respectively. The fits were performed on the 0.002 degree binned LC (Figure 8.5) to properly account for any finer structure. The results are presented in Table 8.3. We found that P1 and P2 are located at phases $\phi_{\mathrm{P1}} = 0.9997 \pm 0.0003$ and $\phi_{\mathrm{P2}} = 0.3973 \pm 0.0009$, respectively, and therefore with a peak separation of $\delta\phi =$

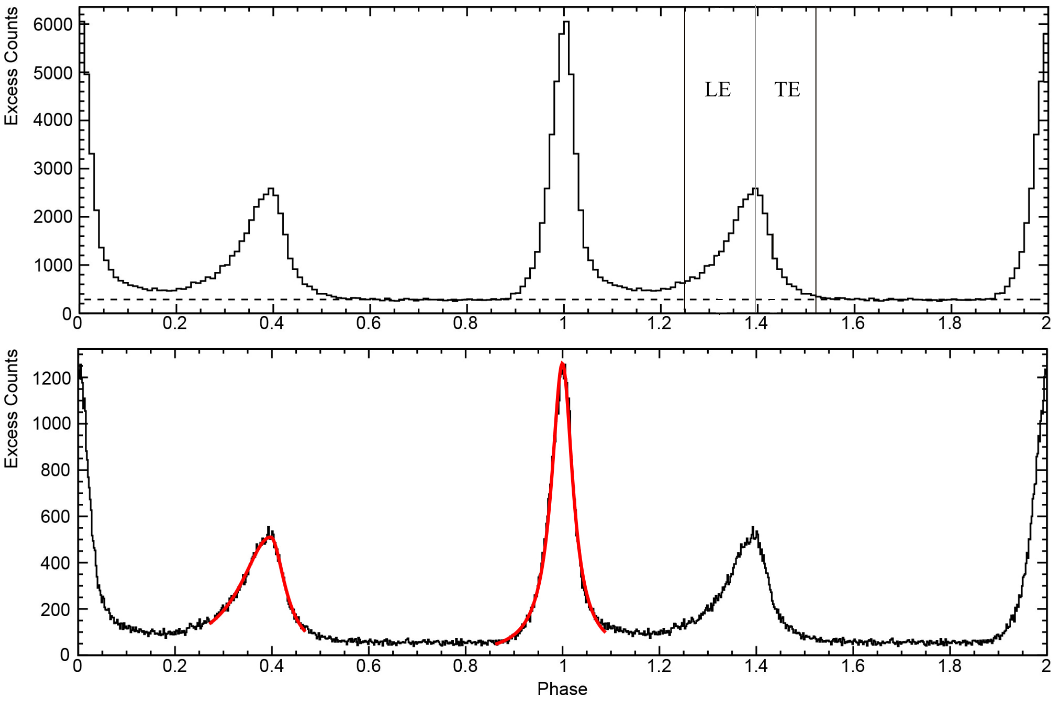

FIGURE 8.5: LC obtained with photons of energies between 100 MeV and 300 GeV within an energy dependent region as described in section 8.2. Data are presented over two rotation periods, to better emphasize the behavior of P1 which lies at ~ phase 0. The LC is displayed with two different binnings. *Top:* Binned to 0.01 in phase. The dashed line shows the constant background level calculated from the off-region. Vertical lines delimit the Trailing Edge (TE) and Leading Edge (LE). *Bottom:* Binned to 0.002 in phase. The fits to the peaks are represented in red.

0.3976 ± 0.0009. These results are comparable to those found in Abdo et al. (2010c) and Abdo et al. (2013).

To study the energy dependent behavior of the two peaks, the 100 MeV–300 GeV energy range has been divided in multiple energy bands. Figure 8.6 shows the pulse profile in the resulting five energy subranges (0.1–0.3 GeV, 0.3–1 GeV, 1–3 GeV, 3–10 GeV and 10–300 GeV). Table 8.3 reports the result of the asymmetric Lorentzian fits in each of the energy bands.

Energy Range (GeV)	ϕ_{P1} ($\times 10^{-2}$)	$HWHM_{\mathrm{L}}^{\mathrm{P1}}$ ($\times 10^{-2}$)	$HWHM_{\mathrm{T}}^{\mathrm{P1}}$ ($\times 10^{-2}$)	ϕ_{P2} ($\times 10^{-2}$)	$HWHM_{\mathrm{L}}^{\mathrm{P2}}$ ($\times 10^{-2}$)	$HWHM_{\mathrm{T}}^{\mathrm{P2}}$ ($\times 10^{-2}$)
0.1–0.3	99.7 ± 0.1	6.4 ± 0.1	5.6 ± 0.1	39.8 ± 0.2	14.3 ± 0.5	9.5 ± 0.5
0.3–1.0	100.0 ± 0.1	5.2 ± 0.1	4.6 ± 0.1	39.7 ± 0.1	14.1 ± 0.4	6.9 ± 0.3
1.0–3.0	99.9 ± 0.1	4.5 ± 0.1	5.9 ± 0.2	40.0 ± 0.2	17.9 ± 0.7	5.2 ± 0.3
3.0–10.0	100.5 ± 0.1	4.6 ± 0.3	6.8 ± 0.4	40.2 ± 0.3	21.0 ± 1.7	4.8 ± 0.5
10.0–300.0	102.1 ± 1.7	15.2 ± 4.3	32.3 ± 11.0	39.9 ± 1.1	26.6 ± 7.7	8.4 ± 2.6
0.1–300.0	99.98 ± 0.03	5.50 ± 0.06	5.18 ± 0.07	39.73 ± 0.09	15.2 ± 0.3	7.1 ± 0.2

TABLE 8.3: Detailed LC fit parameters.

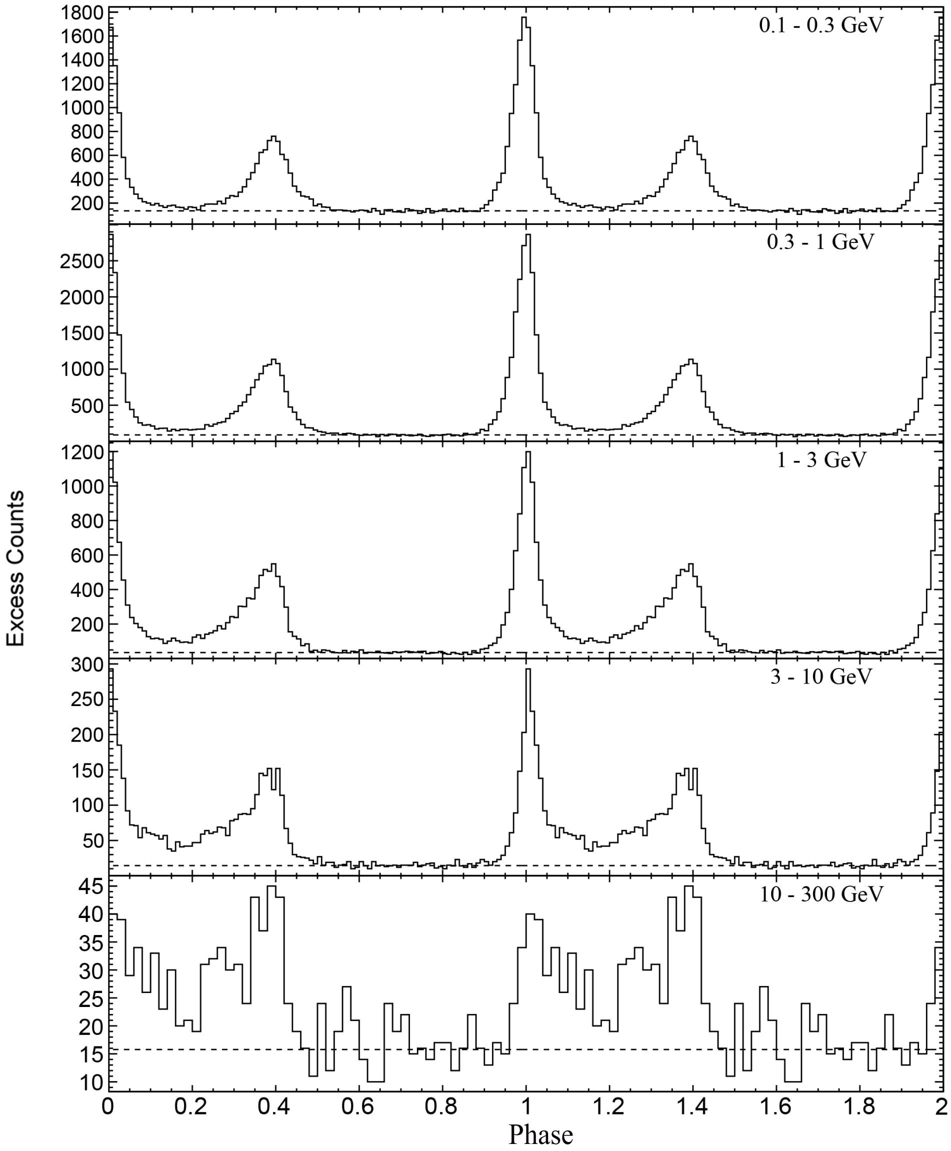

Figure 8.6: LCs in diferent energy bands, from top to bottom 0.1–0.3 GeV, 0.3–1 GeV, 1–3 GeV, 3–10 GeV and 10–300 GeV. Pulse profiles are binned to 0.01 except above 10 GeV, binned to 0.02 in phase. Dashed lines represent the constant background level calculated from the off-region.

While the phases of the peaks do not present any significant shift with energy considering their statistical error, from the pulse profiles it is noticeable that their relative amplitudes, hence the fluxes of the different components, are in fact energy dependent with P2 and the bridge more significant the higher the energy is, contrarily to P1. We quantitatively studied this effect by computing the flux ratio P2/P1 and Bridge/P1 calculated from the number of events detected above background as a function of energy. These results are represented in Figure 8.7. Table 8.4 lists the number excess events with their corresponding errors and the ratios for P2/P1 and Bridge/P1. The Bridge/P1 ratio gradually increases with energy, as well as the P2/P1 ratio but with a

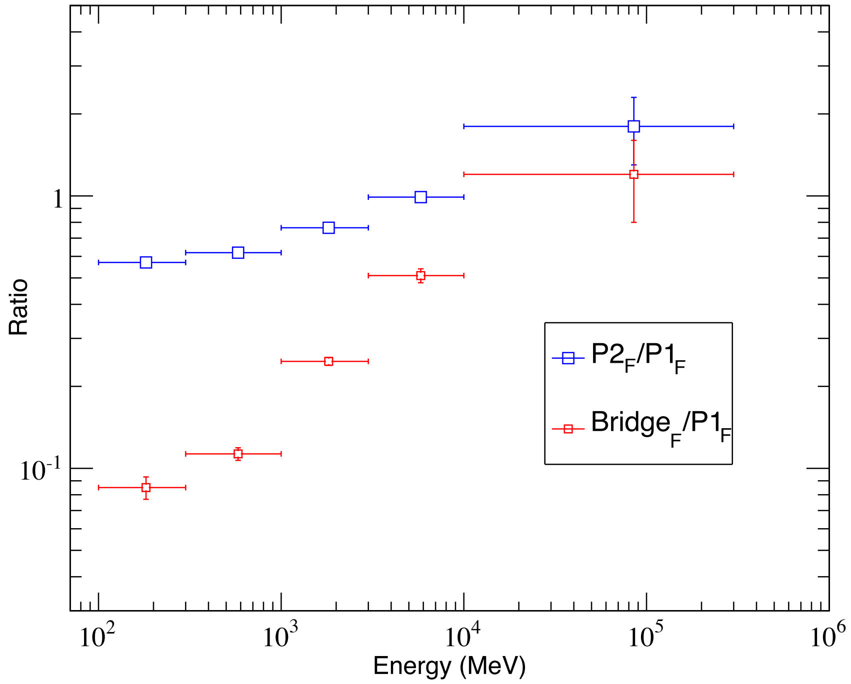

FIGURE 8.7: P2/P1 and Bridge/P1 ratios as a function of energy for *Fermi*-LAT.

Energy Range (GeV)	P1 (excess counts)	P2 (excess counts)	Bridge (excess counts)	P2/P1	Bridge/P1
0.1–0.3	10947 ± 85	6239 ± 85	927 ± 85	0.570 ± 0.009	0.084 ± 0.008
0.3–1.0	17971 ± 112	11121 ± 112	2026 ± 112	0.619 ± 0.007	0.113 ± 0.006
1.0–3.0	7296 ± 54	5572 ± 54	1805 ± 54	0.764 ± 0.009	0.247 ± 0.008
3.0–10.0	1486 ± 37	1477 ± 37	761 ± 37	0.99 ± 0.04	0.51 ± 0.03
10.0–300.0	86 ± 20	152 ± 20	100 ± 20	1.8 ± 0.5	1.2 ± 0.4

TABLE 8.4: Numbers of excess events of P1, P2 and Bridge and their relative component ratios.

rise less pronounced. For energies above 10 GeV the lack of statistics[2] makes difficult any analysis, even so, it is already visible a change in the trend with P2 becoming dominant over P1.

Furthermore, the width of the pulses also change with the energy, in our case, the broader, the higher the energy is. This is illustrated in Figure 8.8, where the last energy bin was excluded due to its poor statistics. We found that the widening of P1 is caused primarily by its trailing edge falling slower than the leading one for increasing energies, whereas the other way around is true for P2. The slight widening of the trailing and leading edge of P1 and P2, respectively, coincide with the rising of the bridge component in between. It might be possible that a contribution from the bridge at the higher energies, where it is more significant, is contaminating the adjacent edges of the peaks and therefore broadening them.

Of particular importance is the last energy bin considered, between 10 GeV and 300 GeV which is the one overlapping with MAGIC. The significances found in this

---

[2] Different binnings were tested to improve the fit yielding all similar results. The election was taken based on the χ^2.

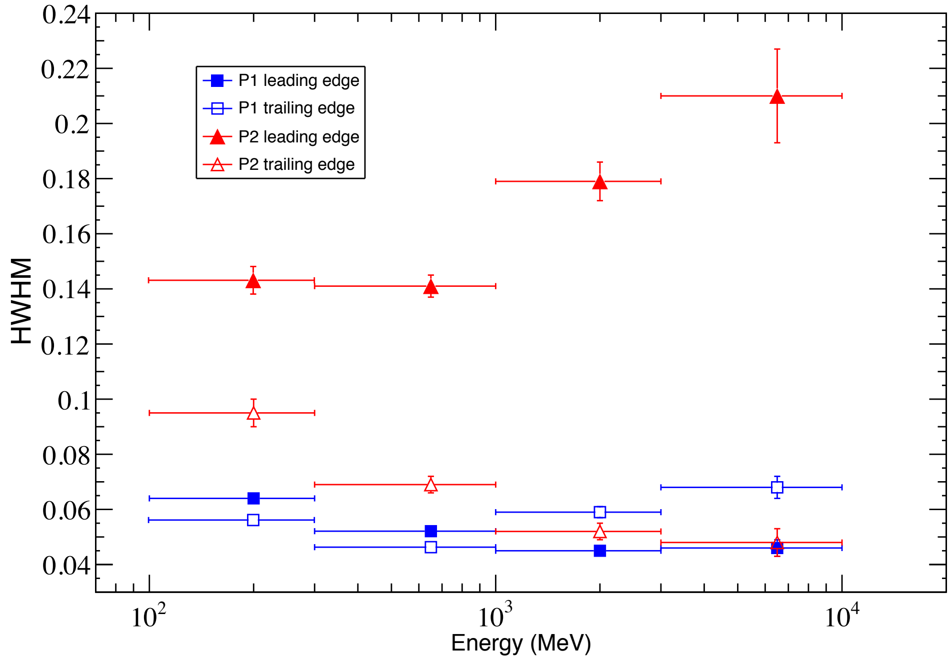

FIGURE 8.8: Measured HWHM of P1 and P2 for the different energy bands.

energy bin for P1 (4.8σ), P2 (7.9σ) and Bridge (5.5σ) show the detection of the three components already above 10 GeV.

8.4.2 Light curve in the MAGIC range

In the search for pulsation above 400 GeV from the Crab Pulsar with MAGIC, we defined the phase ranges of the two peaks according to the results obtained in previous studies (Aleksić et al., 2012a, 2014): P1 $\in (-0.017, 0.026)$ and P2 $\in (0.377, 0.422)$. The interval (0.52, 0.87) was considered as off-pulse region (Fierro et al., 1998) from where we estimated the background to be subtracted from the histograms. Crab Pulsar phase intervals for MAGIC observations are also summarized in Table 8.1

Figure 8.9 shows the folded pulse profile that we obtained between 100 and 400 GeV and above 400 GeV with 318 hours of observation. The choice of the lower energy limit, 100 GeV, it has been made for comparison purposes with previous LCs reported by MAGIC and VERITAS. It is, thus, by no means related to the energy threshold of the observations. In the 100–400 GeV energy range P1 is detected with a significance level of 2.8σ, whereas P2 at 5.6σ after Li and Ma (1983, Eq.17). The statistical significance of the detection of P1 and P2 with this analysis is smaller than that reported in Aleksić et al. (2014) with less than half of the observation time. This is due to the fact that the analysis presented in this work combines many periods with different sensitivities and energy thresholds, and these factors contribute to decreasing the signal-to-noise ratio at the lowest energies, hence worsening the overall signal significance. If we consider only stereo data for zenith angles below 35°, which identify the data sub-sample with the lowest energy threshold and best gamma/hadron separation at the lowest energies, we end up with 152 hours of observation time, yielding a signal significance of 6.6σ and 8.8σ for P1 and P2 respectively in the energy range between 100 and 400 GeV. This is in agreement with the results reported in Aleksić et al. (2014) for the 50–400 GeV

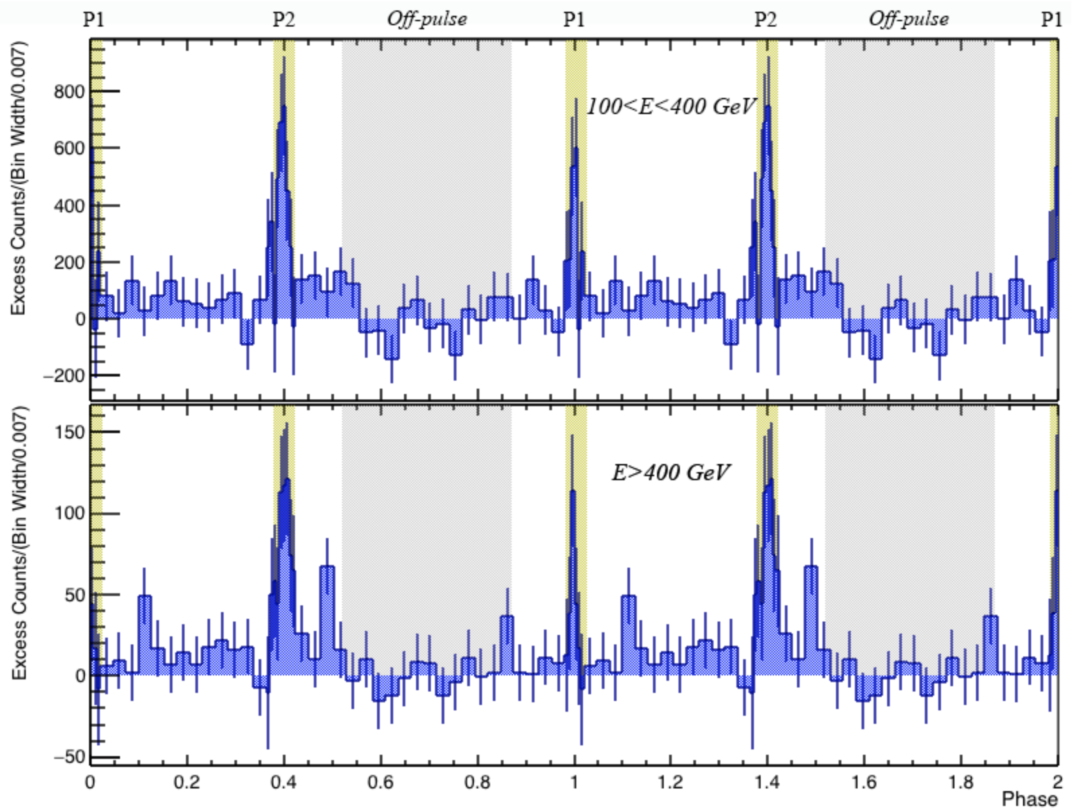

FIGURE 8.9: Pulse profile of the Crab Pulsar between 100 and 400 GeV (upper panel) and above 400 GeV (bottom panel). The pulse profile, shown twice for clarity, is background subtracted. The bin width around the two peaks is 4 times smaller (0.007) than the rest (0.027) in order to highlight the sharpness of the peaks. Yellow-dashed areas identify the phase intervals of the two peaks, whereas the gray areas show the off-pulse region.

energy range. Beyond 400 GeV (above the energy threshold of all the 19 analyses used here) the gamma/hadron separation is efficient for all the analyses and we have a clear gain in the signal significance for the combined sample due to the increase in photon statistics. For energies above 400 GeV, only P2 is significantly detected. The total number of excess events are 544 ± 92 and 188 ± 88 for P2 and P1 respectively corresponding to 6σ and 2.2σ for each peak. With a higher energy cut at 500 GeV, meant to exclude the lower energy events from the LC where no spillover correction is applied, P2 is still detected at 5σ, while P1 shows a 2σ signal with 418 ± 104 and 152 ± 108 excess events, respectively. Table 8.5 summarizes the number of excess events with their corresponding significance for different integral energy ranges. For completeness, Figure 8.10 shows the LCs obtained above 680 GeV and 950 GeV where the peaks are not significantly detected anymore. P2, however, still shows a hint of emission above 680 GeV.
The significance of the pulsation was also tested with the H-test (de Jager et al., 1989) which does not make any a priori assumption on the position and the shape of the pulsed emission, resulting in a 3.5 (2.8)σ significance above 400 (500) GeV.

We fitted the pulse profile above 400 GeV to a finer-binned distribution with two symmetric Gaussian functions (Figure 8.11, as in Aleksić et al. 2012a). The available statistics does not allow us to consider more complicated functions. P1 and P2

Energy Range	P1		P2	
[GeV]	N$_{\rm ex}$	Significance	N$_{\rm ex}$	Significance
100–400	1252 ± 442	2.8 σ	2537 ± 454	5.6 σ
> 400	188 ± 88	2.2 σ	544 ± 92	6.0 σ
> 680	130 ± 66	2.0 σ	293 ± 69	4.3 σ
> 950	119 ± 54	2.2 σ	190 ± 56	3.5 σ

TABLE 8.5: Number of excess events and corresponding significance of P1 and P2 for different energy ranges in ~320 hours of data.

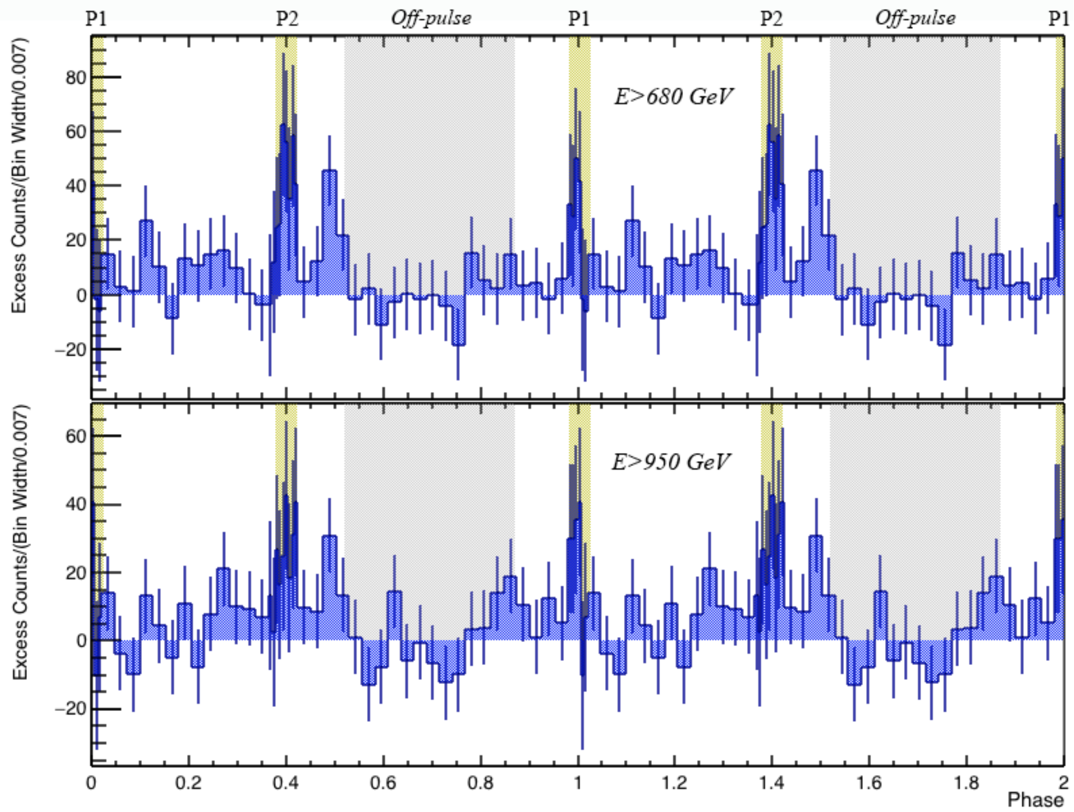

FIGURE 8.10: Same as Figure 8.9 for energies above 680 GeV (upper panel) and above 950 GeV (bottom panel).

are located at the phases $0.9968 \pm 0.0020_{stat} + 0.0055_{syst} - 0.0048_{syst}$ and $0.4046 \pm 0.0035_{stat} + 0.0047_{syst} - 0.0074_{syst}$ respectively, in agreement with the positions found at lower energies between 50 and 400 GeV (Aleksić et al., 2012a). The Full Width at Half Maximum (FWHM) for P1 is $0.010 \pm 0.003_{stat} + 0.003_{syst} - 0.010_{syst}$ and for P2 is $0.040 \pm 0.009_{stat} + 0.005_{syst} - 0.008_{syst}$. The systematic uncertainty on the estimation of the peak positions reflects the precision of the pulsar ephemerides used for this analysis, taking into account the RMS of the timing noise, the uncertainty on the arrival time of the first pulse taken as reference, and the error introduced by the barycentric corrections. Systematic errors also include the effect of the histogram binning. The width of the peaks beyond this energy are compatible within the errors with the value measured below 400 GeV. Note that results reported above 400 GeV for P1 are obtained for a ~2σ signal and should be taken with caution.

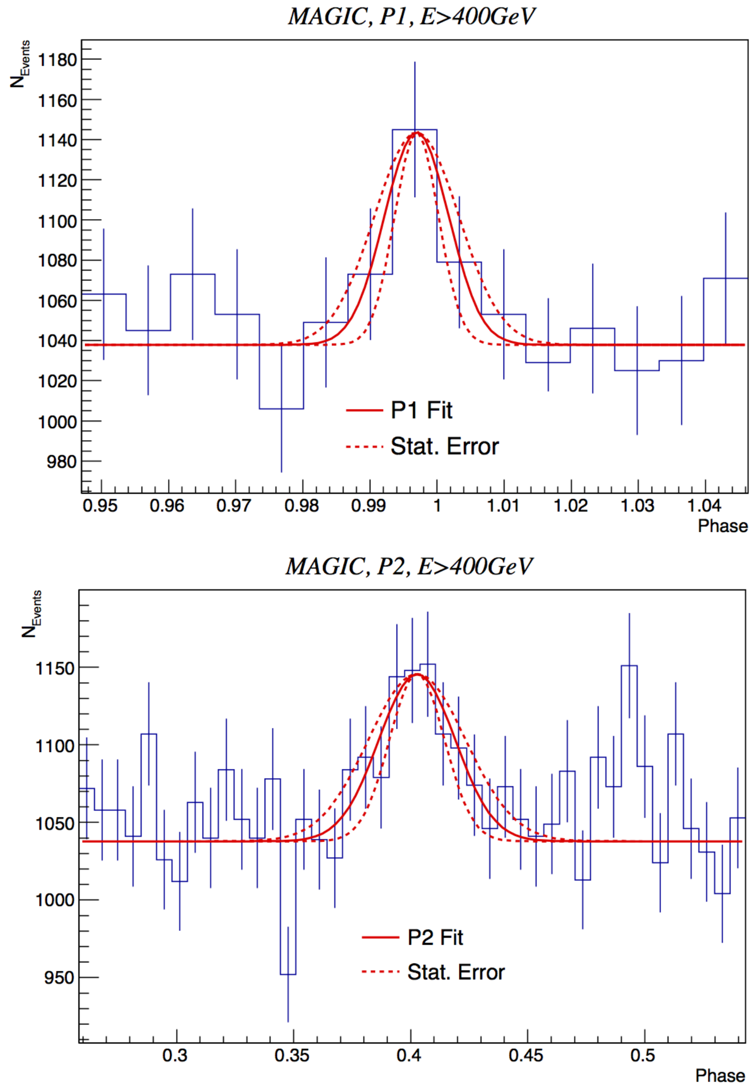

FIGURE 8.11: Pulse shapes near the peaks above 400 GeV, binned to 0.007 in phase. The symmetric Gaussian functions fit to the peaks are represented by the red curve along with their statistical errors (red dashed lines).

8.4.3 Energy spectra

Figure 8.12 shows the MAGIC phase-folded SED of P1 and P2 from ∼70 GeV up to 1.5 TeV, obtained by using the Bertero's unfolding method (Bertero, 1989). Both the differential energy spectra are well-described by power-law functions with a photon index, α, of $3.2 \pm 0.4_{stat} \pm 0.3_{syst}$ and $2.9 \pm 0.2_{stat} \pm 0.3_{syst}$, for P1 and P2, respectively. The results of the fits, shown in Table 8.6 for a normalization energy at 150 GeV (being the decorrelation energy 120 GeV and 190 GeV for P1 and P2 respectively), are in agreement with MAGIC earlier results (Aleksić et al., 2012a, 2014). In the case of P2, the power-law spectrum extends up to 1.5 TeV, whereas P1 cannot be measured beyond 600 GeV. At energies above the last obtained spectral point, we computed ULs to the differential flux, at 95% CL, under the assumption of the power-law spectrum found in this work. However, a 20% change in the photon index yields a variation of less than 15% in the UL. These ULs are not constraining any possible cut-off, given the current sensitivity of the instrument. The spectral points and ULs are listed in

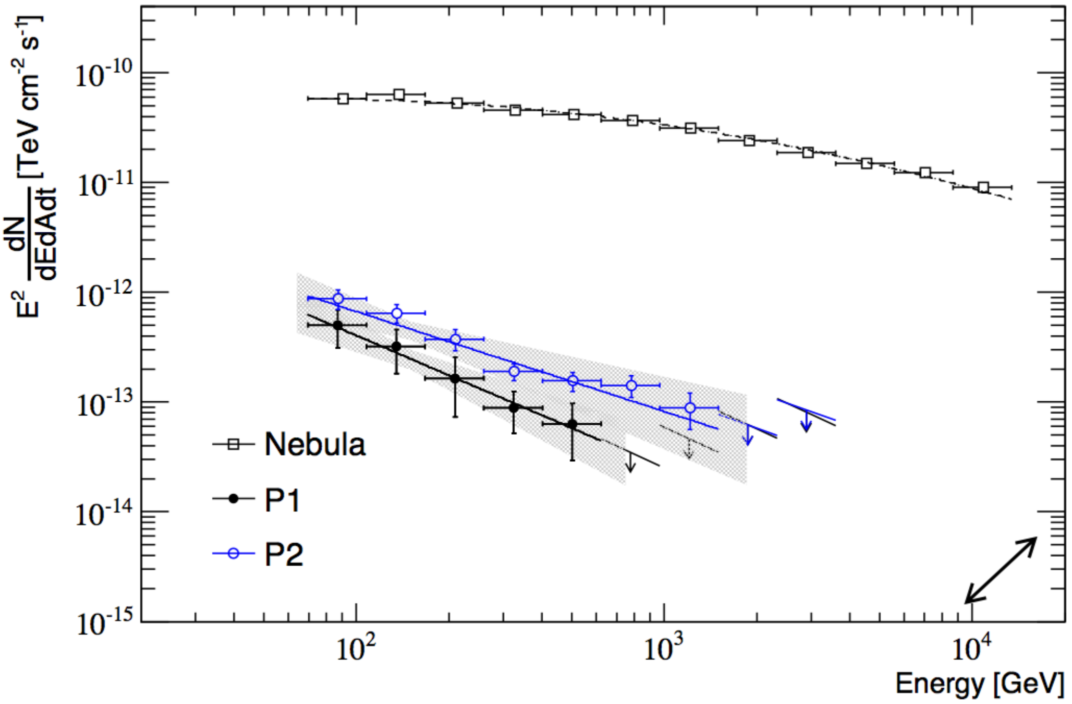

FIGURE 8.12: Phase-folded SED of the Crab P1 (black circles) and P2 (blue circles) measured by MAGIC between ∼70 GeV and 1.5 TeV. The butterfly identifies the systematic uncertainty on the flux normalization and spectral index, whereas the arrow on the bottom right corner corresponds to an energy shift of 17%. The Crab nebula spectrum (open squares) is also shown for comparison. The differential flux ULs, at 95% CL, are computed under the assumption of the power-law spectrum measured in this work.

Table 8.7.

On the other hand, in the *Fermi* energy range (100 MeV-300 GeV) both peaks are well characterized by power-laws with exponential cut-offs such as (Figure 8.13),

$$\frac{dN}{dE} = f_{\mathrm{E_o}} \left(\frac{E}{E_{\mathrm{o}}}\right)^{-\alpha} e^{-E/E_{\mathrm{C}}}$$

where $f_{\mathrm{E_o}}$, α and E_{C} are the differential flux at the decorrelation energy, i.e. 1 GeV, the photon index and the energy cut off, respectively. The best fit parameters describing both components are summarized in Table 8.8, together with their statistical

		$\mathrm{E_o}$ [GeV]	$f_{\mathrm{E_o}}$ [TeV^{-1} cm^{-2} s^{-1}]	α	χ^2/dof
MAGIC	P1	150	$(1.1 \pm 0.3)\times 10^{-11}$	3.2 ± 0.4	0.3/3
	P2	150	$(2.0 \pm 0.3)\times 10^{-11}$	2.9 ± 0.2	5.4/5
Fermi	P1	50	$(5.3 \pm 0.8)\times 10^{-10}$	3.5 ± 0.1	1.5/6
& MAGIC	P2	50	$(5.7 \pm 0.6)\times 10^{-10}$	3.0 ± 0.1	8.4/9

TABLE 8.6: Results of the spectral fit to a power-law function. Errors indicate 1σ statistical uncertainties. $\mathrm{E_o}$ indicates the decorrelation energy.

Energy [GeV]	Bin Center [GeV]	P1 E^2dN/dEdAdt [TeV cm^{-2} s^{-1}] $\times 10^{-13}$	P2 E^2dN/dEdAdt [TeV cm^{-2} s^{-1}] $\times 10^{-13}$
69–108	87	5.0 ± 1.9	8.7 ± 1.8
108–167	135	3.2 ± 1.4	6.5 ± 1.2
167–259	210	1.6 ± 0.9	3.7 ± 0.8
259–402	325	0.9 ± 0.4	1.9 ± 0.3
402–623	504	0.6 ± 0.3	1.6 ± 0.3
623–965	781	< 0.3	1.4 ± 0.3
965–1497	1211	<0.5	0.9 ± 0.3
1497–2321	1879	<0.6	< 0.6
2321-3598	2914	<0.8	< 0.8

TABLE 8.7: Spectral points of the MAGIC measurements shown in Figure 8.12.

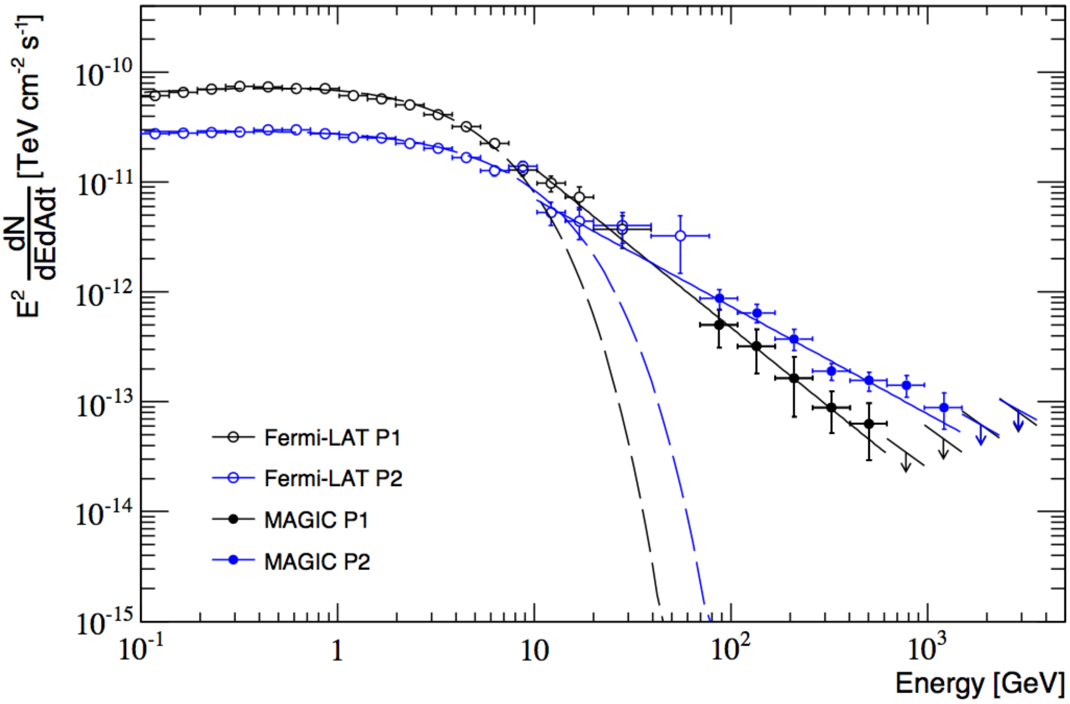

FIGURE 8.13: Phase-folded SED of the Crab P1 (black circles) and P2 (blue circles) at HE and VHE (open and filled circles). The results of the power-law with exponential cut-off fits to the *Fermi* points are illustrated by the dashed lines, whereas the joint *Fermi-LAT*/MAGIC fits to power-law functions above 10 GeV are shown by solid lines. The ULs to the differential flux, at 95% CL, are computed under the assumption of the power-law spectrum found in this work, as represented by the slope of the arrows.

uncertainties.

It can be noticed, however, that spectral points deviate from the exponential cut-off already above few GeVs as expected from VHE observations (Aliu et al., 2011; Aleksić et al., 2011, 2012a). Accordingly, the extrapolation of the MAGIC energy spectra to

		E_o [GeV]	f_{E_o} [MeV^{-1} cm^{-2} s^{-1}]	α	E_C [GeV]	χ^2/dof
Fermi	P1	1	$(8.9 \pm 0.1) \times 10^{-11}$	1.88 ± 0.01	3.7 ± 0.2	49/14
	P2	1	$(3.1 \pm 0.1) \times 10^{-11}$	1.97 ± 0.01	7.2 ± 0.6	23/15

TABLE 8.8: *Fermi*-LAT results of the spectral fit to a power-law with exponential cut-off function. Errors indicate 1σ statistical uncertainties. E_o indicates the decorrelation energy.

lower energies agrees within the statistical errors with the spectra measured with *Fermi* above 10 GeV. A joint correlated-χ^2-fit[3] of MAGIC and *Fermi* spectral points above 10 GeV shows that the new spectral components are well-represented (χ^2/ndf=1.5/6 and χ^2/ndf=8.5/9 for P1 and P2, respectively) by simple power-law functions (see Table 8.6), where the decorrelation energy is set to 50 GeV. The photon indexes of the two power-law functions are $\alpha = 3.5 \pm 0.1$ and $\alpha = 3.0 \pm 0.1$ for P1 and P2, respectively. The difference in the spectral slopes by $\Delta\alpha = 0.5 \pm 0.1$ is significant by more than 3σ, indicating that the intensity of P1 drops more rapidly with energy than that of P2. At X-ray energies (3–10 keV) *NuSTAR* detected a similar spectral behaviour with P2 harder than P1 and the corresponding photon indexes being 1.66 ± 0.02 and 1.80 ± 0.01, respectively (Madsen et al., 2015). A fit to a power-law function plus exponential cut-off allows us to impose a lower limit in the spectral cut-off of 700 GeV at 95% CL.

The measured spectral difference at VHE could be naturally explained either by two distinct production locations for each peak or by the difference in the phase-resolved spectrum of X-rays which act as targets for IC scattering.

We cross-checked the P2 energy spectrum by comparing mono data to the stereo data and found that the results were stable within statistical errors for all the considered unfolding methods. We also computed the Crab Nebula SED, as shown in Figure 8.12 (open squares), using the subsample of the data taken in wobble mode. The nebula spectral measurement was obtained by analyzing the same energy range as the pulsar analysis, using the same energy binning and gamma selection cuts. The results of the LogParabola fit performed, $\frac{dN}{dE} = f_{E_o}\left(\frac{E}{E_o}\right)^{\alpha+\beta\log\left(\frac{E}{E_o}\right)}$, are shown in Table 8.9. The resulting spectral points are consistent with the results presented in Aleksić et al. (2012b, 2015) as can be seen in Figure 8.14. Therefore, we assumed that no extra systematic uncertainty on the total flux is needed for this specific analysis. These systematic uncertainties are 17% on the energy scale, 19% on the flux normalization, and 0.3 on the photon index. The latter error is the only one not in agreement with Aleksić et al. (2012b), and mainly arises from the larger uncertainty of the unfolding given the low statistics of the result.

	E_o [TeV]	f_{E_o} [TeV^{-1} cm^{-2} s^{-1}]	α	β	χ^2/dof
Nebula	1	$(3.30 \pm 0.03)\times 10^{-11}$	-2.41 ±0.01	-0.17 ±0.01	21/9

TABLE 8.9: Results of the spectral fit to a LogParabola function. Errors indicate 1σ statistical uncertainties. E_o indicates the decorrelation energy.

---

[3] The fit takes into account the correlation between the MAGIC spectral points due to the unfolding procedure.

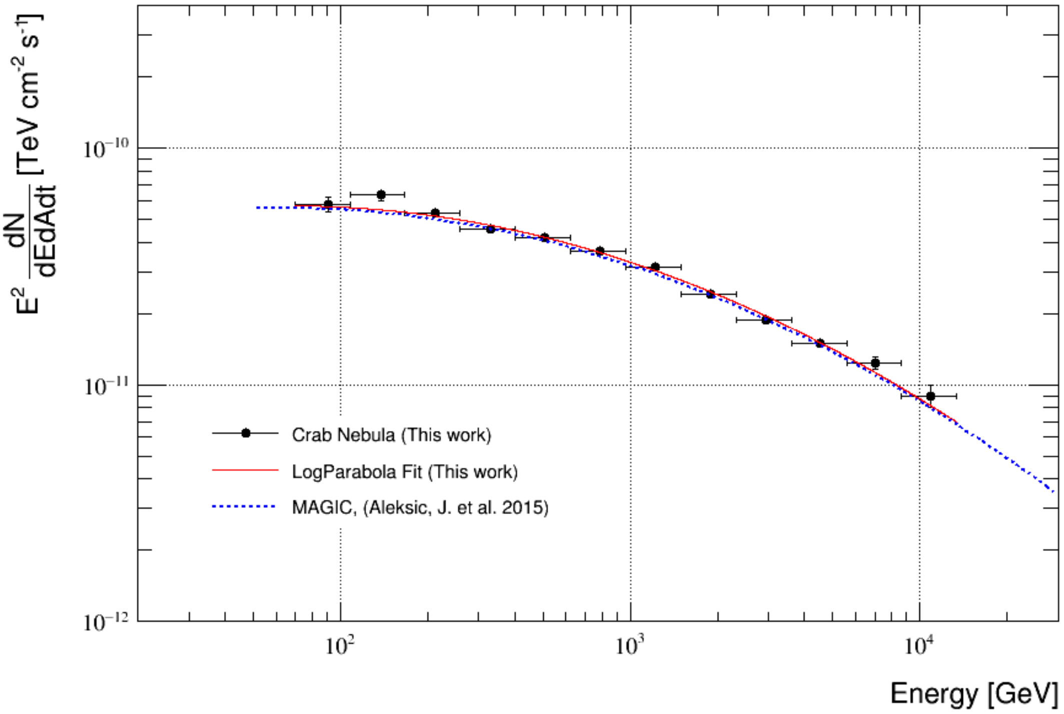

FIGURE 8.14: SED of the Crab Nebula from ~70 GeV to 1.5 TeV obtained in this work with exact same binning and gamma cuts than those used for the analysis of the pulsar. The red solid line represents the LogParabola fit to the data. The blue dashed curve shows the spectral fit of the Crab Nebula derived in Aleksić et al. (2015) from ~50 GeV to 30 TeV.

8.5 Discussion and conclusions

The results presented here probe the Crab Pulsar as the second most compact TeV accelerator known to date after the Vela pulsar which has recently been detected up to 7 TeV (Djannati-Atai et al., 2017). On a side note, in the case of the Vela pulsar, the TeV emission comes from another component whereas in the Crab pulsar it is compatible within systematic errors with a continuation of the GeV component. The remarkable detection of pulsed emission up to 1.5 TeV revealed by MAGIC imposes severe constraints on where and how the underlying electron population produces gamma rays at these energies. The electron population responsible for the VHE emission should have Lorentz factors greater than 5×10^6, which can be responsible for the VHE emission only when accelerated near or beyond the light cylinder (Bogovalov, 2014). The TeV pulsed emission cannot be produced with synchro-curvature radiation within the light cylinder, even in the extreme case in which the magnetic-field-aligned electric field approaches the strength of the magnetic field. In this scenario, the curvature radius would have to be one order of magnitude larger than the typical one, which is believed to be between 0.3 and 2 times the light cylinder radius (Viganò et al., 2015) (for further discussions on this issue we refer to Kalapotharakos et al. 2014; Harding and Kalapotharakos 2015 and references therein). Therefore, the unprecedented measurement of pulsed emission extending up to TeV energies performed with the MAGIC telescopes implies that most likely the IC process is at work in the Crab Pulsar, and that it dominates the emission of gamma rays above 50 GeV. This partially solves the puzzle posed by the previous published results but also opens new challenges.

We note that although other processes (e.g. synchro-curvature radiation (Viganò et al., 2015) or synchrotron radiation (Mochol and Pétri, 2015)) could account for the production of 100–400 GeV photons, the simple power-law function obtained by a joint fit of *Fermi* and MAGIC data from ∼10 GeV up to 1.5 TeV (and 700 GeV for P1) suggests a single mechanism for every peak and it must be Compton up-scattering of soft photons off HE electrons.

The two main IC scenarios proposed to explain the VHE emission below 400 GeV, the magnetospheric SSC model (Aleksić et al., 2011) and the IC in the pulsar wind region model (Aharonian et al., 2012), are not capable of simultaneously predict the VHE LC and the spectral shape obtained in this work.

The former assumes that there are acceleration gaps in the outer magnetosphere (Cheng et al., 1986; Romani and Yadigaroglu, 1995; Cheng et al., 2000; Takata et al., 2006; Arons, 1983; Muslimov and Harding, 2004) where primary positrons propagate outwards and escape, being illuminated by a strong magnetospheric IR photon field which is then up-scattered by positrons to TeV-scale energies. These primary TeV photons are then efficiently absorbed by the same IR field to materialize as secondary $e^{\pm}$ pairs with GeV to several TeV energies. Such secondary pairs are created at a greater distance whereby there is a lower photon-field density, near to and outside the LC, and can up-scatter the IR-UV photons into 10 GeV–5 TeV photons (via SSC process, Hirotani 2013). Some of them escape from the magnetosphere and are observable from Earth. However the synchronization of the pulse profile in the GeV and TeV regimes limits this interpretation, suggesting a similar region of generation, where absorption of TeV photons is unavoidable. The measured time delay between the best-fit peak positions in the MeV–GeV and the TeV regime is $100 \pm 67\mu$s and $245 \pm 121\mu$s for P1 and P2 respectively, which, when considering the relatively large systematics in the determination of the peak positions, are compatible with the hypothesis of no separation between the bulk of the radiation region where all these photons are generated (neglecting more complicated geometrical effects and assuming the simple case of stationary emission regions).

On the other hand, the pulsar wind scenario considers the IC scattering off the synchrotron, pulsed IR and X-ray photons by the particles (electron/positron) of the cold relativistic wind. It is commonly accepted that the pulsar wind is magnetically dominated near the LC. Thus, in the wind model, the wind becomes abruptly particle-kinetic-energy dominated over a short distance (compared to the dimension of the wind region). Based on previous results by Cherenkov telescopes on the Crab Pulsar (Aliu et al., 2011; Aleksić et al., 2012a), this distance was estimated to be 20-50 LC radii (see *left* panel of Figure 8.15, Aharonian et al. (2012)). In this narrow cylindrical zone, electrons and positrons are rapidly accelerated up to Lorentz factors of 5×10^5. The bulk Lorentz factor is assumed to display a power-law dependence on the distance: $\Gamma(R) = \Gamma_0 + (\Gamma_w - \Gamma_0)(\frac{(R-R_0)}{(R_f-R_0)})^{\alpha}$, where Γ_0 and Γ_w are the initial and the maximum wind Lorentz factors, R_0 the distance at which the acceleration starts, R_f the distance at which Γ_w is reached, and the power-law index α ∼1,3,10 (Aharonian et al., 2012). To obtain a Γ_w compatible with the one that is derived from the detection of TeV photons ($\sim 5 \times 10^6$), the region in which particles are accelerated has to extend up to a much larger radius than the one considered in Aharonian et al. 2012. In this case however, the model fails to reproduce the spectral shape below 100 GeV (see *right* panel of Figure 8.15). Instead, a slower and continuous acceleration (for instance due to magnetic reconnection) or a more complex radial dependence could be at play.

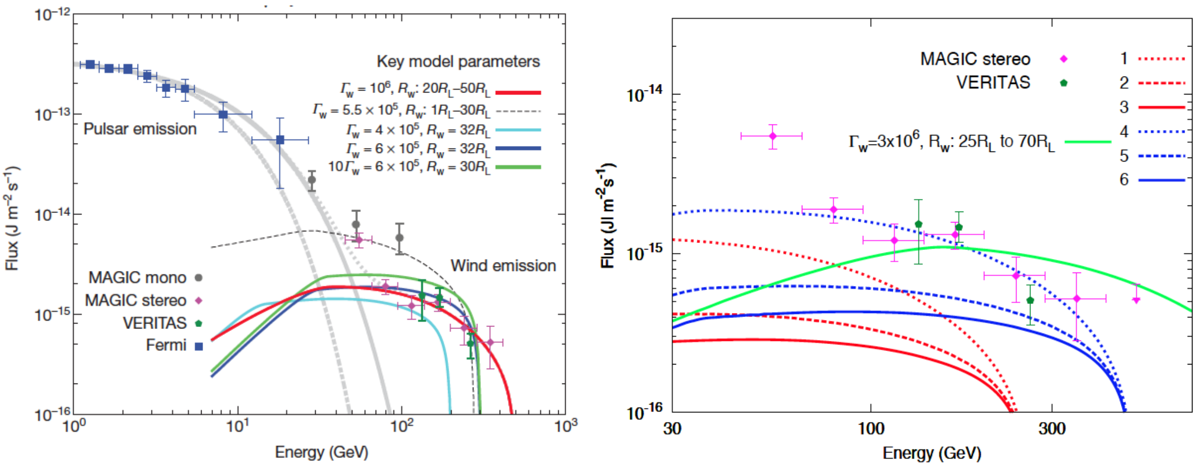

FIGURE 8.15: *Left:* SEDs calculated under different assumptions of the acceleration region and Lorentz factors reached. *Right:* The green curve represents the SED produced by a wind of Lorentz factor of 3×10^6 when the acceleration takes place between 25 to 70 R_L. From Aharonian et al. (2012).

Recently, the TeV pulsed emission has been adressed by Osmanov and Rieger (2017) and Bogovalov et al. (2017) as IC scattering off thermal photons from the pulsar surface. Both results are based on magneto-centrifugal acceleration of plasma close to the light cylinder along open positively curved magnetic field lines (see Figure

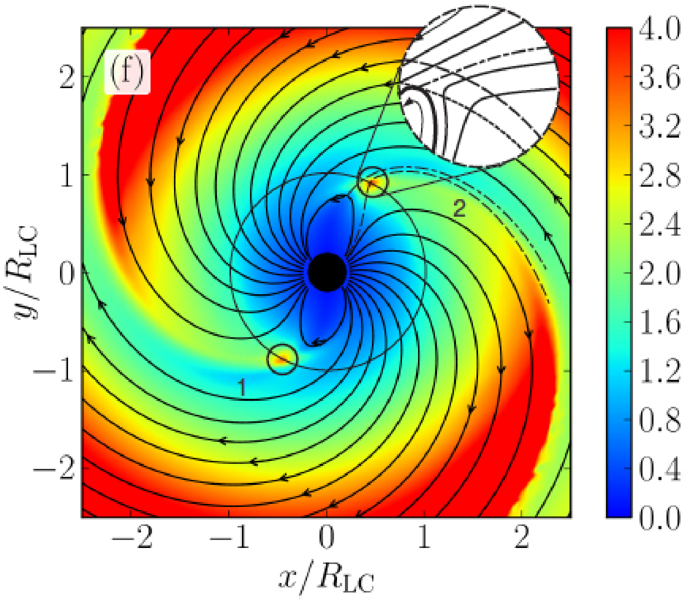

FIGURE 8.16: Equatorial plane of an oblique pulsar's magnetosphere (60° inclination). Solid curves represent the magnetic field structure. Small solid circles show important zones of magneto-centrifugal acceleration. A zoom in of one of these regions is represented at the top right part of the image. In the zoom in region we can see the shape of the positively curved field lines. The short dashed curve represents the Alfven surface while the long dashed curve represents the light cylinder. The dashed-dot line depicts the separatrix field line. From Bogovalov (2014).

8.16), (Bogovalov, 2014; Osmanov and Rieger, 2009). Within this model, particles in the vicinity of the light cylinder can reach Lorentz factors as high as 5×10^7, easily accounting for the lower limit of 5×10^6 estimated in this work. Figure 8.17 shows the resulting photon spectrum obtained by Osmanov and Rieger (2017) assuming up-scattering of thermal photons by a power-law distribution of electrons with index $\alpha \sim 2.5$ in the Klein-Nishina regime. In Bogovalov et al. (2017), the distribution of electrons they assume is slightly softer ($\alpha \sim 3$) and only consider 1% of the rotational energy released in relativistic electrons, see Figure 8.18. Note that magneto-centrifugal models only take into account electrons moving on positively twisted lines, thus, only a fraction of the electrons present in the magnetosphere. Therefore, a full modelling of the pulsar magnetosphere it is crucial to properly assess the correct spectrum and the exact location of the emission.

Another approach in the context of the pulsar wind is presented by Mochol and Pétri (2015) and Mochol (2017). Particles accelerated in current sheets through magnetic reconnection emit synchrotron radiation that is upscattered by the same population of leptons giving rise to a SSC component at VHEs. The SSC component is the one producing the emission detected by MAGIC at TeV energies. As shown from the fits represented in Figure 8.19, Mochol (2017) suggest that the SSC emission detected is produced at small distances from the light cylinder ($< 2R_{LC}$) and foresees a cut-off at few TeVs due to radiative losses.

Concluding, magneto-centrifugal acceleration models (Osmanov and Rieger, 2017; Bogovalov et al., 2017) and striped wind models (Mochol and Pétri, 2015; Mochol, 2017), seem to be capable of explaining the TeV emission detected by MAGIC as IC scattering of thermal photons. However, predictions from these models for the γ-ray LCs remain to be seen.

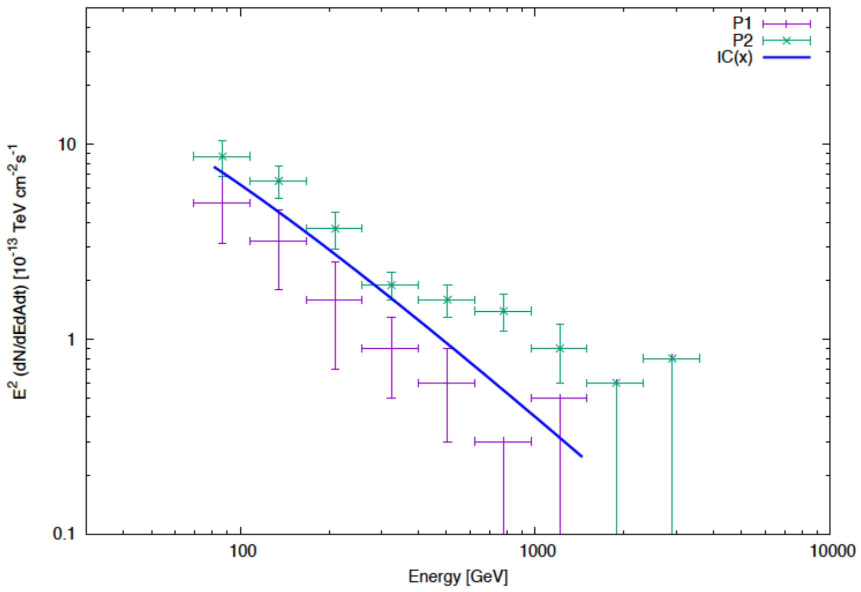

FIGURE 8.17: Energy spectrum of γ-rays produced as a result of IC scattering on thermal photons within the magneto-centrifugal acceleration model. MAGIC phase-resolved spectral points are represented in magenta (P1) and green (P2). From Osmanov and Rieger (2017).

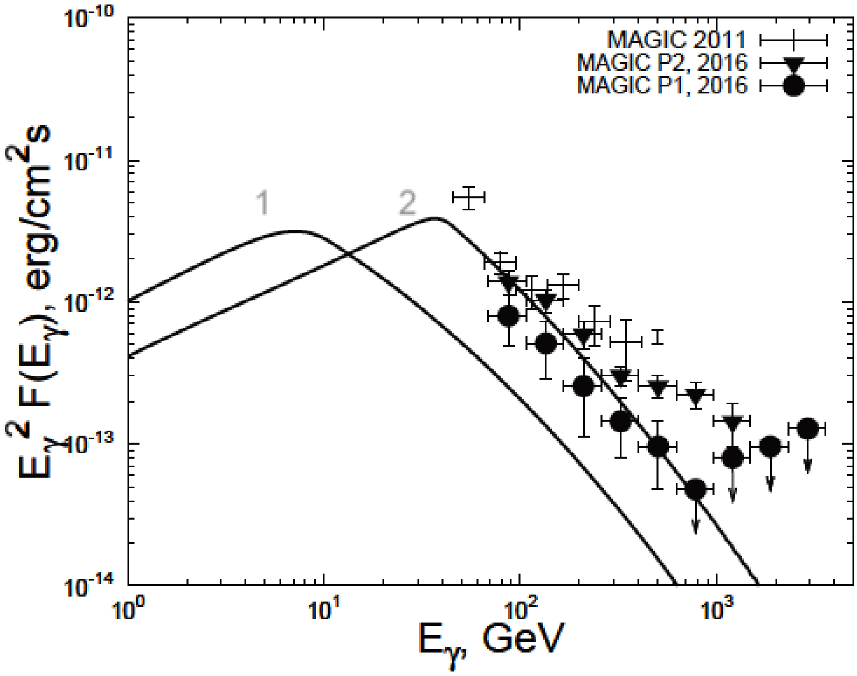

FIGURE 8.18: Energy spectra of γ-rays produced by electrons scattering on thermal photons from the surface. Magneto-centrifugal accelerated electrons have an assumed power-law distribution of $\alpha = 3$ and a low energy cut-off of 6 GeV (curve 1) and 30 GeV (curve 2). The fraction of spin-down luminosity carried away by relativistic electrons is of 1%. From Bogovalov et al. (2017).

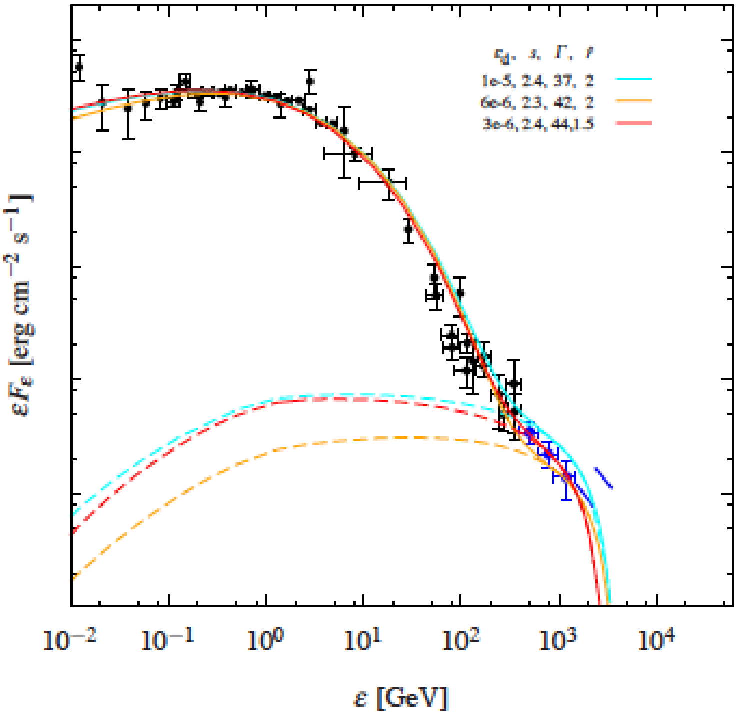

FIGURE 8.19: Spectral fits to the Crab spectrum up to ∼ 2 TeV. Black data points are extracted from Kuiper et al. (2001); Abdo et al. (2010c); Aleksić et al. (2014), while blue data points represent the last MAGIC measurements from this work and Ansoldi et al. (2016). Dashed lines show the SSC component whereas solid lines constitute the total spectrum, synchrotron plus SSC component. ϵ_d, s, Γ and $\hat{r}$ are the dissipation efficiency of magnetic energy into acceleration of particles, the particle index of the fit, the Lorentz factor of the wind and the distance from the light cylinder at which emission is produced, respectively. From Mochol (2017).

Conclusions

The work presented in this thesis covered the study of three sources belonging to two very different classes of astrophysical objects, SNRs and pulsars, observed with *Fermi*-LAT and MAGIC telescopes. The coverage of the gamma-ray domain above 60 MeV up to tens of TeV for Cas A, SNR G24.7+0.6 and the Crab Pulsar, allowed us to investigate them in their wider context.

The results of the Cas A observations are based on 158 hours of data gathered in dark and moonlight conditions with MAGIC telescopes between December 2014 and October 2016 and about 8 years of data collected with Fermi-LAT from August 2008 to December 2016. The derived spectrum of Cas A from 60 MeV to 10 TeV can be well described by a power-law with an exponential cut-off at $E_c = 3.5\,\binom{+1.6}{-1.0}_{stat}\binom{+0.8}{-0.9}_{sys}$ TeV with 4.6σ significance. This analysis provided the first measurement of a turn-off in the gamma-ray spectrum of this historical SNR. The GeV-TeV emission detected can be attributed to a population of accelerated protons with spectral index of ~ 2.2 and an energy cut-off at about 10 TeV. Such a modest acceleration of CRs implies that Cas A, at least at present, cannot account for the HE end ($\sim$PeV) of the Galactic CR spectrum. Considering that Cas A was the main PeVatron candidate, the results obtained in this work challenge the existence of SNRs as galactic Pevatrons and therefore the popular conviction that SNRs are the main source of Galactic CRs up to the *knee*.

On the other hand, observations of the FoV of the SNR G24.7+0.6 with MAGIC for a total of ∼31 hours resulted in a firm detection of two new VHE sources. The first one, MAGIC J1835–069, has been detected up to 5 TeV with a power-law spectrum of spectral index 2.7. Its spectral agreement with our LAT spectrum of FGES J1834.1–0706, associated to the radio source SNR G24.7+0.6, together with their slight overlapping position point to a common origin. The resulting LAT-MAGIC combined spectrum was found to be well described by a power-law with exponential cut-off at $E_c = 1.9 \pm 0.5$ TeV and can be interpreted as the result of proton-proton interaction between runaway protons from the SNR and the CO-rich surrounding. The second source, MAGIC J1837–073, coincident with 3FGL J1837.6–0717, is likely to be associated with a stellar cluster as suggested by its localization in a region rich in molecular content and crowded of sources. The total energy obtained in accelerated protons can be achieved by assuming a quasi-continuous injection of CRs during the cluster lifetime. Concluding, the observations of this complex region with MAGIC and LAT enlarged the known VHE population of stellar clusters and interacting SNRs, and allowed us to associate the VHE emission from MAGIC J1835–069 with the radio SNR G24.7+0.6.

Regarding the study of the Crab Pulsar carried out in this thesis, a large data sample of more than 300 hours of good quality data was collected with MAGIC during a period of seven years. This long term observation resulted in the first detection of very energetic pulsed emission from a pulsar, reaching up to about 1.5 TeV. The LC above 400 GeV shows two peaks (P1 and P2) synchronized with those measured at lower energies. The phase-resolved VHE spectra could be determined and were found to follow power-law functions with different photon indexes and maximum energies.

While the differential energy spectra of P1 has a photon index of $3.2 \pm 0.4_{stat} \pm 0.3_{syst}$ and has been measured up to 600 GeV, the spectrum of P2 is harder with an index of $2.9 \pm 0.2_{stat} \pm 0.3_{syst}$ and extends up to 1.5 TeV. At the low energy end, the MAGIC spectra connect smoothly with the LAT spectra measured above 10 GeV. The resulting LAT-MAGIC joint fit slightly differs from the MAGIC-only spectra, and both peaks are characterized by power-law functions of indexes 3.5 ± 0.1 (P1) and 3.0 ± 0.1 (P2). From the theoretical point of view, the extreme pulsed emission detected by MAGIC has to be produced by electrons with Lorentz factor of at least 5×10^6 scattering low energy photons in the vicinity of the light cylinder. Different scenarios have been proposed to explain where and how these electrons are accelerated and how the gamma-ray emission is produced, however, as of today, none of them is yet capable of reproducing at the same time the LC and the spectral shape for both peaks above 400 GeV.

Appendices

Appendix A

Fermi-LAT Monitoring tool

A.1 Introduction

Monitoring certain astrophysical sources is of extreme importance as they might undergo flaring states where their flux suddenly and unexpectedly increases. The capability to rapidly react to those outburst is crucial in order to activate follow-up MWL observations. For this purpose, the Universitat de Barcelona (UB) group developed a set of computing tools written in *bash*, *C++* and *python* that automatize the analysis of the latest data available in the *Fermi*-LAT Data Center and report any anomalous behavior of the observed source.

A.2 Design and Workflow

The UB monitoring tool, which came online in 2013, was designed to run the analysis automatically with no user contribution needed. The tool is activated on a daily basis at 12AM via *cronjob* and downloads the last 24 hours of data available of the source of interest. Usually, data taken the *Fermi* takes ∼12 hours to be transferred and processed by the LAT Operation Center before being available online, therefore, the dataset downloaded and used by the monitoring tool spans normally from 12AM to 12PM of the previous day.

Data downloaded are analyzed making use of the last version of the Fermi Science Tools available at the moment of the analysis following the analysis procedure seen in Chapter 3. Once the analysis is completed an email message is sent providing the flux, the detection significance and difference with respect to the long term mean flux of the source of interest. If the resulting parameters fulfill certain threshold values, based on TS or flux depending on the source of study, a flare alert is sent instead (see sample of the flare alert below).

| This is an automatically generated message at 2018-03-16 12:48:26 |

Crab **IS** flaring in GeV gamma-rays as seen by Fermi.

The flux calculated through a maximum likelihood analysis in the daily bin between 2018-03-15 00:00:02 and 2018-03-16 00:00:02 is $5.92864e-06 \pm 2.34216e-07$ with a 13.9989σ respect to the long term flux mean 2.64988e-06. Crab in the time bin calculated has a test statistic of $TS = 2664.8$.

The attached plots show the Fermi/LAT light curves for the last 31 and 365 days (1 day bins) along with the long term flux mean (dashed line).

For more information on the analysis contact Daniel Galindo (*dgalindo@fqa.ub.edu*).

The alert is redirected to people in charge of scheduling MAGIC observations that evaluate the interest and feasibility of a MWL observation. The daily/flare report is accompanied by two plots (Figure A.1 and A.2), to ease the evaluation and comparison of the daily result with previous days.

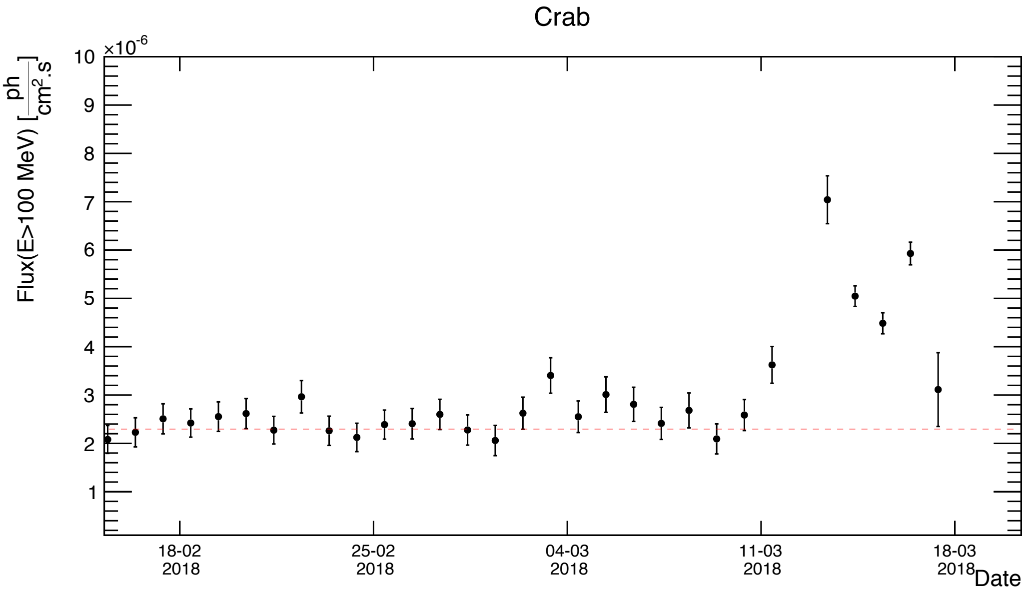

FIGURE A.1: Crab daily fluxes for the past month, computed on March 16, 2018.

A.3 Sources and Results

Currently, the tool is mainly monitoring 3 sources: Cygnus X-1, Cygnus X-3 and Crab. Nonetheless, it has also been used to study sources like PSR J2032+4127, that presented an increase of emission in November 2017, or V404 Cygni, that underwent a huge outburst in June 2015.

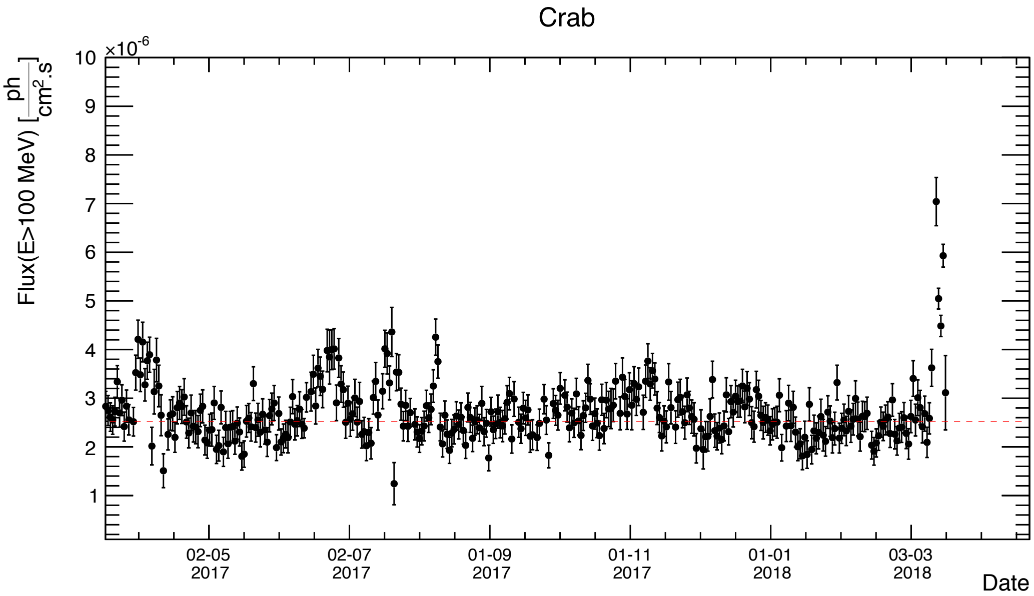

FIGURE A.2: Crab daily fluxes for the past year, computed on March 16, 2018.

For the case of the Crab, based on a flare criteria of 5σ increase between the flux detected and its long term mean flux, we were able to detect every single flare the source underwent and triggered MAGIC observations to look for possible contributions at higher energies. Figure A.3 shows the history of the monitoring analyses with flaring periods highlighted by red arrows as well as different published *ATels* related to our triggers. Flaring periods detected by the monitoring tool were also used to discard affected data from the Crab analysis reported in Chapter 8.

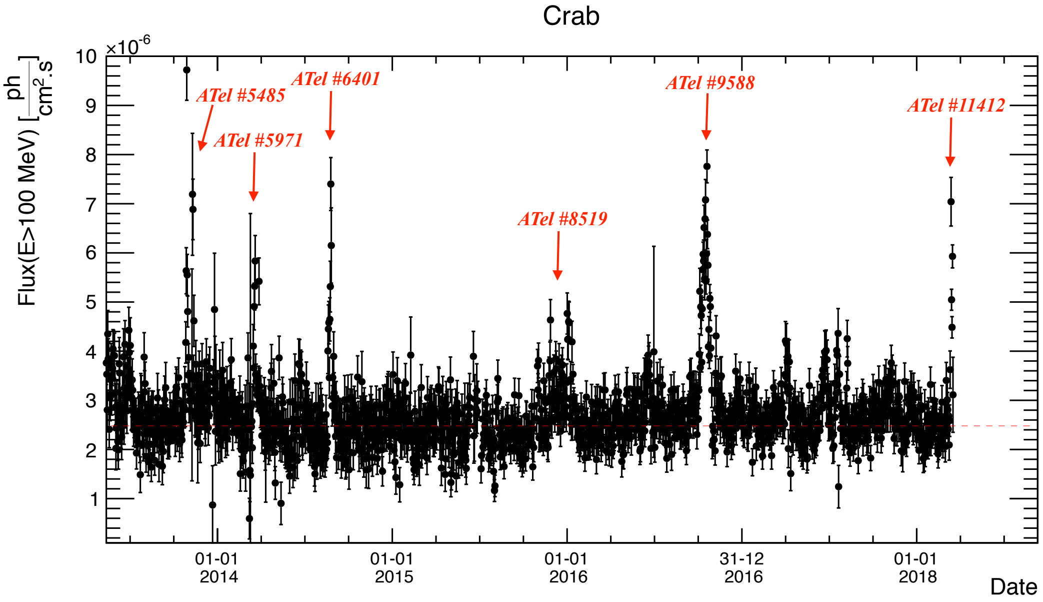

FIGURE A.3: History of the Crab daily fluxes since July 2003.

For both Cygnus sources, we based our flaring criteria on a minimum TS (in this case, TS=13 that corresponds to $\sim 4\sigma$) to assess the source is not on a normal state. This resulted in 2-3 alerts per year. Figure A.4 shows the daily evolution of the TS values starting on the first day of the mission, 5th August 2008, up to mid 2017. Various

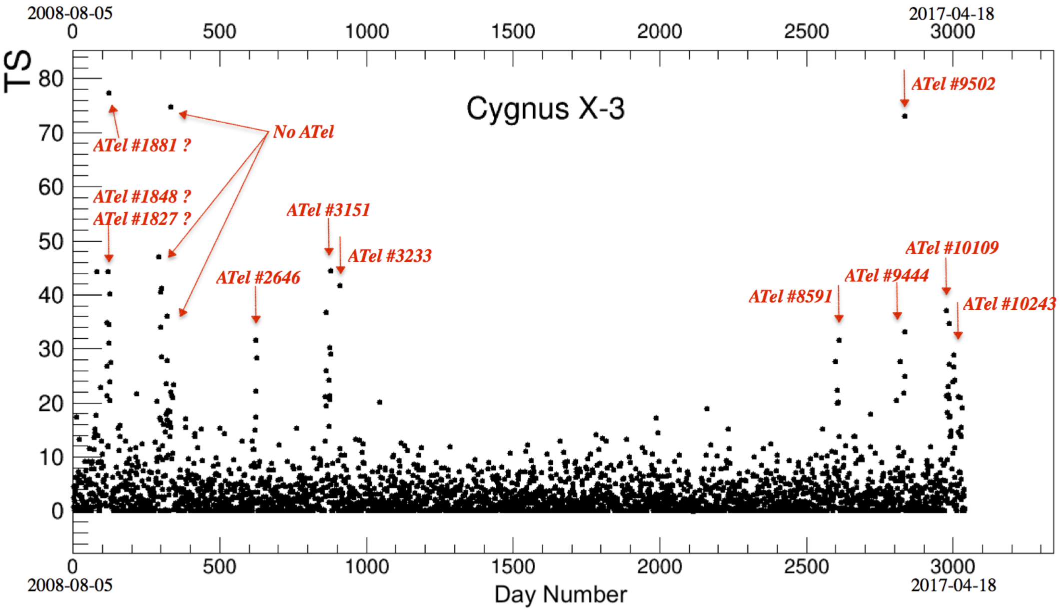

FIGURE A.4: History of the Cygnus X-3 daily Test Statistics since July 2003.

MAGIC observations were triggered by our alerts with no successful detection so far. Additionally, the daily data analyses and results obtained by the monitoring tool were used in Zanin et al. (2016) to report on the detection of GeV emission from Cygnus X-1 probing that the emission is most likely associated with the relativistic jets.

Acronyms

2FGL Second *Fermi*-LAT Source Catalog. 41, 90, 91, 133
3FGL Third *Fermi*-LAT Source Catalog. 41, 57, 67, 68, 70, 131, 132
3FHL Third Catalog of Hard *Fermi*-LAT Sources. 66

ACD Anticoincidence Detector. 38–40
AGN Active Galactic Nuclei. 14
AMC Active Mirror Control. 23

CGRO Compton Gamma-Ray Observatory. 37
CL Confidence Level. 57, 69, 71, 89, 94, 102–105, 134
CMB Cosmic Microwave Background. 4, 10, 13, 51, 62, 92
CR Cosmic Ray. 3–7, 13, 15, 38, 39, 41, 49, 51–56, 62–64, 69, 74–76, 113, 129
CTA Cherenkov Telescope Array. 64

DAQ Data Acquisition. 23, 26, 38, 39, 131
DSA Diffusive Shock Acceleration. 4, 14, 50

EAS Extensive Air Shower. 15, 16, 20, 21, 26, 31, 130
EDISP Energy Dispersion. 41, 57
EGRET Energetic Gamma-Ray Experiment Telescope. 37
EM Electromagnetic. 15–17, 19, 21, 28, 34, 129
EPWL Exponential Power-Law. 58–60, 72, 73, 132

FGES *Fermi*-LAT Galactic Extended Source Catalog. 66, 70, 72, 132
FIR Far Infrared. 56, 62, 92
FoV Field of View. 23, 38, 70, 73, 76, 113, 132
FS Forward Shock. 50, 56, 63
FWHM Full Width at Half Maximum. 101

GRB Gamma-Ray Burst. 14, 24

HAWC High-Altitude Water Cherenkov. 4, 67

HE High Energy. 7, 11, 13–15, 37, 39, 49, 64, 83, 104, 107, 113, 134

HEGRA High Energy Gamma Ray Astronomy. 55

HESS High Energy Stereoscopic System. 4, 21, 71, 73

HGPS Hess Galactic Plane Survey. 66, 67

HV High Voltage. 23, 24, 58

HWHM Half Width at Half Maximum. 95, 99, 134

IACT Imaging Atmospheric Cherenkov Telescope. 20–22, 55, 60

IC Inverse Compton. 8–10, 13, 14, 51, 55, 56, 62, 64, 87–90, 92, 93, 105–109, 129, 133, 135

ICRS International Celestial Reference System. 67, 70

INTEGRAL International Gamma-Ray Astrophysics Laboratory. 62

IR Infrared. 12, 20, 50, 65, 75, 89, 107, 131

IRF Instrument Response Function. 35, 40–42, 56, 67, 90

ISM Interstellar medium. 4, 10, 13, 50, 54

LAT Large Area Telescope. 37–43, 55–57, 60–62, 64–68, 70–76, 90–93, 98, 104, 105, 113, 114, 117, 127, 131–134

LC Light Curve. 83–85, 87, 90, 95–97, 99, 100, 107, 109, 113, 114, 127, 133, 134

LE Leading Edge. 96, 134

LUT Lookup Table. 26, 32, 94

M1 MAGIC-I. 22, 23, 30, 130

M2 MAGIC-II. 22–24, 30, 130

MAGIC Major Atmospheric Gamma-ray Imaging Cherenkov. 4, 15, 20–27, 31–33, 35, 36, 40, 55, 56, 58–64, 67, 69–76, 90, 93, 94, 98, 99, 102–107, 109, 111, 113, 114, 118–120, 127, 129–132, 134, 135

MARS Magic Analysis Reconstruction Software. 25, 69, 93

MC Molecular Cloud. 49–51, 53, 54, 65, 66, 131

MHD MagnetohydroDynamic. 82, 133

MSP Millisecond Pulsars. 81

MWL Multiwavelength. 73, 117, 118

NS Neutron Star. 13, 14, 49, 79–83, 85, 89

NSB Night Sky Background. 23–27, 58

OG Outer Gap. 84, 85, 133

P1 Main Pulse. 89–93, 95–105, 107, 109, 113, 114, 127, 134, 135

P2 Second Pulse. 89–93, 95, 97–105, 107, 109, 113, 114, 127, 134, 135

PC Polar Cap. 83–85, 133

PFF Pair Formation Front. 83

phe Photoelectron. 26, 27

PMT Photo Multiplier Tube. 23, 24, 58

PSF Point Spread Function. 35, 38, 40, 41, 43, 67, 68

PWN Pulsar Wind Nebula. 13, 50, 65, 73, 75

PWNe Pulsar Wind Nebulae. 13, 14, 75

RF Random Forest. 26, 31, 32, 94, 130

RMS Root Mean Square. 28, 101

ROI Region Of Interest. 42–44, 56, 57, 67, 90, 95, 131

RS Reverse Shock. 50, 56, 62

SED Spectral Energy Distribution. 44, 57–60, 62, 63, 71, 72, 92, 102–106, 108, 131–135

SG Slot Gap. 83–85, 133

SN Supernova. 13, 14, 49, 50, 52–55, 79, 89, 131

SNe Supernovae. 49, 50

SNR Supernova Remnant. 13, 49–56, 61, 65–67, 73, 75, 76, 113, 131

SSC Synchrotron-Self-Compton. 10, 87, 107, 109, 111, 135

SSD Silicon Strip Detector. 38, 39, 131

TE Trailing Edge. 96, 134

TS Test Statistic. 44, 57, 68, 117, 119, 120, 132

UB Universitat de Barcelona. 117

UL Upper Limit. 57, 65, 69, 71, 94, 102–104, 134

UV Ultra-Violet. 12, 15, 20, 23, 24, 107

VERITAS Very Energetic Radiation Imaging Telescope Array System. 4, 55, 99

VHE Very High Energy. 3, 8, 12–14, 25, 56, 62–64, 66, 71, 75, 87, 89, 90, 104–107, 109, 113, 134

VLA Very Large Array. 50, 56, 65, 131

List of Tables

List of Figures

Bibliography

B. P. Abbott et al. Gravitational Waves and Gamma-Rays from a Binary Neutron Star Merger: GW170817 and GRB 170817A. *Astrophysical Journal, Letters*, 848: L13, October 2017. doi: 10.3847/2041-8213/aa920c. URL `http://adsabs.harvard.edu/abs/2017ApJ...848L..13A`.

H. Abdalla et al. The population of TeV pulsar wind nebulae in the H.E.S.S. Galactic Plane Survey. *ArXiv e-prints*, February 2017. URL `http://adsabs.harvard.edu/abs/2017arXiv170208280H`.

H. Abdalla et al. The H.E.S.S. Galactic plane survey. *Astronomy and Astrophysics*, 612: A1, April 2018. doi: 10.1051/0004-6361/201732098. URL `http://adsabs.harvard.edu/abs/2018A%26A...612A...1H`.

A. A. Abdo et al. Fermi-Lat Discovery of GeV Gamma-Ray Emission from the Young Supernova Remnant Cassiopeia A. *Astrophysical Journal, Letters*, 710:L92–L97, February 2010a. doi: 10.1088/2041-8205/710/1/L92. URL `http://adsabs.harvard.edu/abs/2010ApJ...710L..92A`.

A. A. Abdo et al. Observation of Supernova Remnant IC 443 with the Fermi Large Area Telescope. *Astrophysical Journal*, 712:459–468, March 2010b. doi: 10.1088/0004-637X/712/1/459. URL `http://adsabs.harvard.edu/abs/2010ApJ...712..459A`.

A. A. Abdo et al. Fermi Large Area Telescope Observations of the Crab Pulsar And Nebula. *Astrophysical Journal*, 708:1254–1267, January 2010c. doi: 10.1088/0004-637X/708/2/1254. URL `http://adsabs.harvard.edu/abs/2010ApJ...708.1254A`.

A. A. Abdo et al. Observations of the Young Supernova Remnant RX J1713.7-3946 with the Fermi Large Area Telescope. *Astrophysical Journal*, 734:28, June 2011. doi: 10.1088/0004-637X/734/1/28. URL `http://adsabs.harvard.edu/abs/2011ApJ...734...28A`.

A. A. Abdo et al. The Second Fermi Large Area Telescope Catalog of Gamma-Ray Pulsars. *Astrophysical Journal Supplement Series*, 208:17, October 2013. doi: 10.1088/0067-0049/208/2/17. URL `http://adsabs.harvard.edu/abs/2013ApJS..208...17A`.

A. U. Abeysekara et al. The 2HWC HAWC Observatory Gamma-Ray Catalog. *Astrophysical Journal*, 843:40, July 2017. doi: 10.3847/1538-4357/aa7556. URL `http://adsabs.harvard.edu/abs/2017ApJ...843...40A`.

J. Abraham et al. Properties and performance of the prototype instrument for the Pierre Auger Observatory. *Nuclear Instruments and Methods in Physics Research A*, 523:50–95, May 2004. doi: 10.1016/j.nima.2003.12.012. URL `http://adsabs.harvard.edu/abs/2004NIMPA.523...50A`.

A. Abramowski et al. Acceleration of petaelectronvolt protons in the Galactic Centre. *Nature*, 531:476–479, March 2016. doi: 10.1038/nature17147. URL `http://adsabs.harvard.edu/abs/2016Natur.531..476H`.

F. Acero et al. Detection of Gamma Rays from a Starburst Galaxy. *Science*, 326:1080, November 2009. doi: 10.1126/science.1178826. URL `http://adsabs.harvard.edu/abs/2009Sci...326.1080A`.

F. Acero et al. Fermi Large Area Telescope Third Source Catalog. *Astrophysical Journal Supplement Series*, 218:23, June 2015. doi: 10.1088/0067-0049/218/2/23. URL `http://adsabs.harvard.edu/abs/2015ApJS..218...23A`.

F. Acero et al. Development of the Model of Galactic Interstellar Emission for Standard Point-source Analysis of Fermi Large Area Telescope Data. *Astrophysical Journal Supplement Series*, 223:26, April 2016a. doi: 10.3847/0067-0049/223/2/26. URL `http://adsabs.harvard.edu/abs/2016ApJS..223...26A`.

F. Acero et al. The First Fermi LAT Supernova Remnant Catalog. *Astrophysical Journal Supplement Series*, 224:8, May 2016b. doi: 10.3847/0067-0049/224/1/8. URL `http://adsabs.harvard.edu/abs/2016ApJS..224....8A`.

M. Ackermann et al. A Cocoon of Freshly Accelerated Cosmic Rays Detected by Fermi in the Cygnus Superbubble. *Science*, 334:1103, November 2011. doi: 10.1126/science.1210311. URL `http://adsabs.harvard.edu/abs/2011Sci...334.1103A`.

M. Ackermann et al. Search for gamma-ray spectral lines with the Fermi Large Area Telescope and dark matter implications. *Physical Review D*, 88(8):082002, October 2013a. doi: 10.1103/PhysRevD.88.082002. URL `http://adsabs.harvard.edu/abs/2013PhRvD..88h2002A`.

M. Ackermann et al. Detection of the Characteristic Pion-Decay Signature in Supernova Remnants. *Science*, 339:807–811, February 2013b. doi: 10.1126/science.1231160. URL `http://adsabs.harvard.edu/abs/2013Sci...339..807A`.

M. Ackermann et al. 2FHL: The Second Catalog of Hard Fermi-LAT Sources. *Astrophysical Journal Supplement Series*, 222:5, January 2016. doi: 10.3847/0067-0049/222/1/5. URL `http://adsabs.harvard.edu/abs/2016ApJS..222....5A`.

M. Ackermann et al. Search for Extended Sources in the Galactic Plane Using Six Years of Fermi-Large Area Telescope Pass 8 Data above 10 GeV. *Astrophysical Journal*, 843:139, July 2017. doi: 10.3847/1538-4357/aa775a. URL `http://adsabs.harvard.edu/abs/2017ApJ...843..139A`.

M. Actis et al. Design concepts for the Cherenkov Telescope Array CTA: an advanced facility for ground-based high-energy gamma-ray astronomy. *Experimental Astronomy*, 32:193–316, December 2011. doi: 10.1007/s10686-011-9247-0. URL `http://adsabs.harvard.edu/abs/2011ExA....32..193A`.

P. A. R. Ade et al. Planck 2013 results. XXVIII. The Planck Catalogue of Compact Sources. *Astronomy and Astrophysics*, 571:A28, November 2014. doi: 10.1051/0004-6361/201321524. URL `http://adsabs.harvard.edu/abs/2014A%26A...571A..28P`.

F. Aharonian et al. Evidence for TeV gamma ray emission from Cassiopeia A. *Astronomy and Astrophysics*, 370:112–120, April 2001. doi: 10.1051/0004-6361:20010243. URL `http://adsabs.harvard.edu/abs/2001A%26A...370..112A`.

F. Aharonian et al. A New Population of Very High Energy Gamma-Ray Sources in the Milky Way. *Science*, 307:1938–1942, March 2005. doi: 10.1126/science.1108643. URL `http://adsabs.harvard.edu/abs/2005Sci...307.1938A`.

F. Aharonian et al. The H.E.S.S. Survey of the Inner Galaxy in Very High Energy Gamma Rays. *Astrophysical Journal*, 636:777–797, January 2006. doi: 10.1086/498013. URL `http://adsabs.harvard.edu/abs/2006ApJ...636..777A`.

F. Aharonian et al. High energy astrophysics with ground-based gamma ray detectors. *Reports on Progress in Physics*, 71(9):096901, September 2008. doi: 10.1088/0034-4885/71/9/096901. URL `http://adsabs.harvard.edu/abs/2008RPPh...71i6901A`.

F. A. Aharonian. *Very high energy cosmic gamma radiation : a crucial window on the extreme Universe*. World Scientific Publishing Co, 2004. doi: 10.1142/4657. URL `http://adsabs.harvard.edu/abs/2004vhec.book.....A`.

F. A. Aharonian and A. M. Atoyan. On the emissivity of πˆ0ˆ-decay gamma radiation in the vicinity of accelerators of galactic cosmic rays. *Astronomy and Astrophysics*, 309:917–928, May 1996. URL `http://adsabs.harvard.edu/abs/1996A%26A...309..917A`.

F. A. Aharonian, S. R. Kelner, and A. Y. Prosekin. Angular, spectral, and time distributions of highest energy protons and associated secondary gamma rays and neutrinos propagating through extragalactic magnetic and radiation fields. *Physical Review D*, 82(4):043002, August 2010. doi: 10.1103/PhysRevD.82.043002. URL `http://adsabs.harvard.edu/abs/2010PhRvD..82d3002A`.

F. A. Aharonian, S. V. Bogovalov, and D. Khangulyan. Abrupt acceleration of a 'cold' ultrarelativistic wind from the Crab pulsar. *Nature*, 482:507–509, February 2012. doi: 10.1038/nature10793. URL `http://adsabs.harvard.edu/abs/2012Natur.482..507A`.

M. L. Ahnen et al. Performance of the MAGIC telescopes under moonlight. *Astroparticle Physics*, 94:29–41, September 2017. doi: 10.1016/j.astropartphys.2017.08.001. URL `http://adsabs.harvard.edu/abs/2017APh....94...29A`.

M. Ajello et al. 3FHL: The Third Catalog of Hard Fermi-LAT Sources. *Astrophysical Journal Supplement Series*, 232:18, October 2017. doi: 10.3847/1538-4365/aa8221. URL `http://adsabs.harvard.edu/abs/2017ApJS..232...18A`.

J. Albert et al. Observation of VHE γ-rays from Cassiopeia A with the MAGIC telescope. *Astronomy and Astrophysics*, 474:937–940, November 2007a. doi: 10.1051/0004-6361:20078168. URL `http://adsabs.harvard.edu/abs/2007A%26A...474..937A`.

J. Albert et al. Unfolding of differential energy spectra in the MAGIC experiment. *Nuclear Instruments and Methods in Physics Research A*, 583:494–506, December 2007b. doi: 10.1016/j.nima.2007.09.048. URL `http://adsabs.harvard.edu/abs/2007NIMPA.583..494A`.

J. Albert et al. Implementation of the Random Forest method for the Imaging Atmospheric Cherenkov Telescope MAGIC. *Nuclear Instruments and Methods in Physics Research A*, 588:424–432, April 2008. doi: 10.1016/j.nima.2007.11.068. URL `http://adsabs.harvard.edu/abs/2008NIMPA.588..424A`.

J. Aleksić et al. Observations of the Crab Pulsar between 25 and 100 GeV with the MAGIC I Telescope. *Astrophysical Journal*, 742:43, November 2011. doi: 10.1088/0004-637X/742/1/43. URL `http://adsabs.harvard.edu/abs/2011ApJ...742...43A`.

J. Aleksić et al. Phase-resolved energy spectra of the Crab pulsar in the range of 50-400 GeV measured with the MAGIC telescopes. *Astronomy and Astrophysics*, 540:A69, April 2012a. doi: 10.1051/0004-6361/201118166. URL `http://adsabs.harvard.edu/abs/2012A%26A...540A..69A`.

J. Aleksić et al. Performance of the MAGIC stereo system obtained with Crab Nebula data. *Astroparticle Physics*, 35:435–448, February 2012b. doi: 10.1016/j.astropartphys.2011.11.007. URL `http://adsabs.harvard.edu/abs/2012APh....35..435A`.

J. Aleksić et al. Detection of bridge emission above 50 GeV from the Crab pulsar with the MAGIC telescopes. *Astronomy and Astrophysics*, 565:L12, May 2014. doi: 10.1051/0004-6361/201423664. URL `http://adsabs.harvard.edu/abs/2014A%26A...565L..12A`.

J. Aleksić et al. Measurement of the Crab Nebula spectrum over three decades in energy with the MAGIC telescopes. *Journal of High Energy Astrophysics*, 5:30–38, March 2015. doi: 10.1016/j.jheap.2015.01.002. URL `http://adsabs.harvard.edu/abs/2015JHEAp...5...30A`.

J. Aleksić et al. The major upgrade of the MAGIC telescopes, Part I: The hardware improvements and the commissioning of the system. *Astroparticle Physics*, 72:61–75, January 2016a. doi: 10.1016/j.astropartphys.2015.04.004. URL `http://adsabs.harvard.edu/abs/2016APh....72...61A`.

J. Aleksić et al. The major upgrade of the MAGIC telescopes, Part II: A performance study using observations of the Crab Nebula. *Astroparticle Physics*, 72:76–94, January 2016b. doi: 10.1016/j.astropartphys.2015.02.005. URL `http://adsabs.harvard.edu/abs/2016APh....72...76A`.

E. Aliu et al. Observation of Pulsed γ-Rays Above 25 GeV from the Crab Pulsar with MAGIC. *Science*, 322:1221–, November 2008. doi: 10.1126/science.1164718. URL `http://adsabs.harvard.edu/abs/2008Sci...322.1221A`.

E. Aliu et al. Improving the performance of the single-dish Cherenkov telescope MAGIC through the use of signal timing. *Astroparticle Physics*, 30:293–305, January 2009. doi: 10.1016/j.astropartphys.2008.10.003. URL `http://adsabs.harvard.edu/abs/2009APh....30..293A`.

E. Aliu et al. Detection of Pulsed Gamma Rays Above 100 GeV from the Crab Pulsar. *Science*, 334:69–, October 2011. doi: 10.1126/science.1208192. URL `http://adsabs.harvard.edu/abs/2011Sci...334...69V`.

R. J. Allen and A. H. Barrett. Absolute Measurements of the Radio Flux from Cassiopeia a and Taurus a at 3.64 and 1.94 CM. *Astrophysical Journal*, 149:1, July 1967. doi: 10.1086/149224. URL `http://adsabs.harvard.edu/abs/1967ApJ...149....1A`.

M. A. Alpar et al. A new class of radio pulsars. *Nature*, 300:728–730, December 1982. doi: 10.1038/300728a0. URL `http://adsabs.harvard.edu/abs/1982Natur.300..728A`.

M. Anderson et al. Relativistic electron populations in Cassiopeia A. *Astrophysical Journal*, 373:146–157, May 1991. doi: 10.1086/170033. URL `http://adsabs.harvard.edu/abs/1991ApJ...373..146A`.

M. C. Anderson and L. Rudnick. The deceleration powering of synchrotron emission from ejecta components in supernova remnant Cassiopeia A. *Astrophysical Journal*, 441:307–333, March 1995. doi: 10.1086/175357. URL `http://adsabs.harvard.edu/abs/1995ApJ...441..307A`.

S. Ansoldi et al. Teraelectronvolt pulsed emission from the Crab Pulsar detected by MAGIC. *Astronomy and Astrophysics*, 585:A133, January 2016. doi: 10.1051/0004-6361/201526853. URL `http://adsabs.harvard.edu/abs/2016A%26A...585A.133A`.

V. B. Anykeyev, A. A. Spiridonov, and V. P. Zhigunov. Comparative investigation of unfolding methods. *Nuclear Instruments and Methods in Physics Research A*, 303:350–369, June 1991. doi: 10.1016/0168-9002(91)90802-W. URL `http://adsabs.harvard.edu/abs/1991NIMPA.303..350A`.

R. F. Archibald et al. On the Braking Index of the Unusual High-B Rotation-Powered Pulsar PSR J1846-0258. *Astrophysical Journal*, 810:67, September 2015. doi: 10.1088/0004-637X/810/1/67. URL `http://adsabs.harvard.edu/abs/2015ApJ...810...67A`.

J. Arons. Pair creation above pulsar polar caps - Geometrical structure and energetics of slot gaps. *Astrophysical Journal*, 266:215–241, March 1983. doi: 10.1086/160771. URL `http://adsabs.harvard.edu/abs/1983ApJ...266..215A`.

J. Arons and E. T. Scharlemann. Pair formation above pulsar polar caps - Structure of the low altitude acceleration zone. *Astrophysical Journal*, 231:854–879, August 1979. doi: 10.1086/157250. URL `http://adsabs.harvard.edu/abs/1979ApJ...231..854A`.

A. M. Atoyan et al. On energy-dependent propagation effects and acceleration sites of relativistic electrons in Cassiopeia A. *Astronomy and Astrophysics*, 354:915–930, February 2000a. URL `http://adsabs.harvard.edu/abs/2000A%26A...354..915A`.

A. M. Atoyan et al. On the gamma-ray fluxes expected from Cassiopeia A. *Astronomy and Astrophysics*, 355:211–220, March 2000b. URL `http://adsabs.harvard.edu/abs/2000A%26A...355..211A`.

W. Atwood et al. Pass 8: Toward the Full Realization of the Fermi-LAT Scientific Potential. *ArXiv e-prints*, March 2013. URL `http://adsabs.harvard.edu/abs/2013arXiv1303.3514A`.

W. B. Atwood et al. The Large Area Telescope on the Fermi Gamma-Ray Space Telescope Mission. *Astrophysical Journal*, 697:1071–1102, June 2009. doi: 10.1088/0004-637X/697/2/1071. URL `http://adsabs.harvard.edu/abs/2009ApJ...697.1071A`.

M. G. Baring. High-energy emission from pulsars: the polar cap scenario. *Advances in Space Research*, 33:552–560, 2004. doi: 10.1016/j.asr.2003.08.020. URL `http://adsabs.harvard.edu/abs/2004AdSpR..33..552B`.

M. G. Baring et al. Radio to Gamma-Ray Emission from Shell-Type Supernova Remnants: Predictions from Nonlinear Shock Acceleration Models. *Astrophysical*

Journal, 513:311–338, March 1999. doi: 10.1086/306829. URL http://adsabs.harvard.edu/abs/1999ApJ...513..311B.

W. Becker and G. Pavlov. *Pulsars and isolated neutron stars*, page 721. Kluwer Academic Publishers, 2002. URL http://adsabs.harvard.edu/abs/2002css1.book..721B.

W. Bednarek. On the origin of sub-TeV gamma-ray pulsed emission from rotating neutron stars. *Monthly Notices of the Royal Astronomical Society*, 424:2079–2085, August 2012. doi: 10.1111/j.1365-2966.2012.21354.x. URL http://adsabs.harvard.edu/abs/2012MNRAS.424.2079B.

A. R. Bell. The acceleration of cosmic rays in shock fronts. I. *Monthly Notices of the Royal Astronomical Society*, 182:147–156, January 1978a. doi: 10.1093/mnras/182.2.147. URL http://adsabs.harvard.edu/abs/1978MNRAS.182..147B.

A. R. Bell. The acceleration of cosmic rays in shock fronts. II. *Monthly Notices of the Royal Astronomical Society*, 182:443–455, February 1978b. doi: 10.1093/mnras/182.3.443. URL http://adsabs.harvard.edu/abs/1978MNRAS.182..443B.

A. R. Bell. Turbulent amplification of magnetic field and diffusive shock acceleration of cosmic rays. *Monthly Notices of the Royal Astronomical Society*, 353:550–558, September 2004. doi: 10.1111/j.1365-2966.2004.08097.x. URL http://adsabs.harvard.edu/abs/2004MNRAS.353..550B.

A. R. Bell. Cosmic ray acceleration. *Astroparticle Physics*, 43:56–70, March 2013. doi: 10.1016/j.astropartphys.2012.05.022. URL http://adsabs.harvard.edu/abs/2013APh....43...56B.

A. R. Bell and S. G. Lucek. Cosmic ray acceleration to very high energy through the non-linear amplification by cosmic rays of the seed magnetic field. *Monthly Notices of the Royal Astronomical Society*, 321:433–438, March 2001. doi: 10.1046/j.1365-8711.2001.04063.x. URL http://adsabs.harvard.edu/abs/2001MNRAS.321..433B.

E. G. Berezhko, G. Pühlhofer, and H. J. Völk. Gamma-ray emission from Cassiopeia A produced by accelerated cosmic rays. *Astronomy and Astrophysics*, 400:971–980, March 2003. doi: 10.1051/0004-6361:20030033. URL http://adsabs.harvard.edu/abs/2003A%26A...400..971B.

J. Beringer et al. Review of Particle Physics. *Physical Review D*, 86(1):010001, July 2012. doi: 10.1103/PhysRevD.86.010001. URL http://adsabs.harvard.edu/abs/2012PhRvD..86a0001B.

M. Bertero. Linear inverse and ill-posed problems. volume 75, pages 1–120. Academic Press, New York, 1989.

V. S. Beskin, S. V. Chernov, C. R. Gwinn, and A. A. Tchekhovskoy. Radio Pulsars. *Space Science Reviews*, 191:207–237, October 2015. doi: 10.1007/s11214-015-0173-8. URL http://adsabs.harvard.edu/abs/2015SSRv..191..207B.

S. V. Bogovalov. Magnetocentrifugal acceleration of bulk motion of plasma in pulsar magnetosphere. *Monthly Notices of the Royal Astronomical Society*, 443:2197–2203, September 2014. doi: 10.1093/mnras/stu1283. URL http://adsabs.harvard.edu/abs/2014MNRAS.443.2197B.

S. V. Bogovalov and F. A. Aharonian. Very-high-energy gamma radiation associated with the unshocked wind of the Crab pulsar. *Monthly Notices of the Royal Astronomical Society*, 313:504–514, April 2000. doi: 10.1046/j.1365-8711.2000.03250.x. URL `http://adsabs.harvard.edu/abs/2000MNRAS.313..504B`.

S. V. Bogovalov, F. Aharonian, and D. Khangulyan. Formation of the pulsed TeV gamma-ray emission at the light cylinder. In *6th International Symposium on High Energy Gamma-Ray Astronomy*, volume 1792 of *American Institute of Physics Conference Series*, page 040010, January 2017. doi: 10.1063/1.4968914. URL `http://adsabs.harvard.edu/abs/2017AIPC.1792d0010B`.

S. Y. Braude et al. The spectra of discrete radio sources at decametric wavelengths-I. *Monthly Notices of the Royal Astronomical Society*, 143:289, 1969. doi: 10.1093/mnras/143.3.289. URL `http://adsabs.harvard.edu/abs/1969MNRAS.143..289B`.

T. Bretz et al. Comparison of On-Off and Wobble mode observations for MAGIC. *International Cosmic Ray Conference*, 4:311, 2005. URL `http://adsabs.harvard.edu/abs/2005ICRC....4..311B`.

T. Bretz et al. The drive system of the major atmospheric gamma-ray imaging Cherenkov telescope. *Astroparticle Physics*, 31:92–101, March 2009. doi: 10.1016/j.astropartphys.2008.12.001. URL `http://adsabs.harvard.edu/abs/2009APh....31...92B`.

N. Chamel et al. On the Maximum Mass of Neutron Stars. *International Journal of Modern Physics E*, 22:1330018, July 2013. doi: 10.1142/S021830131330018X. URL `http://adsabs.harvard.edu/abs/2013IJMPE..2230018C`.

K. S. Cheng, C. Ho, and M. Ruderman. Energetic radiation from rapidly spinning pulsars. I - Outer magnetosphere gaps. II - VELA and Crab. *Astrophysical Journal*, 300:500–539, January 1986. doi: 10.1086/163829. URL `http://adsabs.harvard.edu/abs/1986ApJ...300..500C`.

K. S. Cheng, M. Ruderman, and L. Zhang. A Three-dimensional Outer Magnetospheric Gap Model for Gamma-Ray Pulsars: Geometry, Pair Production, Emission Morphologies, and Phase-resolved Spectra. *Astrophysical Journal*, 537:964–976, July 2000. doi: 10.1086/309051. URL `http://adsabs.harvard.edu/abs/2000ApJ...537..964C`.

R. A. Chevalier. Supernova Remnants in Molecular Clouds. *Astrophysical Journal*, 511:798–811, February 1999. doi: 10.1086/306710. URL `http://adsabs.harvard.edu/abs/1999ApJ...511..798C`.

F. V. Coroniti. Magnetically striped relativistic magnetohydrodynamic winds - The Crab Nebula revisited. *Astrophysical Journal*, 349:538–545, February 1990. doi: 10.1086/168340. URL `http://adsabs.harvard.edu/abs/1990ApJ...349..538C`.

R. Cowsik and S. Sarkar. A lower limit to the magnetic field in Cassiopeia-A. *Monthly Notices of the Royal Astronomical Society*, 191:855–861, June 1980. doi: 10.1093/mnras/191.4.855. URL `http://adsabs.harvard.edu/abs/1980MNRAS.191..855C`.

J. K. Daugherty and A. K. Harding. Gamma-Ray Pulsars: Emission from Extended Polar CAP Cascades. *Astrophysical Journal*, 458:278, February 1996. doi: 10.1086/176811. URL `http://adsabs.harvard.edu/abs/1996ApJ...458..278D`.

O. C. de Jager, B. C. Raubenheimer, and J. W. H. Swanepoel. A poweful test for weak periodic signals with unknown light curve shape in sparse data. *Astronomy* *and Astrophysics*, 221:180–190, August 1989. URL `http://adsabs.harvard.edu/abs/1989A%26A...221..180D`.

C. Deil et al. The H.E.S.S. Galactic plane survey. In *34th International Cosmic Ray Conference (ICRC2015)*, volume 34 of *International Cosmic Ray Conference*, page 773, July 2015. URL `http://adsabs.harvard.edu/abs/2015ICRC...34..773D`.

T. DeLaney and L. Rudnick. The First Measurement of Cassiopeia A's Forward Shock Expansion Rate. *Astrophysical Journal*, 589:818–826, June 2003. doi: 10.1086/374813. URL `http://adsabs.harvard.edu/abs/2003ApJ...589..818D`.

C. D. Dermer. Secondary production of neutral pi-mesons and the diffuse galactic gamma radiation. *Astronomy and Astrophysics*, 157:223–229, March 1986. URL `http://adsabs.harvard.edu/abs/1986A%26A...157..223D`.

A. J. Deutsch. The electromagnetic field of an idealized star in rigid rotation in vacuo. *Annales d'Astrophysique*, 18:1, January 1955. URL `http://adsabs.harvard.edu/abs/1955AnAp...18....1D`.

A. Djannati-Atai et al. H.E.S.S. stereoscopic observations of the Vela Pulsar above 100 GeV. *In preparation*, 2017.

S. Doe et al. Developing Sherpa with Python. In R. A. Shaw, F. Hill, and D. J. Bell, editors, *Astronomical Data Analysis Software and Systems XVI*, volume 376 of *Astronomical Society of the Pacific Conference Series*, page 543, October 2007. URL `http://adsabs.harvard.edu/abs/2007ASPC..376..543D`.

L. O. Drury. An introduction to the theory of diffusive shock acceleration of energetic particles in tenuous plasmas. *Reports on Progress in Physics*, 46:973–1027, August 1983. doi: 10.1088/0034-4885/46/8/002. URL `http://adsabs.harvard.edu/abs/1983RPPh...46..973D`.

D. Ferenc et al. The MAGIC gamma-ray observatory. *Nuclear Instruments and Methods in Physics Research A*, 553:274–281, November 2005. doi: 10.1016/j.nima.2005.08.085. URL `http://adsabs.harvard.edu/abs/2005NIMPA.553..274F`.

E. Fermi. On the Origin of the Cosmic Radiation. *Physical Review*, 75:1169–1174, April 1949. doi: 10.1103/PhysRev.75.1169. URL `http://adsabs.harvard.edu/abs/1949PhRv...75.1169F`.

J. M. Fierro et al. Phase-resolved Studies of the High-Energy Gamma-Ray Emission from the Crab, Geminga, and VELA Pulsars. *Astrophysical Journal*, 494:734–746, February 1998. doi: 10.1086/305219. URL `http://adsabs.harvard.edu/abs/1998ApJ...494..734F`.

V. P. Fomin et al. New methods of atmospheric Cherenkov imaging for gamma-ray astronomy. I. The false source method. *Astroparticle Physics*, 2:137–150, May 1994. doi: 10.1016/0927-6505(94)90036-1. URL `http://adsabs.harvard.edu/abs/1994APh.....2..137F`.

P. Freeman, S. Doe, and A. Siemiginowska. Sherpa: a mission-independent data analysis application. In J.-L. Starck and F. D. Murtagh, editors, *Astronomical Data Analysis*, volume 4477 of *Proceedings of the International Society for Optical Engineering*, pages 76–87, November 2001. doi: 10.1117/12.447161. URL `http://adsabs.harvard.edu/abs/2001SPIE.4477...76F`.

S. Gabici. Gamma-ray emission from supernova remnants and surrounding molecular clouds. In *6th International Symposium on High Energy Gamma-Ray Astronomy*, volume 1792 of *American Institute of Physics Conference Series*, page 020002, January 2017. doi: 10.1063/1.4968887. URL `http://adsabs.harvard.edu/abs/2017AIPC.1792b0002G`.

S. Gabici and F. A. Aharonian. Searching for Galactic Cosmic-Ray Pevatrons with Multi-TeV Gamma Rays and Neutrinos. *Astrophysical Journal, Letters*, 665:L131–L134, August 2007. doi: 10.1086/521047. URL `http://adsabs.harvard.edu/abs/2007ApJ...665L.131G`.

S. Gabici, F. A. Aharonian, and P. Blasi. Gamma rays from molecular clouds. *Astronomy and Astrophysics, Supplement*, 309:365–371, June 2007. doi: 10.1007/s10509-007-9427-6. URL `http://adsabs.harvard.edu/abs/2007Ap%26SS.309..365G`.

B. M. Gaensler and P. O. Slane. The Evolution and Structure of Pulsar Wind Nebulae. *Annual Review of Astron and Astrophys*, 44:17–47, September 2006. doi: 10.1146/annurev.astro.44.051905.092528. URL `http://adsabs.harvard.edu/abs/2006ARA%26A..44...17G`.

G. Giavitto. Oserving the VHE Gamma Ray Sky with the MAGIC Telescopes: the Blazar B3 2247+381 and the Crab Pulsar, PhD. thesis. 2013.

C. Gini. Measurement of inequality of incomes. *The Economic Journal*, 31:22, 1921.

P. Goldreich and W. H. Julian. Pulsar Electrodynamics. *Astrophysical Journal*, 157:869, August 1969. doi: 10.1086/150119. URL `http://adsabs.harvard.edu/abs/1969ApJ...157..869G`.

E. V. Gotthelf and J. P. Halpern. Discovery of a Young, Energetic 70.5 ms Pulsar Associated with the TeV Gamma-Ray Source HESS J1837-069. *Astrophysical Journal*, 681:515-521, July 2008. doi: 10.1086/588779. URL `http://adsabs.harvard.edu/abs/2008ApJ...681..515G`.

E. V. Gotthelf et al. Chandra Detection of the Forward and Reverse Shocks in Cassiopeia A. *Astrophysical Journal, Letters*, 552:L39–L43, May 2001. doi: 10.1086/320250. URL `http://adsabs.harvard.edu/abs/2001ApJ...552L..39G`.

B. W. Grefenstette et al. Locating the Most Energetic Electrons in Cassiopeia A. *Astrophysical Journal*, 802:15, March 2015. doi: 10.1088/0004-637X/802/1/15. URL `http://adsabs.harvard.edu/abs/2015ApJ...802...15G`.

K. Greisen. End to the Cosmic-Ray Spectrum? *Physical Review Letters*, 16:748–750, April 1966. doi: 10.1103/PhysRevLett.16.748. URL `http://adsabs.harvard.edu/abs/1966PhRvL..16..748G`.

I. A. Grenier and A. K. Harding. Pulsar twinkling and relativity. In J.-M. Alimi and A. Füzfa, editors, *Albert Einstein Century International Conference*, volume 861 of *American Institute of Physics Conference Series*, pages 630–637, November 2006. doi: 10.1063/1.2399635. URL `http://adsabs.harvard.edu/abs/2006AIPC..861..630G`.

S. E. G. Hales et al. A revised machine-readable source list for the Rees 38-MHz survey. *Monthly Notices of the Royal Astronomical Society*, 274:447–451, May 1995. doi: 10.1093/mnras/274.2.447. URL `http://adsabs.harvard.edu/abs/1995MNRAS.274..447H`.

W. F. Hanlon. Updated cosmic ray spectrum. 2012. URL `http://www.physics.utah.edu/~whanlon/spectrum.html`.

A. K. Harding. Pulsar High-Energy Emission From the Polar Cap and Slot Gap. *ArXiv e-prints*, October 2007. URL `http://adsabs.harvard.edu/abs/2007arXiv0710.3517H`.

A. K. Harding and C. Kalapotharakos. Synchrotron Self-Compton Emission from the Crab and Other Pulsars. *Astrophysical Journal*, 811:63, September 2015. doi: 10.1088/0004-637X/811/1/63. URL `http://adsabs.harvard.edu/abs/2015ApJ...811...63H`.

W. Heitler. *Quantum theory of radiation*. 1954. URL `http://adsabs.harvard.edu/abs/1954qtr..book.....H`.

E. A. Helder and J. Vink. Characterizing the Nonthermal Emission of Cassiopeia A. *Astrophysical Journal*, 686:1094-1102, October 2008. doi: 10.1086/591242. URL `http://adsabs.harvard.edu/abs/2008ApJ...686.1094H`.

A. Hewish, S. J. Bell, J. D. H. Pilkington, P. F. Scott, and R. A. Collins. Observation of a Rapidly Pulsating Radio Source. *Nature*, 217:709–713, February 1968. doi: 10.1038/217709a0. URL `http://adsabs.harvard.edu/abs/1968Natur.217..709H`.

A. M. Hillas. The Origin of Ultra-High-Energy Cosmic Rays. *Annual Review of Astron and Astrophys*, 22:425–444, 1984. doi: 10.1146/annurev.aa.22.090184.002233. URL `http://adsabs.harvard.edu/abs/1984ARA%26A..22..425H`.

A. M. Hillas. Cerenkov light images of EAS produced by primary gamma. *International Cosmic Ray Conference*, 3, August 1985. URL `http://adsabs.harvard.edu/abs/1985ICRC....3..445H`.

K. Hirotani. Pulsar Outer-gap Electrodynamics: Hardening of Spectral Shape in the Trailing Peak in the Gamma-Ray Light Curve. *Astrophysical Journal, Letters*, 733:L49, June 2011. doi: 10.1088/2041-8205/733/2/L49. URL `http://adsabs.harvard.edu/abs/2011ApJ...733L..49H`.

K. Hirotani. Luminosity Evolution of Gamma-Ray Pulsars. *Astrophysical Journal*, 766:98, April 2013. doi: 10.1088/0004-637X/766/2/98. URL `http://adsabs.harvard.edu/abs/2013ApJ...766...98H`.

G. B. Hobbs, R. T. Edwards, and R. N. Manchester. TEMPO2, a new pulsar-timing package - I. An overview. *Monthly Notices of the Royal Astronomical Society*, 369:655–672, June 2006. doi: 10.1111/j.1365-2966.2006.10302.x. URL `http://adsabs.harvard.edu/abs/2006MNRAS.369..655H`.

W. Hofmann et al. Status of the H.E.S.S. Project. *International Cosmic Ray Conference*, 5:2811, July 2003. URL `http://adsabs.harvard.edu/abs/2003ICRC....5.2811H`.

J. Holder. Latest results from VERITAS: Gamma 2016. In *6th International Symposium on High Energy Gamma-Ray Astronomy*, volume 1792 of *American Institute of Physics Conference Series*, page 020013, January 2017. doi: 10.1063/1.4968898. URL `http://adsabs.harvard.edu/abs/2017AIPC.1792b0013H`.

J. Holder et al. The first VERITAS telescope. *Astroparticle Physics*, 25:391–401, July 2006. doi: 10.1016/j.astropartphys.2006.04.002. URL `http://adsabs.harvard.edu/abs/2006APh....25..391H`.

D. Hrupec. Extragalactic sources of rapidly variable high energy gamma radiation, PhD. thesis. 2008.

J. M. Jackson et al. The Boston University-Five College Radio Astronomy Observatory Galactic Ring Survey. *Astrophysical Journal Supplement Series*, 163:145–159, March 2006. doi: 10.1086/500091. URL `http://adsabs.harvard.edu/abs/2006ApJS..163..145J`.

T. Jogler and S. Funk. Revealing W51C as a Cosmic Ray Source Using Fermi-LAT Data. *Astrophysical Journal*, 816:100, January 2016. doi: 10.3847/0004-637X/816/2/100. URL `http://adsabs.harvard.edu/abs/2016ApJ...816..100J`.

S. Johnston and A. Karastergiou. Pulsar braking and the P-dot{P} diagram. *Monthly Notices of the Royal Astronomical Society*, 467:3493–3499, May 2017. doi: 10.1093/mnras/stx377. URL `http://adsabs.harvard.edu/abs/2017MNRAS.467.3493J`.

E. Kafexhiu et al. Parametrization of gamma-ray production cross sections for p p interactions in a broad proton energy range from the kinematic threshold to PeV energies. *Physical Review D*, 90(12):123014, December 2014. doi: 10.1103/PhysRevD.90.123014. URL `http://adsabs.harvard.edu/abs/2014PhRvD..90l3014K`.

C. Kalapotharakos, A. K. Harding, and D. Kazanas. Gamma-Ray Emission in Dissipative Pulsar Magnetospheres: From Theory to Fermi Observations. *Astrophysical Journal*, 793:97, October 2014. doi: 10.1088/0004-637X/793/2/97. URL `http://adsabs.harvard.edu/abs/2014ApJ...793...97K`.

V. Kalogera and G. Baym. The Maximum Mass of a Neutron Star. *Astrophysical Journal, Letters*, 470:L61, October 1996. doi: 10.1086/310296. URL `http://adsabs.harvard.edu/abs/1996ApJ...470L..61K`.

J. Katsuta, Y. Uchiyama, and S. Funk. Extended Gamma-Ray Emission from the G25.0+0.0 Region: A Star-forming Region Powered by the Newly Found OB Association? *Astrophysical Journal*, 839:129, April 2017. doi: 10.3847/1538-4357/aa6aa3. URL `http://adsabs.harvard.edu/abs/2017ApJ...839..129K`.

S. R. Kelner, F. A. Aharonian, and V. V. Bugayov. Energy spectra of gamma rays, electrons, and neutrinos produced at proton-proton interactions in the very high energy regime. *Physical Review D*, 74(3):034018, August 2006. doi: 10.1103/PhysRevD.74.034018. URL `http://adsabs.harvard.edu/abs/2006PhRvD..74c4018K`.

D. Khangulyan, F. A. Aharonian, and S. R. Kelner. Simple Analytical Approximations for Treatment of Inverse Compton Scattering of Relativistic Electrons in the Blackbody Radiation Field. *Astrophysical Journal*, 783:100, March 2014. doi: 10.1088/0004-637X/783/2/100. URL `http://adsabs.harvard.edu/abs/2014ApJ...783..100K`.

J. G. Kirk, O. Skjæraasen, and Y. A. Gallant. Pulsed radiation from neutron star winds. *Astronomy and Astrophysics*, 388:L29–L32, June 2002. doi: 10.1051/0004-6361:20020599. URL `http://adsabs.harvard.edu/abs/2002A%26A...388L..29K`.

L. Kuiper et al. The Crab pulsar in the 0.75-30 MeV range as seen by CGRO COMPTEL. A coherent high-energy picture from soft X-rays up to high-energy gamma-rays. *Astronomy and Astrophysics*, 378:918–935, November 2001. doi: 10.1051/0004-6361:20011256. URL `http://adsabs.harvard.edu/abs/2001A%26A...378..918K`.

S. Kumar et al. A detailed study of Gamma-ray emission from Cassiopeia A using VERITAS. *ArXiv e-prints*, August 2015. URL http://adsabs.harvard.edu/abs/2015arXiv150807453K.

P. O. Lagage and C. J. Cesarsky. The maximum energy of cosmic rays accelerated by supernova shocks. *Astronomy and Astrophysics*, 125:249–257, September 1983. URL http://adsabs.harvard.edu/abs/1983A%26A...125..249L.

J. M. Laming and U. Hwang. On the Determination of Ejecta Structure and Explosion Asymmetry from the X-Ray Knots of Cassiopeia A. *Astrophysical Journal*, 597:347–361, November 2003. doi: 10.1086/378268. URL http://adsabs.harvard.edu/abs/2003ApJ...597..347L.

J. Lande et al. Search for Spatially Extended Fermi Large Area Telescope Sources Using Two Years of Data. *Astrophysical Journal*, 756:5, September 2012. doi: 10.1088/0004-637X/756/1/5. URL http://adsabs.harvard.edu/abs/2012ApJ...756....5L.

D. A. Leahy. Einstein IPC observations of 6 new radio supernova remnants. *Astronomy and Astrophysics*, 216:193–196, June 1989. URL http://adsabs.harvard.edu/abs/1989A%26A...216..193L.

R. W. Lessard et al. A new analysis method for reconstructing the arrival direction of TeV gamma rays using a single imaging atmospheric Cherenkov telescope. *Astroparticle Physics*, 15:1–18, March 2001. doi: 10.1016/S0927-6505(00)00133-X. URL http://adsabs.harvard.edu/abs/2001APh....15....1L.

T.-P. Li and Y.-Q. Ma. Analysis methods for results in gamma-ray astronomy. *Astrophysical Journal*, 272:317–324, September 1983. doi: 10.1086/161295. URL http://adsabs.harvard.edu/abs/1983ApJ...272..317L.

S. Lombardi. Advanced stereoscopic gamma-ray shower analysis with the MAGIC telescopes. *International Cosmic Ray Conference*, 3:266, 2011. doi: 10.7529/ICRC2011/V03/1150. URL http://adsabs.harvard.edu/abs/2011ICRC....3..266L.

M. S. Longair. *High Energy Astrophysics*. February 2011. URL http://adsabs.harvard.edu/abs/2011hea..book.....L.

D. R. Lorimer and M. Kramer. *Handbook of Pulsar Astronomy*. December 2004. URL http://adsabs.harvard.edu/abs/2004hpa..book.....L.

A. G. Lyne, R. S. Pritchard, and F. Graham-Smith. Twenty-Three Years of Crab Pulsar Rotational History. *Monthly Notices of the Royal Astronomical Society*, 265:1003, December 1993. URL http://adsabs.harvard.edu/abs/1993MNRAS.265.1003L.

M. Lyutikov, N. Otte, and A. McCann. The Very High Energy Emission from Pulsars: A Case for Inverse Compton Scattering. *Astrophysical Journal*, 754:33, July 2012. doi: 10.1088/0004-637X/754/1/33. URL http://adsabs.harvard.edu/abs/2012ApJ...754...33L.

K. K. Madsen et al. Broadband X-ray Imaging and Spectroscopy of the Crab Nebula and Pulsar with NuSTAR. *Astrophysical Journal*, 801:66, March 2015. doi: 10.1088/0004-637X/801/1/66. URL http://adsabs.harvard.edu/abs/2015ApJ...801...66M.

Y. Maeda et al. Suzaku X-Ray Imaging and Spectroscopy of Cassiopeia A. *Publications of the Astronomical Society of Japan*, 61:1217–1228, December 2009. doi: 10.1093/pasj/61.6.1217. URL `http://adsabs.harvard.edu/abs/2009PASJ...61.1217M`.

M. A. Malkov and L. O. Drury. Nonlinear theory of diffusive acceleration of particles by shock waves. *Reports on Progress in Physics*, 64:429–481, April 2001. doi: 10.1088/0034-4885/64/4/201. URL `http://adsabs.harvard.edu/abs/2001RPPh...64..429M`.

R. N. Manchester and J. H. Taylor. *Pulsars*. 1977. URL `http://adsabs.harvard.edu/abs/1977puls.book.....M`.

V. Marandon et al. A closer look at HESS J1837-069 following the pulsar discovery. In F. A. Aharonian, W. Hofmann, and F. Rieger, editors, *American Institute of Physics Conference Series*, volume 1085 of *American Institute of Physics Conference Series*, pages 320–323, December 2008. doi: 10.1063/1.3076671. URL `http://adsabs.harvard.edu/abs/2008AIPC.1085..320M`.

J. R. Mattox et al. The Likelihood Analysis of EGRET Data. *Astrophysical Journal*, 461:396, April 1996. doi: 10.1086/177068. URL `http://adsabs.harvard.edu/abs/1996ApJ...461..396M`.

W. J. Medd and K. V. V. Ramana. Flux-Density Measurements AR 3.15 Gc/s. *Astrophysical Journal*, 142:383, July 1965. doi: 10.1086/148293. URL `http://adsabs.harvard.edu/abs/1965ApJ...142..383M`.

P. G. Mezger et al. Maps of Cassiopeia A and the Crab Nebula at lambda 1.2 MM. *Astronomy and Astrophysics*, 167:145–150, October 1986. URL `http://adsabs.harvard.edu/abs/1986A%26A...167..145M`.

E. R. Micelotta, E. Dwek, and J. D. Slavin. Dust destruction by the reverse shock in the Cassiopeia A supernova remnant. *Astronomy and Astrophysics*, 590:A65, May 2016. doi: 10.1051/0004-6361/201527350. URL `http://adsabs.harvard.edu/abs/2016A%26A...590A..65M`.

R. Mirzoyan. On the Calibration Accuracy of Light Sensors in Atmospheric Cherenkov Fluorescence and Neutrino Experiments. *International Cosmic Ray Conference*, 7:265, 1997. URL `http://adsabs.harvard.edu/abs/1997ICRC....7..265M`.

I. Mochol. Pulsar Striped Winds. In D. F. Torres, editor, *Modelling Pulsar Wind Nebulae*, volume 446 of *Astrophysics and Space Science Library*, page 135, 2017. doi: 10.1007/978-3-319-63031-1_7. URL `http://adsabs.harvard.edu/abs/2017ASSL..446..135M`.

I. Mochol and J. Pétri. Very high energy emission as a probe of relativistic magnetic reconnection in pulsar winds. *Monthly Notices of the Royal Astronomical Society*, 449:L51–L55, April 2015. doi: 10.1093/mnrasl/slv018. URL `http://adsabs.harvard.edu/abs/2015MNRAS.449L..51M`.

A. Moralejo et al. MARS, the MAGIC Analysis and Reconstruction Software. *ArXiv e-prints*, July 2009. URL `http://adsabs.harvard.edu/abs/2009arXiv0907.0943M`.

R. A. Moralejo et al. MARS: The MAGIC Analysis and Reconstruction Software. Astrophysics Source Code Library, November 2010. URL `http://adsabs.harvard.edu/abs/2010ascl.soft11004M`.

J. A. Morse et al. Location of the Optical Reverse Shock in the Cassiopeia A Supernova Remnant. *Astrophysical Journal*, 614:727–736, October 2004. doi: 10.1086/423709. URL http://adsabs.harvard.edu/abs/2004ApJ...614..727M.

A. G. Muslimov and A. K. Harding. High-Altitude Particle Acceleration and Radiation in Pulsar Slot Gaps. *Astrophysical Journal*, 606:1143–1153, May 2004. doi: 10.1086/383079. URL http://adsabs.harvard.edu/abs/2004ApJ...606.1143M.

P. Narayana Bhat et al. The Third Fermi GBM Gamma-Ray Burst Catalog: The First Six Years. *Astrophysical Journal Supplement Series*, 223:28, April 2016. doi: 10.3847/0067-0049/223/2/28. URL http://adsabs.harvard.edu/abs/2016ApJS..223...28N.

Z. Osmanov and F. M. Rieger. On particle acceleration and very high energy γ-ray emission in Crab-like pulsars. *Astronomy and Astrophysics*, 502:15–20, July 2009. doi: 10.1051/0004-6361/200912101. URL http://adsabs.harvard.edu/abs/2009A%26A...502...15O.

Z. Osmanov and F. M. Rieger. Pulsed VHE emission from the Crab Pulsar in the context of magnetocentrifugal particle acceleration. *Monthly Notices of the Royal Astronomical Society*, 464:1347–1352, January 2017. doi: 10.1093/mnras/stw2408. URL http://adsabs.harvard.edu/abs/2017MNRAS.464.1347O.

E. A. Parker. Precise measurement of the flux densities of the radio sources Cas A and Cyg A at metre wavelengths. *Monthly Notices of the Royal Astronomical Society*, 138:407, 1968. doi: 10.1093/mnras/138.4.407. URL http://adsabs.harvard.edu/abs/1968MNRAS.138..407P.

D. J. Patnaude and R. A. Fesen. Small-Scale X-Ray Variability in the Cassiopeia A Supernova Remnant. *The Astronomical Journal*, 133:147–153, January 2007. doi: 10.1086/509571. URL http://adsabs.harvard.edu/abs/2007AJ....133..147P.

A. Petriella, S. Paron, and E. Giacani. The interstellar medium towards the supernova remnant G24.7+0.6. *Boletin de la Asociacion Argentina de Astronomia La Plata Argentina*, 51:209–212, 2008. URL http://adsabs.harvard.edu/abs/2008BAAA...51..209P.

A. Petriella, S. Paron, and E. Giacani. Young stellar objects around the supernova remnant G24.7+0.6. *Boletin de la Asociacion Argentina de Astronomia La Plata Argentina*, 53:221–224, 2010. URL http://adsabs.harvard.edu/abs/2010BAAA...53..221P.

A. Petriella, S. A. Paron, and E. B. Giacani. The molecular gas around the luminous blue variable star G24.73+0.69. *Astronomy and Astrophysics*, 538:A14, February 2012. doi: 10.1051/0004-6361/201118394. URL http://adsabs.harvard.edu/abs/2012A%26A...538A..14P.

V. S. Ptuskin and V. N. Zirakashvili. On the spectrum of high-energy cosmic rays produced by supernova remnants in the presence of strong cosmic-ray streaming instability and wave dissipation. *Astronomy and Astrophysics*, 429:755–765, January 2005. doi: 10.1051/0004-6361:20041517. URL http://adsabs.harvard.edu/abs/2005A%26A...429..755P.

V. Radhakrishnan and G. Srinivasan. On the origin of the recently discovered ultra-rapid pulsar. *Current Science*, 51:1096–1099, December 1982. URL http://adsabs.harvard.edu/abs/1982CSci...51.1096R.

J. E. Reed et al. The Three-dimensional Structure of the Cassiopeia A Supernova Remnant. I. The Spherical Shell. *Astrophysical Journal*, 440:706, February 1995. doi: 10.1086/175308. URL `http://adsabs.harvard.edu/abs/1995ApJ...440..706R`.

W. Reich, E. Furst, and Y. Sofue. Two new filled-center supernova remnants - G24.7+0.6 and G27.8+0.6. *Astronomy and Astrophysics*, 133:L4–L7, April 1984. URL `http://adsabs.harvard.edu/abs/1984A%26A...133L...4R`.

I. Reichardt et al. An extended source of GeV gamma rays coincident with the supernova remnant HB 21. *Astronomy and Astrophysics*, 546:A21, October 2012. doi: 10.1051/0004-6361/201219947. URL `http://adsabs.harvard.edu/abs/2012A%26A...546A..21R`.

E. M. Reynoso and J. G. Mangum. CO Observations toward Supernova Remnants with Associated OH 1720 MHZ Masers. *Astrophysical Journal*, 545:874–884, December 2000. doi: 10.1086/317854. URL `http://esoads.eso.org/abs/2000ApJ...545..874R`.

W. A. Rolke, A. M. López, and J. Conrad. Limits and confidence intervals in the presence of nuisance parameters. *Nuclear Instruments and Methods in Physics Research A*, 551:493–503, October 2005. doi: 10.1016/j.nima.2005.05.068. URL `http://adsabs.harvard.edu/abs/2005NIMPA.551..493R`.

R. W. Romani and I.-A. Yadigaroglu. Gamma-ray pulsars: Emission zones and viewing geometries. *Astrophysical Journal*, 438:314–321, January 1995. doi: 10.1086/175076. URL `http://adsabs.harvard.edu/abs/1995ApJ...438..314R`.

C. Romoli, A. M. Taylor, and F. Aharonian. Cut-off characterisation of energy spectra of bright fermi sources: Current instrument limits and future possibilities. *Astroparticle Physics*, 88:38–45, February 2017. doi: 10.1016/j.astropartphys.2016.12.007.

M. A. Ruderman and P. G. Sutherland. Theory of pulsars - Polar caps, sparks, and coherent microwave radiation. *Astrophysical Journal*, 196:51–72, February 1975. doi: 10.1086/153393. URL `http://adsabs.harvard.edu/abs/1975ApJ...196...51R`.

L. Saha et al. Origin of gamma-ray emission in the shell of Cassiopeia A. *Astronomy and Astrophysics*, 563:A88, March 2014. doi: 10.1051/0004-6361/201323218. URL `http://adsabs.harvard.edu/abs/2014A%26A...563A..88S`.

M. Schmelling. Numerische Methoden der datenanalyse, MPI-K Heidelberg. 1998.

F. D. Seward. Einstein Observations of Galactic supernova remnants. *Astrophysical Journal Supplement Series*, 73:781–819, August 1990. doi: 10.1086/191489. URL `http://adsabs.harvard.edu/abs/1990ApJS...73..781S`.

T. Siegert et al. Revisiting INTEGRAL/SPI observations of ^{44}Ti from Cassiopeia A. *Astronomy and Astrophysics*, 579:A124, July 2015. doi: 10.1051/0004-6361/201525877. URL `http://adsabs.harvard.edu/abs/2015A%26A...579A.124S`.

L. Sironi and A. Spitkovsky. Relativistic Reconnection: An Efficient Source of Non-thermal Particles. *Astrophysical Journal, Letters*, 783:L21, March 2014. doi: 10.1088/2041-8205/783/1/L21. URL `http://adsabs.harvard.edu/abs/2014ApJ...783L..21S`.

A. Spitkovsky. Time-dependent Force-free Pulsar Magnetospheres: Axisymmetric and Oblique Rotators. *Astrophysical Journal, Letters*, 648:L51–L54, September 2006. doi: 10.1086/507518. URL `http://adsabs.harvard.edu/abs/2006ApJ...648L..51S`.

J. Takata et al. A two-dimensional electrodynamical outer gap model for γ-ray pulsars: γ-ray spectrum. *Monthly Notices of the Royal Astronomical Society*, 366:1310–1328, March 2006. doi: 10.1111/j.1365-2966.2006.09904.x. URL `http://adsabs.harvard.edu/abs/2006MNRAS.366.1310T`.

G. A. Tammann, W. Loeffler, and A. Schroeder. The Galactic supernova rate. *Astrophysical Journal Supplement Series*, 92:487–493, June 1994. doi: 10.1086/192002. URL `http://adsabs.harvard.edu/abs/1994ApJS...92..487T`.

T. Tanaka et al. Gamma-Ray Observations of the Supernova Remnant RX J0852.0-4622 with the Fermi Large Area Telescope. *Astrophysical Journal, Letters*, 740:L51, October 2011. doi: 10.1088/2041-8205/740/2/L51. URL `http://adsabs.harvard.edu/abs/2011ApJ...740L..51T`.

M. Tavani et al. The AGILE Mission. *Astronomy and Astrophysics*, 502:995–1013, August 2009. doi: 10.1051/0004-6361/200810527. URL `http://adsabs.harvard.edu/abs/2009A%26A...502..995T`.

A. N. Tikhonov and V.J. Arsenin. Methods of solution of illposed problems, Nauka, Moscow. 1979.

D. F. Torres, A. Y. Rodriguez Marrero, and E. de Cea Del Pozo. MAGIC J0616+225 as delayed TeV emission of cosmic rays diffusing from the supernova remnant IC 443. *Monthly Notices of the Royal Astronomical Society*, 387:L59–L63, June 2008. doi: 10.1111/j.1745-3933.2008.00485.x. URL `http://adsabs.harvard.edu/abs/2008MNRAS.387L..59T`.

D. F. Torres, A. Y. R. Marrero, and E. de Cea Del Pozo. The GeV to TeV connection in the environment of SNR IC 443. *Monthly Notices of the Royal Astronomical Society*, 408:1257–1266, October 2010. doi: 10.1111/j.1365-2966.2010.17205.x. URL `http://adsabs.harvard.edu/abs/2010MNRAS.408.1257T`.

Y. Uchiyama and F. A. Aharonian. Fast Variability of Nonthermal X-Ray Emission in Cassiopeia A: Probing Electron Acceleration in Reverse-Shocked Ejecta. *Astrophysical Journal, Letters*, 677:L105, April 2008. doi: 10.1086/588190. URL `http://adsabs.harvard.edu/abs/2008ApJ...677L.105U`.

C. M. Urry and P. Padovani. Unified Schemes for Radio-Loud Active Galactic Nuclei. *Publications of the ASP*, 107:803, September 1995. doi: 10.1086/133630. URL `http://adsabs.harvard.edu/abs/1995PASP..107..803U`.

P. A. Čerenkov. Visible Radiation Produced by Electrons Moving in a Medium with Velocities Exceeding that of Light. *Physical Review*, 52:378–379, August 1937. doi: 10.1103/PhysRev.52.378. URL `http://adsabs.harvard.edu/abs/1937PhRv...52..378C`.

D. Viganò and D. F. Torres. Modelling of the γ-ray pulsed spectra of Geminga, Crab, and Vela with synchro-curvature radiation. *Monthly Notices of the Royal Astronomical Society*, 449:3755–3765, June 2015. doi: 10.1093/mnras/stv579. URL `http://adsabs.harvard.edu/abs/2015MNRAS.449.3755V`.

D. Viganò et al. An assessment of the pulsar outer gap model - II. Implications for the predicted γ-ray spectra. *Monthly Notices of the Royal Astronomical Society*, 447:2649–2657, March 2015. doi: 10.1093/mnras/stu2565. URL `http://adsabs.harvard.edu/abs/2015MNRAS.447.2649V`.

J. Vink and J. M. Laming. On the Magnetic Fields and Particle Acceleration in Cassiopeia A. *Astrophysical Journal*, 584:758–769, February 2003. doi: 10.1086/345832. URL `http://adsabs.harvard.edu/abs/2003ApJ...584..758V`.

H. J. Völk and K. Bernlöhr. Imaging very high energy gamma-ray telescopes. *Experimental Astronomy*, 25:173–191, August 2009. doi: 10.1007/s10686-009-9151-z. URL `http://adsabs.harvard.edu/abs/2009ExA....25..173V`.

Ie. Vovk, M. Strzys, and C. Fruck. A spacial likelihood analysis for MAGIC telescope data. From instrument response modelling to spectral extraction. *"In preparation"*, 2018.

R. Wagner. Measurement of VHE gamma-ray emission from four blazars using the MAGIC telescope and a comparative blazar study., PhD. thesis. 2006.

W. Wang and Z. Li. Hard X-Ray Emissions from Cassiopeia A Observed by INTEGRAL. *Astrophysical Journal*, 825:102, July 2016. doi: 10.3847/0004-637X/825/2/102. URL `http://adsabs.harvard.edu/abs/2016ApJ...825..102W`.

T. Weisgarber. The High-Altitude Water Cherenkov Observatory: First Light. In *APS Meeting Abstracts*, page D14.004, April 2013. URL `http://adsabs.harvard.edu/abs/2013APS..APRD14004W`.

R. L. White and K. S. Long. Supernova remnant evolution in an interstellar medium with evaporating clouds. *Astrophysical Journal*, 373:543–555, June 1991. doi: 10.1086/170073. URL `http://adsabs.harvard.edu/abs/1991ApJ...373..543W`.

M. Wood et al. Fermipy: An open-source Python package for analysis of Fermi-LAT Data. *ArXiv e-prints*, July 2017. URL `http://adsabs.harvard.edu/abs/2017arXiv170709551W`.

R.-z. Yang, E. de Oña Wilhelmi, and F. Aharonian. Diffuse gamma-ray emission in the vicinity of young star cluster Westerlund 2. *ArXiv e-prints*, October 2017. URL `http://adsabs.harvard.edu/abs/2017arXiv171002803Y`.

Y. Yuan et al. Fermi Large Area Telescope Detection of a Break in the Gamma-Ray Spectrum of the Supernova Remnant Cassiopeia A. *Astrophysical Journal*, 779:117, December 2013. doi: 10.1088/0004-637X/779/2/117. URL `http://adsabs.harvard.edu/abs/2013ApJ...779..117Y`.

V. Zabalza. Naima: a Python package for inference of particle distribution properties from nonthermal spectra. In A. S. Borisov, V. G. Denisova, Z. M. Guseva, E. A. Kanevskaya, M. G. Kogan, A. E. Morozov, V. S. Puchkov, S. E. Pyatovsky, G. P. Shoziyoev, M. D. Smirnova, A. V. Vargasov, V. I. Galkin, S. I. Nazarov, and R. A. Mukhamedshin, editors, *34th International Cosmic Ray Conference (ICRC2015)*, volume 34 of *International Cosmic Ray Conference*, page 922, July 2015. URL `http://adsabs.harvard.edu/abs/2015ICRC...34..922Z`.

R. Zanin et al. MARS, the MAGIC analysis and reconstruction software. *International Cosmic Ray Conference*, 1:773, 2013.

R. Zanin et al. Gamma rays detected from Cygnus X-1 with likely jet origin. *Astronomy and Astrophysics*, 596:A55, November 2016. doi: 10.1051/0004-6361/201628917. URL `http://adsabs.harvard.edu/abs/2016A%26A...596A..55Z`.

G. T. Zatsepin and V. A. Kuz'min. Upper Limit of the Spectrum of Cosmic Rays. *Soviet Journal of Experimental and Theoretical Physics Letters*, 4:78, August 1966. URL `http://adsabs.harvard.edu/abs/1966JETPL...4...78Z`.

V. N. Zirakashvili et al. Nonthermal Radiation of Young Supernova Remnants: The Case of CAS A. *Astrophysical Journal*, 785:130, April 2014. doi: 10.1088/0004-637X/785/2/130. URL `http://adsabs.harvard.edu/abs/2014ApJ...785..130Z`.